IKE Institut für Kernenergetik
und Energiesysteme

Determination of Kinetic Parameters for Monitoring Source Driven Subcritical Transmutation Devices

Maarten Becker

Universität Stuttgart

März 2014 IKE 6-213

IKE Institut für Kernenergetik
und Energiesysteme

Determination of Kinetic Parameters for Monitoring Source Driven Subcritical Transmutation Devices

von der Fakultät Energie-, Verfahrens-
und Biotechnik der Universität Stuttgart
zur Erlangung der Würde eines
Doktor-Ingenieurs (Dr.-Ing.)
genehmigte Abhandlung

vorgelegt von

Diplom-Ingenieur
Maarten Becker

geboren in Bonn

Hauptberichter:
Prof. G. Lohnert, Ph.D.

Mitberichter:
Prof. Dr. V. Heinzel

Tag der Einreichung: 29.12.2012

Tag der mündlichen Prüfung: 20.08.2013

ISSN – 0173 – 6892

März 2014 IKE 6-213

Universität Stuttgart

To Jakob, Johan, and Svenja

Contents

Appendices

List of Figures

List of Tables

Nomenclature

Letters indicating variables are written in *italic* font. Letters in **bold** print are vectors or matrices otherwise scalar quantities. Abbreviations and specifiers with a fixed meaning are written in normal upright letters.

Units are not necessarily SI units. The units fitting best to the context of the equation and corresponding to common quantities of the reactor physics area are preferred. The units are given in the most general way. For example the unit of the neutron angular density N is defined as $[\mathrm{cm}^{-3}\,\mathrm{sr}^{-1}\,\mathrm{eV}^{-1}]$ [1]. The unit of the neutron angular flux defined as product of neutron velocity and neutron angular density $v\,N$ consequently is $[\mathrm{cm}^{-2}\,\mathrm{sr}^{-1}\,\mathrm{eV}^{-1}\,\mathrm{s}^{-1}]$. However, in the discrete ordinates transport codes the angular flux must have the same unit as the scalar flux, because $\phi = \sum\limits_u w_u \psi(\boldsymbol{\Omega}_u)$ and the quadrature weight has no unit [2]. To get the neutron angular flux as mentioned above the discrete ordinates angular flux $\psi(\boldsymbol{\Omega}_u)$ has to be divided by the full solid angle 4π. Thus, the unit of the variable depends sometimes on the context of its usage.

Latin variables

Variable	Unit	Description
A	–	integration area, normalization constant
a	cm	length
B	–	surface
C	cm^{-3}	precursor nuclide concentration
E	eV	neutron energy
F	–	normalization integral
$\boldsymbol{F}$	–	fission source operator
f	–	function, Legendre coefficient
I	s^{-1}	source intensity
J		neutron current
k	–	effective multiplication factor, eigenvalue
$\boldsymbol{L}$	–	transport operator
M	–	source multiplication
$\boldsymbol{M}$	–	total operator
N	$\mathrm{cm}^{-3}\,\mathrm{sr}^{-1}\,\mathrm{eV}^{-1}$	neutron angular density
N	–	spherical harmonics normalization factor
$\boldsymbol{n}$	–	normal vector
n	–	neutral particle
L	–	Legendre order
P	–	amplitude function, (associated) Legendre polynomial
Q	$\mathrm{cm}^{-3}\,\mathrm{s}^{-1}$	external neutron source
q	$\mathrm{cm}^{-3}\,\mathrm{s}^{-1}$	source term
r	cm	radius
$\boldsymbol{r}$	cm	position vector
S	$\mathrm{cm}^{-3}\,\mathrm{s}^{-1}$	source term
t	s	time variable
u	–	lethargy
v	$\mathrm{cm}\,\mathrm{s}^{-1}$	neutron velocity
V	cm^{3}	Volume
w	–	quadrature weight
Y	–	spherical harmonics function

Greek variables

Variable	Unit	Description
α	s^{-1}	time eigenvalue
β	–	delayed neutron fraction
$\upbeta$	–	beta particle
γ	–	factor of implicit time scheme
$\upgamma$	–	photon particle
Δ	–	difference
ϵ	–	convergence criterion
η	–	general eigenvalue
Λ	s	mean neutron generation time
λ	s^{-1}	decay constant
μ	–	scattering cosine
ν	–	neutron yield
φ	rad	azimuthal angle
ϕ	$\mathrm{cm}^{-2}\,\mathrm{s}^{-1}$	scalar neutron flux
χ	–	fission spectrum, emission spectrum
ψ	$\mathrm{cm}^{-2}\,\mathrm{sr}^{-1}\,\mathrm{eV}^{-1}\,\mathrm{s}^{-1}$	angular neutron flux
Σ	cm^{-1}	macroscopic cross section
ρ	–	reactivity
θ	rad	polar angle
$\boldsymbol{\Omega}$	sr	solid angle

Index abbreviations

Index	Description
α	alpha particle
0	fundamental mode
eff	effective
c	capture
d	delayed, deuterium, detector
e	elastic
f, fiss	fission
γ	photon particle
hom	homogeneous
inel, i	inelastic
inf	infinite
inh	inhomogeneous
n	neutral particle
p	prompt
s	scattering
src	source
ss	steady-state
reg	region
rel	relative
t	total, tritium
x	multiplicity in (n,xn) reactions
$\dagger$	adjoint

Index variables

Index	Description
g	energy group
i	isotope, mesh interval in x-direction (or radial)
j	delayed neutron time group, mesh interval in y-direction
k	flux modes, mesh interval in z-direction
l	Legendre order
m	moment of the associated Legendre function
n	volume element counter
t	time
τ	time step index
u, v	discrete direction

Acronyms

ADS Accelerator Driven System.

BC Boundary Condition.

CRP Coordinated Research Project.

EC Experimental Channel.

FA Fuel Assembly.
FBR Fast Breeder Reactor.
FDF Formula Definition File.

GRS Gesellschaft für Anlagen- und Reaktorsicherheit.

IAEA International Atomic Energy Agency.

JIPNR Joint Institute for Power and Nuclear Research.

LLFP Long-Lived Fission Products.
LWR Light Water Reactor.

MA Minor Actinides.
MC Monte Carlo.
MOX Mixed Oxide.

NR Narrow-Resonance.

PE Polyethylene.
PNS Pulsed Neutron Source.
PWR Pressurized Water Reactor.

RSICC Radiation Safety Information Computational Center.

TLLWR Tight Lattice Light Water Reactor.
TSO Technical Safety Organization.

Abstract

ADS are considered as an option for the irradiation facility in partitioning and transmutation concepts for highly radioactive waste from spent nuclear fuel. Due to the hard neutron energy spectrum and the subcriticality of the reactor ADS provide a good compromise between transmutation performance and safety aspects. For the safe operation, but also for the overall optimization of the facility, the determination of the subcriticality level is essential.

To investigate experimental methods in Pulsed Neutron Source (PNS) experiments for the determination of the subcriticality level the ADS experiment YALINA-Thermal is thoroughly analyzed in this work. The experiment has been performed from 2005-2010 in Minsk, Belarus.

Most of the related experimental methods rely on point kinetic equations. This approach introduces two main approximations. Firstly, the point kinetic equation cannot describe the transition of the neutron distribution from the source operation to the source shutdown. After shutdown, the neutron population would redistribute to establish the fundamental decay mode. This violates the point kinetic assumption of neutron flux spectra constant in time. Secondly, to calculate kinetic parameters like the neutron mean generation time and the effective delayed neutron fraction the neutron flux distribution of the effective multiplication factor equation is typically used, which is equivalent to an artificial critical steady-state reactor. However, it is the time-dependence of the decay of the neutron populations including their redistribution in space and energy, which affects the analyzed kinetic parameters. Consequently, this work aims for the accurate simulation of these phenomena with particular emphasis on the quality of the effective neutron cross sections.

In this work new microscopic master libraries based on the JEFF 3.1, JEFF 3.1.1 and ENDF/B VII.0 evaluations are developed with a general purpose 350 energy groups structure for the deterministic reactor physics code system KANEXT.

The time-dependent transport code TORT-TD developed by Gesellschaft für Anlagen- und Reaktorsicherheit (GRS) is extended in this work for a time-dependent external neutron source. This new option and the fully implicit time integration scheme provides a very accurate simulation of PNS experiments considering non-asymptotic neutron distributions and delayed neutrons. After neutron source shutdown the code allows for the decay of the neutron populations based on the physical principles. These time-dependent neutron fluxes are used for the calculation of time-dependent kinetic parameters.

The simulation of the YALINA-Thermal experiment with the extended TORT-TD code and the new cross section data shows, that the impact of delayed neutrons manifests before the fundamental decay mode is established and thus needs to be considered in the experimental evaluation. Comparing the neutron mean generation time calculated with the neutron flux of the effective multiplication factor solution and with the time-dependent flux yields a 16 % difference. The effective delayed neutron fraction - as expected - is indifferent to the above method, as the delayed neutron yield of the main fissionable isotope $^{235}_{92}$U is constant below 0.01 MeV.

Zusammenfassung

Zur Reduzierung von Lagerdauer und -kapazität sowie Radiotoxizität von hoch radioaktivem Abfall größtenteils aus der zivilen Nutzung der Kernenergie in Kernkraftwerken werden weltweit im Rahmen von Transmutations- und Partitionierungsstrategien Beschleuniger getriebene Systeme, im Englischen ADS, als Bestrahlungseinrichtung diskutiert. ADS bieten mit Verweis auf das harte Neutronenspektrum und auf die Unterkritikalität des Reaktors einen guten Kompromiss zwischen Transmutationsleistung und Sicherheitseigenschaften. Für den sicheren Betrieb, aber auch für die Optimierung der Gesamtanlage, ist die Überwachung der Unterkritikalität essenziell.

Um vorgeschlagene, experimentelle Methoden mit gepulsten Neutronenquellen, im Englischen Pulsed Neutron Source (PNS), zur Kritikalitätsüberwachung zu qualifizieren, wird in dieser Arbeit das ADS-Experiment YALINA-Thermal eingehend analysiert, das zwischen 2005 und 2010 in Minsk, Weißrussland, durchgeführt wurde.

Praktisch alle experimentellen Methoden zur Bestimmung der Unterkritikalität beruhen auf dem Ansatz der Punktkinetik. Ein Nachteil dieser Näherung besteht darin, dass die Punktkinetik den instationären Übergang vom kurzzeitigen Ein- und Abschalten der Neutronenquelle und dem nachgelagerten Abklingen der Neutronenpopulationen nicht beschreiben kann. Dies führt dazu, dass die Voraussetzung der zeitlich konstanten Neutronenflussspektren im betrachteten Zeitfenster nicht gegeben ist. Des Weiteren werden typischerweise zur Berechnung der Punktkinetikparameter wie der effektiven Neutronengenerationsdauer oder des effektiven Anteils der verzögerten Neutronen die Neutronenflussspektren der statischen Lösung der Boltzmann-Transportgleichung für den effektiven Multiplikationsfaktor verwendet. Dabei hat gerade die räumliche und energetische Reorganisation der Neutronen während des Abklingvorgangs einen maßgeblichen Einfluss auf die kinetischen Parameter. Diese Arbeit zielt auf die genaue Beschreibung dieser Phänomene unter besonderer Berücksichtigung der Qualität der effektiven Neutronenwirkungsquerschnitte ab.

In dieser Arbeit werden neue, 350 Energiegruppen umfassende, mikroskopische Masterbibliotheken basierend auf den JEFF 3.1, JEFF 3.1.1 und ENDF/B VII.0 Evaluationen für das modulare, deterministische Programmsystem KANEXT entwickelt.

Für die zeitabhängige Untersuchung wird im Rahmen dieser Arbeit das deterministische Neutronentransportprogramm TORT-TD, das von der GRS entwickelt wird, um eine zeitabhängige Option für Quellneutronen erweitert. Aufgrund der vollimpliziten Zeitintegration kann eine sehr genaue zeitabhängige Simulation eines gepulsten Experiments unter Berücksichtigung von nicht-asymptotischen Neutronenfeldern und der Bilanzierung der lokalen verzögerten Neutronen erfolgen. Darüber hinaus lässt dieses Verfahren nach Beendigung des Pulses das Abklingen der Neutronenpopulationen zu, sodass aus diesen Spektren zeitabhängige kinetische Parameter berechnet werden können.

Es zeigt sich in der Nachrechnung der YALINA-Thermal Experimente mit dem erweiterten TORT-TD Programm und den neuen Wirkungsquerschnittsdaten, dass die Ausbildung des Hauptabklingmodus vom Einfluss der verzögerten Neutronen überlagert wird und damit in der experimentellen Auswertung berücksichtigt werden muss. Es ergibt sich für die Neutronengenerationsdauer, berechnet mit den statischen Flussspektren sowie mit den zeitabhängigen Flussspektren, ein Unterschied von 16 %. Für den effektiven Anteil der verzögerten Neutronen ist erwartungsgemäß kein Einfluss festgestellt worden, da die Ausbeute der verzögerten Neutronen unterhalb von etwa 0.01 MeV für den Hauptspaltstoff $^{235}_{92}\mathrm{U}$ konstant verläuft.

Chapter 1

Introduction

One of the key issues in the use of nuclear energy is the long-term storage of highly radioactive and radiotoxic spent fuel. For almost two decades a remarkable endeavor was put to investigate Minor Actinides (MA) and Long-Lived Fission Products (LLFP) of spent fuel. A significant reduction of the long-term spent fuel toxicity and storage period can be achieved by partitioning and transmuting these nuclei. It was shown that a potential reduction from 100 000 y to about 1000 y is feasible, if it is related to the radiotoxicity of natural uranium depending on fuel cycle concepts [3, 4].

Within the relevant reactors for waste incineration one usually counts two types: fast critical reactors and fast spectra Accelerator Driven System (ADS). The above mentioned first type benefits from its evolutionary design based on experience of former fast reactor concepts like the Enrico Fermi fast breeder reactor in the United States, Super-Phénix 1 and 2 in France, MONJU in Japan or SNR in Germany [5, 6]. Their disadvantage as far as transmutation is concerned is that MA deteriorate the safety characteristics namely the delayed neutron fraction and feedback coefficients [7]. On the other hand, the ADS cores suffer obviously from lack of existing experience. The feasibility of the combination of a large proton beam spallation source with a subcritical core has still to be demonstrated. Nevertheless, the attractiveness of the ADS type originates in its enhanced safety characteristics due to its subcriticality.

The intense scientific work on ADS was originally triggered by a LANL work [8], where a subcritical Molten Salt reactor driven by a spallation neutron source with very high thermal neutron flux was investigated for waste transmutation, and an US NRC report on transmutation with one dedicated ADS concept [9, 10]. In Europe the ADS concept was driven initially by the energy amplifier concept of Carlo Rubbia [11] as a "totally safe" ADS alternative to the critical reactor designs. Later on, it was converted into the transmutation concept parallel to the developments in the US. Since then several projects were launched to deal with the importance of transmutation features as can be seen in table 1.1.

An important additional project YALINA was initiated in the Joint Institute for Power and Nuclear Research (JIPNR) located at Sosny nearby Minsk, Belarus. The project was embedded also in an International Atomic Energy Agency (IAEA) Coordinated Research Project (CRP) and moreover in the ECATS domain of the EUROTRANS project (*see* table 1.1). It was the first of its kind in the sense of coupling an external neutron source with a multiplying medium in a subcritical, thermal system with fresh enriched uranium fuel and large graphite reflector.

Table 1.1: European projects on ADS research

Project	Period	Aim
IABAT	1996 - 1999	Broad assessment of system and fuel cycle issues, nuclear and material data and accelerator technology [12]
MUSE	1996 - 2004	Neutron physical characterization of a fast zero-power ADS in measurement and simulation [13, 14]
TRADE	2002 - 2004	Investigation of feedback effects in a subcritical, thermal low power TRIGA reactor coupled with a spallation neutron source (abandoned for financial reasons) [15]
MEGAPIE	2001 - 2006	Target physics and design of intense proton beam spallation neutron sources [16]
PDS-XADS	2001 - 2004	Preliminary design studies for an experimental ADS with 80 MW thermal power [17]
IP-EUROTRANS	2005 - 2010	The large European project governing 5 technical and scientific domains (DM): **DM1 DESIGN:** Development of reference designs under which the short-term demonstration of transmutation of a small scale ADS (XT-ADS) and the long-term demonstration of industrial scale transmutation (EFIT) **DM2 ECATS:** Experimental reactivity assessment with the projects YALINA-Booster and GUINEVERE as continuation of the MUSE experiments for subcriticality monitoring with pulsed, continuous and interrupted source [18] **DM3 AFTRA:** Investigation of alternative uranium-free fuel to support partitioning aims **DM4 DEMETRA:** Assessment of heavy liquid metal coolants suitable for core and target cooling and its thermal-hydraulic impacts **DM5 NUDATRA:** Examination and completion of the nuclear data needs for transmutation
FREYA	2011 - 2015	Continuation of GUINEVERE for subcritical monitoring of ADS and accompanying the MYRRHA project
MYRRHA	2010 - 2023	Building a multipurpose irradiation facility with critical and ADS operation; envisaged to be commissioned in the year 2023

The main idea was to launch experiments for the determination of the subcriticality level. The motivation lays in the fact that the common experimental methods are either for critical $k_{\text{eff}} \simeq 1$ or for deep subcritical, unreflected systems $k_{\text{eff}} < 0.9$. Contrarily, ADS reactors are foreseen to operate at about $0.95 \leq k_{\text{eff}} \leq 0.98$ with optimized neutron economy by means of reflectors. Mathematically, the governing reactor physics equation of a critical reactor is a homogeneous eigenvalue equation, while ADS are described by an inhomogeneous fixed source equation. And finally, in the Pulsed Neutron Source (PNS) experiment, the transition of both the shortly operating neutron source and the subcritical, source-free decay of the neutron population are encountered.

The reactivity control and monitoring is however essential, since in the initial designs no control rods were foreseen. Moreover, the deployment of fuel with MA constitutes a reduction in safety characteristics, which emphasizes once more the need for accurate evaluation of the operating reactivity level.

The experiment-based YALINA-Thermal benchmark was adapted to provide a comprehensive investigation involving nuclear data and methods of time-dependent neutron propagation in multiplying medium. Based on the YALINA-Thermal experiments this study aims at analyzing current methods for the calculation of subcritical kinetic parameters such as mean neutron generation time, effective delayed neutron fraction and reactivity as well as exploring a new innovative three-dimensional neutron transport solution for the accurate evaluation of the mentioned parameters.

The work is organized in the following manner:

Chapter 2 The reactor physical theory is summarized in view of the experimental methods for reactivity determination, its application to the experimental situation and the demands for an accurate simulation including the neutron source operation, instationary effects and the transition into the quasi-static delayed neutron background. As a final requirement the need for a deterministic time-dependent transport code based on a direct time-dependent method is formulated.

Chapter 3 This chapter deals with the preparation of effective cross sections from the underlying general nuclear data evaluations. In this context new microscopic fine-group master libraries are created suitable for the homogenization procedure in the deterministic reactor physics code system `KANEXT`. The peculiarities related to the use in multigroup transport codes are analyzed. The validation is performed on the basis of a code-to-code comparison with a Monte Carlo (MC) based solution on pin and core level. From this static, asymptotic solution the classic effective kinetic parameters are calculated according to perturbation theory methods in order to compare with the time-dependent solution procedure.

Chapter 4 The new developed time-dependent source capability in the neutron transport code `TORT-TD` and a new method for providing the energy-angle dependent neutron source is presented. In addition, an improvement for the spectral dependent delayed neutron production is proposed.

Chapter 5 In this chapter the new capability of `TORT-TD` is applied to the YALINA-Thermal experiment for validation purposes. It is shown that the kinetic parameters can be calculated more accurately with help of the new flux solution than with the common static flux approach.

Chapter 6 The last chapter summarizes the accomplished tasks. Moreover, it outlines the achievements and points to potential future applications and improvements.

Chapter 2

Theory of Neutron Transport in Pulsed Neutron Source Experiments

In this chapter the relevant reactor theory and the numerical treatment is described in order to underline the appropriateness and shortcomings of the common approaches to interpret the results of Pulsed Neutron Source (PNS) experiments. In the first section 2.1 the fundamental time-dependent transport equation is described which governs in general the neutron physics of nuclear reactors. Subsections explain the important adaptions of the general transport equations to special cases (energy discretization, time-independent effective multiplication, time eigenvalue problem). These special cases are recalled in the description of the PNS experiment and the determination of the subcriticality. A detailed discussion on the methods, their validity and applicability follows in section 2.2. Finally, in section 2.3 the base of the new approach applied in this thesis is given with an alternative method to solve the time-dependent transport equation including an external neutron source.

2.1 The Time-Dependent Transport Equation

The evolution of neutrons in a multiplying medium with external neutron source is described by the time-dependent transport equation (2.1) with an additional volume source term [1,19]. Note that all variables and indices are defined in the chapter Nomenclature (page xvii).

$$\begin{aligned}
&\underbrace{\frac{1}{v}\frac{\partial}{\partial t}\psi(\boldsymbol{r},\boldsymbol{\Omega},E,t)}_{\text{Rate of change}} + \underbrace{\boldsymbol{\Omega}\cdot\nabla\psi(\boldsymbol{r},\boldsymbol{\Omega},E,t)}_{\text{Streaming}} + \underbrace{\Sigma_{\mathrm{t}}(\boldsymbol{r},E)\,\psi(\boldsymbol{r},\boldsymbol{\Omega},E,t)}_{\text{Total collision}} \\
&\qquad = \underbrace{\int \mathrm{d}E' \int \mathrm{d}\boldsymbol{\Omega}'\,\Sigma_{\mathrm{s}}(\boldsymbol{r},E'\to E,\boldsymbol{\Omega}'\to\boldsymbol{\Omega})\,\psi(\boldsymbol{r},\boldsymbol{\Omega}',E',t)}_{\text{Scattering including }\Sigma_{\mathrm{e}}\,,\ \Sigma_{\mathrm{i}}\,,\ \Sigma_{\mathrm{n,2n}}\,,\ \dots\,,\ \Sigma_{\mathrm{n},x\mathrm{n}}} \\
&\qquad\quad + \underbrace{\chi_{\mathrm{p}}(\boldsymbol{r},E)\int \mathrm{d}E'\,\nu_{\mathrm{p}}(\boldsymbol{r},E')\,\Sigma_{\mathrm{f}}(\boldsymbol{r},E')\,\phi(\boldsymbol{r},E',t)}_{\text{Prompt fission neutrons}} \\
&\qquad\quad + \underbrace{\sum_j \chi_j(\boldsymbol{r},E)\,\lambda_j\,C_j(\boldsymbol{r},t)}_{\text{Delayed fission neutrons}} + \underbrace{Q(\boldsymbol{r},\boldsymbol{\Omega},E,t)}_{\text{External source}}
\end{aligned} \tag{2.1}$$

This integro-differential equation is solved for the dependent variable angular neutron flux ψ denoting the expected rate of neutrons crossing a unit area in direction of the solid angle $\boldsymbol{\Omega}$ with energy E per unit time at position $\boldsymbol{r}$ and at time t. Since neutron-neutron collisions are neglected, it is linear and depends in the most complex case on seven variables $(\boldsymbol{r}(x, y, z), \boldsymbol{\Omega}(\theta, \varphi), E, t)$, which result from the three dimensions of space, the polar and azimuthal angle of the solid angle, the energy and the time [20].

The interpretation of equation (2.1) denotes the right-hand side as the rate at which neutrons enter the actual phase space $(\boldsymbol{r}, \boldsymbol{\Omega}, E)$. The possible origin of those neutrons are the fission reactions integrated over E' and emitting isotropically neutrons with an energy distribution $\chi_{\mathrm{p}}(\boldsymbol{r}, E)$. Another source are neutrons that are scattered at incident energies E' and solid angles $\boldsymbol{\Omega}'$ to the actual energy E and solid angle $\boldsymbol{\Omega}$. The differential scattering cross section Σ_{s} includes the elastic and inelastic scattering and also the $(\mathrm{n}, x\mathrm{n})$ reactions with multiplicity $x \geq 2$. If the nuclear system is driven by an external neutron source these neutrons are to be considered at their rate of injection Q.

The fission neutrons appear mainly prompt, i.e. instantaneously after the fission reaction. A minor fraction of the neutrons, in case of ${}^{235}_{92}\mathrm{U}$ about 0.7 %, are released by associated precursors seconds to minutes after the fission event [21]. For these an additional set of equations (2.2) is needed to account for the production of the precursor nuclides. The origin of these delayed neutrons are in general attributed to β^--decay of highly excited fission products and their decay products. Other mechanisms exist however in special nuclear systems, where photoneutron reactions (γ,n) produce additional neutrons with deuterium in heavy water or beryllium. Some neutron absorption reactions like ${}^{17}\mathrm{O}(\mathrm{n,p}){}^{17}\mathrm{N}$ lead in consequence to emission of delayed neutrons by the decay of ${}^{17}\mathrm{N}$ [20]. Delayed neutrons may also appear due to the α-decay of uranium or MA isotopes and the (α,n) reaction with oxygen of the oxide fuel e.g. $\mathrm{UO_2}$, where the delay is caused by the decay constant of the isotopes.

The precursor nuclides are grouped into few decay time groups or families and as much precursor equations exist as time groups are to be considered. The emitted delayed neutrons appear as an additional source term at the rate of the precursor decay with an energy distribution $\chi_j(\boldsymbol{r}, E)$ which is slightly softer than that of prompt fission neutrons.

$$\frac{\partial}{\partial t} C_j(\boldsymbol{r}, t) = \int \mathrm{d}E' \, \nu_j(\boldsymbol{r}, E') \, \Sigma_{\mathrm{f}}(\boldsymbol{r}, E') \, \phi(\boldsymbol{r}, E', t) - \lambda_j \, C_j(\boldsymbol{r}, t) \tag{2.2}$$

The production of neutrons competes against the removal from the phase space on the left-hand side of eq. (2.1). This may happen by any reaction, e.g. absorption or scattering, and is expressed by the total rate of collisions. Neutrons may also leave or enter the control volume as consequence of the random walk through the medium. This is commonly called the streaming term of the transport equation. The streaming of neutrons is directly linked to the leakage of neutrons from the reactor, when streaming on the reactor boundaries is looked at.

When production and losses do not balance each other, the neutron population will change in time. Thus, the difference of these per unit time defines the rate at which the neutron angular density $N(\boldsymbol{r},\boldsymbol{\Omega},E,t)=\frac{1}{v}\psi(\boldsymbol{r},\boldsymbol{\Omega},E,t)$ changes.

To complete the set of equations, the initial condition of the time-dependent transport equation is defined in eq. (2.3) and the boundary condition is given in terms of the nonreentrant surface B of the reactor volume in eq. (2.4) [20].

$$\psi(\boldsymbol{r},\boldsymbol{\Omega},E,0)=\psi_0(\boldsymbol{r},\boldsymbol{\Omega},E) \tag{2.3}$$

$$\psi(\boldsymbol{r}_B,\boldsymbol{\Omega},E,t)=0 \quad \text{if} \quad \boldsymbol{\Omega}\cdot\boldsymbol{n}_B<0\,, \quad \boldsymbol{r}_B\in B \tag{2.4}$$

2.1.1 Energy Discretization

The neutron energies encountered in reactor calculations usually range from 0.001 eV to about 20 MeV. If a spallation neutron source would be used in ADS it could even range to some hundreds of MeV [22]. This huge span of about ten orders of magnitude has been traditionally discretized for the use in deterministic transport methods. While the increasing computing power allows nowadays the use of continuous energy Monte Carlo (MC) codes for many types of calculations, have deterministic multigroup methods retained their predominant role in full core and time-dependent reactor calculations.

When defining the energy group it is customary to address the group of highest energy as the first group. This leads to the fact that $E_{g-1}>E_g$. The definition of the involved multigroup variables is the following [20]:

$$\phi_g=\int_{E_g}^{E_{g-1}}\mathrm{d}E\,\phi(E) \qquad \text{group flux} \tag{2.5}$$

$$\Sigma_{\mathrm{x}g}=\frac{1}{\phi_g}\int_{E_g}^{E_{g-1}}\mathrm{d}E\,\Sigma_x(E)\,\phi(E) \qquad \text{cross section of type x} \tag{2.6}$$

$$\Sigma_{\mathrm{s}g'g}=\frac{1}{\phi_{g'}}\int_{E_g}^{E_{g-1}}\mathrm{d}E\int_{E_{g'}}^{E_{g'-1}}\mathrm{d}E'\,\Sigma_{\mathrm{s}}(E'\to E)\,\phi(E') \qquad \text{group transfer cross section} \tag{2.7}$$

$$\chi_g=\int_{E_g}^{E_{g-1}}\mathrm{d}E\,\chi(E) \qquad \text{fission spectrum} \tag{2.8}$$

$$\frac{1}{v_g}=\frac{1}{\phi_g}\int_{E_g}^{E_{g-1}}\mathrm{d}E\,\frac{1}{v(E)}\,\phi(E) \qquad \text{neutron group velocity} \tag{2.9}$$

Various methods exist to provide suitable weighting spectra $\phi(E)$ for the generation of group constants, which can be recalled to a great extent in the nuclear data processing code `NJOY` [23]. In the further reading the multigroup formalism will be used extensively.

2.1.2 The k_{eff} Eigenvalue Problem

The complete form of the transport equation is usually adapted to more simple forms, which are easier to solve and still adequate to cover the physical processes. If we consider a time-invariant system like an operating nuclear power reactor at nominal conditions, then the losses balance exactly the production. In other words the time derivative of eq. (2.1) is zero. Since the neutron chain reaction is self-sustaining, the external neutron source term of that equation vanishes, too.

In computer codes the balance cannot be met exactly. Therefore, a parameter called the effective multiplication factor k_{eff} is introduced into the static transport equation (2.10) that manipulates the total number of emitted fission neutrons (yield) $\frac{\nu_t(E)}{k_{\text{eff}}}$ in order to get the numerical equilibrium.

$$\begin{aligned}\boldsymbol{\Omega}\cdot\nabla\psi_g(\boldsymbol{r},\boldsymbol{\Omega}) + \Sigma_{\text{t}g}(\boldsymbol{r})\,\psi_g(\boldsymbol{r},\boldsymbol{\Omega}) &\\ = \sum_{g'}\int \mathrm{d}\boldsymbol{\Omega}'\,\Sigma_{\text{s}g'g}(\boldsymbol{r},\boldsymbol{\Omega}'\to\boldsymbol{\Omega})\,\psi_{g'}(\boldsymbol{r},\boldsymbol{\Omega}') &\\ + \frac{\chi_g(\boldsymbol{r})}{k_{\text{eff}}}\sum_{g'}\nu_{\text{t}g'}(\boldsymbol{r})\,\Sigma_{\text{f}g'}(\boldsymbol{r})\,\phi_{g'}(\boldsymbol{r}) &\end{aligned} \tag{2.10}$$

This equation indicates a constant rate of the delayed neutron emission, or better a saturated precursor concentration, which allows to use the total fission yield as the sum of prompt and delayed neutrons in eq. (2.11) and the fission spectrum averaged for prompt and delayed neutrons with the physical fraction $\beta_j = \frac{\nu_j}{\nu_t}$ in eq. (2.12).

$$\nu_{\text{t}g} = \nu_{\text{p}g} + \sum_j \nu_{jg} \tag{2.11}$$

$$\chi_g = (1-\beta)\,\chi_{\text{p}g} + \sum_j \beta_j\,\chi_{jg} \tag{2.12}$$

The nonreentrant boundary condition is applied to eq. (2.10) in the multigroup form of eq. (2.13).

$$\psi_g(\boldsymbol{r}_B,\boldsymbol{\Omega}) = 0 \quad \text{if} \quad \boldsymbol{\Omega}\cdot\boldsymbol{n}_B < 0 \quad \boldsymbol{r}_B \in B \tag{2.13}$$

From this equations it is evident that $k_{\text{eff}} = 1$ means the exact balance of production and loss in the critical reactor. For k_{eff} greater than unity the production exceeds the loss term and the reactor is said to be supercritical. If k_{eff} is smaller than unity the loss prevails the production term and the neutron yield is artificially enlarged. Equations without external source are also called "homogeneous" throughout this work.

It is obvious that this equation is only physically meaningful if k_{eff} is near unity. Then, the flux distribution is that of the critical reactor. The more the effective multiplication factor deviates from unity the more a real reactor would change its neutron distribution with time. Since all terms of the transport equation would change considerably [24], the resulting neutron distribution would be artificial. On the other hand, the effective multiplication factor is a measure how far away the reactor is from the critical state. For this reason, it is of great importance for ADS.

Mathematically, k_{eff} corresponds to the dominant eigenvalue of eq. (2.10) and this means the solution space includes also any linear dependent solution. In other words, the neutron flux can be normalized to any value and from an engineering objective a neutron flux could be chosen that corresponds to the thermal power of the reactor. In case of the solution of the inhomogeneous equation (2.1) of a subcritical system there exists only one unique neutron flux distribution imposed by the external neutron source [25,26]. A defined thermal power can be met only with adaption of the source strength.

2.1.3 The α Eigenvalue Problem

If the multiplication factor k_{eff} is smaller than unity the homogeneous form of the transport equation (2.1) will only have the zero flux solution because the loss rate preponderates the production rate. If a subcritical reactor was driven by an external neutron source, which stops operation at time t_0, the time-asymptotic zero flux solution will be finally obtained, but the reactor system will show a decay in the neutron population till the final state is reached. One of the suitable equations describing the transition of the homogeneous reactor system to the final state is the α or time eigenvalue equation (2.14).

$$\begin{aligned}\boldsymbol{\Omega} \cdot \nabla \psi_g(\boldsymbol{r}, \boldsymbol{\Omega}) + \left(\Sigma_{\text{t}g}(\boldsymbol{r}) + \frac{\alpha}{v_g}\right) \psi_g(\boldsymbol{r}, \boldsymbol{\Omega}) \\ = \sum_{g'} \int \mathrm{d}\boldsymbol{\Omega}' \, \Sigma_{\text{s}g'g}(\boldsymbol{r}, \boldsymbol{\Omega}' \to \boldsymbol{\Omega}) \, \psi_{g'}(\boldsymbol{r}, \boldsymbol{\Omega}') \\ + \chi_g(\boldsymbol{r}) \sum_{g'} \nu_{\text{t}g'}(\boldsymbol{r}) \, \Sigma_{\text{f}g'}(\boldsymbol{r}) \, \phi_{g'}(\boldsymbol{r}) \end{aligned} \quad (2.14)$$

This equation is derived by using an eigenvalue expansion with flux solutions of the form

$$\psi_g(\boldsymbol{r}, \boldsymbol{\Omega}, t) = A\, \psi_g(\boldsymbol{r}, \boldsymbol{\Omega})\, e^{\alpha\, t} \tag{2.15}$$

inserted into the source-free multigroup version of eq. (2.1). Equation (2.14) is solved for the k-th eigenvalue (or mode) α_k and corresponding eigenfunction ψ_{kg}. The general analysis of the spectrum of the time eigenvalue defines α as a complex number, however in the way it is used in reactor physics investigations, only the real part is of interest [1]. In the following the notation α will refer to the real part of the time eigenvalue.

The time-dependent neutron (angular) flux is constructed as sum of the product of the modal flux, the α_k exponential term and a normalization constant A_k. This however implies, that the α eigenvalues are discrete and no continuous spectrum exists [1].

$$\psi_g(\mathbf{r}, \boldsymbol{\Omega}, t) = \sum_{k=0}^{\infty} A_k(t)\, \psi_{kg}(\mathbf{r}, \boldsymbol{\Omega})\, e^{\alpha_k\, t} \tag{2.16}$$

The dominant or fundamental time eigenvalue α_0 is understood as the mode, which governs the decay of the reactor to the final state, when all higher modes have gone due to the shorter presence indicated by the vanishing time exponential with $\alpha_k\, t > \alpha_{k+1}\, t > \ldots > \alpha_K\, t$.

The initial condition for this time-dependent equation is written in eq. (2.17) analogously to eq. (2.3) and the nonreentrant boundary condition is again applied in eq. (2.18).

$$\psi_g(\boldsymbol{r}, \boldsymbol{\Omega}, 0) = \psi_{0g}(\boldsymbol{r}, \boldsymbol{\Omega}) \tag{2.17}$$

$$\psi_g(\boldsymbol{r}_B, \boldsymbol{\Omega}, t) = 0 \quad \text{if} \quad \boldsymbol{\Omega} \cdot \boldsymbol{n}_B < 0\,, \quad \boldsymbol{r}_B \in B \tag{2.18}$$

In the same manner that sub-, super- and criticality were defined for values of the multiplication factor k_eff, it can be associated to values of α_0. Then, $\alpha_0 = 0$ will describe the exact balance between the loss and production rate and therefore yield the identical flux solution as is obtained for $k_\text{eff} = 1$ in eq. (2.10). The subcritical reactor will have $\alpha_0 < 0$ and so will the impact of the prompt modes or harmonics stay as long as the $e^{\alpha_k\, t}$ exponential term has not decayed. When the fundamental decay mode has established, then eq. (2.16) shows that the spectral properties do not change anymore with time. Only the normalization constant and the exponential term change and these can be interpreted as the amplitude function, which decays according to the subcriticality of the system. This is immediately the connection to the justification of the point kinetic equations of section 2.1.5.

In equation (2.14) no distinction between prompt and delayed neutrons is made. When delayed neutrons are to be considered in PNS experiments they appear as delayed neutron modes or harmonics. Due to the completely different time scales of prompt and delayed neutrons, usually only the prompt modes are considered [1].

In case of the isotropic diffusion equation as low order angular approximation to the transport equation there may be as much modes as the remaining phase space variables $(\boldsymbol{r}, E_g)$ can deliver. The maximum is the product of the number of energy groups and the number of mesh points [27]. If we extend this to the transport equation, the number of potential modes increases to account for the anisotropy of the problem imposed by the approximation for the solid angle and the anisotropic scattering. The complexity of the solution of the time eigenvalue equation is attended by the complexity which is acting by the considered phase space $(\boldsymbol{r}, \boldsymbol{\Omega}, E_g)$ on the transport equation. In real applications it is almost impossible to verify, that the eigenvalue spectrum is composed of discrete ones only.

When α_0 is significantly different from zero the flux solution must be different compared to the flux solution of the k_{eff} eigenvalue problem. In case of a subcritical time eigenvalue problem the $\frac{\alpha}{v_g}$ term is negative and reduces the total cross section. This effectively will shift the flux spectrum to softer energies [1]. Obviously, the neutronic properties of a time-dependent subcritical reactor are considerably different from a "pseudo" critical reactor in a k_{eff} problem. The spectrum softening will have a complex influence on certain parts of the transport equation, e.g. prompt fission neutron source and leakage, and may concern the kinetic properties as well [24].

2.1.4 The Adjoint Equation

It has been very early observed that the solution of an equation adjoint to one of the equations (2.1),(2.10) or (2.14) called adjoint flux can be advantageously used as a weighting function in perturbation theory [28], sensitivity and uncertainty analysis [29]. The adjoint flux is introduced here for the later use in the calculation of kinetic parameters (*see* section 2.1.5). Equation (2.19) is the equation adjoint to the k_{eff} equation (2.10), where the dagger of $\psi^\dagger$ denotes the adjoint flux.

$$\begin{aligned} -\boldsymbol{\Omega}\cdot\nabla\psi_g^\dagger(\boldsymbol{r},\boldsymbol{\Omega}) &+ \Sigma_{\text{t}g}(\boldsymbol{r})\,\psi_g^\dagger(\boldsymbol{r},\boldsymbol{\Omega}) \\ &= \sum_{g'}\int \mathrm{d}\boldsymbol{\Omega}'\,\Sigma_{\text{s}gg'}(\boldsymbol{r},\boldsymbol{\Omega}\to\boldsymbol{\Omega}')\,\psi_{g'}^\dagger(\boldsymbol{r},\boldsymbol{\Omega}') \\ &\quad + \frac{1}{k_{\text{eff}}^\dagger}\sum_{g'}\chi_{g'}(\boldsymbol{r})\nu_{\text{t}g}(\boldsymbol{r})\,\Sigma_{\text{f}g}(\boldsymbol{r})\,\phi_{g'}^\dagger(\boldsymbol{r}) \end{aligned} \tag{2.19}$$

$$\psi_g^\dagger(\boldsymbol{r}_B,\boldsymbol{\Omega}) = 0 \quad \text{if} \quad \boldsymbol{\Omega}\cdot\boldsymbol{n}_B > 0\,, \quad \boldsymbol{r}_B \in B \tag{2.20}$$

Apart from the special noting of the adjoint flux, the inconspicuous changes in the sign of the streaming term and in the scattering and fission term have to be emphasized.

The fission and differential scattering is now from energy group g to g' and the latter from direction $\boldsymbol{\Omega}$ to $\boldsymbol{\Omega}'$. This and the opposite sign of the streaming term point to the nomenclature of the adjoint equation as the "backward" transport equation. The flight path of the neutron is followed from the ending to the starting point [1].

In order to emphasize some of the relevant properties of this fundamentally important adjoint function it is advantageous to introduce the time-independent transport operator in eq. (2.21) and its adjoint equivalent eq. (2.22).

$$\begin{aligned} \boldsymbol{L}\,\psi_g(\boldsymbol{r},\boldsymbol{\Omega}) = -\boldsymbol{\Omega}\cdot\nabla\psi_g(\boldsymbol{r},\boldsymbol{\Omega}) - \Sigma_{\mathrm{t}g}(\boldsymbol{r})\,\psi_g(\boldsymbol{r},\boldsymbol{\Omega}) \\ + \sum_{g'}\int \mathrm{d}\boldsymbol{\Omega}'\,\Sigma_{\mathrm{s}g'g}(\boldsymbol{r},\boldsymbol{\Omega}'\to\boldsymbol{\Omega})\,\psi_{g'}(\boldsymbol{r},\boldsymbol{\Omega}') \end{aligned} \tag{2.21}$$

$$\begin{aligned} \boldsymbol{L}^\dagger\,\psi^\dagger_g(\boldsymbol{r},\boldsymbol{\Omega}) = \boldsymbol{\Omega}\cdot\nabla\psi^\dagger_g(\boldsymbol{r},\boldsymbol{\Omega}) - \Sigma_{\mathrm{t}g}(\boldsymbol{r})\,\psi^\dagger_g(\boldsymbol{r},\boldsymbol{\Omega}) \\ + \sum_{g'}\int \mathrm{d}\boldsymbol{\Omega}'\,\Sigma_{\mathrm{s}gg'}(\boldsymbol{r},\boldsymbol{\Omega}\to\boldsymbol{\Omega}')\,\psi^\dagger_{g'}(\boldsymbol{r},\boldsymbol{\Omega}') \end{aligned} \tag{2.22}$$

Moreover, the production operator of a multiplying medium may be defined according to equation eq. (2.23) and its adjoint according to eq. (2.24).

$$\boldsymbol{F}\,\psi_{g'}(\boldsymbol{r},\boldsymbol{\Omega}') = \sum_{g'} \chi_g(\boldsymbol{r})\,\nu_{\mathrm{t}g'}(\boldsymbol{r})\,\Sigma_{\mathrm{f}g'}(\boldsymbol{r})\,\psi_{g'}(\boldsymbol{r},\boldsymbol{\Omega}') \tag{2.23}$$

$$\boldsymbol{F}^\dagger\,\psi^\dagger_{g'}(\boldsymbol{r},\boldsymbol{\Omega}') = \sum_{g'} \chi_{g'}(\boldsymbol{r})\,\nu_{\mathrm{t}g}(\boldsymbol{r})\,\Sigma_{\mathrm{f}g}(\boldsymbol{r})\,\psi^\dagger_{g'}(\boldsymbol{r},\boldsymbol{\Omega}') \tag{2.24}$$

Since the operators $\boldsymbol{L}$, $\boldsymbol{F}$ and their adjoints $\boldsymbol{L}^\dagger$, $\boldsymbol{F}^\dagger$ are generally different in their formulation, they are principally not self-adjoint and by this the neutron flux ψ and the adjoint flux $\psi^\dagger$ are not equal. The only exception occurs when looking at the monoenergetic diffusion equation for which the scalar flux ϕ and its adjoint $\phi^\dagger$ are equal.

The source-free transport equation can now be written in operator notation in the real form in eq. (2.29) and the subscript "hom" of the angular flux emphasizes the solution of the homogeneous system.

$$\underbrace{\Big[\boldsymbol{L} - \eta\,\boldsymbol{F}\Big]}_{\boldsymbol{M}}\,\psi_{\mathrm{hom}} = 0 \tag{2.25}$$

and in the adjoint form in eq. (2.26). In order to avoid the connotation of the effective multiplication factor equation the $\frac{1}{k}$ expression is replaced by η.

$$\underbrace{\left[\boldsymbol{L}^{\dagger} - \eta^{\dagger}\boldsymbol{F}^{\dagger}\right]}_{\boldsymbol{M}^{\dagger}} \psi^{\dagger}_{\text{hom}} = 0 \tag{2.26}$$

To illustrate some very important properties of the reformulated equations (2.25) and (2.26) we define the basic requirement of the total adjoint operator $\boldsymbol{M}^{\dagger}$ in equation (2.27), namely the inner product of the adjoint flux and the total operator applied to the real flux must be equal to the inner product of the real flux and the total adjoint operator applied to the adjoint flux.

$$\left\langle \psi^{\dagger}, \boldsymbol{M}\,\psi \right\rangle = \left\langle \psi, \boldsymbol{M}^{\dagger}\,\psi^{\dagger} \right\rangle \tag{2.27}$$

Inserting eq. (2.25) and eq. (2.26) into eq. (2.27) leads to the fundamental equation (2.28).

$$\left(\eta - \eta^{\dagger}\right)\left\langle \psi^{\dagger}_{\text{hom}}, \boldsymbol{F}\,\psi_{\text{hom}} \right\rangle = 0 \tag{2.28}$$

In reactor physics applications the inner product of the flux and its adjoint is generally non-zero. In turn the eigenvalues to the real and adjoint eigenfunctions must be equal [1]. Thus, a homogeneous equation with $\eta \neq 0$ has associated an adjoint equation. In the manifold of solutions the forward dominant eigenvalue and eigenfunction are identical to the inverse of the effective multiplication factor k_{eff} and the angular flux ψ, respectively.

For further discussion the inhomogeneous time-independent transport equation in operator notation is given in eq. (2.29) and the angular flux solution is indicated with the subscript "inh". The variable η is kept in this equation and its meaning will be explained in this context.

$$\left[\boldsymbol{L} - \eta\,\boldsymbol{F}\right]\psi_{\text{inh}} = Q \tag{2.29}$$

Stumbur [24] and in more recent context Cacuci [25] have pointed out that the inhomogeneous transport equation (2.29) and the homogeneous transport equation (2.25) correspond to the first and second alternative of the Fredholm Alternative Theorem (also called Riesz-Schauder Theorem) [26], respectively. In particular it is stated in the first alternative that, if the homogeneous equation has only the time-asymptotic zero solution as it occurs in a subcritical state, the corresponding inhomogeneous equation with external source has a unique solution. Equation (2.30) denotes the formal solution to the inhomogeneous equation (2.29), but now η is part of the resolvent [24, 25] constituting mathematically the unique solution to the inhomogeneous transport equation.

$$\psi_{\text{inh}} = \Big[\boldsymbol{L} - \eta\,\boldsymbol{F}\Big]^{-1} Q \tag{2.30}$$

Thus, for the inhomogeneous equation the requirement of equations (2.27) and (2.28) cannot be fulfilled and a mathematical connection between the homogeneous adjoint equation and the inhomogeneous equation (2.29) cannot be established.

The second alternative refers to the homogeneous equation (2.29), for which an adjoint equation exists, if the solution is nonzero and the eigenvalues are identical according to equation (2.28). Under the condition that $\left\langle \psi^{\dagger}_{\text{inh}}, Q \right\rangle = 0$ for the solution $\psi^{\dagger}_{\text{inh}}$ of the homogeneous adjoint equation there exists a non-unique solution to the inhomogeneous equation (2.29). However, this condition is unlikely to be fulfilled, since there is no orthogonality relation between the external source and the homogeneous adjoint flux, and only the trivial $Q = 0$ satisfies the condition.

On the other hand, the inhomogeneous adjoint equation in the form of eq. (2.31) can be found in various textbooks e.g. of Bell [1] or Duderstadt [20].

$$\underbrace{\Big[\boldsymbol{L}^{\dagger} - \eta^{\dagger}\boldsymbol{F}^{\dagger}\Big]}_{\boldsymbol{M}^{\dagger}} \psi^{\dagger}_{\text{inh}} = Q^{\dagger} \tag{2.31}$$

In this case the adjoint source $Q^{\dagger}$ is interpreted as an arbitrary detector cross section Σ_{d} and the importance $\psi^{\dagger}_{\text{inh}}$ is understood as the expected detector counts because of neutrons at a certain point in phase space or secondary neutrons produced by these neutrons due to scattering or fission. With this example the meaning of the nomenclature "forward" and "backward" equation can be understood. In the inhomogeneous "forward" equation (2.29) the flux denotes the asymptotic distribution of neutrons, which are all secondaries of the initial external source neutrons. The external source can thus be seen as the starting point. In the "backward" equation the adjoint source $Q^{\dagger} = \Sigma_{\text{d}}$ is the target of interest and the detector response $\left\langle \Sigma_{\text{d}}, \psi^{\dagger}_{\text{inh}} \right\rangle$ due to neutrons at a certain position and energy is equal to the adjoint flux. It is the importance based on the knowledge of the neutron history, thus looking back from the ending to the starting point.

This short summary of the application of the adjoint function to the homogeneous and inhomogeneous transport equation shows that the validity of methods developed for critical, source-free reactors in the frame of subcritical reactors driven by an external neutron source must be carefully checked as far as adjoint function based methods like perturbation theory are concerned.

2.1.5 The Point Kinetic Equations

When the time-dependent transport equation (2.1) and the continuous energy version of the adjoint equation (2.10) are multiplied by the adjoint flux $\psi^\dagger$ and the real flux ψ, respectively, and both modified equations then are subtracted from each other and integrated over the phase space, the amplitude function of the point kinetic equations (2.32) can be derived [1,30,31]. The amplitude P means the adjoint weighted number of neutrons in the reactor volume eq. (2.34). A similar procedure with a factor $\chi_j\,\psi^\dagger$ can be applied to the precursor equations (2.2), which yields the integral weighted precursor equations of eq. (2.33).

$$\frac{\mathrm{d}P(t)}{\mathrm{d}t} = \frac{\rho(t)-\beta_{\mathrm{eff}}(t)}{\Lambda(t)}P(t) + \sum_j \lambda_j C_j(t) + Q(t) \tag{2.32}$$

$$\frac{\mathrm{d}C_j(t)}{\mathrm{d}t} = \frac{\beta_{\mathrm{eff}j}(t)}{\Lambda(t)}P(t) - \lambda_j C_j(t) \qquad j = 1,\ldots,\{6,8\} \tag{2.33}$$

$$P(t) = \iiint \mathrm{d}V\,\mathrm{d}E\,\mathrm{d}\boldsymbol{\Omega}\,\frac{1}{v(E)}\psi(\boldsymbol{r},\boldsymbol{\Omega},E,t)\,\psi^\dagger(\boldsymbol{r},\boldsymbol{\Omega},E) \tag{2.34}$$

The introduced kinetic parameters are defined in equations (2.35) to (2.41).

$$\begin{aligned}\rho(t) = \frac{1}{F}\Big\{&\int\cdots\int \mathrm{d}V\,\mathrm{d}E\,\mathrm{d}E'\,\mathrm{d}\boldsymbol{\Omega}\,\mathrm{d}\boldsymbol{\Omega'}\,\psi(\boldsymbol{r},\boldsymbol{\Omega},E',t)\,\psi^\dagger(\boldsymbol{r},\boldsymbol{\Omega},E)\\ &\times\Delta\Big[\Sigma_{\mathrm{s}}(\boldsymbol{r},E'\to E,\boldsymbol{\Omega'}\to\boldsymbol{\Omega},t) + \chi(\boldsymbol{r},E)\,\nu_{\mathrm{t}}(\boldsymbol{r},E',t)\,\Sigma_{\mathrm{f}}(\boldsymbol{r},E',t)\Big]\\ &-\iiint \mathrm{d}V\,\mathrm{d}E\,\mathrm{d}\boldsymbol{\Omega}\,\Delta\Sigma_{\mathrm{t}}(\boldsymbol{r},E,t)\,\psi(\boldsymbol{r},\boldsymbol{\Omega},E,t)\,\psi^\dagger(\boldsymbol{r},\boldsymbol{\Omega},E)\Big\}\end{aligned} \tag{2.35}$$

$$\beta_{\mathrm{eff}}(t) = \sum_j \beta_{\mathrm{eff}j}(t) \tag{2.36}$$

$$\begin{aligned}\beta_{\mathrm{eff}j}(t) = \frac{1}{F}&\int\cdots\int \mathrm{d}V\,\mathrm{d}E\,\mathrm{d}E'\,\mathrm{d}\boldsymbol{\Omega}\,\mathrm{d}\boldsymbol{\Omega'}\,\chi_j(E)\,\nu_j(\boldsymbol{r},E')\,\Sigma_{\mathrm{f}}(\boldsymbol{r},E')\\ &\times\psi(\boldsymbol{r},\boldsymbol{\Omega'},E',t)\,\psi^\dagger(\boldsymbol{r},\boldsymbol{\Omega},E)\end{aligned} \tag{2.37}$$

$$\Lambda(t) = \frac{1}{F}\iiint \mathrm{d}V\,\mathrm{d}E\,\mathrm{d}\boldsymbol{\Omega}\,\frac{1}{v}\psi(\boldsymbol{r},\boldsymbol{\Omega},E,t)\,\psi^\dagger(\boldsymbol{r},\boldsymbol{\Omega},E) \tag{2.38}$$

$$C_j(t) = \frac{1}{\Lambda F}\iiint \mathrm{d}V\,\mathrm{d}E\,\mathrm{d}\boldsymbol{\Omega}\,\chi_j(E)\,C_j(\boldsymbol{r},t)\,\psi^\dagger(\boldsymbol{r},\boldsymbol{\Omega},E) \tag{2.39}$$

$$Q(t) = \frac{1}{\Lambda F}\iiint \mathrm{d}V\,\mathrm{d}\boldsymbol{\Omega}\,\mathrm{d}E\,Q(\boldsymbol{r},\boldsymbol{\Omega},E,t)\,\psi^\dagger(\boldsymbol{r},\boldsymbol{\Omega},E) \tag{2.40}$$

$$
\begin{aligned}
F(t) = \int \cdots \int & \mathrm{d}V \, \mathrm{d}E \, \mathrm{d}E' \, \mathrm{d}\boldsymbol{\Omega} \, \mathrm{d}\boldsymbol{\Omega}' \chi(E) \, \nu(\boldsymbol{r}, E') \, \Sigma_{\mathrm{f}}(\boldsymbol{r}, E') \\
& \times \psi(\boldsymbol{r}, \boldsymbol{\Omega}', E', t) \, \psi^{\dagger}(\boldsymbol{r}, \boldsymbol{\Omega}, E)
\end{aligned}
\tag{2.41}
$$

To this point no approximation is introduced and the solution of equations (2.32 - 2.33) is equivalent to the solution of equations (2.1) and (2.2) [32]. The approximate character of the point kinetic equations follows from the fact that the kinetic parameter equations (2.35 - 2.41) are usually taken time-independent, i.e. with $\psi(\boldsymbol{r}, \boldsymbol{\Omega}, E, t) = \psi_0(\boldsymbol{r}, \boldsymbol{\Omega}, E)$ being the scalar fundamental mode flux of the homogeneous transport equation (2.10). This fundamental mode state is used as the reference state and changes in the reactor configuration are considered in the parameter ρ of equation (2.35) as integral over the differences between the actual time-dependent and reference state. The introduction of time-independent kinetic parameters corresponds to the assumption that the neutron flux shape does not vary during the time-dependent simulation.

It also defines the initial condition of the amplitude P in eq. (2.42). To find the initial condition on the effective precursor concentrations $C_{0j}(t = 0)$ one may assume the equilibrium precursor concentrations with the consequence of $\frac{\partial}{\partial t} C_j(\boldsymbol{r}, t) = 0$ in eq. (2.2).

$$
P_0 = \iiint \mathrm{d}V \, \mathrm{d}E \, \mathrm{d}\boldsymbol{\Omega} \, \frac{1}{v(E)} \psi_0(\boldsymbol{r}, \boldsymbol{\Omega}, E) \, \psi^{\dagger}(\boldsymbol{r}, \boldsymbol{\Omega}, E) \tag{2.42}
$$

The choice of the weighting function is already indicated in the nomenclature of the adjoint flux introduced in section 2.1.4. In principle every suitable function is allowed for the phase space integration. Several authors have pointed out that the adjoint flux is an exceptionally well suited weighting function, since it keeps the validity to the first order, if small perturbations e.g. control rod movement or coolant density changes are acting on the neutron flux distribution [32]. Another reason for choosing the adjoint function is that analyses with variational methods show that the error in the integration of two "inaccurate" functions, like in the approximation of the time-dependent real and adjoint flux by the static, fundamental mode real and adjoint flux, can be minimized by involving the adjoint of the problem [1].

The normalization integral F in eq. (2.41) is chosen in a way that the parameters can be interpreted in a physical manner. The effective delayed neutron fraction β_{eff} accounts for the softer delayed neutron energy spectrum χ_j, which is given a specific importance by the adjoint function. In thermal reactor systems an enlargement up to 20 % may occasionally be observed in comparison to the physical delayed neutron fraction [1]. Another important parameter is the mean neutron generation time Λ, which is understood as the average live-time of a neutron from its birth to its absorption leading to another fission event [20].

In zero-power reactors where no temperature feedback or other influences like control rod movement are expected, the point kinetic equations are linear [1].

The neutron flux calculations typically are based on the real and adjoint effective multiplication factor equations of eq. (2.10) and therefore are only valid for small deviations of k_{eff} from unity. The use of the critical flux may be questionable, when the real flux deviates considerably as it occurs e.g. in subcritical reactors either driven by a neutron source or transitioning to the time-asymptotic state by decay of the neutron population [24].

The first term on the right hand side of eq. (2.32) is called prompt decay constant [20] (*see* eq. (2.43)). This constant matches the fundamental time eigenvalue only, if the prerequisites of the point kinetic equations are fulfilled, i.e. the flux of the reference state is a good approximation to the transient flux. If the reactor is considerably subcritical the involved parameters can change due to the dependence on the real time-dependent flux in the original equations (2.35) to (2.41).

$$\alpha_0 = \frac{\rho - \beta_{\text{eff}}}{\Lambda} \tag{2.43}$$

If the condition is fulfilled, then ρ is connected to the static effective multiplication factor problem as shown in eq. (2.44) and characterizes the static reactivity.

$$\rho = \frac{k_{\text{eff}} - 1}{k_{\text{eff}}} \tag{2.44}$$

2.2 Pulsed Neutron Source Experiments

PNS experiments have been used in the very beginning of experimental reactor physics to investigate the kinetic properties of nuclear systems [33]. Main investigation areas were devoted to neutron lifetime measurements, neutron thermalization and neutron spectra in time-of-flight measurements. The main idea of PNS experiments is to deliver source neutrons to a subcritical or near critical reactor within a very short time interval and to measure the local response as a function of time.

Many details have to be considered for the planning of such experiments and their impact on the quantity of interest must be reflected.

Neutron source Several kinds of external neutron sources exist: spallation, fusion, spontaneous fission and also (α,n) neutron sources. The most intense neutron source is achieved with accelerated protons impinging on a target e.g. lead in a spallation reaction. It is observed that the number of neutrons released per proton and per proton energy can be enhanced with increasing proton energy, but stagnates at 1 GeV. For this optimized proton energy one spallation reaction would release about 20 to 30 neutrons and the total neutron source intensity can only be further increased by increasing the accelerator current [34], which makes these devices very expensive and technically challenging. The neutron source intensity can range between 10^{12} to 10^{14} neutrons per second. This neutron source emits neutrons with very high energies, which can be spread up to the GeV range. Potential accelerator types are the Cyclotron for beam currents up to about 10 mA and the Linac for higher currents.

In small experimental facilities monoenergetic fusion neutron sources are applied [35], which obey either the relationship

$$^{3}_{1}\mathrm{H} + ^{2}_{1}\mathrm{H} \longrightarrow ^{4}_{2}\mathrm{He} + ^{1}_{0}\mathrm{n} \tag{2.45}$$

called (d,t) neutron source and an average neutron energy of 14.1 MeV or

$$^{2}_{1}\mathrm{H} + ^{2}_{1}\mathrm{H} \longrightarrow ^{3}_{2}\mathrm{He} + ^{1}_{0}\mathrm{n} \tag{2.46}$$

called (d,d) neutron source and an average neutron energy of 2.5 MeV. Again depending on the accelerator current such fusion neutron sources can emit 10^{8} to 10^{11} neutrons per second.

Another common neutron source is the $^{252}_{98}\mathrm{Cf}$ source. With a branching ratio of 3.1 % this isotope disintegrates by spontaneous fission releasing about 3.756 neutrons per event [36, 37]. The number of emitted neutrons is proportional to the total mass of the isotope and can be quantified to $2.314\,\mathrm{s}^{-1}\,\mu\mathrm{g}^{-1}$. The neutron energy distribution obeys a typical fission energy spectrum with a maximum probability at 0.7 MeV and an average energy of 2.1 MeV [38].

As a last example the combination of an α-particle emitting material such as radium, polonium or americium and a material with large (α,n) cross section like beryllium is used as a neutron source.

$$^{9}_{4}\mathrm{Be} + ^{4}_{2}\alpha \longrightarrow ^{12}_{6}\mathrm{C} + ^{1}_{0}\mathrm{n} \tag{2.47}$$

Source intensities of about 10^{7} neutrons per second have been used [39]. The average neutron energy depends on the energy of the α-particle, but is around 4 MeV [40].

Reactor properties For measuring material properties in PNS experiments typically compact nuclear reactors without reflector are used. In view of experiments for transmutation reactors reflected reactor systems are used. The reflector adds generally a portion of complexity to the kinetic description, because neutron lifetimes or moderating properties may be quite different from those of reactor cores. For transmutation purposes fast spectrum cores are preferred. However, in recent hybrid designs thermal neutron energy spectrum regions for isotope production are foreseen [41]. In some of the ADS projects like the YALINA [42] or the planned and finally discontinued TRADE [43] experiments, thermal spectrum reactors coupled with an external neutron source were considered. In the latter the time-dependent behavior including thermal feedback effects should have been addressed. These design items are accompanied by fundamental physical differences in the reactor properties such as the larger diffusion length and reduced reaction probabilities in fast reactors, which must be compensated by higher enrichment of the fissile isotopes. In terms of the kinetic behavior the time constants (mean neutron generation time) deviate by several order of magnitude $10^{-7}\,\mathrm{s}$ to $5 \cdot 10^{-6}\,\mathrm{s}$ in fast and $10^{-5}\,\mathrm{s}$ to $10^{-4}\,\mathrm{s}$ in thermal systems [20]. With the choice for fuel containing plutonium and other MAs the second important kinetic parameter (effective delayed neutron fraction) deteriorates in comparison to pure UO_2 fuel.

Detector The response of the reactor system during the experiment is measured in detectors. From several detector responses at distributed positions the wanted quantity has to be extracted. Since neutrons cannot be measured directly, secondary reaction products are counted. Common neutron detectors are fission detectors, which contain small amounts of ${}^{235}_{92}\mathrm{U}$ for thermal and fast neutrons or ${}^{238}_{92}\mathrm{U}$ for fast neutrons only. Each fission event will emit characteristic γ-rays recorded in a measurement device. Another measuring method is the (n,p) reaction of ${}^{3}_{2}\mathrm{He}$. The emitted proton can easily be detected. Since this cross section exhibits a $\frac{1}{v}$-shape over a large energy range, it predominantly will absorb thermal neutrons.

$$
{}^{3}_{2}\mathrm{He} + {}^{1}_{0}\mathrm{n} \longrightarrow {}^{3}_{1}\mathrm{H} + {}^{1}_{1}\mathrm{p} \tag{2.48}
$$

2.2.1 Phenomenology

In fig. 2.1 a simulated reaction rate of a PNS experiment with a (d,d) neutron source in a YALINA-Thermal like subcritical reactor is shown. It results from an injection of neutrons during a pulse width of 5 µs in the very middle of a subcritical thermal reactor. At several positions the ${}^{3}_{2}\mathrm{He}$(n,p) reaction rate is measured. For the moment it is sufficient to mention that all detectors are axially at the height of the neutron source and the Experimental Channels (ECs) numbering is such that in increasing order the radial distance from the source increases as well. ECs 1-3 are located in the core, EC5 and EC6 in the reflector. The pulse frequency is 50 Hz which corresponds to a pulse period of 20 ms. Before relevant measurements are performed the PNS operates for several minutes in order to allow for the build-up of the delayed neutron precursor concentration specific to the pulse frequency.

The pulse period roughly is subdivided into four time intervals for which the physical phenomena will be explained in more detail. When we start with interval T_1 the neutron distribution at 20 ms may be thought of to be the initial condition at $t = 0$. During the first 5 µs of this first time interval the source emits neutrons in the center of the reactor. Generally, the arrival of the neutrons at certain radial and axial positions will take a specific time which is correlated to the velocity of the neutrons and their slowing-down because of collisions. It is however likely that many neutrons counted at EC1 can reach the detector without many collisions and therefore the counting rate raises immediately. From the inner to the outer radial positions in the reactor a significant amount of time can be deduced for the neutron propagation into the reflector. The maximum rate is counted in the outermost detector EC6 latest about 1 ms after the neutron pulse.

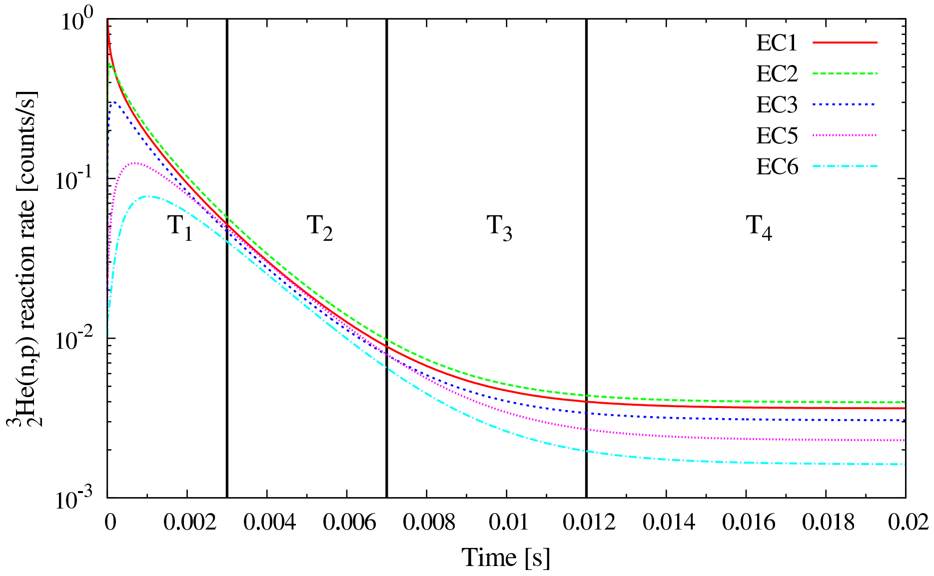

Figure 2.1: Classification of time intervals in the PNS experiment

For the duration of the pulse width the neutron distribution tries to develop to the asymptotic distribution of the inhomogeneous transport equation (2.1), where the neutron flux and power are peaked at the center of the neutron source and diminish with a convexly shaped distribution towards the outer bounds of the reactor [44]. However, this state cannot be reached in due time, so that the neutron field/system is highly excited and will redistribute the neutrons according to the source-free time eigenvalue transport equation (2.10) with the excited state as initial condition. The description of section 2.1.3 relates the redistribution and position dependent decaying behavior to the existence of the "higher modes" of the time eigenvalue problem. Additionally to the spatial diffusion of the source and fission neutrons, which cause the "harmonic distortion", the "kinetic distortion" has been identified [45,46]. It is encountered in reactors with heterogeneous material distribution, where the materials have significantly different diffusion length and moderating ratios. The larger the diffusion length the longer the neutrons stay in that region. In view of the time scales of the PNS experiment it may happen that neutrons of the same fission chain stay in the fuel region or diffuse into the reflector undergoing a slowing-down process of another velocity and diffuse later back to the fuel region. The latter neutrons will be distributed differently in energy than their sisters.

After a considerable amount of time - 3 ms in fig. 2.1 - the short-lived modes with the severest kinetic impact have decayed away. The count rate decays with a similar slope at all detector positions of the reactor. This phase is attributed to the second time interval T_2 and is interpreted as the tendency of the reactor to find the fundamental decay mode as the stable decay path. In other words, with only one dominant decaying exponential of eq. (2.16) the curve of the count rate would develop to a straight line in a semi-logarithmic plot. It is obvious that from this part of the measurement nearest to the fundamental decay mode an important amount of the kinetic characteristic of the system can be derived. The slope method relying on this will be described in section 2.2.3.

The remaining phases of fig. 2.1 are directly related to the existence of the delayed neutrons. Time interval T_3 denotes thereby the transition from the prompt decay phase to the "quasi" constant delayed neutron background in T_4. It is once more emphasized that the transition is position dependent. In common notation this effect is attributed to the "delayed harmonics" [1], which appear in the time frames of the delayed neutron time group decay constants. Because the delayed neutron source term is entirely located in the fuel, the transition effect is much stronger in the reflector due to the necessary diffusion of the delayed neutrons and by those generated prompt neutrons from the fuel region into the reflector.

2.2.2 The Area Method

The Sjöstrand or area (ratio) method relates the area caused by prompt neutrons to the area attributed to the constant delayed neutron background [47].

The simple relationship between the reactivity in unit Dollar and the areas derives from the integration of the point kinetic equations (2.49) and (2.50) without feedback and without changes in the reactor configuration as described by Bell [1]. The short pulse width of the external neutron source allows the use of a Dirac delta function $\delta(t)$.

$$\frac{\mathrm{d}P(t)}{\mathrm{d}t} = \frac{\rho - \beta_{\text{eff}}}{\Lambda} P(t) + \sum_j \lambda_j C_j(t) + Q\,\delta(t) \tag{2.49}$$

$$\frac{\mathrm{d}C_j(t)}{\mathrm{d}t} = \frac{\beta_{\text{eff},j}}{\Lambda} P(t) - \lambda_j C_j(t) \qquad j = 1, \ldots, \{6, 8\} \tag{2.50}$$

To yield the pure prompt area indicated in fig. 2.2, eq. (2.49) is integrated without

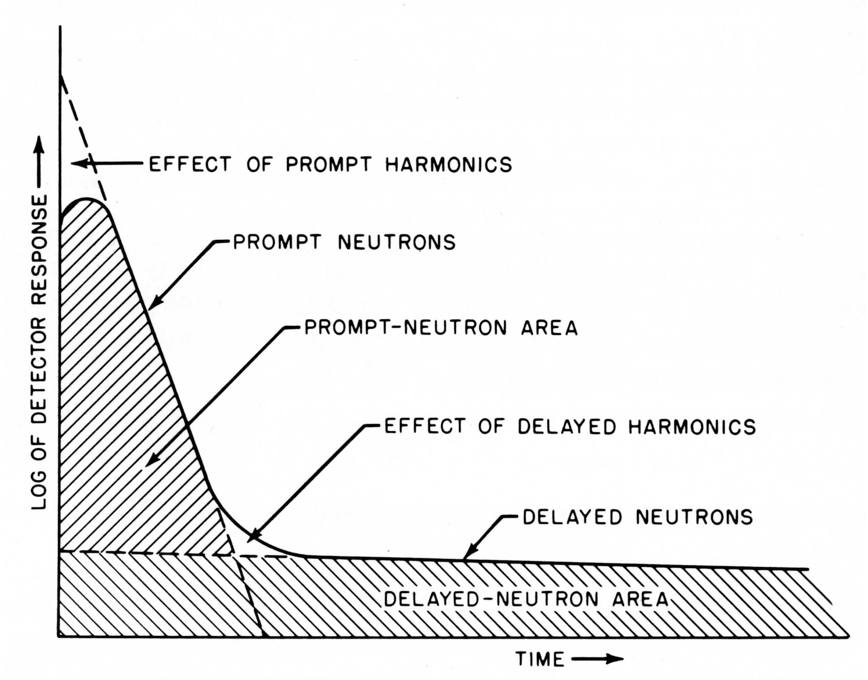

Figure 2.2: Schematic detector response to a pulse (copy from Bell [1])

considering the delayed neutron term over the pulse period T obtaining eq. (2.51).

$$A_p \equiv \int_0^T P_p(t)\,\mathrm{d}t = -\frac{Q\Lambda}{\rho - \beta_{\mathrm{eff}}} \tag{2.51}$$

When integrating equations (2.49) and (2.50) over the pulse period for the total area eq. (2.52) in fig. 2.2 from which the delayed neutron area may be deduced by subtracting the prompt area of eq. (2.51) it yields the final equation (2.53).

$$A_t \equiv \int_0^T P(t)\,\mathrm{d}t = -\frac{Q\Lambda}{\rho} \tag{2.52}$$

$$-\frac{\rho}{\beta_{\mathrm{eff}}} = \frac{A_p}{A_t - A_p} = \frac{A_p}{A_d} \tag{2.53}$$

To determine the reactivity in Dollar of a reactor after a PNS experiment one would simply have to integrate the detector signal and measure the delayed neutron background. If other background neutron sources exist, they need to be quantified and subtracted [48]. In order to achieve the static reactivity ρ, the effective delayed neutron fraction must be known or calculated. This simple method is said to be the most promising one in PNS reactivity determination methods [48,49]. The reason for this is that the integration over the pulse period will smooth out strong deviations from the canonical average of the detector count due to the relatively small time periods. This method therefore is called stable or insensitive, since the obtained reactivities do not spatially deviate so much as they do with other methods [1]. However, this is at the same time a disadvantage of the area method, because the fundamental decay mode required by the point kinetic assumption is not assured to appear purely for the integration. This is qualitatively seen by comparing the ideally straight line of fig. 2.2 in the prompt decay region and the analogous part T_2 in fig. 2.1. The latter more realistic curve for PNS experiments in thermal research reactors involves a slight change in curvature at every detector position. If the area method was to be applied blindly, then only $\frac{\mathrm{T}_2}{\mathrm{T}_1+\mathrm{T}_2+\mathrm{T}_3} \simeq 30\,\%$ of the measured curve would approximately be (the slight change in curvature neglected) a valid range for the integration of the fundamental prompt neutron decay mode.

To remove the influence of the higher prompt modes at the beginning of the measurements, Gozani proposed the backward extrapolation of the "straight" fundamental decay mode line to time zero as indicated with the dashed line in fig. 2.2 [50]. The backward extrapolation of the curves slightly changing in fig. 2.1 emphasizes immediately the problem that a small change in the slope of the tangent could generate a significant change in the extrapolated prompt area. As underlined by Gozani the correction cannot account for the effect of kinetic exchange of neutrons from the reflector into the core ("kinetic distortion").

2.2.3 The Slope Fit Method

The slope fit (or prompt decay fitting) method obeys the idea of measuring or finding the fundamental mode prompt decay constant α_0. The prompt decay constant corresponds to the exponent in the delayed-neutron-free point kinetic equation (2.49). Conceptually, the decay constant is also congruent to the time eigenvalue of the zeroth mode (*see* section 2.1.3), which however is based on a more physical ground. If the decay constant α_0 was measured and the effective delayed neutron fraction β_{eff} and the mean neutron generation time Λ calculated, the static reactivity ρ could be calculated by using eq. (2.54) [51].

$$\alpha_0 = \frac{\rho - \beta_{\mathrm{eff}}}{\Lambda} \tag{2.54}$$

Generally, the same restrictions hold for this method as mentioned for the area method in section 2.2.2. But the application of this method shows a significant sensitivity on the position of the detector. Moreover, it shows an unfavorable dependence on the fitting method itself or the evaluator, who fits numerically the exponentials to the measured curve. There is no stringent evidence that the numerical fit would achieve the physical decay constant, if the pure fundamental mode decay was visible.

2.3 Application of the Fully Implicit Time Integration Scheme

Both methods, area and slope fit method, were designed for unreflected reactors [51]. Consequently, methods have been studied to extract the fundamental mode from measurements or generate correction factors based on higher modes calculations [27, 52, 53]. In recent developments the attempt is made to solve the time eigenvalue equation for higher modes. Cao has introduced this capability in a two-dimensional diffusion code and used it to simulate a configuration of the MUSE-4 experiment. With help of the higher prompt modes and eigenfunctions correction factors are calculated for the area method [54, 55].

Lathouwers developed a Finite Element Even Parity transport code [56] with the capability of calculating the time eigenvalues and eigenfunctions for large numbers of modes. In an application to the current GUINEVERE reactor [57] it is shown that a very high number of modes has to be accounted for in a two-dimensional calculation, in order to describe the time-dependent behavior of the PNS experiment in a modal synthesis approach. The numerical effort for a full three-dimensional calculation with a suitable energy group representation seems to be very challenging. A disadvantage of this approach is the fact that the time eigenvalue equation is a homogeneous equation with no account for the external neutron source. To achieve a suitable guess of the initial condition with external source, approximations have been proposed [55, 57] which are a combination of the modal synthesis approach and the external source.

The prompt decay of the PNS experiment can be simulated with MC codes. Several works have been performed calculating the time-dependent detector responses with the `MCNP5` or the `MCNPX` code [48, 49, 58, 59]. These codes include the simulation of delayed neutrons, but the build-up during the initial phase of the experiments to get the constant background is not easy to calculate. Talamo [60] proposed the pulse superimposition method, where the detector response is tallied for one pulse once for a very long time and the delayed neutron tail is afterward constructed by repeatedly superposing the detector response shifted in time in accordance with the pulse width. This method is generally valid for the zero-power reactor without feedback. The drawback of the use of MC codes on top of the computing challenge is that to get a local response as a function of the pulse width the variance reduction techniques have to be massively used in general. Thus, instead of the full phase space neutron flux solution of the pulse a local quantity is achieved only. This makes it almost impossible to look for observed physical effects, when they are not known before.

The summarized reactor theory in view of the PNS experiment and the described reactivity determination methods lead to the observation that a simulation tool, which can overcome the mentioned drawbacks and can combine most of their advantages is not yet available. Here is pointed out in short form, what is expected from a suitable simulation tool:

- Solution of the time-dependent transport equation
- Time-, energy-, solid-angle-dependent external neutron source
- No dependence on adjoint weighted parameters
- Evaluation of local quantities (detector response, ...)
- Calculation of integral parameters (k_{eff}, k_{src}, ...)
- Full solution in phase space in acceptable time

The fully implicit time discretization scheme inserted in a suitable transport code is a promising candidate for the investigation of the PNS experiments. First applications have appeared in the development of the `TIMEX` [61] and `TRANZIT` [62] codes in the early seventies. Because of the huge computational effort, these programs could only be used for small and prompt supercritical problems without delayed neutrons. Recent developments of the discrete ordinates transport codes `PARTISN` [63] and `TORT-TD` [64] make use of this method, the first without delayed neutrons but time-dependent external source and the latter only for the homogeneous form of the transport equation.

The main approximation of the time discretization is displayed in equation (2.55). It expresses the time differential of the angular neutron flux at time $t_{\tau+1}$ as difference of the flux at $t_{\tau+1}$ and t_τ over the time step $\Delta t = (t_{\tau+1} - t_\tau)$.

$$\frac{1}{v_g}\frac{\partial}{\partial t}\psi_g(\boldsymbol{r}, \boldsymbol{\Omega}, t)\Big|_{t_{\tau+1}} \simeq \frac{\psi_g(\boldsymbol{r}, \boldsymbol{\Omega}, t_{\tau+1}) - \psi_g(\boldsymbol{r}, \boldsymbol{\Omega}, t_\tau)}{v_g\,\Delta t} \tag{2.55}$$

The same time discretization must be applied to the precursor equation (2.56).

$$\frac{\partial}{\partial t}C_j(\boldsymbol{r}, \boldsymbol{\Omega}, t)\Big|_{t_{\tau+1}} \simeq \frac{C_j(\boldsymbol{r}, t_{\tau+1}) - C_j(\boldsymbol{r}, t_\tau)}{\Delta t} \tag{2.56}$$

The time discretizations of eq. (2.55) and eq. (2.56) are now inserted into equation (2.1) and (2.2), respectively. On the right hand side of the resulting equation (2.57) the time-dependent variables are integrated from t_τ to $t_{\tau+1}$.

$$\frac{\psi_g(\boldsymbol{r}, \boldsymbol{\Omega}, t_{\tau+1}) - \psi_g(\boldsymbol{r}, \boldsymbol{\Omega}, t_\tau)}{v_g\,\Delta t} = -\int\limits_{t_\tau}^{t_{\tau+1}} \mathrm{d}t\,\boldsymbol{\Omega}\cdot\nabla\psi_g(\boldsymbol{r}, \boldsymbol{\Omega}, t)$$

$$-\int\limits_{t_\tau}^{t_{\tau+1}} \mathrm{d}t\,\Sigma_{\mathrm{t}g}(\boldsymbol{r})\,\psi_g(\boldsymbol{r}, \boldsymbol{\Omega}, t) + \sum_{g'}\int \mathrm{d}\boldsymbol{\Omega}'\,\Sigma_{\mathrm{s}g'g}(\boldsymbol{r}, \boldsymbol{\Omega}' \to \boldsymbol{\Omega})\int\limits_{t_\tau}^{t_{\tau+1}} \mathrm{d}t\,\psi_{g'}(\boldsymbol{r}, \boldsymbol{\Omega}', t)$$

$$
\begin{aligned}
&+ \chi_{\mathrm{p}g}(\boldsymbol{r})(1-\beta)\sum_{g'} \nu_{\mathrm{t}g'}(\boldsymbol{r})\,\Sigma_{\mathrm{f}g'}(\boldsymbol{r}) \int\limits_{t_\tau}^{t_{\tau+1}} \mathrm{d}t\,\phi_{g'}(\boldsymbol{r},t) \\
&+ \sum_j \chi_{jg}(\boldsymbol{r})\,\lambda_j \int\limits_{t_\tau}^{t_{\tau+1}} \mathrm{d}t\,C_j(\boldsymbol{r},t) + \int\limits_{t_\tau}^{t_{\tau+1}} \mathrm{d}t\,Q_g(\boldsymbol{r},\boldsymbol{\Omega},t) \qquad (2.57)
\end{aligned}
$$

The integration is carried out in the form of equation (2.58).

$$
\int\limits_{t_\tau}^{t_{\tau+1}} \mathrm{d}t\,a(t) \simeq a(t_{\tau+1})\,\Delta t \qquad (2.58)
$$

The execution of the integration for the precursor term in the last line of equation (2.57) yields the precursor concentration $C_j^{t_{\tau+1}}$ which in turn depends on the flux of the actual time step $\phi_{g'}^{t_{\tau+1}}$ (compare eq. (2.61)) for which the modified transport equation is solved. To remedy the mutual dependence the precursor concentration of eq. (2.61) is inserted in the equation, thereby gaining the known precursor concentration of the last time step and an additional occurrence of $\phi_{g'}^{t_{\tau+1}}$. The resulting terms can be ordered in a way that the final equation (2.59) looks formally like the common inhomogeneous or fixed source transport equation, even if the static problem was the homogeneous equation.

$$
\begin{aligned}
\Big[\boldsymbol{\Omega}\cdot\nabla + \tilde{\Sigma}_g(\boldsymbol{r})\Big]\,\psi_g^{t_{\tau+1}}(\boldsymbol{r},\boldsymbol{\Omega}) = &\sum_{g'} \int\limits_{4\pi} \mathrm{d}\boldsymbol{\Omega}'\,\Sigma_{\mathrm{s}g'g}(\boldsymbol{r},\boldsymbol{\Omega}'\cdot\boldsymbol{\Omega})\,\psi_{g'}^{t_{\tau+1}}(\boldsymbol{r},\boldsymbol{\Omega}') \\
&+ \tilde{\chi}_g \sum_{g'} \nu_{\mathrm{t}g'}\Sigma_{\mathrm{f}g'}(\boldsymbol{r})\,\phi_{g'}^{t_{\tau+1}}(\boldsymbol{r}) + q_g^{t_{\tau+1}}(\boldsymbol{r},\boldsymbol{\Omega}) \qquad (2.59)
\end{aligned}
$$

The fixed source is constructed of the real external neutron source, the delayed neutron source and a new term called time source (eq. (2.60)). The time source holds the connection to the preceding time iteration. Neutrons from the previous time step reenter into the actual time step.

$$
q_g^{t_{\tau+1}}(\boldsymbol{r},\boldsymbol{\Omega}) = \underbrace{\frac{1}{\Delta t}\sum_j \chi_{jg}\lambda_j\gamma_j C_j^{t_\tau}(\boldsymbol{r})}_{\text{Delayed neutron source}} + \underbrace{\frac{1}{v_g\Delta t}\psi_g^{t_\tau}(\boldsymbol{r},\boldsymbol{\Omega})}_{\text{Time source}} + \underbrace{Q_g^{t_{\tau+1}}(\boldsymbol{r},\boldsymbol{\Omega})}_{\text{External source}} \qquad (2.60)
$$

After the flux solution of the $t_{\tau+1}$ time step was achieved, the new precursor concentration will be evaluated with equation (2.61).

$$
C_j^{t_{\tau+1}}(\boldsymbol{r}) = \gamma_j\Big[\frac{1}{\Delta t}C_j^{t_\tau}(\boldsymbol{r}) + \beta_j\Delta t\sum_{g'} \nu_{\mathrm{t}g'}\Sigma_{\mathrm{f}g'}(\boldsymbol{r})\,\phi_{g'}^{t_{\tau+1}}(\boldsymbol{r})\Big] \qquad (2.61)
$$

The reordering has changed the meaning of some of the common constants of the transport equation. Modified constants are indicated by the tilde, so as the modified total cross section, which now has an additional "time absorption" term (eq. (2.62)). Moreover, the former prompt fission spectrum carries now an additional term involving the delayed neutron fission spectra (eq. (2.63)).

$$\tilde{\Sigma}_g(\boldsymbol{r}) = \Sigma_{\mathrm{t}g}(\boldsymbol{r}) + \frac{1}{v_g \Delta t} \tag{2.62}$$

$$\tilde{\chi}_g(\boldsymbol{r}) = \chi_{\mathrm{p}g}(\boldsymbol{r})\,(1-\beta) + \sum_j \chi_{jg}\lambda_j\gamma_j\beta_j \tag{2.63}$$

$$\gamma_j = \frac{\Delta t}{1+\lambda_j \Delta t} \tag{2.64}$$

Other possible time discretization schemes are the explicit and the central-difference scheme. While the implicit and explicit schemes are accurate only to the order $O(\Delta t)$, the central-difference scheme is accurate to the order $O(\Delta t^2)$ [65]. However, the accuracy can be always improved with a sufficiently small time step. The reason for the choice of the implicit scheme is the unconditional stability that can be proved. This property leads to the preferable behavior that an error in the time discretization - introduced by a too large time step - will not grow with every time step. The central-difference scheme is also unconditional stable, but the numerical effort significantly higher, so that the implicit scheme seems to be a good compromise.

As can be seen so far in the time discretization of the time-dependent transport equation, the only approximations applied were the implicit time scheme and multigroup representation of the energy dependence. If the energy group structure can cover the general physical effects of the problem and the time steps are chosen properly to not violate the restrictions given by the discretization scheme, then the correct implementation of equations (2.59) and (2.60) can describe the propagation of neutrons after a neutron pulse, the redistribution of the neutron field from a very excited state to a potential fundamental mode decay till the neutron flux stabilizes on the level of the delayed neutron background. This simulation will therefore incorporate completely the effects, for which a huge number of modes would be needed to include the "harmonic distortion", and will resemble the "kinetic distortion", because the neutrons are allowed to move according to the underlying physical principles.

Wigner mentions the shortcoming of the time-dependent diffusion equation, in that the wave-like propagation of neutrons after a pulse cannot be properly taken into account [66]. The reason is that the static diffusion equation is equivalent to the spherical harmonics approximation of the transport equation truncated after the first order (P_1 approximation). The commonly used time-dependent diffusion equation skips additional time-dependent terms, which origin from the time-derivative applied on the spherical harmonics flux representation. The time-derivatives considered lead to the "Telegrapher's equation", in which the spatial flux propagation obeys a "wave front". The neutron velocity however is still wrong by a factor of $\sqrt{3}$. The general conclusion is that if the solid angle is represented in a suitable manner and the time-derivative can be resolved properly, which is the case in the discrete ordinates transport approximation, then this physical effect of the very fast wave-like neutron propagation through the reactor medium could be accounted for. However, studies show a very short time interval in the range of $10^{-8}\,\mathrm{s}$ to $10^{-7}\,\mathrm{s}$, where such effects are visible [67].

Chapter 3

Development of a New Microscopic Master Library for General Reactor Calculations

Deterministic cross section code systems use typically a two step approach for whole core calculations. The first step is devoted to the generation of effective macroscopic cross sections of material regions. The procedures rely on cell calculation methods, which especially account for energy and spatial self-shielding effects. The energy group structure thus is sufficiently fine and the geometry is largely resolved to treat the heterogeneity of the cell. The obtained neutron fluxes of the material regions are used for the homogenization and collapsing to few group constants. In the second step parts of or the whole reactor is subdivided into coarser material regions without internal structure and the transport or diffusion equation is solved for the neutron flux. The first three sections 3.1, 3.2 and 3.3 of this chapter deal with the refinement of the energy structure in the `KANEXT` code system leading to a new group structure for general reactor calculations, the processing of the continuous energy cross sections to the multigroup form and the validation in a unit cell calculation of the YALINA-Thermal reactor, respectively. Then, section 3.4 relates to the development of tools for the generation of constants needed for time-dependent core calculations. Finally, the second step is addressed in section 3.5, where the validation work is continued on the core level of the YALINA-Thermal reactor.

3.1 Development of a Flexible Energy Group Structure

The early `KANEXT` master libraries were based on a 26 groups structure for fast reactor applications [68,69]. It was in particular for the sodium cooled fast reactor purpose observed that the slowing down was not correctly accounted for in the coarse group structure, so that a 208 groups fine structure was employed for the improvement of the scattering treatment [68, 70, 71]. The extension of `KANEXT` to the field of Light Water Reactor (LWR) lead to the implementation of the original 69 groups `WIMS` structure [72, 73]. This famous energy group structure is characterized by 14 fast energy groups from 10 MeV to 9.118 keV, 13 resonant energy groups from 9.118 keV to 4 eV and 42 thermal energy groups from 4 eV to 0.001 eV. This structure has been used for a broad range of (epi)thermal and fast reactor calculations, because it combines the advantages of thermal and fast calculation characteristics like detailed up- and downscattering.

Based on this extensively validated `WIMS` group structure the recent JEFF 3.1, JEFF 3.1.1 and ENDF/B VII.0 evaluations were adapted to 69 groups master libraries. In order to account for the high energetic neutrons from the (d,t) neutron source, the upper group boundaries have to be extended. The energy subdivision above 10 MeV should reflect the current knowledge of suitable group structures for fusion neutrons with deterministic codes.

For this study, a new 350 energy groups master library has been created, which is more generally applicable to account for high energy neutrons from fusion neutron sources that are often used in ADS experiments. Therefore, the energy structure above 10 MeV is refined with 16 additional energy groups with the group boundaries of the `VITAMIN-J` group structure [74]. The various `VITAMIN` structures have been used for shielding investigations of fusion neutrons and can be considered as validated. In view of a library for general application in LWRs and Fast Breeder Reactors (FBRs) the energy structure below 10 MeV is also refined. Between 4 eV and 10 MeV the energy boundaries of a 334 group library investigated and approved by Broeders [73] have been applied. With this very much refined group structure the slowing-down of the neutrons can generally much better be described in the epithermal and fast energy range. Moreover, the broader resonances of many important nuclides towards higher energies are directly accounted for. The resulting 350 energy groups neutron flux will serve as a general and improved weighting flux for the homogenization procedure.

The summarized properties of the 350 energy groups microscopic master library are:

- Extension to the maximum neutron energy of 19.64 MeV
- 16 energy groups above 10 MeV with an energy spacing about 0.5 MeV, narrowed to 0.35 MeV around 14.1 MeV
- The energy boundaries between 4 eV and 10 MeV are generated with a lethargy width $\Delta u = \log(\frac{E_g}{E_{g+1}}) \simeq 0.05$, resulting in 292 energy groups
- Dominant resonances are carefully covered
- Below 4 eV the 42 energy groups of the original `WIMS` structure is kept with a minimum energy of 0.001 eV
- Between 0.001 eV and 10 MeV the original 69 energy group boundaries are included as a subset for the purpose of group collapsing

See Appendix B.1 for a complete listing of both energy group structures.

Although the energy limit of about 20 MeV is well below the energies of spallation neutrons, it is possible to use these libraries in case of deterministic reactor calculations with spallation sources. Investigations show that about 86 % of the neutrons leaving the target window have energies below 20 MeV [44].

3.2 Processing of the `ENDF-6` Data Files

The microscopic multigroup cross section libraries for the `KANEXT` system are generated with a well validated procedure shown in fig. 3.1. To prepare the cross sections, the nuclear data processing code `NJOY` is used [23]. It reads the `ENDF-6` formatted evaluated data files [75], adds both resolved and unresolved resonance data to the continuous energy data and generates multigroup cross section data by means of the module `GROUPR`. The main cross section data is stored in the `MATXS` format, delayed neutron data in the `DLAYXS` format. All file formats of `NJOY` are available from the manual [23]. The conversion code `NJOYPROC` (see Appendix B.2.3.2) transfers these cross section data to the `KANEXT` format `GRUBA` [76] which can be handled directly with the group constant management program `GRUMA` [77]. Finally, all nuclide cross sections are stored into a microscopic master library.

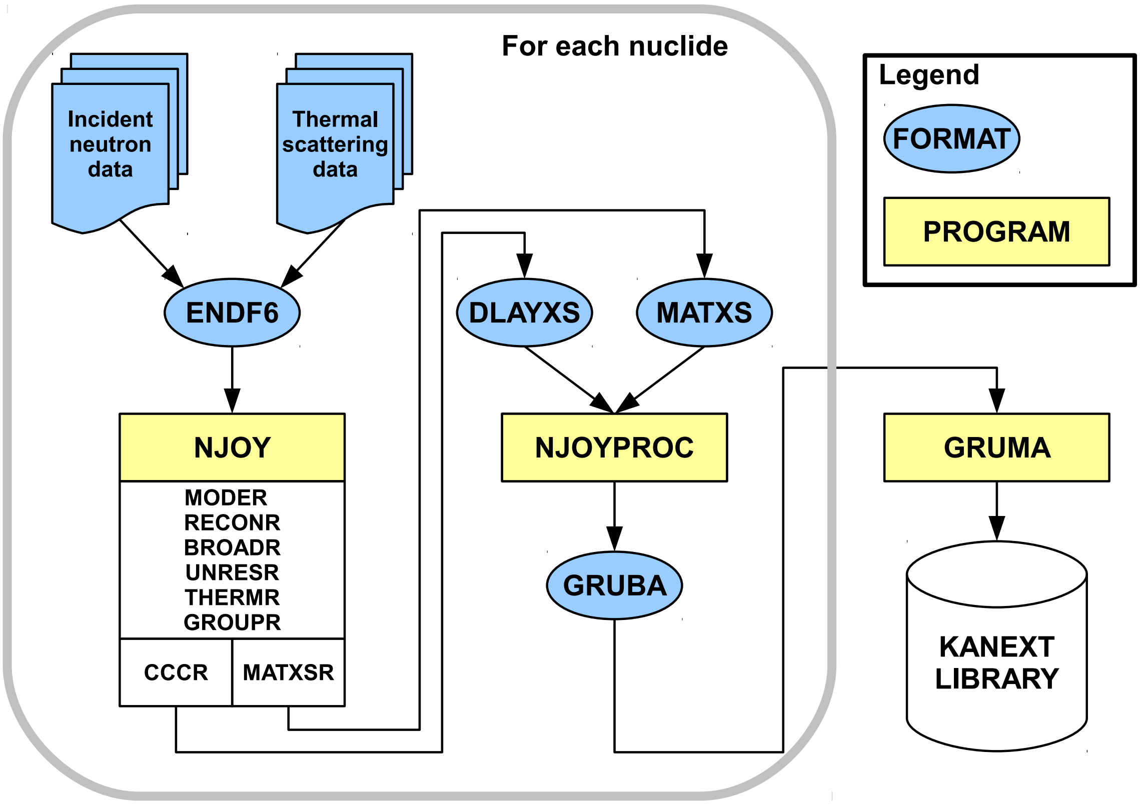

Figure 3.1: NJOY flow chart

To the common properties of all new `KANEXT` libraries belong the set of temperatures (300 K, 900 K, 1200 K, 1500 K, 2000 K and 3000 K), for which complete multigroup cross section data sets exist. The Legendre expansion of all scattering-like, i.e. (n,n), (n,n′), (n,n), (n,2n), (n,3n), (n,4n), (n,xn), transfer cross sections is stored up to the fifth order. For all materials processed the free gas thermal scattering transfer cross sections [1, 23] are added. Only for hydrogen in water, hydrogen in Polyethylene (PE) and carbon in graphite the corresponding thermal cross sections are prepared with the S(α, β) tables of the evaluation data file in section MF7 [75] together with the `THERMR` module of `NJOY`. As a last point exhaustive retaining of reaction types is practiced for usage and combination at run time.

For thermal reactor investigations a slightly modified EPRI-CELL weighting spectrum of the `NJOY` code is used [23]. The original spectrum exhibits a local maximum at fusion neutron energies around 14.1 MeV. For the generation of the new libraries this spectral maximum is smoothed out, since the new group structure is sufficiently fine on one hand and on the other it would misweight the cross sections in the rather broad first energy group between 6.0655 MeV and 20 MeV of the 69 groups library in case of a neutron-source-free problem.

According to this procedure, the master libraries are generated for the JEFF 3.1, JEFF 3.1.1, and ENDF/B VII.0 evaluated data files. The libraries of the JEFF data files are complemented by the activation nuclide data sets [78] containing only scalar cross sections for capture, fission, (n,2n), etc. This extended nuclide data set allows the generation of problem dependent burn-up cross sections, but cannot be used for transport calculations due to the lack of energy-angle transfer cross sections. In table 3.1 these extended libraries are marked with the letter "A". The suffix "LWR" indicates the thermal reactor weighting spectrum. The 350 groups libraries are generated as well with the modified EPRI-CELL spectrum, but disclaim this suffix, because they show very satisfactory performance in both thermal and fast reactor applications due to the fine group structure.

Table 3.1: New generated multigroup libraries

File name	Evaluation	Number of materials
G69P5JEFF31ALWR	JEFF 3.1	799 (381 full evaluated + 3 thermal + 415 activation and pseudo nuclides)
G69P5JEFF311ALWR	JEFF 3.1.1	799 (381 full evaluated + 3 thermal + 415 activation and pseudo nuclides)
G69P5E70BLWR	ENDF/B VII.0	406 (393 full evaluated + 3 thermal + 10 pseudo nuclides)
G350P5JEFF31A	JEFF 3.1	799 (381 full evaluated + 3 thermal + 415 activation and pseudo nuclides)
G350P5JEFF311A	JEFF 3.1.1	799 (381 full evaluated + 3 thermal + 415 activation and pseudo nuclides)
G350P5E70B	ENDF/B VII.0	406 (393 full evaluated + 3 thermal + 10 pseudo nuclides)

For easier referencing table 3.2 presents the abbreviations for short-hand use in the next chapters.

Table 3.2: Abbreviations of the libraries

Abbreviation	File name	Evaluation
B69a	G69P5JEFF31ALWR	JEFF 3.1
B69b	G69P5JEFF311ALWR	JEFF 3.1.1
B69c	G69P5E70BLWR	ENDF/B VII.0
B350a	G350P5JEFF31A	JEFF 3.1
B350b	G350P5JEFF311A	JEFF 3.1.1
B350c	G350P5E70B	ENDF/B VII.0

3.2.1 Thermal Scattering Cross Sections

The YALINA-Thermal reactor is built up of significant masses of well moderating materials. The fuel rods are contained in a matrix of PE blocks constituting the fuel assembly. The reflector consists of large blocks of graphite. Both materials have large moderating ratios. A report [79] mentions for the relevant energy range a ratio of about 122 for PE. The ratio of graphite is listed in textbooks e.g. [80] to be around 200. Consequently, it is of great importance to handle the scattering properties of these materials to the best available knowledge.

The thermal scattering cross sections for certain nuclides bound in molecules are found in the MF7 section of the evaluated nuclear data files. Here, the files for hydrogen bound in PE and carbon in graphite files have to be processed, in order to get the complex scattering matrices in the thermal neutron energy range into the `KANEXT` multigroup libraries. The neutron energy group structure between 0.001 eV and 4 eV is generally that of the `WIMS` reactor physics code system [72] and all presented group structures use this thermal structure below 4 eV.

Some of the important scattering properties like the energy transfer and angular dependence are furthermore analyzed in view of the use in deterministic transport solvers. The relevant results of the YALINA-Thermal pin cell characterization of section 3.3.1 are therefore anticipated as far as average neutron energy and energy of the peak flux are concerned.

3.2.1.1 Polyethylene

PE is defined by the molecule formula CH_2 and is used as moderator mainly in zero-power research reactors and cold neutron facilities. All recent nuclear data evaluations provide the MF7 $S(\alpha, \beta)$ tables for PE. The origin of all of them is the work of Sprevak and Koppel [81]. In recent evaluations only adjustments to new hydrogen cross section measurements and additional temperatures and energy ranges (cold neutron applications) have been added without changing the theory in the original energy range [82].

PE briefly is characterized as a macro molecule of infinite length, where the CH_2 radicals are positioned at the vertex of a "zig-zag" chain [81]. Because of the weak coupling of neighboring chains the incoherent approximation is chosen for the scattering law. While the resulting $S(\alpha, \beta)$ table only describes the hydrogen bound in PE, the carbon is modeled in the free gas approximation. The thermal multigroup scattering cross section set for PE is generated according to the flow diagram of fig. 3.1. The input options of the `THERMR` module are such that they consider the incoherent elastic scattering contributing to the self-scatter part of the transfer matrices and the incoherent inelastic scattering for all energy transfer from the $S(\alpha, \beta)$ tables [23]. The available temperatures are 293.6 K and 350 K and the maximum thermal energy is defined as 10 eV in the `NJOY` input.

Fig. 3.2a compares the total microscopic scattering cross section of three variants of hydrogen at 293.6 K in the multigroup form. It is obvious that the free gas treatment of hydrogen cannot be used to approximate the scattering cross section of PE. In comparison to the scalar cross section of hydrogen in water, small differences are observed. The neighboring graph (fig. 3.2b) distinguishes between the incoherent elastic and inelastic scattering cross sections of PE, which in sum constitute the total scattering cross section.

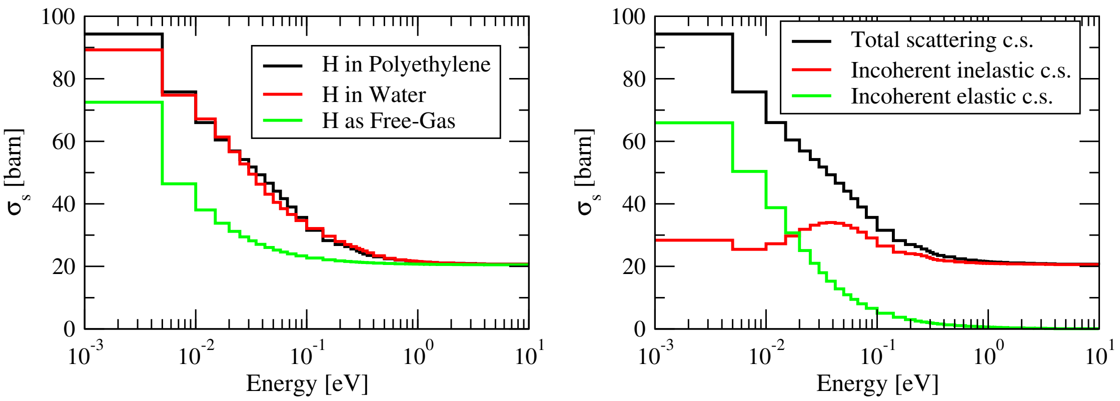

(a) Three variants of hydrogen total scattering cross sections

(b) Total scattering cross section of hydrogen in PE and its contributing reactions

Figure 3.2: Scalar scattering cross sections at 293.6 K

The next diagram (fig. 3.3) shows the energy transfer of PE for thermal neutron energies up to 10 eV. Mathematically, the energy transfer matrix is given by the zeroth moment of the Legendre representation of the energy-angle dependent scattering. The thin lines represent the energy group boundaries. The abscissa specifies the incident neutron energy for which a secondary energy distribution exists on the ordinate. The diagonal line of squares marks the scattering of the neutron from the incident energy group to the same energy group (self-scattering). All what is located above this diagonal, is scattering towards higher energy groups (upscattering), and everything below is scattering towards lower energy groups (downscattering). In terms of the theory of two body scattering, hydrogen is an "ideal" scatterer, since it allows the maximal energy transfer by collision of particles of similar size. This is underlined by the fact that all downscatter positions are filled with non-zero probabilities. Additionally, one observes significant upscattering in the very thermal energy groups which ranges over almost two decades of energy.

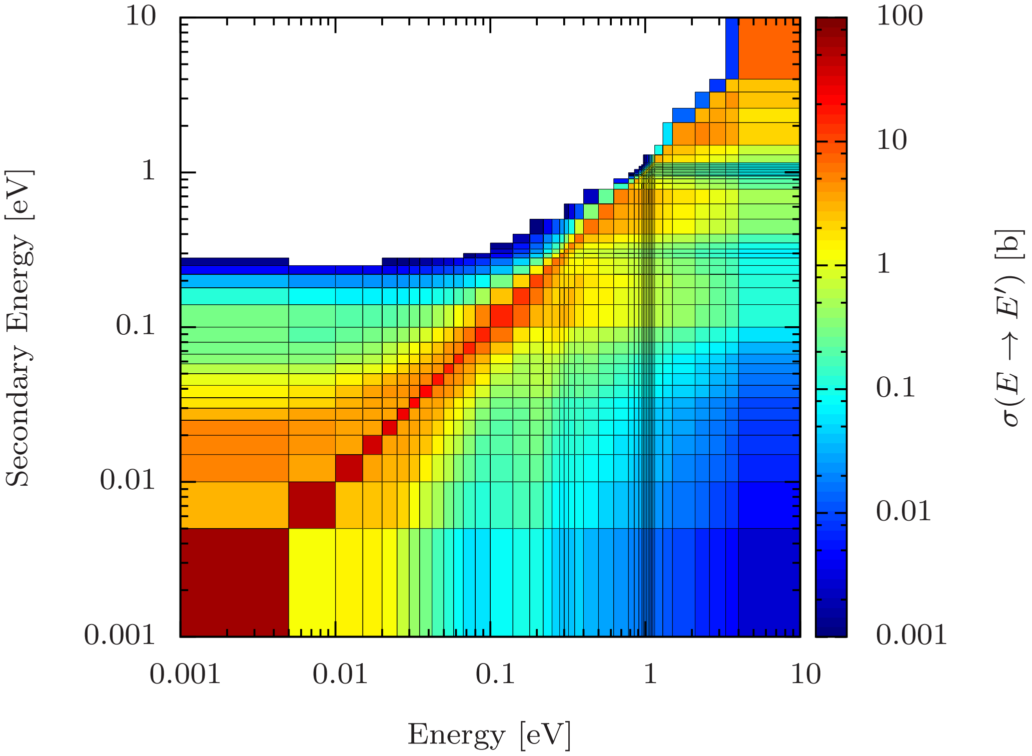

Figure 3.3: Energy transfer of PE at 293.6 K

The anisotropy of the scattering reaction in deterministic methods is approximated by the Legendre moments higher than the zeroth. Applying the newly developed `KANEXT` module `SCAPLO` (Appendix B.2.1), the angular neutron distribution can be plotted in the dependence on the energy group. The flux solution of a YALINA-Thermal unit cell calculation (anticipating section 3.3.1) yields an average neutron energy of 3.73 eV in the fuel region and 2.05 eV in the moderator region. For the energy groups of the formerly described energy structures enclosing these averages the angular neutron distribution will be investigated. The first graph in fig. 3.4a describes the average probability of the neutron to be emitted with a particular direction (written as μ, the cosine of the scattering angle θ) for a neutron with the incident energy laying between 2.1 eV to 2.6 eV. In the common scattering nomenclature $\mu = -1$ is the full backward scattering with the scattering angle $\theta = 180°$. Then, $\mu = 1$ denotes the full forward scattering with the scattering angle $\theta = 0°$. Note that the specification of the Legendre order in the legend of the graph denotes the sum of the contributions up to the specified Legendre moment rather than the isolated distribution of one of the Legendre moments. For this energy group a preferred scattering into the forward directions is observed, for which the following two figures 3.4b and 3.5a are additional examples. This directional dependence can only be described satisfactorily, if a Legendre series expansion of order higher than one is used. Applying the first moment (linear anisotropy) may be the worst, since not only the complex structure of the directional dependence is getting lost, but also a non-physical negative scattering contribution is added in the backward direction, where the scattering is essentially almost zero. This truncation error may lead to numerical problems in neutron transport codes in terms of negative fluxes.

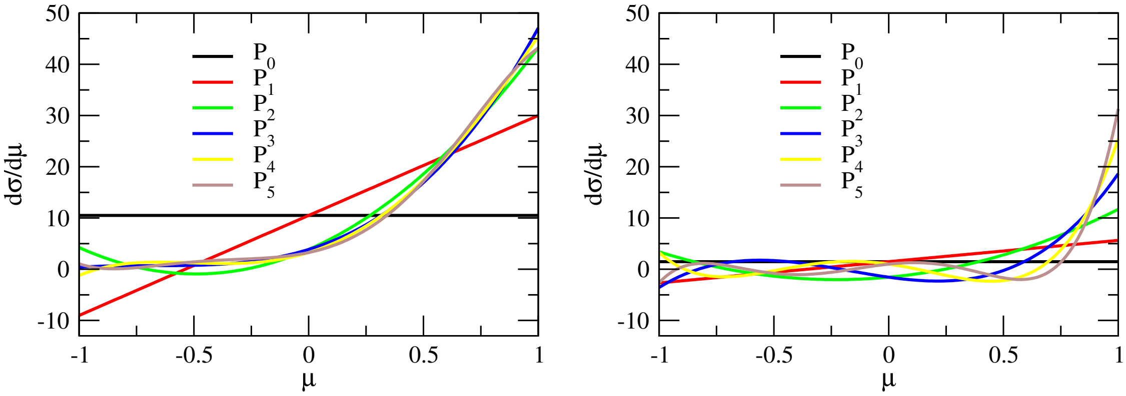

(a) Averaged over all outgoing energies

(b) Scattering into the same energy group

Figure 3.4: Differential scattering cross section at the incident neutron energy range 2.1 eV to 2.6 eV as function of the cosine of the scattering angle μ and the order of the Legendre expansion at 293.6 K for PE

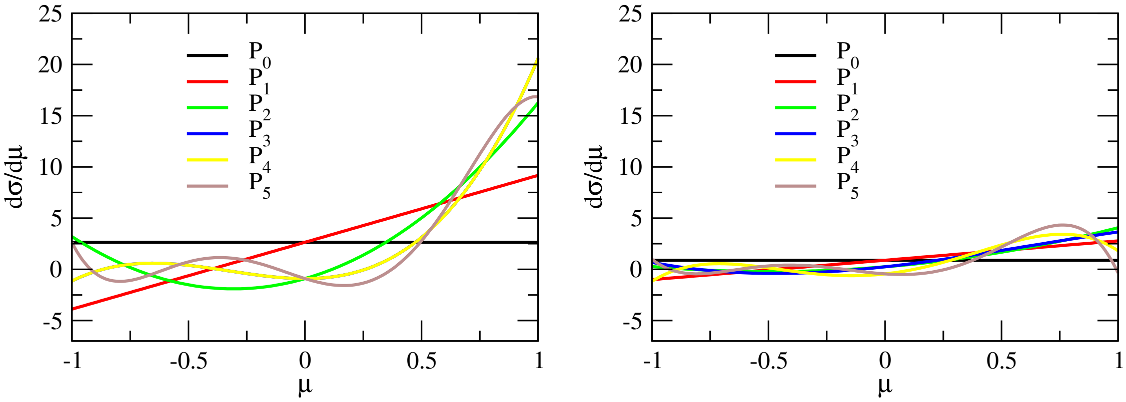

(a) Downscattering into the first adjacent group (1.5 eV to 2.1 eV)

(b) Downscattering into the second adjacent group (1.3 eV to 1.5 eV)

Figure 3.5: Differential scattering cross section at the incident neutron energy range 2.1 eV to 2.6 eV as function of the cosine of the scattering angle μ and the order of the Legendre expansion at 293.6 K for PE

The following angular distributions of fig. 3.6 belong to the neutron energy group of the peak flux of the unit cell calculation (*see* section 3.3.1). It is located at a typical thermal neutron energy range (0.025 eV to 0.03 eV) close to the 2200 m s^{-1} neutron velocity. This energy group obeys the trend of preferred forward scattering (fig. 3.6a) which is enforced by the dominant self-scattering part (*see* fig. 3.6b). The plotted up- and downscatter parts (fig. 3.7a and fig. 3.7b) scatter more isotropically with rather low probability. For these graphs the first moment fits better to the averaged behavior, but produces nevertheless negative contributions.

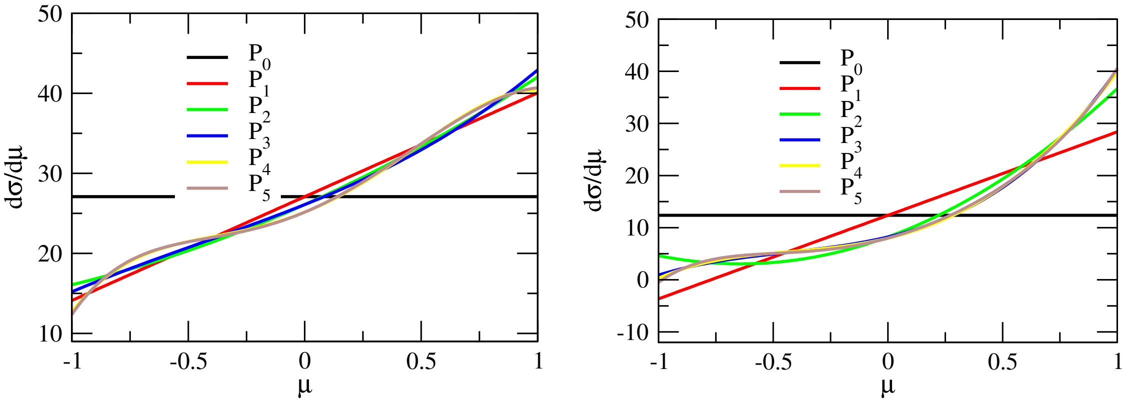

(a) Averaged over all outgoing energies

(b) Scattering into the same energy group

Figure 3.6: Differential scattering cross section at the incident neutron energy range 0.025 eV to 0.03 eV as function of the cosine of the scattering angle μ and the order of the Legendre expansion at 293.6 K for PE

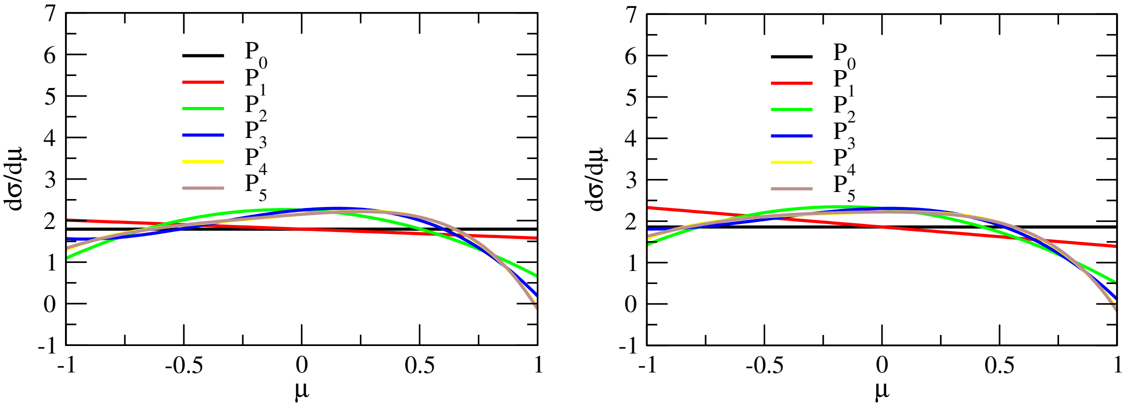

(a) Upscattering into the first adjacent group (0.03 eV to 0.035 eV)

(b) Downscattering into the first adjacent group (0.02 eV to 0.025 eV)

Figure 3.7: Differential scattering cross section at the incident neutron energy range 0.025 eV to 0.03 eV as function of the cosine of the scattering angle μ and the order of the Legendre expansion at 293.6 K for PE

The up- and downscattering over the large energy group ranges will have its influence on the iteration in any deterministic code. However, the original fine group structure is mainly used in cell calculations, so that the demand in terms of the scattering treatment is huge, but in terms of the geometry rather limited to some material zones in a cylindrical cell.

The thermal scattering cross section and matrices are stored on the recent `KANEXT` multigroup libraries under the nuclide name `'HPOLY___'` for the temperatures 293.6 K and 350 K, in between which every temperature can be linearly interpolated (as recommended by McFarlane [23] and Keinert and Mattes [83]). The Legendre order may be chosen up to the fifth order. Above 10 eV the original hydrogen cross sections are added. The recommended [84] carbon cross sections treated as free gas and compiled for the appropriate temperatures are available under the nuclide name `'CPOLY___'`.

3.2.1.2 Graphite

The thermal cross sections for graphite originate from the work of Young and Koppel [85] and Young et al. [86]. For subsequent evaluations Keinert and Mattes for JEFF 3.1 [87] and McFarlane for ENDF/B VI [88] refined the α and β grid and ranges of the $\mathrm{S}(\alpha, \beta)$ tabulation. In addition, the scalar cross section has been adjusted to more recent measurements. A thorough investigation by Mattes and Keinert [87] confirmed recently the overall accurateness of the nearly 45 years old methodology in comparison to two additional models.

Graphite is hexagonal in its planar structure holding effectively four atoms in a unit cell. Fig. 3.8a underlines the need to consider the thermal scattering in carbon bound in graphite separately from the free gas model. The binding between the planar sheets have been found weakly coupled, while the binding in between the hexagonal planes is strong. This fact of interfering elements in a crystal lattice becomes important, when the de Broglie wavelength of the neutron is of similar size as the lattice spacing [1]. This happens for energies around 0.01 eV and as shown in fig. 3.8b is observed between 0.001 eV to 0.1 eV for graphite. At these energies Bragg effects cause sharp spikes in the course of the scattering cross section, which are computed for the coherent elastic scattering by the `THERMR` module of `NJOY`. Additionally, the incoherent inelastic scattering cross section is taken into account through the $\mathrm{S}(\alpha, \beta)$ tables of the MF7 file, which is a smooth function of energy. The sum of contributing scattering reactions forms the total scattering cross section and the associated scattering matrices.

The energy transfer of graphite is visualized in fig. 3.9. For this graph the same formal description holds as for fig. 3.3. It is obvious that the energy range of downscattering is much smaller than for hydrogen in PE, which is firstly a consequence of the less good scattering properties due to the larger molar mass. Moreover, the scattering probability reduces very much when the diagonal element is left in both directions of the secondary energy distribution. Upscattering appears relevant only for the first neighboring energy group, thus the self-scattering is the main scattering mechanism and is dominated below 0.1 eV by the coherent elastic scattering cross section.

When assessing the anisotropic scattering property, the behavior can be subdivided into two parts. When incoherent inelastic scattering is dominant or non-self-scattering is

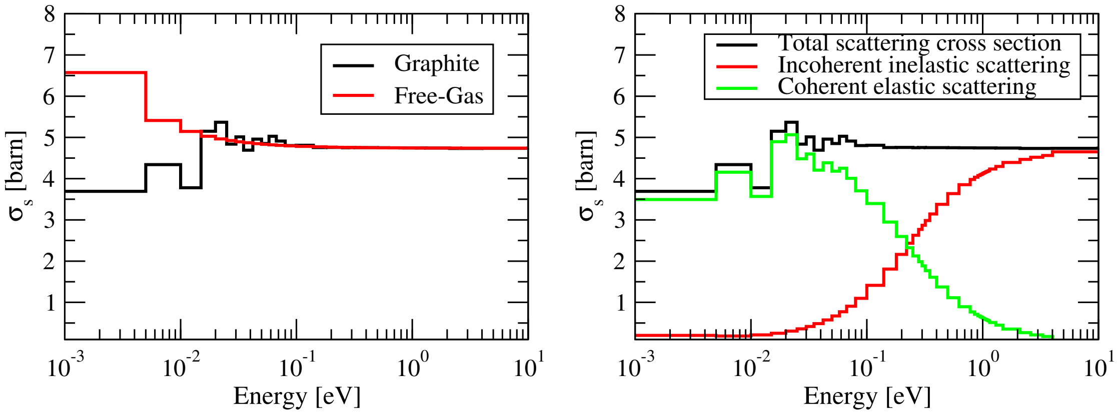

(a) Total scattering cross section of carbon in graphite and modeled as free gas

(b) Total scattering cross section of graphite and its contributing reactions

Figure 3.8: Scalar scattering cross sections at 293.6 K of carbon

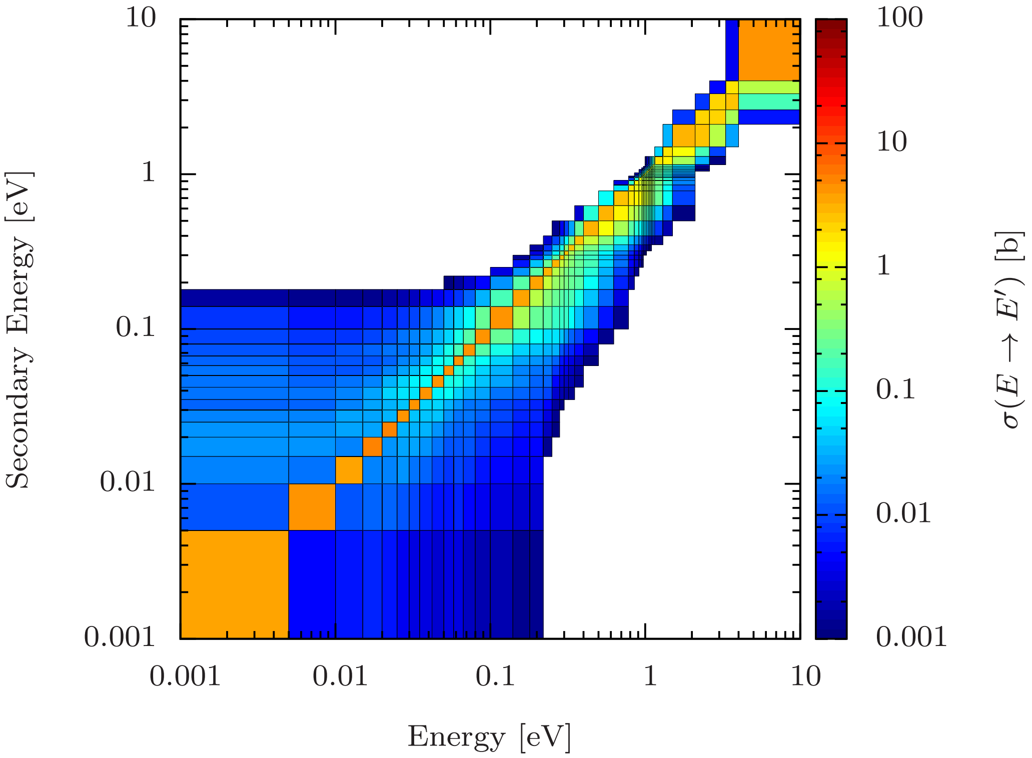

Figure 3.9: Energy transfer of graphite at 293.6 K

regarded, even the first Legendre moment can reproduce the general trend (*see* figures 3.10a, 3.10b, 3.11b). As soon as the focus switches to the coherent elastic scattering (always the self-scattering part), the comparison of different Legendre orders for the cross section reconstruction shows no convergence up to the ninth Legendre order (fig. 3.11a).

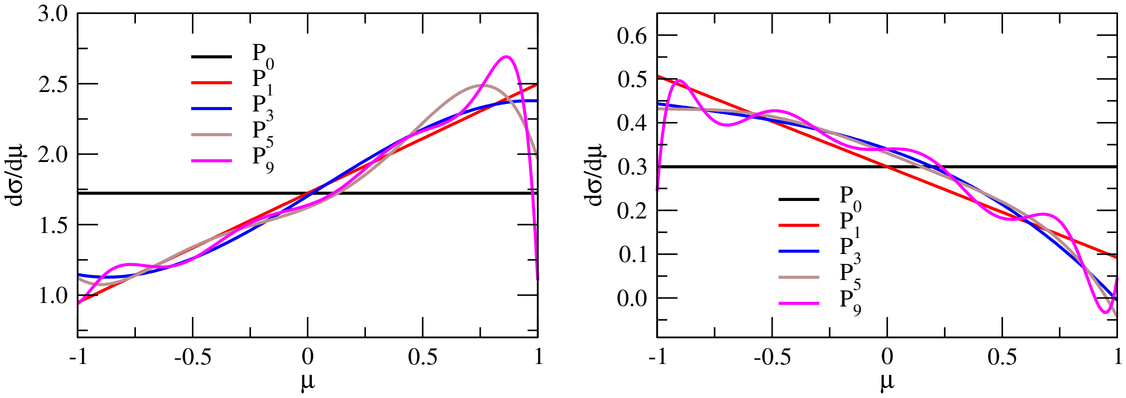

(a) Scattering into the same energy group

(b) Downscattering into the first adjacent group (0.14 eV to 0.18 eV)

Figure 3.10: Differential scattering cross section at the incident neutron energy range 0.18 eV to 0.22 eV in the upper graphs and 0.025 eV to 0.03 eV in the other as function of the cosine of the scattering angle μ and the order of the Legendre expansion at 293.6 K for graphite

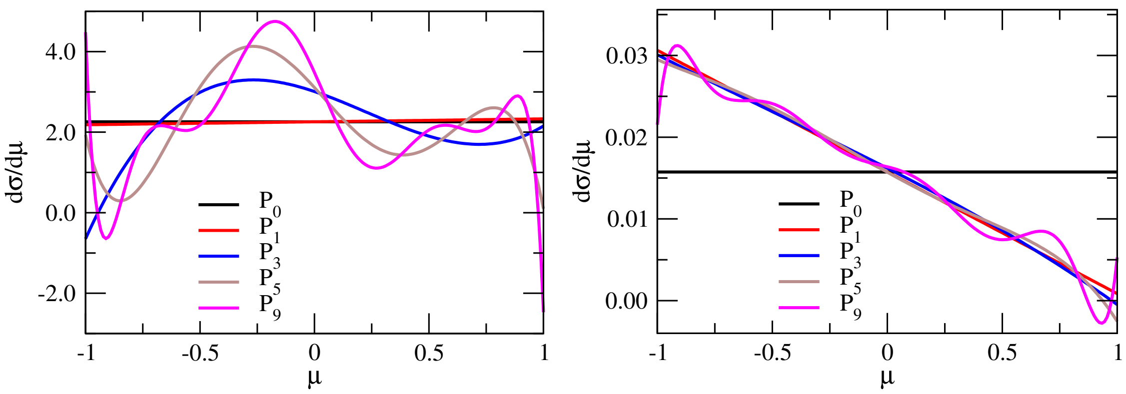

(a) Scattering into the same energy group

(b) Downscattering into the first adjacent group (0.02 eV to 0.025 eV)

Figure 3.11: Differential scattering cross section at the incident neutron energy range 0.18 eV to 0.22 eV in the upper graphs and 0.025 eV to 0.03 eV in the other as function of the cosine of the scattering angle μ and the order of the Legendre expansion at 293.6 K for graphite

From this investigation it can be concluded that having significant flux below 0.1 eV in the range of dominant coherent elastic scattering makes the treatment of the anisotropy difficult for deterministic transport methods in the frame of the Legendre expansion.

Graphite is available under the name `'CGRPH___'` in the recent `KANEXT` libraries. It has been prepared for ten temperatures (293.6 K, 400 K, 500 K, 600 K, 700 K, 800 K, 1000 K, 1200 K, 1600 K and 2000 K), which are used as linear interpolation basis for every temperature in between. The Legendre order may be chosen up to the fifth order. Above 10 eV the original carbon cross sections are added.

3.2.1.3 Conclusion on the Thermal Scattering Cross Sections

The energy and angular scattering transfer properties have been outlined for the materials PE and graphite. In both cases difficulties are observed to describe the combined energy-angle scattering behavior in terms of the Legendre expansion.

It is quite common to apply one- or two-dimensional discrete ordinates transport codes for the cell calculation with detailed energy representation. The angular plots of the last two sections can be directly interpreted in that context. The continuous scattering cosine of the abscissa denoted by μ becomes a cosine of discrete directions u and v given by the dot product $\mu_{uv} = \mathbf{\Omega}_u \cdot \mathbf{\Omega}_v$ of all possible directions imposed by the angular quadrature set. The higher the quadrature order, the more will the cosine range be subdivided and involve parts of the curve that violate the required positivity of the scattering transfer values depending on the applied Legendre order.

Further investigations have to analyze how the violation of the physical and numerical requirements with the truncated Legendre expansion relates to the energy discretization applied in the microscopic cross section library. The numerical reason of these issues may be found in the use of small energy groups which in turn can lead to the fragmentation of the angular distribution. Since the Legendre functions themselves are smooth functions over the scattering angle, discontinuous curves have to be constructed from high order superpositions of the functions. With a truncation of the Legendre expansion at usually an order smaller than 3 in typical reactor calculations such situations cannot be covered.

When the fine group transfer cross sections are collapsed to effective few group cross sections, the broadening of the energy group boundaries and the flux-weighted averaging of the Legendre coefficients most likely wash out the fragmentation. The few group scattering cross sections may be therefore numerically less violating. Further investigations should lead to a quantification of the impact on key quantities introduced by inappropriate Legendre expansion usage in fine energy calculations for the generation of few group cross sections.

3.3 Validation on YALINA-Thermal Pin Cell Level

3.3.1 Reference Monte Carlo Pin Cell Characterization

Monte Carlo (MC) codes are often used to provide reference solutions for deterministic calculations where experimental results are not available. They offer exact geometry representation of typical geometric patterns and use usually continuous energy cross sections. However, the stochastic treatment of the neutron transport equation introduces also the full range of statistical problems, which can lead to difficulties in obtaining the target quantity with small standard deviation.

For the validation of the deterministic pin cell investigation MC calculations with the exact geometry (*see* fig. A.6a) are carried out and compared successively with the geometric approximations leading to the deterministic model of the three zones Wigner-Seitz cell (fig. A.6b). The detailed description of the unit cell simplifications are summarized in Appendix A.3.1. The MC code used is `MCNP5` v1.51 [89] with JEFF 3.1 continuous energy cross sections [90] processed and provided by the OECD/NEA data service. In general, the steps of geometric simplification and the influence of the Boundary Condition (BC) are investigated.

Table 3.3 lists the obtained multiplication factors of the approximation steps. As standard deviation the value of the 1σ confidence interval is given in parentheses. The first three entries are related to the exact geometry with a square unit cell. For this type of cell, the correct boundary condition for an infinite number of these cells is the periodic boundary condition [1, 91]. If the cell is reduced to the Wigner-Seitz cell, the recommendation states that the neutron should reenter with an isotropic distribution to impose a more diffusive reflection. This is equivalent to the white boundary condition. As a side note, the reflective condition could be used in the case that the moderator region had a thickness of several mean free paths. The mean free path is about 4.4 mm, thus almost as long as the thickness of the moderator (5.8 mm).

The result of C2 confirms that the air gap may be smeared with the cladding by extending the clad radius to the outer gap radius and reducing the cladding density accordingly. It adds a small amount of 15 pcm to the multiplication factor. This is the postulate of the simplified geometry to fit in the `KANEXT` unit cell model. It is also seen that using the Wigner-Seitz approximation with the aforementioned white boundary condition introduces about 220 pcm of additional reactivity for case C4b. This case must be used when the direct comparison with the `KANEXT` pin cell calculation is performed, however it is kept in mind that the real multiplication factor of the infinite cell is somewhat lower.

Fig. 3.12 shows the neutron flux in the fuel and moderator region in unit lethargy calculated by MC. Since a 350 energy group structure is used in the deterministic calculation this is employed here as well. The group boundaries can be found in Appendix B.1. The standard deviation of the flux is generally small in the energy range of thermal neutrons up to the average energy of the fission neutrons, in real values we obtain between 0.001 eV and 2 MeV a standard deviation smaller than 0.003. The standard deviation increases the more the emission probability of the fission neutrons decreases. Above 10 MeV the standard deviation is not smaller than 0.016. While the total flux in the fuel is in general

Table 3.3: MC infinite cell multiplication factors

Case	Description	BC	k_{inf} (1σ [10^{-5}])
C1a	Geometry of fig. A.6a	periodic	1.366 24(13)
C1b	Geometry of fig. A.6a	reflective	1.366 07(13)
C1c	Geometry of fig. A.6a	white	1.366 10(13)
C2	Geometry of fig. A.6a without air	periodic	1.366 09(12)
C3a	Wigner-Seitz with air	reflective	1.372 73(13)
C3a	Wigner-Seitz with air	white	1.368 17(12)
C4a	Wigner-Seitz without air	reflective	1.372 86(13)
C4b	Wigner-Seitz without air	white	1.368 43(13)

greater than in the moderator, a little softer neutron energy spectrum can be seen in the moderator. A calculated average neutron energy states for the fuel 3.73 eV with a maximum flux between 0.03 eV and 0.035 eV. We find an average energy of 2.05 eV for the moderator with a maximum flux between 0.025 eV and 0.03 eV. Between 6 eV and 40 eV the three s-wave resonances of $^{238}_{92}$U can easily be identified. With a closer look to the resonances of $^{235}_{92}$U the smaller dips around 8.7 eV and 12.4 eV can be understood.

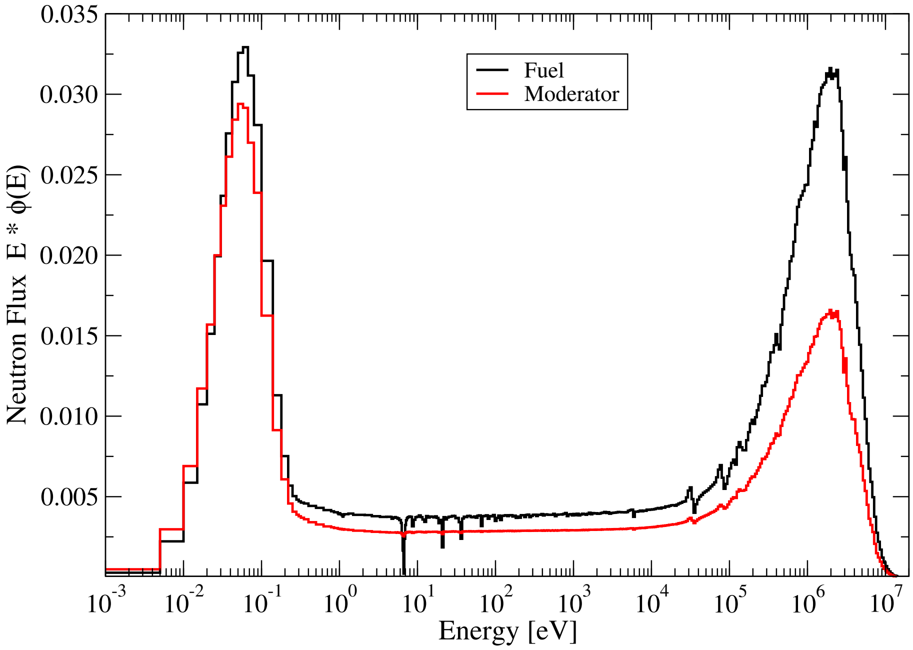

Figure 3.12: Neutron flux for case C4b in the fuel and moderator region as calculated by MC

3.3.2 Macroscopic Cross Section Generation

Deterministic transport solvers are fed with effective macroscopic group constants for homogenized zones. They are created in a procedure, in which the heterogeneity of the actual cell, its neighboring cells and additionally the need for a reduced number of neutron energy groups in the core calculation is reflected.

In fig. 3.13 a flowchart of the cross section generation scheme of the `KANEXT` module `KARBUS` is presented [92]. It starts with the initialization of a structured archive file. The internal organization of `KANEXT` allows for storing of dedicated results like cross sections, geometry information, burn-up states from every execution step into this archive and enables the retrieval for subsequent purposes afterward.

On the basis of volume or weight fractions, material densities, etc., module `NDCALC` supplies the number densities of all defined mixtures with their corresponding geometry information. When all details of the mixtures are known, `KARBUS` enters a loop to process the cross sections of all mixtures.

The following paragraph is a brief summary of the comprehensive investigation and implementation work of Broeders [73], in order to describe the actual generation of effective cross sections. Module `GRUCAL` (*see* [93, 94]) creates effective macroscopic cross sections of each nuclide, and then sums up all these to effective cross sections of the mixture. Formally, all resonance self-shielding is done by the Bondarenko method [95], thus determining an appropriate background cross section of the mixture and interpolating the proper self-shielding factor from a tabulation. Generally, these tabulated values originate from the Narrow-Resonance (NR) approximation. Module `GRUCAL` distinguishes between fast reactor cells and heterogeneous three region Wigner-Seitz cells. The latter can be used for the spatial resolution of the neutron flux for the homogenization, but special care must be taken for the resonance self-shielding in thermal systems. When using a 69 groups library as described above, a fine flux calculation is necessary for the correct resonance self-shielding. A subsection is devoted to this issue (*see* section 3.3.4). Moreover, it is accounted for in the background cross section that the resonance absorption at the surface of a fuel rod is stronger than in the center because of the resonance energy "filtering" at the surface. In the end the impact of neighboring fuel rods on the global behavior of an infinite lattice of cells is considered by the Dancoff correction according to Sauer [96] including also the improved Bell-Levine factor formalism [97, 98].

The usage of the microscopic cross sections of the `GRUBA` library is not hard-coded in module `GRUCAL`, but flexibly defined in an external Formula Definition File (FDF). From this file `GRUCAL` is instructed e.g. which reaction labels contain the self-shielding factors and which formula is to be used to interpolate for the actual background cross section and temperature. 50 formulas exist to sum, multiply, interpolate library data or already calculated data. In order to account for the changes introduced during the creation of the new microscopic master library the FDF is completely rewritten and its details can be found in Appendix B.2.3.1.

After `GRUCAL` has delivered the self-shielded group cross sections of each mixture in the standard `KANEXT` format `SIGMN` [99, 100], a cell calculation is carried out, either with

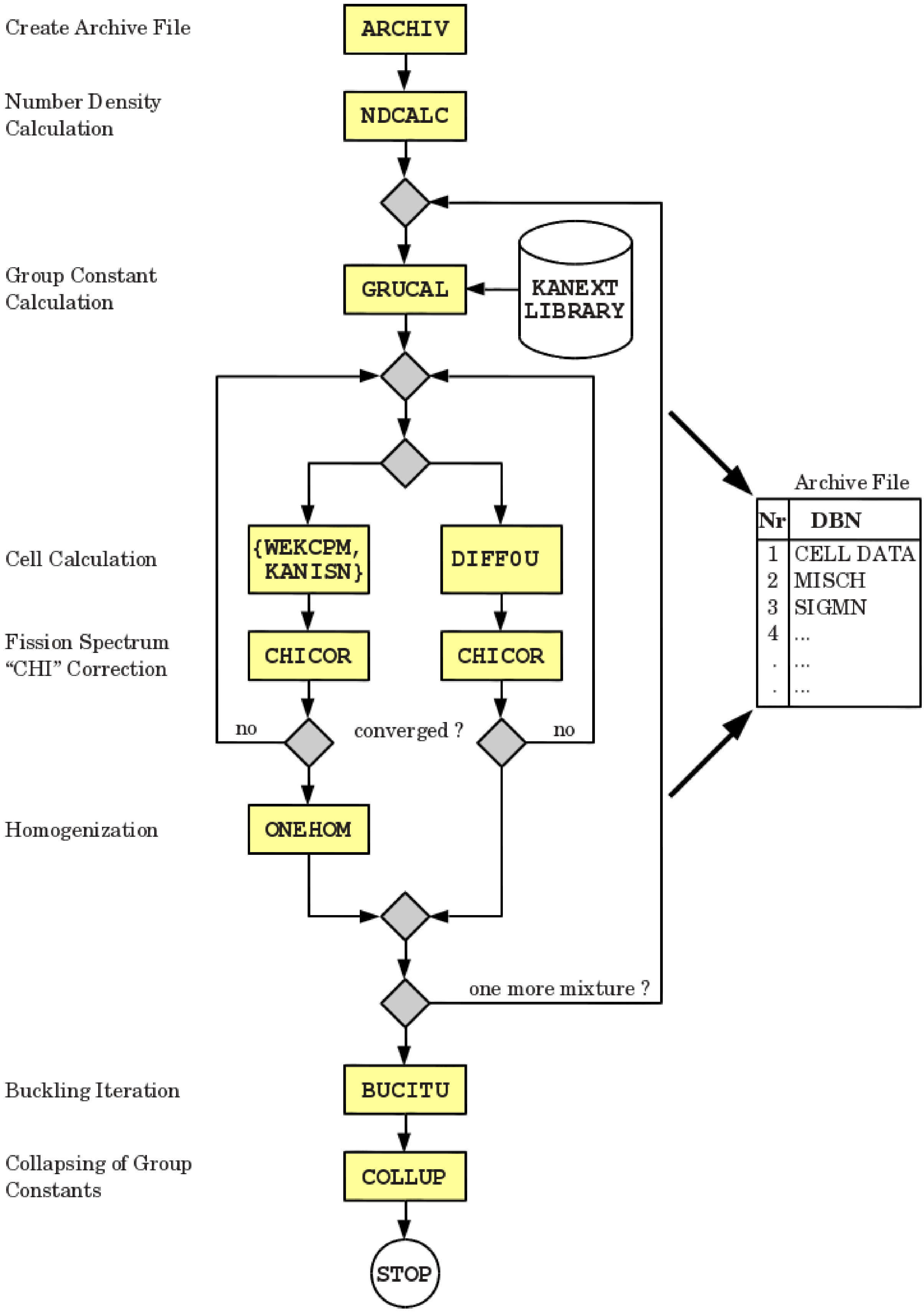

Figure 3.13: The KARBUS cross section generation sequence

a spatially resolved one-dimensional transport code or with a zero-dimensional diffusion calculation in case of homogenized number densities. Both paths of the branch in fig. 3.13 are used. The mixture of the fuel unit cell contains three cell mixtures (fuel, clad, moderator) and its cross sections are transferred to the transport module. The standard cell module is the first collision module `WEKCPM` [101]. It solves the one-dimensional integral transport equation with isotropic scattering and a transport correction of the total cross section. In order to make available a transport code with full anisotropic scattering capabilities, the new module `KANISN` [102] is introduced for a one-dimensional transport calculation based on the discrete ordinates transport method. Further details to this development can be found in Appendix B.2.2. The other branch calls module `DIFF0U` [103] for a zero-dimensional diffusion calculation.

The cell calculation resides in a second loop, which aims at providing the correct fission spectrum of the fissionable nuclides. If there is more than one fissionable nuclide, the fission spectra need to be weighted by the fission rate of the nuclides. The fission rate however is not known until the cell calculation provides the flux in the fuel region. The applied strategy is to define the main fission nuclide, for which the fission spectrum is taken for the initial cell calculation. With the resulting fuel region flux the module `CHICOR` [104] averages the fission spectra [73]. The change in the fission spectrum affects the eigenvalue and fluxes. Thus, the second loop is terminated, when the eigenvalue has converged within some tight convergence criterion.

In case of a multiregion calculation the regions of the cell are homogenized with the zone fluxes in the module `ONEHOM` [105]. The resulting homogenized cross sections of all mixtures are then given to the module `BUCITU` [106]. It uses the module `DIFF0U` to perform a buckling iteration by adjusting the leakage of the system to achieve a multiplication constant equal unity. The resulting fluxes are needed for the collapsing of the cross sections. Finally, the homogenized collapsed cross sections are stored in the prepared archive file.

A further remark relates to the treatment of mixtures without fissionable nuclides. For the core calculation these cross sections need also to be collapsed. Common approaches are to use a standard e.g. Pressurized Water Reactor (PWR) spectrum or the spectrum of the cell calculation. The `KANEXT` approach is different. Module `NDCALC` uses mixtures with the identical amount of nuclides per mixture. This is a concession to the design of module `SIGMUT` [99], where only the coupling of cross section data blocks with exactly the same nuclides and reaction types was possible. Consequently, tiny amounts of fissile materials proportional to the cell material definition are found in non-fissile mixtures. The `KANEXT` procedure is to use the sequence of fig. 3.13 and to branch into the `DIFF0U` path. The resulting eigenvalue is obviously meaningless but the flux includes the fission spectrum information of the fissioning nuclides and the energetic self-shielding of the remaining material. To get the weighting flux for the collapsing of the cross sections in module `BUCITU` the module `DIFF0U` is used then with zero buckling.

3.3.3 Results of the Pin Cell Calculation

For the comparison with reference MC pin cell results of section 3.3.1 an optimized setup has been used. The summarized items of the cell calculation are:

- The new 350 energy groups libraries of table 3.2 with the new FDF FENDFJEF (Appendix B.2.3.1)
- Fine flux calculation between 4 eV and 500 eV with the module `ULFISP` for the self-shielding of the scalar elastic, capture and fission cross section (*see* section 3.3.4)
- Cell calculation with the newly introduced 1-D discrete ordinates transport module `KANISN` (Appendix B.2.2) using S_8P_2 approximation and a point flux convergence criterion of 10^{-6}
- Fission spectrum calculation for steady-state fission spectrum including the delayed neutron spectra with the extended module `CHICOR` (*see* section 3.4.2)
- Case C4b of table 3.3: Three region Wigner-Seitz geometry with white boundary condition

In the first step of the comparison the multiplication factors obtained with JEFF and ENDF/B data sets are shown in table 3.4. Note that in case of the JEFF cross sections, the JEFF 3.1 cross sections have been used in both MC calculations. The agreement between `KANEXT` and MC for all libraries is very good within 45 pcm. For comparison, the difference between the `KANEXT` and the MC results for the original geometry (case C4a) is about 300 pcm.

Table 3.4: Comparison of the final `KANEXT` multiplication factor with the MC reference calculation

Library	$k_{\text{inf}}^{\texttt{KANISN}}$	$k_{\text{inf}}^{\texttt{MCNP5}}$	$\Delta k_{\text{inf}}^{\text{C4b}}$ [pcm]	$\Delta k_{\text{inf}}^{\text{C4a}}$ [pcm]
B350a	1.368 76	1.368 43^{a}	33	264
B350b	1.368 87	1.368 43^{a}	44	275
B350c	1.369 33	1.368 93^{b}	40	294^{c}

^{a} JEFF 3.1 ^{b} ENDF/B VII.0 ^{c} C4a recalculated with ENDF/B VII.0

At this stage, the energy dependent group fluxes calculated by module `KANISN` and MC are analyzed. Looking to the high energy range of fig. 3.14 an oscillation of the difference with a big amplitude above 10 MeV is noticed. Here, the absolute flux values are very small, because the appearance of fission neutrons is unlikely. In the deterministic case even small appearances of neutrons can be transported without problems. In the case of MC the flux is delivered with large statistical errors and a dedicated variance reduction with an energy weight window may halve the error, but even then it is above 20 % in this calculation. However, for the actual comparison the MC related problem is not too important, the interest lies in the group fluxes below 10 MeV. Very small differences are observed down to 1 eV, except for the resonance energies of $^{238}_{92}$U as will be discussed in section 3.3.4. These significant differences are restricted to the energy intervals containing the resonance energy only.

Finally, the main deviation can be found between 0.1 eV and 0.28 eV. It yields at maximum about 15 % and is located at the rising wing of the Maxwell-Boltzmann like thermal equilibrium. By inspecting the group structure a widening of the energy mesh from $\Delta E = 0.02$ to $\Delta E = 0.04$ is exactly found there. A comparison of the relevant part of the `SCALE` [107] 238 energy group structure with the applied `WIMS` structure shows a drastic concentration of finer energy groups in the thermal energy region with almost twice as much energy groups. Test calculations show that applying a finer energy mesh can reduce the maximum difference, but the pronounced difference, however, still remains about 10 %.

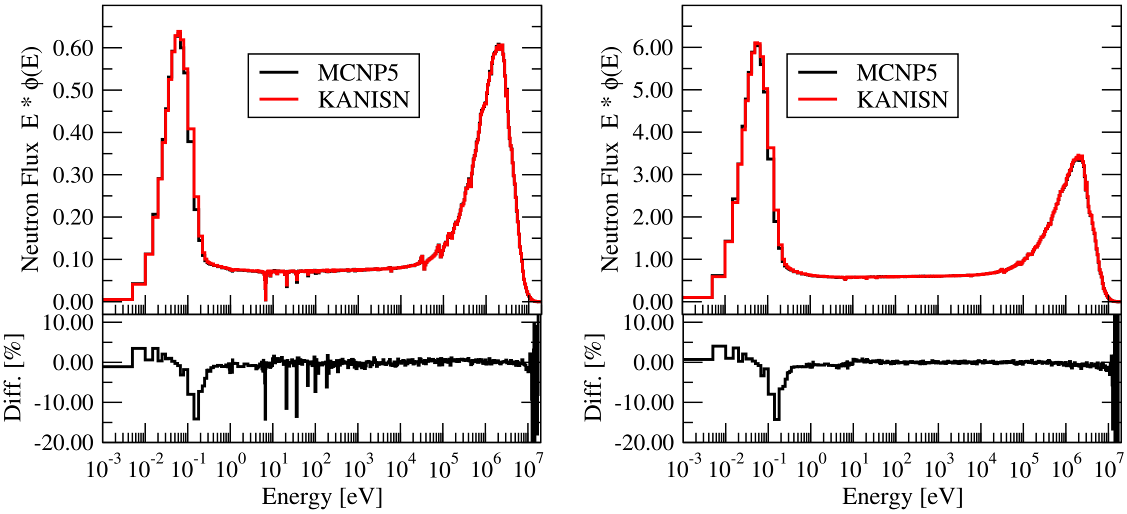

(a) Fuel region

(b) Moderator region

Figure 3.14: Comparison of the `KANISN` 350 energy groups flux with the MC reference

The suitability of the 350 groups flux as weighting flux for coarse group calculations is analyzed. The cross sections are collapsed with the region flux of the cell calculation. The coarse group structure is that of the modified 69 groups `WIMS` structure and a cell calculation is carried out under the same conditions as before. A small difference of 2 pcm is achieved in the multiplication factor which confirms the consistency and quality of the 350 groups weighting flux.

The MC calculation is repeated for the coarser 69 groups structure and serves again as a reference in fig. 3.15. Additionally, the flux resulting from a calculation with the 69 groups master library and resulting from the collapsed cross section set are plotted. Since the thermal energy groups are identical, no change is expected in this region. Above 10 keV a remarkable reduction of the flux difference between MC and `KANISN` is observed for both the fuel and moderator region. The reason for the improvement is due to the oxygen resonances between 0.4 MeV to 10 MeV, for which the new group structure can account directly.

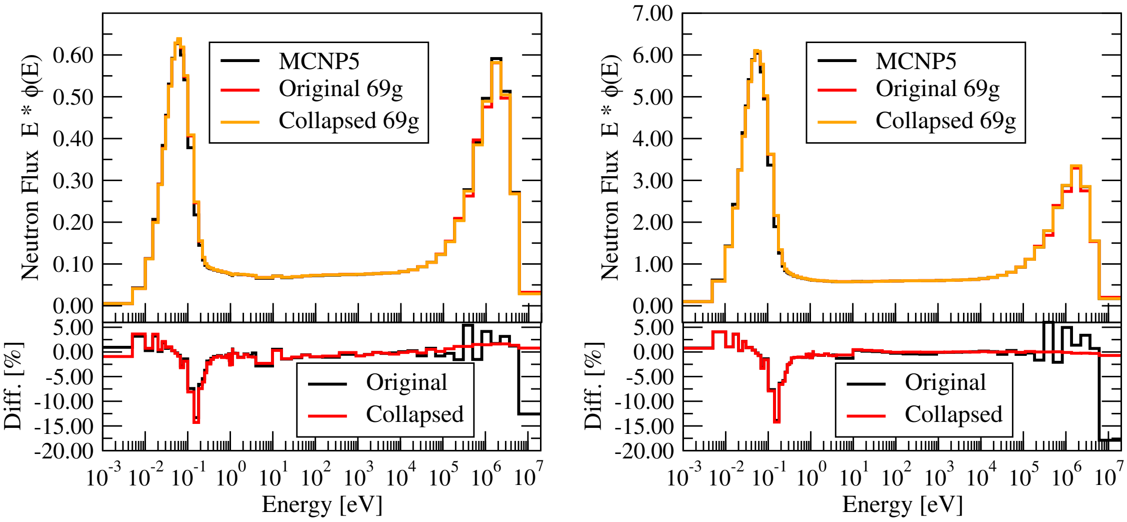

(a) Fuel region (b) Moderator region

Figure 3.15: Comparison of `KANISN` 69 energy groups flux with the MC reference

The detailed comparison of MC and `KANISN` results, using the newly generated master libraries, shows overall good agreement for the selected group structures. The advantages of the 350 groups library are slightly better agreement with MC, potential use in providing a weighting flux for the group collapsing and refined high energy group intervals for the treatment of external source neutrons. In further investigations the refinement of the thermal energy group structure will be considered as a potential improvement for the detailed thermal scattering description.

3.3.4 Impact of the Fine Flux Approach For Energetic Self-Shielding

In any reactor system the energetic self-shielding plays an important role in the accurate description of the neutron reactions. Over a broad energy range the Narrow-Resonance (NR) method can describe the effects reasonably well. In the thermal and lower epithermal energy range other methods are physically more appropriate. For the pin cell calculation the fine flux treatment of the module `ULFISP` [73, 108] is used. It solves the slowing-down equation with the first collision probability method for a two region (fuel and moderator) problem, assuming the flux shape to be constant over the region corresponding to the "flat flux" approximation. In the module `KARBUS` sequence the call of module `ULFISP` is organized before the call of module `GRUCAL` in fig. 3.13. The new self-shielded microscopic cross sections resulting from the fine flux calculation are stored in a `GRUBA` [76] formatted file. In order to use this alternative data instead of the master library data the so called secondary input option of module `GRUCAL` [93] is applied.

The energy grid of the slowing-down equation is generated depending on the user requested maximum error of the linear cross section interpolation. For the subsequent calculation this value is set to 0.01 %. Module `ULFISP` can handle Doppler broadened continuous energy cross sections of the `NJOY` produced `PENDF` format [23] and the equivalent of the `SCALE` code system [107], namely the cross sections for the MC code `KENO` in the ENDF/B VI.8 version [109]. Since the continuous energy cross sections for PE are not easily available in the `PENDF` format, the `SCALE` cross section file is used instead. For all other nuclides the `NJOY` processed JEFF 3.1 cross sections have been applied. The fine flux calculation ranges from 4 eV to 500 eV.

The influence of the fine flux self-shielding treatment is shown in table 3.5. For two libraries with 350 and 69 energy groups and the JEFF 3.1 library the multiplication factors resulting from `KANISN` calculations are listed on the one hand for the default (NR) treatment and on the other hand for the `ULFISP` self-shielding method. Note that the k_{inf} of the latter is reported in the preceding chapter. For both group structures the multiplication factor is improved, most significantly in case of the 69 energy group structure.

Table 3.5: Impact of the fine flux treatment on the multiplication factor

Library	$k_{\text{inf}}^{\text{Default}}$	$k_{\text{inf}}^{\texttt{ULFISP}}$	Δk_{inf} [pcm]
B350a	1.370 07	1.368 76	131
B69a	1.372 64	1.369 89	275

In order to understand the reason for the fine-flux impact, the cross section structure of ${}^{238}_{92}$U is discussed briefly. In fig. 3.16 the first resonance of ${}^{238}_{92}$U at 6.67 eV is predominantly a capture resonance, because the scattering probability at the resonance energy is about 15 times lower. Looking to the next resonance energy at 20.87 eV the scattering amplitude is closer to the capture reaction, and in several of the following resonances at e.g. 36.68 eV, 66.03 eV, and 102.56 eV it is on the same level. As the scattering gains in importance, the differences between the shielding methods are increasing. This is illustrated in fig. 3.17. In fig. 3.17a the effective macroscopic capture cross section of ${}^{238}_{92}$U is shown in the two mentioned energy group structures and for the two approximations in the energy range from 1 eV to 500 eV. Also plotted is the difference between the two methods for each group structure. The neighboring graph fig. 3.17b shows the macroscopic elastic scattering cross section under the same conditions. The slowing down treatment enhances the capturing strongly and the elastic scattering slightly for the 69 group library. Here, the difference in the capture cross section is above 10 % with a maximum of about 40 % in the third resonance energy group. Less pronounced but with the same trend the differences in the elastic scattering cross section can be observed. In case of the 350 group library the differences are generally lower. How well the default treatment is without fine flux calculation depends strongly on the cell characteristics. For example, the lattice pitch-to-diameter ratio influences directly the Dancoff factor, hence the probability that neutrons stay in the fuel for the next collision or change to another region.

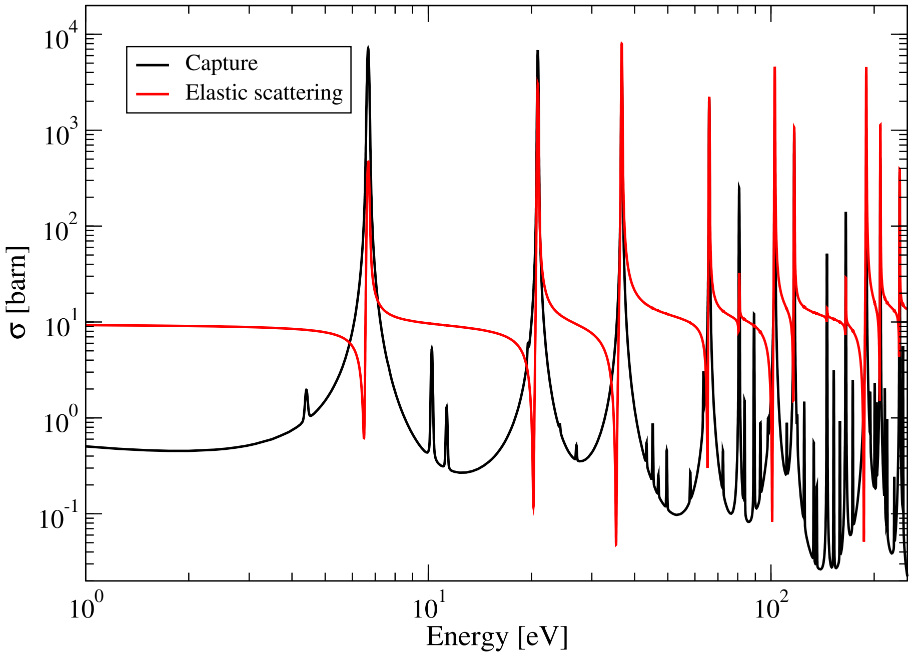

Figure 3.16: Microscopic capture and elastic scattering cross section of ${}^{238}_{92}$U

For the moment it is considered that a neutron in the fuel region acts on the coarse energy mesh. Being scattered into the group that includes the 36.68 eV resonance of ${}^{238}_{92}$U means that the next collision is independent of having energies on the right or left wing of the resonance. A collision, which leads to scattering with ${}^{238}_{92}$U induces only a little change in energy due to the scattering law. If the neutron that could stay in the fuel region after the scattering reaction resides on the right wing of the resonance, the next collision is most probably a scattering reaction. On the left wing, the neutron is probably captured due to the dip in the scattering cross section (compare fig. 3.16). This mechanism is explicitly addressed in the fine flux calculation. The coarse energy structure cannot consider this effect at all, but the relatively fine energy mesh of the 350 group libraries can cover a great part of it, since it reproduces the shape of the resonances explicitly (fig. 3.17) and permits an adequate neutron transport in the cell calculation. For certain fine mesh energy intervals the difference can however be remarkable, indicating that the energy mesh locally is still too coarse for this effect.

In order to evaluate the quality of the fine flux improvement, the effective cross sections

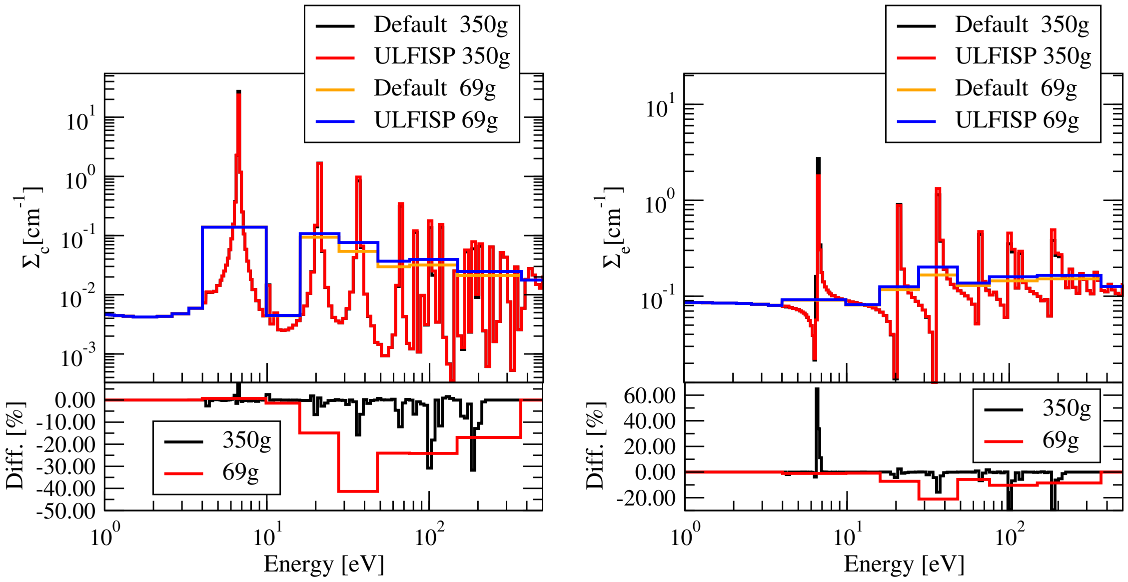

(a) Capture cross section

(b) Elastic scattering cross section

Figure 3.17: Effective cross sections of $^{238}_{92}$U with and without fine flux treatment of module `ULFISP` for 350 and 69 energy groups

are also calculated with MC (fig. 3.18). These are obtained by defining two tallies: one pure flux tally in the requested group structure and one flux tally with a multiplier card to assign the number density, single material and the reaction type. The latter gives the reaction rate, which divided by the flux yields the effective cross section. Fig. 3.18a and fig. 3.18b show the direct comparison of the effective cross sections of the capture and the elastic scattering reaction obtained by module `ULFISP` and MC. The difference for both reactions and group structures is generally within 10 % and mostly within 5 % of the MC result.

This investigation shows the necessity of a refined method for resonance self-shielding in case of the 69 energy group library, where the NR method in combination with the coarse energy groups in the important $^{238}_{92}$U resonance region underestimates the effective capture cross section. The direct comparison with MC generated effective cross sections confirms the self-shielding methodology of the `KANEXT` code system.

For the 350 energy groups library the resonance treatment is of smaller influence on the integral result. It is concluded that the finer energy mesh is to some extent capable of accounting for the self-shielding effect. The new 350 group master libraries are therefore an improvement over the coarse group libraries, when they are used for scoping calculations without detailed fine flux treatment.

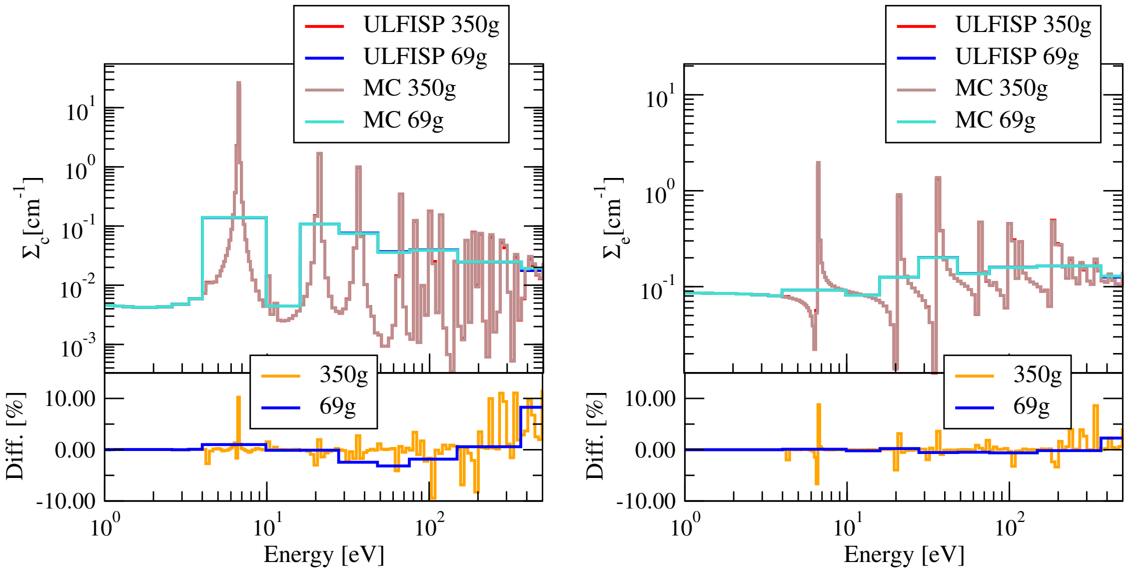

(a) Capture cross section

(b) Elastic scattering cross section

Figure 3.18: Effective cross sections of ${}^{238}_{92}\mathrm{U}$ as calculated with MC and module `ULFISP` for 350 and 69 groups

3.4 Constants for Time-Dependent Calculation

In addition to the usual cross sections prepared for a static transport calculation, a time-dependent code covering the time discretization described in section 2.3 needs the physical delayed neutron fraction, the delayed neutron abundances and their delayed fission spectra, the prompt fission spectrum and last the neutron group velocity. The neutron group velocities are directly connected to the (original or coarse) energy group structure and will be flux-weighted according to eq. (2.9) with the group- and zone-wise neutron flux spectrum.

It is common practice, to use tabulated or compiled nuclear data for known fuel types, e.g. from Keepin [21] or Tuttle [110]. This approach is limited, when the composition of the fuel includes exotic materials as may encountered in highly depleted fuel, MOX or potential MA fuels of ADS systems. In such cases material-wise fission rates are needed to properly include the impact of each fissionable nuclide and its delayed neutron characteristic.

3.4.1 The Physical Delayed Neutron Fraction

A general procedure implemented in the new module `DLAYPM` [111] is developed to calculate the problem dependent physical delayed neutron fraction for a mixture of fissionable nuclides and for the single fissionable nuclide itself. The need for averaging is obvious and is formulated by Keepin [21], but the physical delayed neutron fractions of the single nuclide are assumed to be known there. In contrast to that approach, the nuclide and consequently the averaged delayed neutron fraction are extracted from the nuclear data itself, accounting for the energy dependence of the delayed and prompt neutron yields and the problem dependent fission rate. The lack of such a procedure within the `KANEXT` environment is precisely mentioned by Thiem [112].

The implemented eq. (3.1) considers the flux spectrum dependent production of delayed neutrons for each time group j and nuclide i. The flux weighted sum of the delayed neutron production is then related to the total production of neutrons (prompt and delayed neutrons) of the mixture. The flux spectrum is that of the actual cell calculation after the treatment of module `CHICOR` (*see* fig. 3.13).

$$\beta = \sum_j \beta_j = \sum_j \sum_i \beta_j^i = \sum_j \sum_i \frac{\sum\limits_g \nu_{jg}^i \, \Sigma_{\mathrm{f}g}^i \, \phi_g}{\sum\limits_g \nu_{\mathrm{t}g} \, \Sigma_{\mathrm{f}g} \, \phi_g} \tag{3.1}$$

In order to compare intermediate results with values from the literature, eq. (3.2) is additionally evaluated for the physical delayed neutron fraction of the single nuclide. The delayed neutron production is now related to the total neutron production of the single nuclide, thus resulting in the nuclide specific delayed neutron fraction.

$$\beta^i = \sum_j \beta_j^i = \sum_j \frac{\sum\limits_g \nu_{jg}^i \, \Sigma_{\mathrm{f}g}^i \, \phi_g}{\sum\limits_g \nu_{\mathrm{t}g}^i \, \Sigma_{\mathrm{f}g}^i \, \phi_g} \tag{3.2}$$

The total neutron yield and the total delayed neutron yield is calculated according to eq. (3.3).

$$\nu_{\mathrm{x}}^i = \frac{\sum\limits_g \nu_{\mathrm{x}g}^i \, \Sigma_{\mathrm{f}g}^i \, \phi_g}{\sum\limits_g \Sigma_{\mathrm{f}g}^i \, \phi_g} \qquad \mathrm{x} : \begin{cases} \mathrm{t} & \text{total neutron fission yield} \\ \mathrm{d} & \text{total delayed neutron fission yield} \end{cases} \tag{3.3}$$

Table 3.6 compares the calculated problem dependent total and delayed neutron yields of the uranium isotopes with measured data from Keepin [21]. The measured data of ${}^{235}_{92}\mathrm{U}$ is taken from fission at thermal neutron energies, whereas only fast data for ${}^{238}_{92}\mathrm{U}$ is available. The Keepin data exhibit the advantage that this data set was redistributed to the new 8 delayed neutron time group representation proposed by Spriggs et al. [113]. This permits the comparison of one experimental data set to JEFF 3.1 and ENDF/B VII.0 which use 8 and the classical 6 time groups , respectively. It can be stated that all calculated results lay in between the measuring uncertainty. The delayed neutron fraction of the single nuclide of ${}^{235}_{92}\mathrm{U}$ is 2.3 % larger in JEFF 3.1 than in ENDF/B VII.0, in case of ${}^{238}_{92}\mathrm{U}$ the difference is 7.4 %. For both uranium isotopes the results of ENDF/B VII.0 seem to be closer to the (old) measured data, but recent recommendations of Rowlands and others [114, 115] point to the JEFF 3.1 data on the basis of comparison with integral experiments. The absolute delayed neutron yield is given there as 0.0162 for $^{235}_{92}$U and as 0.0465 for $^{238}_{92}$U, which is the largest yield of all actinides.

Table 3.6: Calculated integral delayed neutron parameters (eqs. (3.2), (3.3)) compared to experimental data from Keepin [21]

	$^{235}_{92}$U			$^{238}_{92}$U		
	B350a^a	B350c^b	Exp.	B350a^a	B350c^b	Exp.
ν_t	2.436 60	2.437 33	2.43 ±0.02	2.824 23	2.801 65	2.79 ±0.10
ν_d	0.016 20	0.015 85	0.0158±0.0005	0.046 08	0.042 55	0.0412±0.0017
β_i	0.006 65	0.006 50	0.0065±0.0002	0.016 32	0.015 19	0.0148±0.0008

^{a} JEFF 3.1 ^{b} ENDF/B VII.0

In the next tables 3.7 and 3.8 the calculated relative abundances are compared to the Keepin data. Additionally, the half-lives of the time groups are listed. The new arrangement of time groups demands a redistribution of the old 6 time groups data, which Spriggs calls a least-squares fit of least-squares fitted data [113]. This redistributed data has then been recommended for inclusion into the JEFF 3.1 library for $^{235}_{92}$U and $^{238}_{92}$U [115]. The calculation reproduces the recommended abundances, which is a confirmation of the correct implementation. Differently in case of ENDF/B VII.0, the evaluators have used the code `CINDER90` [116] to follow individual fission products and their β^- decay and fitted the contributions according to six time groups and abundances [117]. By this approach, the maximum reduction of 24 % in the second time group compared to Keepin's data is observed for $^{235}_{92}$U. For $^{238}_{92}$U the maximum reduction is 22 % in the third time group, but the impact of the fast energy threshold fission reaction on thermal reactors is low as expected.

Table 3.7: Comparison of calculated and measured relative abundance a_j, redistributed into 8 groups by Spriggs et al. [113] for $^{235}_{92}$U

	B350a^a		Exp.	B350c^b		Exp.
j	$T_{1/2}$ [s]	$a_j = \frac{\beta_j}{\beta}$	Keepin [21]	$T_{1/2}$ [s]	$a_j = \frac{\beta_j}{\beta}$	Keepin [21]
1	55.600	0.0328	0.0330±0.0042	55.494	0.0320	0.0330±0.0030
2	24.500	0.1539	0.1540±0.0061	21.781	0.1664	0.2190±0.0090
3	16.300	0.0913	0.0910±0.0091	6.337	0.1613	0.1960±0.0220
4	5.210	0.1969	0.1970±0.0236	2.187	0.4596	0.3950±0.0110
5	2.370	0.3308	0.3310±0.0066	0.512	0.1335	0.1150±0.0090
6	1.040	0.0902	0.0900±0.0045	0.080	0.0472	0.0420±0.0080
7	0.424	0.0812	0.0810±0.0016			
8	0.195	0.0229	0.0250±0.0009			

^{a} JEFF 3.1 ^{b} ENDF/B VII.0

The mixture averaged delayed neutron fractions are calculated for the YALINA-Thermal

Table 3.8: Comparison of calculated and measured relative abundance a_j, redistributed into 8 groups by Spriggs et al. [113] for $^{238}_{92}$U

	B350a^a		Exp.	B350c^b		Exp.
j	$T_{1/2}$ [s]	$a_j = \frac{\beta_j}{\beta}$	Keepin [21]	$T_{1/2}$ [s]	$a_j = \frac{\beta_j}{\beta}$	Keepin [21]
1	55.600	0.0084	0.0080±0.0010	55.478	0.0103	0.0130±0.0010
2	24.500	0.1040	0.1040±0.0020	22.910	0.1148	0.1370±0.0020
3	16.300	0.0375	0.0380±0.0008	5.979	0.1278	0.1620±0.0200
4	5.210	0.1370	0.1370±0.0205	2.030	0.4518	0.3880±0.0120
5	2.370	0.2940	0.2940±0.0118	0.526	0.2335	0.2250±0.0130
6	1.040	0.1980	0.1980±0.0020	0.069	0.0617	0.0750±0.0050
7	0.424	0.1280	0.1280±0.0128			
8	0.195	0.0931	0.0930±0.0372			

^{a} JEFF 3.1 ^{b} ENDF/B VII.0

fuel pin according to eq. (3.1). The results are shown in table 3.9 and 3.10 for the two data libraries and time group structures. The final delayed neutron fraction averaged for the mixture is 0.067 18 for the JEFF 3.1 library and hence about 1.8 % higher than that of $^{235}_{92}$U for its own because of the $^{238}_{92}$U fast fission contribution. A similar ratio is observed for ENDF/B VII.0.

Table 3.9: Physical delayed neutron fractions of the YALINA-Thermal fuel mixture and the JEFF 3.1 library

	β [%]	β_j [%]							
		1	2	3	4	5	6	7	8
$^{235}_{92}$U	0.6600	0.0216	0.1016	0.0603	0.1300	0.2183	0.0596	0.0536	0.0151
$^{238}_{92}$U	0.0118	0.0001	0.0012	0.0004	0.0016	0.0034	0.0023	0.0015	0.0011
Total	0.6718	0.0217	0.1028	0.0607	0.1316	0.2218	0.0619	0.0551	0.0162

Table 3.10: Physical delayed neutron fractions of the YALINA-Thermal fuel mixture and the ENDF/B VII.0 library

	β [%]	β_j [%]					
		1	2	3	4	5	6
$^{235}_{92}$U	0.6457	0.0206	0.1074	0.1074	0.2968	0.0862	0.0305
$^{238}_{92}$U	0.0110	0.0001	0.0013	0.0013	0.0050	0.0026	0.0007
Total	0.6567	0.0208	0.1087	0.1087	0.3017	0.0888	0.0312

With this approach, consistent sets of delayed neutron fractions and abundances are derived from the underlying nuclear data libraries. With 2.3 % the mixture averaged delayed neutron fraction for JEFF 3.1 is slightly larger than the ENDF/B VII.0 fraction, which corresponds to the mentioned $^{235}_{92}$U difference in the total delayed neutron fraction between

JEFF 3.1 and ENDF/B VII.0. The relative abundances differ, however, significantly. The influence of these differences on the calculations envisaged in this work is expected to be rather small, because the response of the reactor to the neutron pulse is driven mainly by prompt neutrons. The background of delayed neutrons establishes itself according to the fission rate in a much longer time scale, so that only the absolute delayed neutron yield will be important.

3.4.2 Fission Spectra for Direct Time-Dependent Methods

The time-independent Boltzmann equation includes the mixture averaged total neutron yield as sum of the prompt and delayed neutron yields. Associated with the yield is the energy spectrum of the fission or secondary neutrons. Principally, delayed neutrons have a softer spectrum than prompt neutrons, e.g. for $^{235}_{92}$U the average emission energy of prompt neutrons is about 2 MeV, whereas for delayed neutrons it is about 0.43 MeV [21]. Thus, a steady-state fission spectrum includes all spectra weighted by the neutron production rate of the particular prompt or delayed neutrons. On the other hand, transient calculations with direct time-dependent methods require mixture averaged prompt and delayed neutron time group specific spectra separately.

The module `CHICOR` [104] has been extended to calculate the mixture averaged steady-state fission spectrum and the averaged prompt and delayed neutron spectra. The governing equation is still that given by Broeders [73], but modified to include the delayed part [23]. The resulting equation (3.4) sums up a term very similar to the fission source of the transport equation for every isotope i, while considering the emission of prompt and delayed neutrons into the energy group g due to a fission reaction in energy group g'. In this equation the energy dependence of each variable is considered and weighted with the problem dependent flux. Thus, the resulting quantities are consistent with the delayed neutron fraction calculation of section 3.4.1.

Commonly, the prompt fission spectrum of a nuclide is used independent of the incident neutron energy. This is justified by the fact that the spectrum is constant below a certain incident neutron energy. Above this energy the spectrum depends on the energy and `NJOY` provides the full fission matrix in this context. Module `CHICOR` can handle the fission matrix stored in the `KANEXT` library, which gives a "scatter" like distribution $\chi^i_{\mathrm{p}g'g}$ of fission neutron emissions due to fission in group g' and fission neutron emission into group g. This distribution is normalized to unity per incident energy group. If the standard incident-energy-independent prompt neutron energy spectrum is to be used instead, the mentioned distribution reduces to $\chi^i_{\mathrm{p}g}$. The resulting fission source is normalized to the total neutron production giving the average steady-state fission spectrum χ^{ss} of a mixture.

$$\chi_g^{\text{ss}} = \frac{\sum\limits_i \sum\limits_{g'} \big(\nu^i_{\text{p}g'}\, \Sigma^i_{\text{f}g'}\, \chi^i_{\text{p}g'g}\, \phi_{g'} + \sum\limits_j \chi^i_{jg}\, \nu^i_{jg'}\, \Sigma^i_{\text{f}g'}\, \phi_{g'} \big)}{\sum\limits_i \sum\limits_g \sum\limits_{g'} \big(\nu^i_{\text{p}g'}\, \Sigma^i_{\text{f}g'}\, \phi_{g'} + \sum\limits_j \nu^i_{jg'}\, \Sigma^i_{\text{f}g'}\, \phi_{g'} \big)} \tag{3.4}$$

The corresponding prompt and delayed spectra (eqs. 3.5 and 3.6) are calculated by considering only the relevant parts of equation 3.4.

$$\chi_{\text{p}g} = \frac{\sum\limits_i \sum\limits_{g'} \nu^i_{\text{p}g'}\, \Sigma^i_{\text{f}g'}\, \chi^i_{\text{p}g'g}\, \phi_{g'}}{\sum\limits_i \sum\limits_g \sum\limits_{g'} \nu^i_{\text{p}g'}\, \Sigma^i_{\text{f}g'}\, \phi_{g'}} \tag{3.5}$$

$$\chi_{jg} = \frac{\sum\limits_i \sum\limits_{g'} \chi^i_{jg}\, \nu^i_{jg'}\, \Sigma^i_{\text{f}g'}\, \phi_{g'}}{\sum\limits_i \sum\limits_g \sum\limits_{g'} \nu^i_{jg'}\, \Sigma^i_{\text{f}g'}\, \phi_{g'}} \tag{3.6}$$

When mixture averaged fission spectra are available, the more common notation [118] of the steady-state fission spectrum (eq. 3.7) is usable with β being the physical delayed neutron fraction of the mixture as described in section 3.4.1.

$$\chi_g^{\text{ss}} = (1-\beta)\,\chi_{\text{p}g} + \sum_j \beta_j \chi_{jg} \tag{3.7}$$

The result of eq. (3.4) for the 350 group library averaged over $^{235}_{92}$U and $^{238}_{92}$U is plotted in fig. 3.19. The influence of the delayed neutron fission spectra shows up below 1 MeV and increases towards lower energies. The discontinuous shape of the delayed spectra (fig. 3.20) can be partially identified in the steady-state spectrum as in the case of the seventh delayed time group above 10 keV. The JEFF 3.1 prompt fission spectra generally are cut at 10 eV, leaving the space for the pure delayed neutron spectra. However, the magnitude of the distribution values is too small to have noticeable impact on the calculation.

The calculation of the averaged delayed neutron spectra is redundant in case of JEFF 3.1, since all fissionable nuclides exhibit the same spectra when the relative abundance is removed by normalizing each spectrum to unity. In the ENDF/B VII.0 library each fissionable nuclide has its particular delayed neutron spectrum for each time-group (family) and these need to be averaged for $^{235}_{92}$U and $^{238}_{92}$U. Of course, the impact of $^{238}_{92}$U will be limited due to the small fission probability in this case.

The sensitivity of the multiplication factor to changes in the fission spectrum cannot generally be predicted, but the slight softening of the steady-state fission spectrum is not expected to cause large differences compared to the pure prompt spectrum. The softening itself can cause opposed effects. Namely, the increased emission of neutrons with lower energies will positively affect the probability for a later fission, while the reduced emission

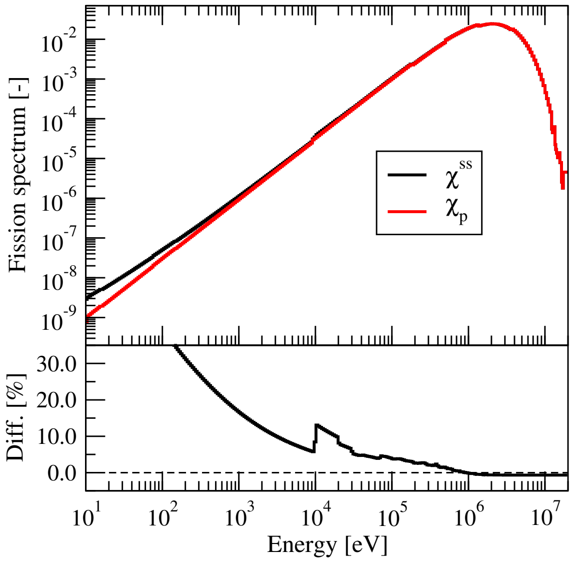

Figure 3.19: Steady-state and prompt fission spectra averaged for the YALINA-Thermal fuel with JEFF 3.1

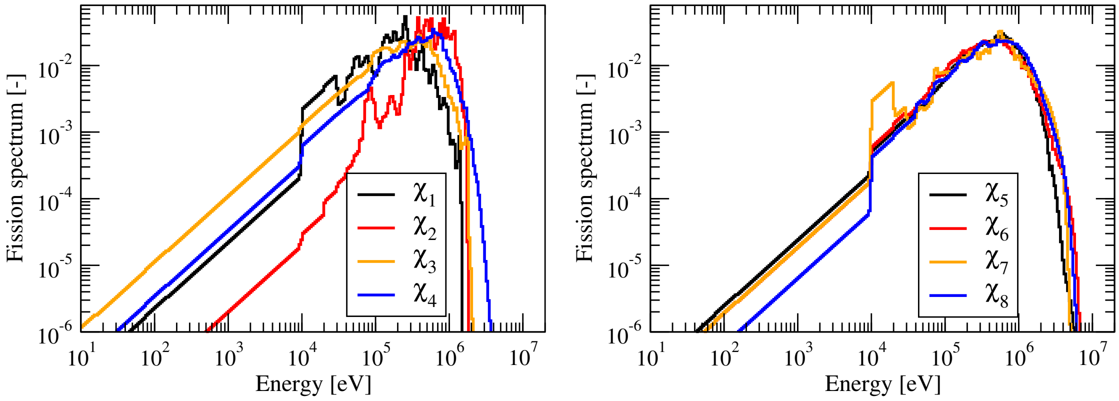

(a) Time groups 1 to 4

(b) Time groups 5 to 8

Figure 3.20: Delayed neutron spectra for the YALINA-Thermal fuel with JEFF 3.1

of very fast neutrons decreases the fast fission in $^{238}_{92}$U.

The above presented equations are applied to the YALINA-Thermal pin cell in the known configuration. The options listed in table 3.11 denote first the exclusive use of the prompt fission spectrum of $^{235}_{92}$U, which is used as the initial guess in the first cell calculation, second the use of the energy-independent prompt spectra averaged for $^{235}_{92}$U and $^{238}_{92}$U, then the combined energy-independent prompt and delayed neutron spectra, and last the energy-dependent prompt fission spectra together with the delayed fission spectra. As expected the multiplication factors do not show a considerable sensitivity to the varied input parameter, because $^{235}_{92}$U is the dominant fission isotope.

Table 3.11: Sensitivity of the multiplication factor on the fission spectrum processing

	χ_p ($^{235}_{92}$U)	χ^i_p	$\chi^i_\mathrm{p} + \chi^i_\mathrm{d}$	$\chi^i_{\mathrm{p}g'g} + \chi_\mathrm{d}$
B350a[a]	1.368 79	1.368 79	1.368 76	1.368 75
B350c[b]	1.369 36	1.369 36	1.369 33	1.369 33

[a] JEFF 3.1 [b] ENDF/B VII.0

3.5 Validation on YALINA-Thermal Core Level

The numerical solution of the transport equation is computationally demanding. It is worthwhile to investigate the impact of the approximations involved, in order to assure that the resulting accuracy is sufficient for the parameters focused on and the performance is in line with the desired accuracy. This is even more important, when we switch from the static transport solution to the time-dependent solution which was understood in section 2.3 to be a continuous repetition of a modified but complete fixed source problem. The resulting model of this optimization study will be used to simulate parts of the YALINA-Thermal experiment in chapter 5 and to validate the developments with experimental measurements.

The following sections discuss the sophistication needed for the accurate description of the YALINA-Thermal reactor depending on the various approximations that have to be made. Thereby, the coarse energy group structure is discussed in section 3.5.1 and the approximation of the flux and scattering anisotropy in section 3.5.2 for the homogeneous, source-free YALINA-Thermal reactor and in section 3.5.3 for the inhomogeneous case.

The multigroup discrete ordinates transport equation is solved for the YALINA-Thermal core by the codes `TORT` v3.2a [2] and `PARTISN` v5.97 [63]. The `TORT` code serves as the basis of the time-dependent solver introduced in chapter 4. In order to use the standard `TORT` code in modern computing environments the source files need to undergo some modifications concerning the memory allocation. `PARTISN` is compiled as delivered by the Radiation Safety Information Computational Center (RSICC).

All static and later-on time-dependent deterministic core calculations share the same geometric model and meshing and the associated transport cross sections. The details of the YALINA-Thermal reactor and its modeling are described in Appendix A.

The summary of the core calculation setup is:

- The calculation is carried out for the YALINA-Thermal configuration with 280 fuel pins
- The reactor is subdivided into 84 × 83 × 26 mesh intervals in the x-, y-, z-direction, respectively; the core region and several cm of the surrounding reflector use a fine mesh with a radial mesh interval smaller than or equal to 2 cm; all other mesh intervals are not larger than 5 cm
- For 17 regions cross sections are calculated with the `KANEXT` code system and the new developed JEFF 3.1 master library; the new developed `KANEXT` interface module `CRGIP` [119] (*see* also Appendix B.2.4) and the standard interface module `TRANSX` [120] deliver the cross sections to `TORT` and `PARTISN`, respectively
- The same level symmetric Gauss-Legendre quadrature is used for all discrete ordinates transport codes provided by the subroutine *tsncon3d* of the `PARTISN` code
- The main convergence criteria on the eigenvalue or the multiplicity $\epsilon_{\{k_{\text{eff}},M\}}$, on the point-wise flux ϵ_{ψ_g} and on the fission source ϵ_{fiss} are tightly set to 10^{-6}

In the following comparisons energy group integrated scalar fluxes and their relative differences to reference cases are compared for varying approximation orders. The formulas used are:

$$\bar{\phi}(\boldsymbol{r}) = \int \phi(\boldsymbol{r}, E)\,\mathrm{d}E \tag{3.8}$$

$$\Delta\bar{\phi}^{\text{rel}}(\boldsymbol{r}) = \frac{\left|\bar{\phi}(\boldsymbol{r}) - \bar{\phi}^{\text{ref}}(\boldsymbol{r})\right|}{\bar{\phi}^{\text{ref}}(\boldsymbol{r})} \tag{3.9}$$

$$\left\langle \Delta\bar{\phi}^{\text{rel}} \right\rangle = \frac{1}{V_{\text{tot}}} \int\limits_{\substack{V_{\text{tot}} \\ \boldsymbol{r}\in V_{\text{tot}}}} \Delta\bar{\phi}^{\text{rel}}(\boldsymbol{r})\,\mathrm{d}V \tag{3.10}$$

$$\bar{\phi}_{\text{reg}} = \int\limits_{\substack{V_{\text{reg}} \\ \boldsymbol{r}\in V_{\text{reg}}}} \bar{\phi}(\boldsymbol{r})\,\mathrm{d}V \tag{3.11}$$

$$\Delta\bar{\phi}^{\text{rel}}_{\text{reg}} = \frac{\left|\bar{\phi}_{\text{reg}} - \bar{\phi}^{\text{ref}}_{\text{reg}}\right|}{\bar{\phi}^{\text{ref}}_{\text{reg}}} \tag{3.12}$$

By eq. (3.8) the local total flux is given, which enables flux comparison regardless of the neutron energy group structure, whereas the region integrated total flux eq. (3.11)

Table 3.12: Optimized 27 coarse energy group structure for the YALINA-Thermal analysis

Group	$E_{\max}$ [MeV]	Group	$E_{\max}$ [eV]
1	19.640	11	9118.000
2	14.550	12	1498.500
3	13.840	13	148.728
4	12.840	14	27.700
5	3.679	15	9.877
6	3.166	16	4.000
7	2.019	17	3.300
8	1.353	18	1.150
9	0.500	19	0.850
10	0.067	20	0.400
		21	0.140
		22	0.080
		23	0.050
		24	0.035
		25	0.020
		26	0.010
		27	0.005

establishes a global view on the accuracy. The mentioned integrations are carried out by a self-made utility program, which reads either `VARSCL` or `FLXMOM` [2] formatted binary files in case of `TORT` or `RTFLUX` or `RMFLUX` formatted files of `PARTISN` [63].

3.5.1 Impact of the Coarse Group Structure

For the full core calculation a suitable coarse energy group cross section set must be available that reduces significantly the time of the full transport solution in view of the envisaged repetitive solution of one fixed source problem per time step. However, the coarse group structure must be capable of including potential spectral effects. The result of an optimization study for YALINA-Thermal yields a 27 energy group structure with the energy group boundaries listed in table 3.12.

It comprises relatively fine energy intervals at about 14 MeV for the (d,t) neutron source and at about 2.5 MeV for the (d,d) neutron source used in the YALINA-Thermal experiments. Below 3 MeV several groups are dedicated to establish the fission spectrum and the slowing-down of the neutrons to the thermal energy range. Further 13 energy groups are defined to describe the detailed thermal neutron interaction below 10 eV which is especially important for the huge amount of graphite and PE. The importance of the thermal groups is underlined by the fact that for certain incident energy groups upscattering occurs over a maximum range of 8 groups. In order to achieve a deterministic reference case the homogenized cross sections are collapsed from the 350 energy groups structure of the master library to the modified 69 energy groups `WIMS` structure. The results of a

Table 3.13: Impact of the neutron energy discretization on the effective multiplication factor of the full core calculation as obtained with `TORT`

Approximation	69g	27g	Δk [pcm]
S_8P_1	0.959 09	0.962 22	313
S_8P_2	0.961 22	0.963 63	241
$S_{16}P_5$	0.960 31	0.962 73	242

parameter variation in view of the quadrature and scattering Legendre order are presented for the reference and the cross sections collapsed to the coarse group structure in table 3.13.

The effective multiplication factors are listed either with the S_8P_1 or the S_8P_2 approximation, but also with the very demanding $S_{16}P_5$ approximation, which serves as reference for the lower order cases. The coarser group structure increases the eigenvalue by about 300 pcm for the P_1 approximation. With the S_8P_2 approximation the results for both energy group structures slightly increase. The results of the reference approximation orders are however in between. For the higher orders the differences between the two group structures reduce to about 240 pcm. The sensitivity of the multiplication factor on the two energy group structures is found to be acceptable.

Talamo reported independently a multiplication factor 0.959 00(8) for the YALINA-Thermal reactor with 280 fuel pins using `MCNPX` v2.6f with JEFF 3.1 continuous energy cross sections [121]. The deterministic results are in this sense confirmed and deviate in case of the 27 energy group structure between 322 pcm and 463 pcm for the S_8P_1 and S_8P_2, respectively. The results for the 69 energy group structure are nearby the MC result.

The detailed investigation of the impact of the group structure is presented in table 3.14. The table shows the relative differences of the region-integrated total flux of eq. (3.12) for variations of the approximation orders and the group structures. The detailed listing of the regions is available in table A.1 of the appendix. To mention the most important ones, region 14 is the whole fuel volume, whereas region 4 represents the whole graphite reflector. Region 5 is simply the cumulated air. The smallest region 16 denotes the copper target of the fusion neutron source admixed with either ${}^2_1$H or ${}^3_1$H. As reference the very demanding solution of the $S_{16}P_5$ approximation has been used together with cross sections collapsed to the extended 69 energy group structure (compare section 3.2). Comparing the S_8P_1 solutions for both energy groups with respect to the reference solution the differences are most times lower than 1 % with only few exceptions. Comparing the S_8P_2 solutions in the same manner the differences decrease noticeably with 69 energy groups. However this effect originates from the higher scattering order, since it is not observed for the S_8P_1 case. The section hereafter will handle this topic in more detail.

Thus, the comparison of the eigenvalues and the region-integrated total flux indicate that the coarse energy group structure is properly constructed and is a valid energy discretization

Table 3.14: Relative difference of the region integrated total flux with respect to the approximation order used with 69 energy groups

Region	Volume [cm^3]	$\Delta\bar{\phi}^{\mathrm{rel}}_{\mathrm{reg}}$ (ref: $(S_{16}P_5)^{69g}$) [%]			
		$(S_8P_1)^{27g}$	$(S_8P_2)^{27g}$	$(S_8P_1)^{69g}$	$(S_8P_2)^{69g}$
1	5731.2	0.979	0.730	1.021	0.009
2	10 054.8	1.788	0.293	1.816	0.070
3	984.8	0.569	0.040	0.597	0.051
4	1 119 096.0	0.777	0.310	0.823	0.059
5	45 060.9	0.688	0.272	0.724	0.039
6	1680.0	1.260	0.475	1.271	0.094
7	3686.4	0.903	0.336	0.940	0.077
8	7372.8	0.955	0.517	0.993	0.009
9	8524.8	0.742	0.329	0.774	0.002
10	3472.0	0.860	0.080	0.875	0.026
11	3686.4	0.968	0.613	1.006	0.016
12	779.0	0.211	0.586	0.226	0.056
13	1227.7	0.066	0.435	0.064	0.056
14	56 000.0	0.251	0.195	0.248	0.063
15	560.1	0.413	0.532	0.432	0.027
16	2.9	0.073	0.859	0.082	0.058
17	5040.0	0.968	0.376	1.006	0.070

for the full core calculation.

3.5.2 Impact of the S_N Quadrature and P_L Scattering Expansion Order

The calculations carried out in this section use generally the coarse energy group cross sections. The setup of the discrete ordinate calculations is the same as before except for the specific variation of the quadrature and Legendre order.

At this occasion the multiplication factor calculations have been carried out additionally with the `PARTISN` code. As listed in table 3.15 the eigenvalue difference between the codes `TORT` and `PARTISN` is for the lowest orders of approximations about 320 pcm. Dependent on the approximation orders this difference decreases for higher orders. This differences are however not expected since the cross section sets are identical as are the quadrature set and the geometric model and meshing.

It is also seen that the impact of the Legendre order on the eigenvalue is stronger than the already sophisticated S_8 quadrature order. For Legendre orders higher than P_3 a large quadrature order as of S_{16} is needed to make the eigenvalue in line with lower order results. From fig. 3.11a of section 3.2.1.2 can be understood that a high Legendre order possibly makes the angular dependence of the differential scattering cross section complicated. In turn, a finer angular discretization is needed, in order to integrate the anisotropy of the scattering source correctly [63]. The eigenvalues of the $S_{12}P_{L\geq4}$ and $S_{16}P_{L\geq4}$ tend to confirm the $S_8P_{L\leq 3}$ results.

Table 3.15: Impact of the S_N quadrature and P_L scattering expansion orders on the criticality with 27 energy groups

Quadrature order	Legendre order	Eigenvalue `TORT`	Eigenvalue `PARTISN`	Δk [pcm]
S_8	P_1	0.962 22	0.965 47	325
	P_2	0.963 63	0.960 60	−303
	P_3	0.963 48	0.960 44	−304
	P_4	0.956 83	0.955 79	−104
	P_5	0.956 84	0.955 79	−105
S_{12}	P_4	0.960 23		
	P_5	0.959 90		
S_{16}	P_4	0.962 73	0.960 48	−225
	P_5	0.962 73	0.960 47	−226

In the discussion about the necessity of higher order approximations in the transport calculation we come back to table 3.14. In case of the 69 energy group structure the S_8P_2 approximation reduces noticeable the difference to the reference solution in all regions in comparison to the S_8P_1 solution. Looking to the results for the 27 energy groups the differences are not reduced as much as before and for some of the small regions the difference even increases. Thus, the advantage of a high order approximation is not obvious at this point. This impression is confirmed by looking at the impact of the approximation order on the total flux at the detector positions in table 3.16. The total flux is now integrated over the mesh belonging to the detector volume as described in Appendix A.3.4. For all detector positions within the fuel region (EC{1,2,3,4}) the S_8P_1 solution agrees somewhat better, for the detectors in the graphite reflector (EC{5,6,7}) the S_8P_2 approximation has a slightly better agreement with the $S_{16}P_5$ reference. The latter observation may be explained by the complicated anisotropic scattering behavior of graphite. However, it was shown in section 3.2.1.2 that even very high Legendre orders cannot cover consistently the angular distribution in certain cases. Consequently, the S_8P_2 approximation may change the scattering in the reflector, but this change is not necessarily an improvement.

Concluding this section it is discovered that key quantities like the multiplication factor or region-integrated and detector-volume-integrated total flux of the coarse energy group core calculation are not likely to be significantly improved over the S_8P_1 solution with higher approximation orders of the quadrature or scattering.

3.5.3 Main Parameters of the Heterogeneous Core Calculation

Deterministic codes like `TORT` and `PARTISN` deliver as integral result of the fixed source calculation the multiplicity M. In the ADS analysis typically the so called source multiplication

Table 3.16: Maximum and average relative difference of the cell-wise integrated total flux with respect to $S_{16}P_5$ solution with 27 energy groups

		S_8P_1			S_8P_2	
Detector	$\Delta\bar{\phi}^{\mathrm{rel}}_{\max}(\boldsymbol{r})$	$(i,j,k)_{\max}$	$\langle\Delta\bar{\phi}^{\mathrm{rel}}\rangle_{\mathrm{EC}}$	$\Delta\bar{\phi}^{\mathrm{rel}}_{\max}(\boldsymbol{r})$	$(i,j,k)_{\max}$	$\langle\Delta\bar{\phi}^{\mathrm{rel}}\rangle_{\mathrm{EC}}$
EC1	0.326	(29,41,16)	0.092	0.357	(32,41,12)	0.106
EC2	0.306	(20,17,11)	0.235	0.304	(20,17,12)	0.234
EC3	0.177	(48,16,08)	0.099	0.287	(48,16,12)	0.208
EC4	1.235	(33,30,01)	0.636	1.258	(32,29,01)	0.424
EC5	1.436	(13,28,01)	0.683	1.135	(13,30,01)	0.138
EC6	0.957	(51,49,16)	0.765	0.804	(51,48,20)	0.202
EC7	0.847	(53,27,12)	0.665	0.278	(53,27,12)	0.141

factor k_{src} ("k source") is preferred and the relation to the multiplicity is shown in eq. (3.13). The multiplicity is interpreted as, how many times neutrons from one fission chain lead to fission before the chain dies away. Since the reactor is subcritical, the multiplicity is finite.

$$M = \frac{1}{1 - k_{\mathrm{src}}} \tag{3.13}$$

The k_{src} concept introduces the physical meaning of the homogeneous eigenvalue ("production over losses") to the inhomogeneous problem. Compared to the homogeneous eigenvalue it reflects the impact of the position and spectrum of the external neutron source on the integral production and leakage and leads dependent on the source to a value smaller or larger than the homogeneous eigenvalue.

The impact of the neutron source energy for the (d,t) and (d,d) reaction is explored with an isotropic source in the second and sixth energy group of the 27 energy group structure (*see* table 3.12) corresponding to the emission energy of the (d,t) and (d,d) neutron source.

These calculations have been prepared again for `TORT` and `PARTISN` with the known setup. However, severe convergence problems are observed for the `PARTISN` code, which may be related to general problems with the diffusion-synthetic-acceleration scheme as reported by Azmy [122] for very heterogeneous geometries with large density fluctuations between neighboring cells. This is the case for the modeling of the beam tube. The tube is directly integrated in the geometric core model, which causes very fine spatial intervals at the core center (*see* fig. A.12). In case of the `TORT` code the convergence is monotonically reached and the multiplicity M is delivered.

As shown in table 3.17 the k_{src} of the (d,t) neutron source case is almost identical to the homogeneous eigenvalue, while the (d,d) source increases the k_{src} to be significantly larger by about 721 pcm. This effect of the neutron sources is attributed to two main reasons. First, the very fast neutrons are more likely to leak out of the system, since their mean free path is much larger than that of the (d,d) source neutrons. Second, the (d,d) source neutrons are emitted near the average fission neutron energy of 2 MeV and have an importance for the chain reaction comparable to that of the fission neutrons. Contrarily, the (d,t) source neutrons have first to slow down from 14.1 MeV to 2.5 MeV in order to appear at fission neutron energies and during this process they undergo reactions like absorption or leave the reactor system. As opposed effect, the (n,xn) reactions, mainly (n,2n), occur at higher neutron energies, and sustain the neutron production of the balance equation. The results indicate however that the leakage and absorption are dominant on the k_{src} of the (d,t) neutrons source solution.

Table 3.17: Impact of the external neutron source type on the source multiplication factor using `TORT` with 27 energy groups and the S_8P_1 approximation

Source type	$\bar{E}$ [MeV]	k_{eff}	M	k_{src}
(d,d)	2.5	0.962 22	32.718	0.969 44
(d,t)	14.1	0.962 22	25.483	0.960 76

The source multiplication factors have been evaluated by Talamo [121] with `MCNPX` v2.6b using ENDF/B VI.6 continuous energy cross sections for both sources. The k_{src} is reported to be 0.968 48 for the (d,d) case and 0.955 05 for the (d,t) case. Unfortunately, both results are given without standard deviation. With this reservation it is concluded that the coarse energy group structure is suitably defined for the simulation of the YALINA-Thermal reactor operating with (d,d) neutron source. This is especially important, because the YALINA-Thermal experimental data is only available for the (d,d) neutron source and therefore used extensively in the next two chapters.

The larger difference of 570 pcm for the (d,t) neutron source is probably only for a small part related to the different JEFF 3.1 and ENDF/B VI.6 cross section evaluations. It may indicate a problem with the 27 energy group structure. The energy interval of the fourth group amounts to 9.161 MeV. For a (d,t) neutron source calculation the impact of a refinement would have to be carried out. In view of the (d,d) source related next chapters the achieved coarse energy group structure is certainly appropriate.

3.6 Point Kinetic Parameters for the YALINA-Thermal Reactor

The effective delayed neutron fraction β_{eff} and the mean neutron generation time Λ of the point kinetic parameters are calculated with the classical approach for critical reactors according to equations (2.36) and (2.38). The `TORT` discrete ordinates transport code in the mentioned setup and the JEFF 3.1 27 energy group structure are used to provide the real and adjoint flux of the static homogeneous effective multiplication factor equations (2.10) and (2.19).

Table 3.18: Effective delayed neutron fraction of YALINA-Thermal with 280 fuel rods and 27 energy groups `TORT` calculation

β_{eff} [%] Total	$\beta_{\text{eff}j}$ [%] 1	2	3	4	5	6	7	8
0.7553	0.0217	0.1185	0.0670	0.1503	0.2488	0.0692	0.0618	0.0181

Table 3.19: Mean neutron generation time of YALINA-Thermal with 280 fuel rods and 27 energy groups `TORT` calculation

Region	XS set	Volume [cm^3]	$\Lambda\,[\cdot 10^{-5}\,\text{s}]$	Fraction	Description
1	5	961 444.8	1.620	0.20	Graphite reflector
3	23	22 261.4	0.137	0.02	Air
6	20	3686.4	0.077	0.01	Flux channel: PE
7	21	7372.8	0.140	0.02	Flux channel: PE, Air
8	19	8524.8	0.260	0.03	Pin without fuel
10	22	3686.4	0.062	0.01	Flux channel: Air
12	10	1227.7	0.067	0.01	Lead
13	11	56 000.0	5.682	0.70	Fuel
Total		1 085 760.0	8.134	1.00	

The multigroup form of the point kinetic parameter equations is used in the module `KSAUDI` to which the real and adjoint flux are delivered (*see* Appendix B.2.6).

The effective delayed neutron fraction yields in total 0.7553 %, which is an increase of 12.4 % compared to the physical delayed neutron fraction of the fuel investigation of section 3.4.1. The fractions of the time-groups are listed in table 3.18

The mean neutron generation time is determined for the most important material zones and as sum of these. The total mean generation time of 81.3 µs is composed of 70 % fuel unit cell region contribution and of 20 % reflector contribution. The remaining percentage is distributed mainly over regions containing amounts of PE.

Chapter 4

Development of a New External Source Capability in a Time-Dependent Transport Code

The fully implicit time integration scheme (*see* 2.3) was implemented under the name `DORT-TD` into the two-dimensional discrete ordinates transport code `DORT` [123] of the `DOORS` family of transport codes by Pautz [65] in the year 2003. The implementation is related to the homogeneous form of the transport equation, however the validity of the method for external source problems is also addressed there, if the external neutron source is included correctly to the modified source term as described in section 2.3. On this basis the time integration was implemented in the three-dimensional transport code `TORT` of the same origin by Seubert [64] in 2005. Both codes are currently maintained and further developed.

`DORT-TD` and `TORT-TD` are applied as reference time-dependent neutron physics solutions for reactor dynamics in the German Technical Safety Organization (TSO) GRS. The continuous development and application allows to consider the codes to be thoroughly validated for time-dependent problems, whereas the static codes `DORT` and `TORT` have been applied for many years and thus are presumed to be validated even more. This approved validated code environment has motivated the choice of `TORT-TD` in the current thesis.

The author of this thesis initiated therefore a substantial cooperation with GRS to make the external source capability available in `TORT-TD` and moreover to investigate the additional needs and the correct usage for the PNS experiments and ADS application. The first part was accomplished by Seubert [124] and is briefly summarized in section 4.1 and section 4.2. The new development of the spherical harmonics representation of the external neutron source is addressed in section 4.3. In section 4.4 an improvement of the time-integrated transport equation is discussed to consider spectral effects on the delayed neutron yield for PNS and ADS applications.

4.1 `TORT-TD`: Methods and Capabilities

In the time-dependent loop `TORT-TD` will solve eq. (2.59) with the discrete ordinates approximation of the solid angle. This implies that the continuous solid angle $\mathbf{\Omega}$ is discretized into several rays $\mathbf{\Omega}_u$ of direction u. The discretization is used in combination with a quadrature integration scheme to achieve e.g. the total flux. A typical quadrature set is the level-symmetric Gauss-Legendre quadrature [19].

$$\phi_g = \frac{1}{2} \sum_u w_u \, \psi_g(\Omega_u) \text{ with } \sum_u w_u = 2 \tag{4.1}$$

The final time-dependent discrete ordinates transport equation is written in the form of eq. (4.2).

$$\left[\boldsymbol{\Omega}_u \cdot \nabla + \tilde{\Sigma}_g(\boldsymbol{r})\right] \psi_g^{t_\tau+1}(\boldsymbol{r}, \boldsymbol{\Omega}_u) = S_g^{t_\tau+1}(\boldsymbol{r}, \boldsymbol{\Omega}_u) \tag{4.2}$$

The entire source term located at the right-hand side is now abbreviated by the variable S. The intention is to separate the left-hand side, which will be described in the discrete ordinates representation in `TORT`/`TORT-TD`, and the spherical harmonics form of the source equation (4.3). This representation is in agreement with the form used by the author of this work [125] and will be extended by the source term of the external neutron source in section 4.3. Using this representation all integrals are converted into sums. For brevity all variables without time step indicator are thought to be of the time step $t_{\tau+1}$.

$$\begin{aligned} S_g^{t_\tau+1}(\boldsymbol{r}, \boldsymbol{\Omega}_u) = & \underbrace{\sum_{l=0}^{L} \sum_{m=-l}^{l} Y_l^m(\boldsymbol{\Omega}_u) \sum_{g'=1}^{G} \Sigma_{\mathrm{s}g'gl}^{m}(\mathbf{r}) \, \phi_{g'l}^{m}(\mathbf{r})}_{\text{Scattering source}} \\ & \underbrace{+ \, \tilde{\chi}_g \sum_{g'} \nu\Sigma_{\mathrm{f}g'}(\boldsymbol{r}) \, \phi_{g'0}(\boldsymbol{r})}_{\text{Prompt fission source}} + \underbrace{\frac{1}{\Delta t} \sum_j \chi_{gj} \lambda_j \gamma_j C_j^{t_\tau}(\boldsymbol{r})}_{\text{Delayed neutron source}} + \underbrace{\frac{1}{v_g \, \Delta_t} \sum_{l=0}^{L} \sum_{m=-l}^{l} Y_l^m(\boldsymbol{\Omega}_u) \; {}^{t_\tau}\phi_{gl}^{m}(\boldsymbol{r})}_{\text{Time source}} \end{aligned} \tag{4.3}$$

The prompt fission and delayed neutron source terms cause no problem in terms of numerical complexity, since they are isotropically distributed and may be generated by the zeroth flux moment $\phi_{g'0}$.

For the scattering source term the anisotropic flux has to be expanded in terms of the spherical harmonics function Y_l^m to the needed scattering Legendre order L of eq. (4.4). If this expansion was carried out without much loss in accuracy, then the scattering contribution from other directions can be simply mapped on the actual direction. The more the flux is subject to distinct anisotropy the higher the order must be to obtain an accurate spherical harmonics representation of the discrete ordinates angular flux.

$$\phi_{gl}^{m}(\boldsymbol{r}) = \sum_u w_u Y_l^m(\boldsymbol{\Omega}_u) \, \psi_g(\boldsymbol{r}, \boldsymbol{\Omega}_u) \tag{4.4}$$

The time source term of eq. (4.3) must be considered under this perspective as well.

Pautz [65] reports that the conversion of eq. (4.4) generally leads to an unstable numerical behavior e.g. a disturbance of the presumably constant total power in steady-state transients. Thus, the time source must be added directly in the discrete ordinates sweep of the inner iteration, in order not to loose the anisotropic structure of the flux and not to add numerical noise to the source term.

Since homogeneous and inhomogeneous problems will be treated as modified fixed source problems in the time-dependent calculation, acceleration methods were investigated and implemented in these codes to optimize as much as possible the numerical burden per time step i.e. per fixed source iteration.

In the following a summary of properties of the `DORT` and `TORT` codes collected from [2,123] is given.

- Multigroup solution for homogeneous and inhomogeneous transport problems
- Cartesian coordinates in 2-D (xy, rz, $r\theta$) and 3-D (xyz, $r\theta z$)
- Arbitrary discrete ordinates quadrature order N and Legendre scattering order L ($\mathrm{S}_N\mathrm{P}_L$)
- Typical inner/outer iteration scheme
- Outer iteration accelerated by error mode extrapolation, fission rescaling method and upscattering rebalance method
- Inner iteration accelerated by the coarse mesh rebalance method

Additional features of `TORT-TD` [64, 65] are:

- The time source is handled in the angular representation and not in the spherical harmonics form of the right-hand side of the discrete ordinates transport equation, which results in the demanding storage of the angular flux
- Acceleration by a flux extrapolation method using a "reactor period"-like exponential for the flux guess of the next time step
- Acceleration of the upscatter convergence with an improved upscatter loop
- Acceleration of the fission source by Chebyshev extrapolation
- Material-wise prompt and delayed fission spectra and neutron group velocities

The development of `TORT-TD` has also afforded a comprehensive tool collection called `PreDOORS` [126], which produces the geometry input of the `TORT` code part on the basis of a generalized input description. The semi-automatic input production comprises also the generation of the quadrature set, the cross section handling and also the mapping of thermo-hydraulic properties on the neutron physics area for coupled calculations. In the kinetics part of the `TORT-TD` input the kinetic data i.e. decay constants, delayed neutron fractions and prompt and delayed neutron spectra must be given.

4.2 Implementation of the Time-Dependent Source Capability

The classical understanding of the transport equation is that the loss rate balances the production rate as outlined in chapter 2.1 and loss and production are distinguished by the placement on the left or right-hand side of the equation, respectively. Numerically, the left and right-hand side of the discrete ordinates transport equation are distinguished by the mathematical treatment. While the production or total source on the right-hand side is represented by means of the spherical harmonics of eq. (4.3) and moreover is part of the outer iteration, the left-hand side is situated in the inner iteration or transport sweep within the discrete ordinates frame. Thus, each quantity can be located at the mathematically most suitable place. E.g. the anisotropic scattering treatment makes use of the advantageous properties of the orthogonal Legendre functions, which are the polar angle subset of the spherical harmonics functions. Since for most problems a truncated expansion of order $L \leq 3$ is sufficient to describe the scattering anisotropy, the placement of the scattering source is most efficiently handled on the right-hand side of the transport equation. All kinds of fission sources are even more easily to account for, because they are constructed by the scalar flux, the equivalent to the zeroth flux moment.

There is little information in the literature on the usage of external neutron volume sources with distinct anisotropy in deterministic code systems. As outlined the source could be added in the discrete ordinates form or in the spherical harmonics representation. The mathematically uniform approach found in all transport codes like `TORT`, `DORT` but also `PARTISN` is to apply the volume source in the spherical harmonics form [2, 63]. In `TORT-TD` the external neutron source Q is implemented according to eq. (2.60) and eq. (4.2) in the spherical harmonics frame having followed the interpretation as a neutron production term.

In the original `TORT` code the fixed source can be given in several ways. Either in the text input file, if only the spatial and energy distribution is to be defined, or in a binary data file that is conform to the `FLXMOM` format [2]. The latter obviously allows for higher spherical harmonics orders than the zeroth which aims at the anisotropy of the neutron distribution. However, the time-dependent volume source in `TORT-TD` has been implemented by Seubert [124] in a `TORT-TD` specific subroutine called *timsr{1,2}*. The energy-angle-time-dependent external neutron source is given in the spherical harmonics frame in eq. (4.5) and added together with the time source and delayed neutron source terms to the total source of eq. (4.3). For a certain position and energy group the source is composed of a global intensity I defined in the `TORT-TD` input and the spherical harmonics coefficients of the external source Q_{gl}^{m} eventually interpolated (therefore $\bar{Q}$) to the global time regime and given for the necessary time steps in an additional source related text input file. The provision of the Q_{gl}^{m} is developed by the author of the thesis [125] and extensively discussed in the next section 4.3.

$$Q_g(\boldsymbol{r}, \boldsymbol{\Omega}_u, t_{\tau+1}) = I \sum_{l=0}^{L} \sum_{m=-l}^{l} Y_l^m(\boldsymbol{\Omega}_u)\, \bar{Q}_{gl}^{m}(\boldsymbol{r}, t_{\tau+1}) \tag{4.5}$$

4.3 On the Use of an Energy-Angle Dependent Neutron Source in Deterministic Transport Codes

4.3.1 Characterization of the (d,d) and (d,t) Fusion Neutron Sources

In the YALINA-Thermal experiments both kinds of fusion neutron sources (d,d) and (d,t) were applied. The author of this thesis developed the derivation of the energy-angle dependent neutron source in terms of the spherical harmonics functions [125]. Since the spherical harmonics representation appears to be the usual treatment of the production rate in deterministic transport codes, this method was applied because of its generality. The cited work describes the application to the (d,t) neutron source. This section summarizes briefly the method and results for the (d,t) neutron source and continues with the application to the (d,d) neutron source, for which solely experimental results are available.

The angular distributions of source neutrons originating from (d,d) or (d,t) neutron sources and a deuteron beam energy of 0.25 MeV are shown in fig. 4.1 provided by the `DROSG-2000` code [127]. The horizontal 0° line is thought to run parallel to and in direction of the deuteron beam and thus parallel to and in the negative direction of the z-axis of the YALINA-Thermal model of fig. A.2. The plot contains the dependence of the neutron emission on the polar angle θ in form of a differential cross section in unit barn normalized to the maximum of the (d,t) and (d,d) cross section, 155.814 mb and 6.965 mb, respectively. It underlines that the treatment of the (d,t) neutron source as completely isotropic is a valid approximation and can reduce the numerical effort significantly. The (d,d) source exhibits a clear anisotropy in the way that neutrons are emitted most preferentially in forward direction and significantly in backward direction but only with about 30 % of the 0° probability perpendicular to the beam axis.

The same relationship is drawn in fig. 4.2 for the (d,t) source in a linear plot, but now in connection with the energy dependence on the left-hand side. One may observe the direct link between the emission angle and the emission energy of the neutron. The energy ranges between 13.1 MeV and 15.2 MeV and the curvature is similar to the direction dependence.

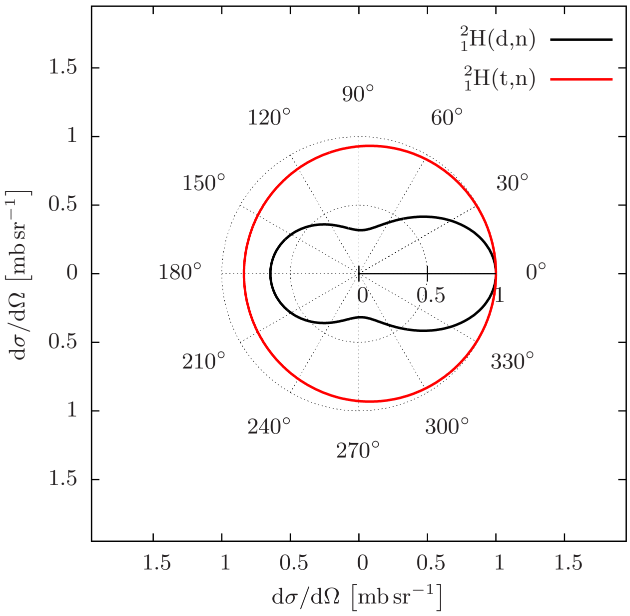

Figure 4.1: Distribution of source neutrons of 0.25 MeV beam energy for the polar angle in the laboratory system

Thus, neutrons with the highest energy are preferentially emitted in forward direction.

4.3.2 Development of a New Original Solution

The use of the energy-angle dependent neutron source in deterministic multigroup transport codes requires the energy distribution to be discretized along with the multigroup structure of the cross sections and the angular distribution to be converted to the mathematical representation of the anisotropy. For discrete ordinates transport codes like `PARTISN` and `TORT` this means the change in energy and angle of the neutron after a collision is described with help of the spherical harmonics expansion.

Any continuous, square integrable function can be represented exactly in terms of spherical harmonics with the expansion order $l \to \infty$ in eq. (4.6) [1, 128].

$$f(\theta, \phi) = \sum_{l=0}^{\infty} \sum_{m=-l}^{l} Q_l^m \, Y_l^m(\theta, \phi) \tag{4.6}$$

The real-valued spherical harmonics function Y of order l and moment m is defined in eq. (4.7)

$$Y_l^m = \begin{cases} \sqrt{2}\,\Re(Y_l^m) = \sqrt{2}\,N_l^m \,\cos(m\phi)\,P_l^m(\cos\theta) & \text{if } m > 0 \\ Y_l^0 = N_l^0\,P_l^0(\cos\theta) & \text{if } m = 0 \\ \sqrt{2}\,\Im(Y_l^m) = \sqrt{2}\,N_l^{|m|}\,\sin(|m|\phi)\,P_l^{|m|}(\cos\theta) & \text{if } m < 0 \end{cases} \tag{4.7}$$

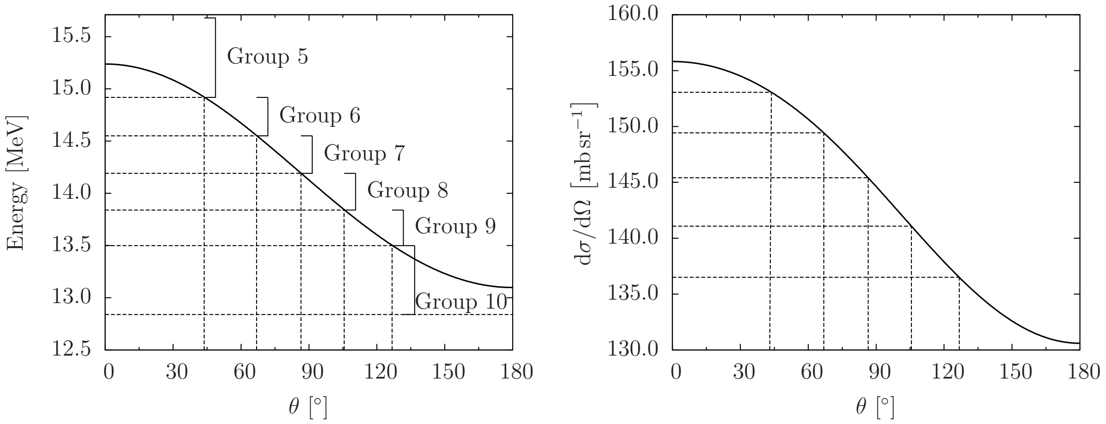

(a) Projection of the energy group boundaries on the angle axis

(b) Projection of the angle intervals on the angular distribution

Figure 4.2: Dependency of emission energy and probability on polar angle θ of the (d,t) neutron source

as product of the normalization factor N in eq. (4.8)

$$N_l^m = \sqrt{\frac{2l+1}{4\pi}\,\frac{(l-m)!}{(l+m)!}} \tag{4.8}$$

and the associated Legendre polynomial P in eq. (4.9)

$$P_l^m = \frac{(-1)^m}{2^l\,l!}\,\sqrt{(1-(\cos\theta)^2)^m}\,\frac{\mathrm{d}^{l+m}}{\mathrm{d}(\cos\theta)^{l+m}}((\cos\theta)^2-1)^l \tag{4.9}$$

as one of the many definitions of the real spherical harmonics [118]. Numerically, the associated Legendre polynomials are calculated with help of the recurrence relation of eq. (4.10) [128].

$$\begin{aligned} P_m^m(x) &= (-1)^m\,(2m-1)!!(1-x^2)^{m/2} \\ P_{m+1}^m(x) &= x\,(2m+1)\,P_m^m(x) \\ (l-m)\,P_l^m(x) &= x\,(2l-1)\,P_{l-1}^m(x) - (l+m-1)\,P_{l-2}^m(x) \end{aligned} \tag{4.10}$$

When the energy discretization is fixed by the energy structure of the `KANEXT` 350 groups library (*see* chapter 3 and section B.1.2), then the angle intervals are determined as well. This is indicated by the dashed lines in fig. 4.2 and applied in table 4.1.

Consequently, function f is now a step function of each energy group in eq. (4.11).

$$f_g(\theta,\phi) = \begin{cases} 0 & \text{if } \theta < \theta_g \text{ or } \theta > \theta_{g+1} \\ f(\theta,\phi) & \text{if } \theta_g \le \theta \le \theta_{g+1} \end{cases} \tag{4.11}$$

Table 4.1: Correlation of the master library fine energy structure and the angle intervals of the neutron emission for the (d,t) source

g	E_g	E_{g+1}	θ_g	θ_{g+1}
5	15.683	14.918	0.00	43.74
6	14.918	14.550	44.25	66.87
7	14.550	14.191	67.37	86.48
8	14.191	13.840	86.98	105.59
9	13.840	13.499	106.09	126.70
10	13.499	12.840	127.21	180.00

The mentioned transport codes expect the coefficient Q_l^m for each energy group to be determined after eq. (4.12). In the definition of eq. (4.12) $\cos\theta$ is integrated from -1 to 1 corresponding to the integration from $-180°$ to $0°$.

$$Q_{gl}^m = \int\limits_{\phi=0}^{2\pi} \int\limits_{\cos\theta=-1}^{1} f_g(\theta,\phi)\, Y_l^m(\theta,\phi)\, \mathrm{d}(\cos\theta)\, \mathrm{d}\phi \tag{4.12}$$

This new procedure is implemented in the program `MKSRC` (section C.1.1). The procedure and results obtained for the (d,t) neutron source [125] are outlined here in brevity. The group-wise spherical harmonics coefficients are calculated after eq. (4.12) for a truncated expansion order L with the integration limits of table 4.1 and the original data is afterward reconstructed on the basis of eq. (4.6). Fig. 4.3 demonstrates that the subdivision of the energy into a fine group scheme leads to step functions which can only approximate the original data for a sufficiently large expansion order (fig. 4.3b). Since this expansion order is not manageable for transport codes, the result of a realistic expansion order $L = 5$ is drawn in fig. 4.3a. It may be observed that on top of the fact, that the original data can not be reconstructed the truncated expansion would produce significant negative function values and therefore would disturb the numerics leading potentially to negative flux occurrences.

In order to keep the anisotropy information but circumvent the step function characteristic of the neutron source, the integration of the function in eq. (4.11) is carried out including the complete emission range in energy and angle. As consequence the neutron source emits neutrons mono-energetically. If this mono-energetic source is used in a transport code, the multigroup cross sections have to provide exactly this energy interval, i.e. from 13.499 MeV to 15.683 MeV and from 2.015 87 MeV to 3.121 51 MeV for the (d,t) and (d,d) source, respectively. As consequence the first expansion order does already approximate satisfactorily the original data of the (d,t) neutron source (fig. 4.4a).

In case of the (d,d) neutron source the calculation of energy discretized spherical harmonics coefficients is skipped for the reasons mentioned earlier. Instead, the one group coefficient is determined directly and the reconstructed curve is plotted together with the original data in fig. 4.4b. Unlike the (d,t) neutron source an expansion order of $L = 2$

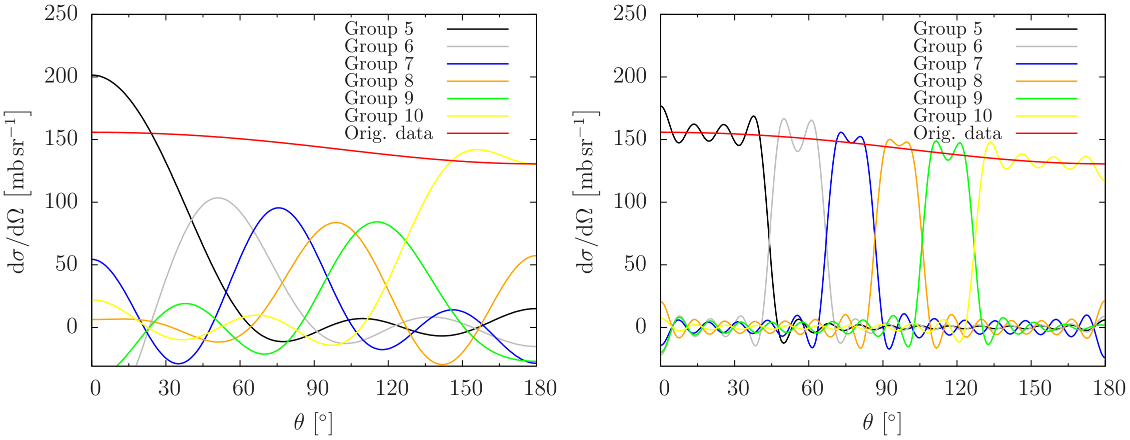

(a) Expansion order $L = 5$ (b) Expansion order $L = 28$

Figure 4.3: Spherical harmonics expansion of the (d,t) neutron source generated with 0.25 MeV deuteron energy

is needed to regain the two inflection points. However, the curve of the first and last 30° deviate apparently from the original data. A quite good agreement with the original curve can be achieved for $L \geq 3$.

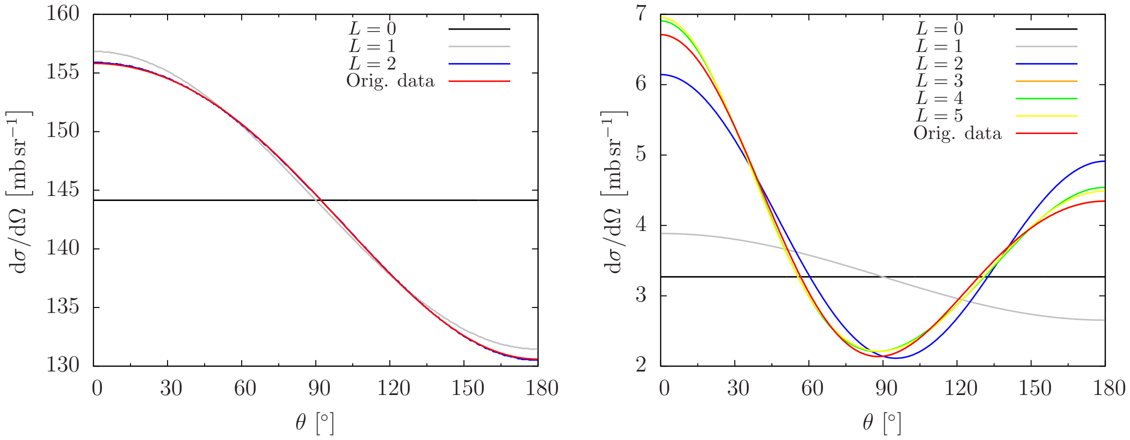

(a) Reconstruction of the (d,t) neutron source (b) Reconstruction of the (d,d) neutron source

Figure 4.4: Spherical harmonics expansion of neutron sources with one energy group generated with 0.25 MeV deuteron energy

This new developed procedure allows for the generation of the energy-angle dependent neutron source in terms of the spherical harmonics expansion. Since this representation is mostly used in deterministic transport codes, it is generally applicable. The strong concentration of the neutron emission in forward and backward direction of the (d,d) neutron source necessitates at least a third order expansion of the source for the mono-energetic neutron distribution. The energy discretization in several fine groups leads to step functions which demand a high order spherical harmonics expansion and is therefore not applicable in common deterministic transport codes.

4.3.3 Outlook for Future Work

The discrete ordinates transport code `PARTISN` uses a definition of the solid angle components θ and ϕ, the polar and azimuthal angle, respectively, non-conform to that of the spherical harmonics development in this work [125]. This characteristic has also been encountered in `TORT`/`TORT-TD`. The rotational axis of the azimuthal angle is not the z-axis as assumed and in consequence the anisotropy of the neutron emission may be found along the x-axis. In further investigations spherical harmonics rotations could be a possibility to make use of the source anisotropy in deterministic transport codes. The rotation of a $L = 1$ expansion is easily accomplished by interchanging the Q_1^m coefficients. Thus, a (d,t) neutron source could be represented correctly in that sense. The rotation of higher order expansion is more complicated and exceeds the scope of this work.

As an alternative, the development of the energy-angle dependent neutron source can be thought in the discrete ordinates frame. After the reported results and drawback of the spherical harmonics expansion the neutron source can be provided for all discrete directions $\mathbf{\Omega}_u$ and energy groups.

4.4 On the Extension of the Time-Integrated Transport Equation for Spectral Effects on the Delayed Neutron Production

In the following a possible extension of the time-dependent discrete ordinates transport equation in the form of the combined equations (4.2) and (4.3) is presented.

ADS neutron sources release neutrons with energies considerably higher than fission neutron energies in critical reactors. Situations may therefore arise in which quantities like the physical delayed neutron fraction must be differently evaluated for the ADS or PNS experiment in general, and with special interest for the time-dependence of the propagation of the very fast source neutrons in the reactor. In the latter case delayed neutrons from other fissionable nuclei than the main fissile nuclides may contribute to quantities of interest while the thermalization is not yet finalized or no equilibrium in the neutron balance can be achieved within reasonable time periods corresponding to reliable detector rates in a subcritical reactor.

As an example serves the very basic and for this work relevant discussion of the UO_2 fuel enriched in $^{235}_{92}U$. Whenever fast neutron energies are predominant concurrent fission in $^{238}_{92}U$ will occur. The fission reaction of $^{238}_{92}U$ has a threshold of about 1 MeV and the comparison of the fission cross section of the $^{235}_{92}U$ and $^{238}_{92}U$ isotopes in fig. 4.5b shows that the probability of fission approaches quickly half the probability of fission in $^{235}_{92}\mathrm{U}$. Since $^{238}_{92}\mathrm{U}$ has the largest delayed neutron yield of all fissile materials (fig. 4.5a), roughly a factor of 4 compared to $^{235}_{92}\mathrm{U}$ in the lower MeV range, the delayed neutron production ($\nu_\mathrm{d}\Sigma_f$) of $^{238}_{92}\mathrm{U}$ develops to the same order as $^{235}_{92}\mathrm{U}$ above the threshold energy. This extreme situation is only imaginable in the very first µs of a PNS experiment, when the fission events are mainly due to fast neutrons. Moreover, when several fissionable nuclei are involved like in Mixed Oxide (MOX) fuel or special MA fuel, the composition of the yields will be more complex and must be calculated for the actual condition.

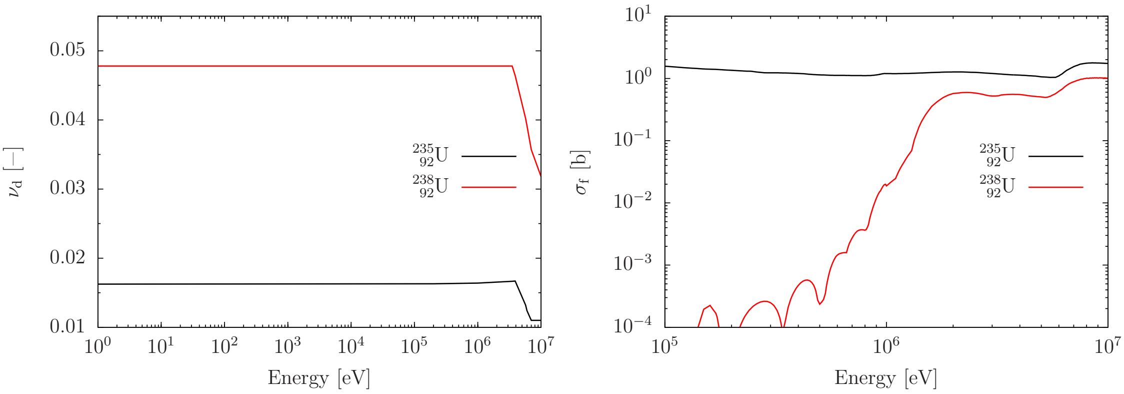

(a) Delayed neutron yields

(b) Microscopic fission cross sections

Figure 4.5: Delayed neutron yields and fission cross sections for $^{235}_{92}\mathrm{U}$ and $^{238}_{92}\mathrm{U}$ of the JEFF 3.1 evaluation

The inclusion of spectral effects in `TORT-TD` concerns all locations, where the constant delayed neutron fraction β appears in the implementation of the time-integrated transport equation. The straight-forward manner is to consider the energy-dependence of the delayed neutron yields directly in the precursor equation. That is to say that the former precursor equation (2.61) of the implicit time integration scheme is rewritten to equation (4.13).

$$C_j^{t_\tau+1}(\boldsymbol{r}) = \gamma_j \left[\frac{1}{\Delta t} C_j^{t_\tau}(\boldsymbol{r}) + \Delta t \sum_{g'} \nu_{jg} \Sigma_{\mathrm{f}g'}(\boldsymbol{r})\, \phi_{g'}^{t_\tau+1}(\boldsymbol{r})\right] \tag{4.13}$$

The additional term of the back-substitution of the precursor concentration, which is organized in the modified fission source $\tilde{\chi}_g \sum_{g'} \nu_\mathrm{t} \Sigma_{\mathrm{f}g'}(\boldsymbol{r})\, \phi_{g'}^{t_\tau+1}(\boldsymbol{r})$ of equation (2.59) changes to equation (4.14).

$$\chi_{\mathrm{p}g} \sum_{g'} \nu_{\mathrm{p}g'} \Sigma_{\mathrm{f}g'}(\boldsymbol{r})\, \phi_{g'}^{t_\tau+1}(\boldsymbol{r}) + \sum_j \chi_{jg} \lambda_j \gamma_j \sum_{g'} \nu_{jg'} \Sigma_{\mathrm{f}g'}\, \phi_{g'}^{t_\tau+1}(\boldsymbol{r}) \tag{4.14}$$

The new form of the implicit time-integrated transport equation accounts for the spectral influence by applying the energy dependent precursor yield rather than the constant delayed neutron fraction. In the written form it does not fit so well to the textbook-like style of the fixed source equation, the implementation however is smooth and on top of the modifications necessary to implement the time integration.

Chapter 5

Results of the YALINA-Thermal (d,d) Pulsed Neutron Source (PNS) Experiment Simulation

The `TORT-TD` code in the version RTZ-0.5 is used to simulate the (d,d) PNS experiments with 280 and 216 fuel rods. In the next section 5.1 the `TORT-TD` specific program setup is described, which is used to get the simulation results of section 5.2. This is followed by the discussion of two aspects of the simulation in section 5.3, namely the difference of the measured and calculated detector rates in the first µs and the change of the neutron current spectrum at the core boundary with time. Finally, the impact of the advanced simulation capability on the calculation of kinetic parameters is assessed in section 5.4.

5.1 `TORT-TD` Model and Configuration

The time-dependent calculation is based on the `TORT` geometry model of the static calculation (*see* section 3.5 and appendix A.5). The main simulation settings of `TORT-TD` are:

- Spatial discretization of the reactor in 83 × 82 × 25 mesh volumes
- JEFF 3.1 cross sections and 27 groups energy discretization with the structure discussed in section 3.5.1
- Isotropic, mono-energetic (d,d) neutron source with triangular time shape; pulse width of 5 µs and maximum source intensity at 2.5 µs
- Time discretization as tabulated in table 5.1
- Level symmetric Gauss-Legendre quadrature and scattering order: S_8P_1
- Static convergence criteria of zeroth time step $\epsilon_{k_{\text{eff}}}$, ϵ_{ψ_g}, $\epsilon_{\text{fiss}} \leq 10^{-6}$
- Time-dependent error criteria on $\epsilon_{\tilde{M}}$, ϵ_{ψ_g}, $\epsilon_{\text{fiss}} \leq 10^{-6}$
- Prompt and delayed neutron spectra, delayed neutron precursor abundances and decay constants of section 3.4
- The Chebyshev extrapolation instead of the standard error-mode extrapolation is used to accelerate the convergence of the fission source

Table 5.1: Time discretization of the `TORT-TD` YALINA-Thermal simulation

Time interval [s]	Time step Δt [s]
$0.00 \geq t < 10^{-5}$	$5 \cdot 10^{-7}$
$10^{-5} \geq t < 10^{-4}$	$5 \cdot 10^{-6}$
$10^{-4} \geq t < 10^{-3}$	$5 \cdot 10^{-5}$
$10^{-3} \geq t < 0.02$	$1 \cdot 10^{-4}$

From the explanation of the principal processes in PNS experiments in section 2.2 it is understood that the neutron distribution at the ending of a pulse period (here 20 ms) is the initial condition of the time-dependent simulation for the next pulse period. The difficulty is therefore accentuated to provide the initial condition if the delayed neutron background is part of the simulation.

Talamo has proposed the pulse super-imposition method [60] for the Monte-Carlo simulation with delayed neutrons. The method is also applicable to deterministic solutions. The procedure applied in this thesis differs in that a guess of the delayed neutron precursors and the neutron distribution is delivered based on an effective multiplication factor calculation followed by the determination of the equilibrium precursor concentration. The time interval denoted T_4 in fig. 2.1 may be interpreted as a constant fixed source problem with the delayed neutron emission as a neutron source which initiates a finite fission chain causing the emission of prompt neutrons. Since the precursors are distributed over the whole fuel region and emit neutrons with a spectrum only slightly softer than the prompt fission spectrum the constant neutron distribution contains a characteristic similar to the fundamental mode distribution of neutrons. Thus, in the zeroth time step of the `TORT-TD` simulation the initial condition for the time-dependent calculation is approximated by a k_{eff} eigenvalue solution after which the equilibrium precursor concentration in every mesh volume is calculated. This flux serves as initial flux guess with similar properties as the unknown flux at the end of the pulse period.

In order to compare the simulation to the experimental results, a scale adaption is generally required. With the external source strength given the absolute flux and every other related quantity could be directly determined. Unfortunately, the (d,d) source was not calibrated in the beginning of the experiment and the strength is therefore unknown. Since the reactor operates at zero-power the power-to-flux normalization can be applied neither. As a workaround the simulated delayed neutron background of EC2 is chosen to match that of the experiment and the source strength is adjusted in `TORT-TD` to comply with the situation at the beginning of the pulse. For all presented results only one normalization to one detector location has been performed. It is however obvious that the local distribution of the delayed neutron precursors depends strongly on the fission rate integrated over the pulse periods, for which the guess may not be completely adequate.

5.2 Simulation of the (d,d) Neutron Source Experiment

After the official end of the combined IAEA CRP "Analytical and Experimental Benchmark Analysis on Accelerator Driven Systems" and "Low Enriched Uranium Fuel Utilization in Accelerator Driven Systems" [42] a publication outlined that for the comparison of the experimental data with time-dependent simulation the knowledge of the real fuel composition is of importance [121]. According to this the simplified benchmark fuel definition of YALINA-Thermal does not specify the content of ${}^{234}_{92}$U, which accumulates during the enrichment process of ${}^{235}_{92}$U, and further fuel impurities. As a result of a gamma spectroscopy of all 280 fuel rods a 2.1 % reduced uranium mass was found. The criticality impact of both, the extended composition and reduced mass, adds up to nearly 1000 pcm reported for a MC calculation. Moreover, it is reported that for the detector EC2 measurement an additional detector at EC3 was placed in the fuel region, while the reflector detectors were left empty. In case of the EC5 detector measurement again EC6 contained the detector device, too. The benchmark specification however demanded a detector device free simulation. The reaction rates were calculated as sum of the group flux and detector cross section product in a subsequent evaluation step. The impact of the presence of two detectors in the fuel region was investigated [121] and quantified to a 480 pcm reduced criticality compared to the detector free reactor.

Thus, between the benchmark specification and real reactor setup there exists a discrepancy that amounts in a reduced criticality of about 1500 pcm. For the time behavior of the reactor discussed hereafter a steeper decay in terms of reaction rates is to be expected and when comparing the time-dependent simulation results with the measurement this must be carefully taken into account. The static calculations with the adjusted number densities for the impurities and the reduced uranium mass are repeated with the few group structure of 27 energy groups and the effective multiplication factors are listed in table 5.2. The achieved difference of 1108 pcm based on the deterministic calculation and the reported difference agree well. Note that there is a small difference of 71 pcm between the `TORT` multiplication factor of section 3.5 and the `TORT-TD` result.

Table 5.2: Integral results of `TORT-TD` with 27 energy groups and `MCNPX` for the modified fuel composition

Case	$k_{\mathrm{eff}}^{\texttt{TORT-TD}}$	$k_{\mathrm{eff}}^{\texttt{MCNPX}*}$
Benchmark specification	0.961 51	0.959 00(8)
${}^{234}_{92}$U and 2.1 % mass reduction	0.950 43	0.949 61(4)
Difference [pcm]	1108	939

* From [121]

Figure 5.1 shows the simulation results of `TORT-TD` for the case of the 280 fuel rods configuration in comparison to the available experimental data for the (d,d) neutron source and a pulse period of 20 ms. The ${}^{3}_{2}$He(n,p) reaction rate is integrated over neutron energy and detector volume for detector EC2 and EC5 for each time step (*see* fig. A.1). The rates are plotted with semi-logarithmic scale and a coarse time abscissa in order to highlight the correlation between the experimental result and the different levels of subcriticality achieved by the benchmark and real fuel definition, which are not subject to other physical or numerical aspects discussed in section 5.3. In the EC2 detector an immediate response to the (d,d) neutron pulse in terms of the reaction rate is observed. The reaction rate then diminishes continuously to the quasi-constant neutron background within about 8 ms. The reaction rate in the EC5 detector increases to a maximum value after 1 ms and decays within about 9 ms to the delayed neutron background counted from the time point of the maximum value. For both detectors the finding is true that the slope of the reaction rate decay flattens as the criticality approaches unity. Only a slight tendency to decay faster than the curves of the corrected reactor specification is observed for the measured rate. The difference between the absolute values in EC5 amounts to about 30 %, but the shape of the corresponding normalized curve matches almost exactly the shape of the experimental data over the whole period.

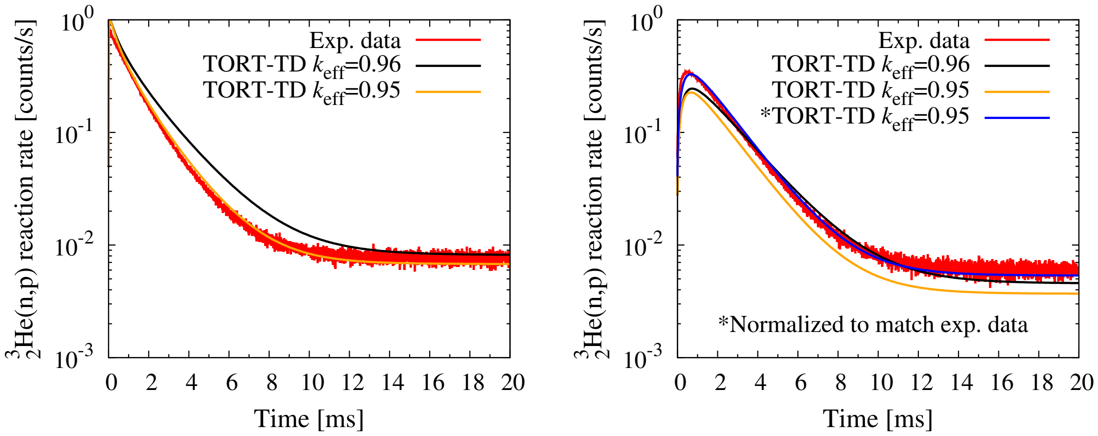

(a) Detector position EC2

(b) Detector position EC5

Figure 5.1: Comparison of simulated and experimental ${}^{3}_{2}$He(n,p) reaction rates for the (d,d) neutron source and 280 fuel rods configuration

The origin of the absolute difference was subject to a deeper investigation. As potential reason for the absolute difference of the curves in EC5, a tighter spatial discretization in the vicinity of the boundary to the reflector was investigated, but did not indicate a significant relation to the problem. Other investigations related to the anisotropy of the (d,d) neutron source have shown only a minor impact on the absolute values. Barbarino [129] investigated the numerical distortion of time-dependent ray effects in time-dependent discrete ordinates transport codes. For low quadrature orders and low fraction of scattering, for which static discrete ordinates transport codes are already known to fail, the ray effect develops to a time component, since neutrons being forced to follow a discrete ray will reach different points in space with their specific velocity. On the other hand the authors show that a "standard" quadrature order S_8 reduces the impact significantly. To consider also this potential reason, a S_{12} calculation has been carried out and the comparison of the reaction rates yields a difference below 3 % in all detector positions in the first 1.5 ms. After that period the difference increases to a maximum of 10 % at 6 ms in EC1 and EC2 detectors. The impact of the quadrature order is seen, but it is not the reason for the observed difference. The reason for the difference cannot be explained satisfactorily from the numerical point of view. Others have also encountered this problem [121, 130]. It cannot be excluded however that this problem is related to uncertainties in the experimental setup as already observed.

With the same `TORT-TD` numerical setup the reaction rates are calculated for the 216 fuel rods configuration of the YALINA-Thermal reactor and shown in fig. 5.2. Its static criticality is determined to 0.877 17. The k_{eff} value is in good agreement with those of other benchmark participants like Talamo [121]. Contrarily to the case above, the normalization to the delayed neutron background is skipped, because it affords a series of recalculations for the source strength adjustment. For the deep subcritical configuration a fast decay of the reaction rate is noticed in the EC2 detector of fig. 5.2a. The decay of the reaction rate is more linear in the logarithmic ordinate scale during the first 3.5 ms than in the 280 fuel rods configuration and develops afterward a slight curvature. In the EC5 detector location in fig. 5.2b again a build-up phase in the first ms is observed and followed by a less steep decay to the delayed neutron background. The `TORT-TD` result shows again a good agreement with the experimental data for the prompt decay phase of the experiment.

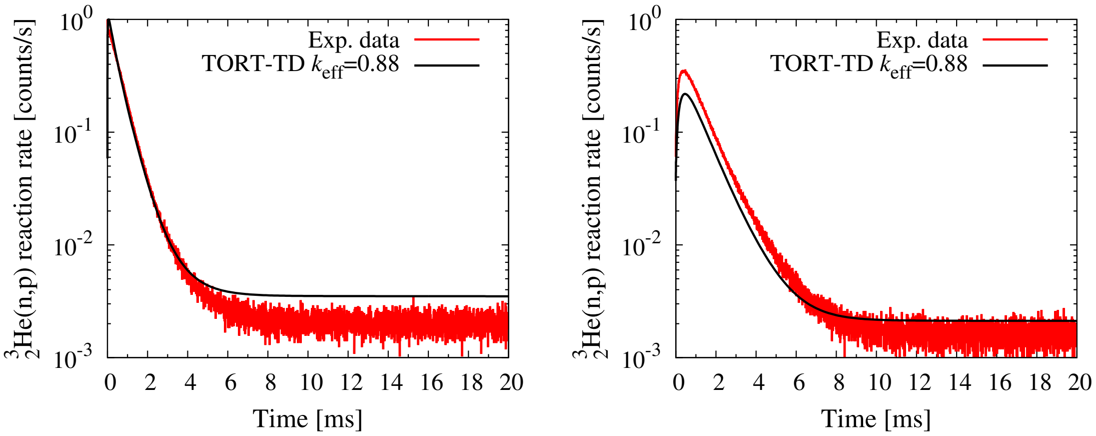

(a) Detector position EC2

(b) Detector position EC5

Figure 5.2: Comparison of simulated and experimental $^3_2$He(n,p) reaction rates for the (d,d) neutron source and 216 fuel rods configuration

It was shown that a PNS experiment with a real reactor configuration as the YALINA-Thermal experiment can be simulated with help of the `TORT-TD` code. With the knowledge of certain deviations from the benchmark specifications a good agreement with the measured data can be achieved in view of the slope and shape of the decaying reaction rates. It is concluded that `TORT-TD` performs quite well on this kind of problem enabling detailed investigations of the subcritical behavior of the reactor. Since the more general investigations in the next sections do not depend on the real knowledge of the reactor configuration, the benchmark configuration with the details described in section 3.5 and appendix A is used hereafter.

5.3 Physical Observations

5.3.1 Short-Time Detector Characteristic Immediately after the Pulse

When looking at the immediate response in terms of reaction rates of the experiment and simulation in fig. 5.3a a principal difference is noticed in that the simulation exhibits a complex shape of the rate. The reaction rate raises very fast during source operation and reduces continuously the slope after source shut-off indicated by the dashed line. After 75 µs the rate starts to diminish. On the other hand, the experimental data starts with the maximum value and decays monotonously from the very beginning. After the first time interval of 5 µs, which resembles the time resolution and thus comprising the complete source operation, a discontinuous decrease of the rate is observed, after which the rate diminishes more slowly.

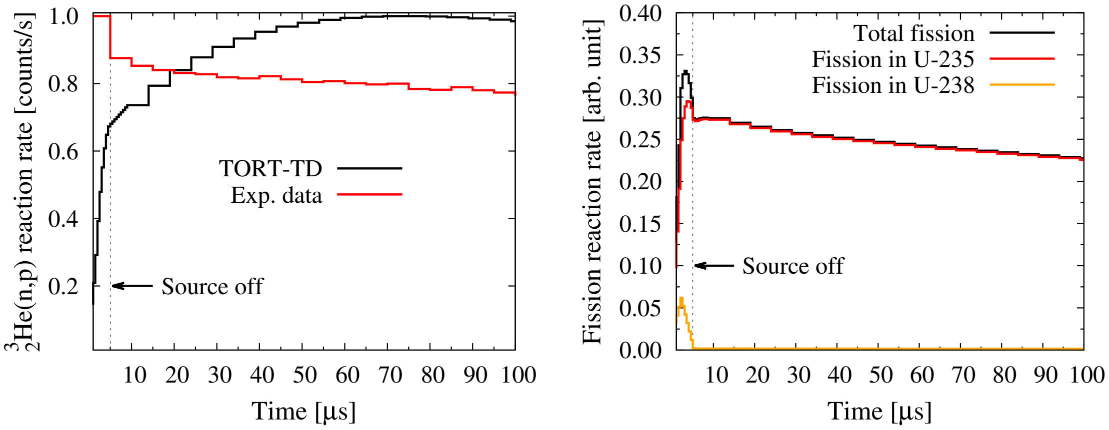

(a) Normalized $^3_2$He(n,p) rate at detector EC2 (b) Total fission rate of YALINA-Thermal

Figure 5.3: Comparison of simulated and experimental reaction rates for the (d,d) neutron source and 280 fuel rods configuration during the first 100 µs

In order to identify this effect, the fission reaction rate integrated over the whole fuel

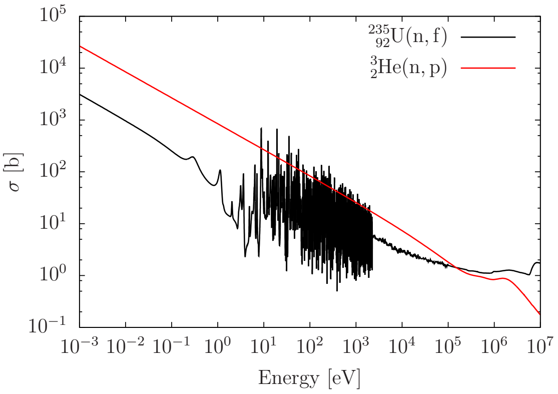

Figure 5.4: Microscopic cross sections of $^{235}_{92}$U and $^{3}_{2}$He

region is plotted in fig. 5.3b. The fission rate follows exactly the triangular time shape of the neutron source with the maximum source strength at 2.5 µs. After that it continuously decreases. Thus, the effect looking at is different from the fission rate behavior and does not explain the inertia of the $^{3}_{2}$He(n,p) reaction rate in EC2 directly. It is however observed that the fission rate between 5 µs and 75 µs changes only by about 10 %.

From the physical point of view it may be assumed that the moderation and thermalization of neutrons in the reactor is not finalized. This means the time of travel and successive collisions (which are immediate) will be noticeable in this time scale. From fig. 5.4 we can deduce the consequence that the probability of a $^{3}_{2}$He(n,p) reaction increases towards thermal energies practically with a $\frac{1}{v}$ shape and may therefore enhance the rate as integral over flux and cross section competing with the general decay of the neutron population due to the subcriticality of the reactor. This result has also been confirmed independently by Talamo [121] and Persson [131] in a different setup of the YALINA-Thermal configuration both using MC codes.

With this discussion it is emphasized again that the comparison between experiment and simulation is not only complicated due to the choice for approximations and methods, but obviously also by the uncertainties and limitations of the experimental setup in terms of the materials and hardware involved. It was outlined before that the experimental specification is not detailed enough. Some possible reasons for differences between experiment and simulation can be guessed. The real detector is a device containing structure material like copper and nickel. This means that the detector may shield to a certain extent neutrons from the $^{3}_{2}$He-filled reaction chamber. On the other hand cables of the detector device can contain carbon and hydrogen, so that local scattering/slowing-down effects may play a role. Finally, the efficiency of the detector may generally be dependent on the neutron energy.

5.3.2 Investigation of the Neutron Current at Core Boundary

The `TORT-TD` code has implemented a subroutine that provides the mesh-cell- and region-wise leakages used to calculate diffusion coefficients of that region. This option allows also for the definition of an arbitrary cube surface, for which the net neutron current J is delivered as energy-group-wise and total vector quantity. In general notation the net current is defined as the sum of the partial currents J^+ and J^- which point into direction of a normal vector $\boldsymbol{n}$ on a surface either in positive or negative axis direction (eq. (5.1)-(5.3)) [19].

$$J_{\boldsymbol{n}}(\boldsymbol{r},\boldsymbol{\Omega},E,t) = J_{\boldsymbol{n}}^{+}(\boldsymbol{r},\boldsymbol{\Omega},E,t) - J_{\boldsymbol{n}}^{-}(\boldsymbol{r},\boldsymbol{\Omega},E,t) \tag{5.1}$$

$$J_{\boldsymbol{n}}^{+} = \int\limits_{\boldsymbol{\Omega}\cdot\boldsymbol{n}>0} d\boldsymbol{\Omega}\,\boldsymbol{n}\cdot\boldsymbol{\Omega}\,\psi(\boldsymbol{r},\boldsymbol{\Omega},E,t) \tag{5.2}$$

$$J_{\boldsymbol{n}}^{-} = \int\limits_{\boldsymbol{\Omega}\cdot\boldsymbol{n}<0} d\boldsymbol{\Omega}\,\left|\boldsymbol{n}\cdot\boldsymbol{\Omega}\right|\psi(\boldsymbol{r},\boldsymbol{\Omega},E,t) \tag{5.3}$$

The leakage through a cube surface is given by `TORT-TD` for the six surfaces with their directional sign and have been evaluated according to eq. (5.1). The cube dimensions and position match the active zone of the YALINA-Thermal reactor. Thus, the leakage specifies directly the net current between the fuel region and the reflector region.

Fig. 5.5 shows the net current through the surface between the active zone and the reflector. The current is given energy-group-wise and divided by the width of the energy group necessitating a logarithmic scale of the abscissa. The third dimension is the time of the pulse period, which is also drawn with logarithmic scale. In the figure two data sets are used, which had to be separated in order to enable the logarithmic representation. The red colored data set denote the net neutron current, which leaves the fuel region and enters the reflector region. The blue data set denote the opposite direction of the net current from the reflector into the fuel region. At the data points, where a change of the sign occurs, the data item is set to a very small number. Thus, the valleys between the curves of varying colors represent the discontinuity of the zero crossing. The plot software applies at this point an interpolation, which leads partially to fragmentary three-dimensional surfaces. Additional to the uniform energy group ordinate, the upper energy boundary of certain groups are given in the figure. When in the following a group number is used, say group 6, we find the data in the interval between 6 and 7.

The simulation and the plot start at 0.5 µs with a time step width of 0.5 µs right after the static k_{eff} calculation. The neutron source is immediately active with the maximum intensity at 2.5 µs marked in the plot for group 6. Keeping in mind that neutrons have to travel at least 20 cm in radial direction and 25 cm in axial direction from the center of the core, the response is in majority immediate at the surface due to the large velocity of the

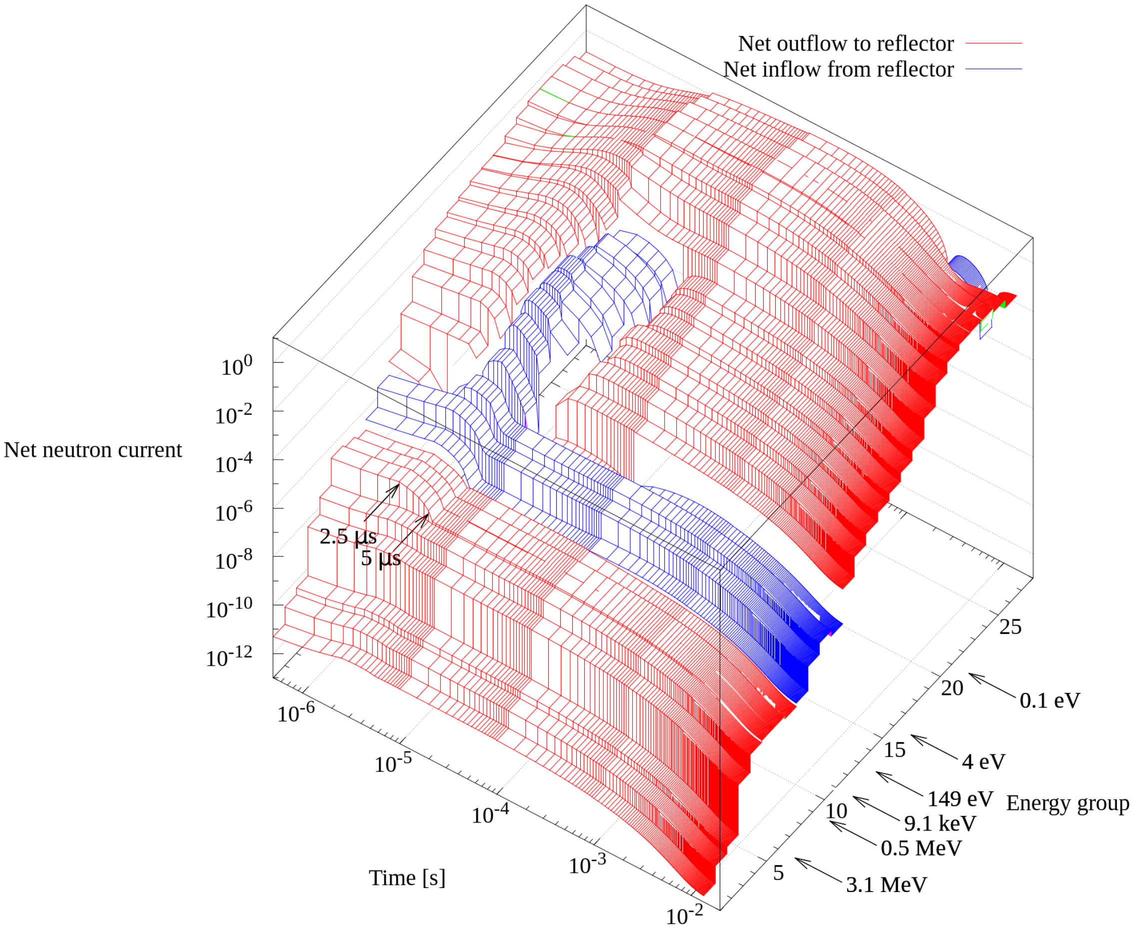

Figure 5.5: Net neutron current between core and reflector decomposed in out- and inflow for the (d,d) neutron source and 280 fuel rods configuration

neutrons and the associated large mean free path. The source shut-off at 5 µs is indicated also and the right-hand side of the triangular time shaped pulse causes a direct reduction of even the 20th group current with only minor delay. Already in the final phase of the source decrease at about 4 µs there is a turning point of net current in the groups 11 to 18, which corresponds to the energy interval of 9.118 keV and 0.4 eV. The net current changes its direction. More neutrons enter the fuel region through the surface than leave into the reflector for these energy groups. This situation continues till about 50 µs after which the net current stabilizes to be the net streaming from the fuel region into the reflector again.

The interpretation of this observation is, that, during the time the source is operating in the subcritical reactor, a net streaming from the fuel region into the reflector is obvious due to the flux gradient at the boundary. When the source operation terminates, the neutron production due to fission will decrease like e.g. in fig. 5.3b. According to the multiplication factor and the mean generation time evaluated in section 3.5 and section 3.6 the fission neutrons reduce every 80 µs by a factor of ≈ 0.96, which is slow compared to the slowing-down time of neutrons in hydrogenous media. In water this time is around 6 µs, but it does not take into account the effects of the chemical binding and upscattering at thermal energies [39]. Thus, the thermalization time, in which neutrons are distributed with a Maxwell-Boltzmann like shape in energy and have found an (quasi) equilibrium in space by the fundamental (decay) mode distribution, will last longer depending on the material and medium size. The slowing-down time in the hydrogen of the PE fuel matrix will have a similar time behavior, which means that the source neutrons within the fuel region slow down quickly to the thermal energies after the pulse has been injected. The slowing-down time in the reflector graphite is likewise found to be about 24 µs from 1 MeV to 1 eV. However, the thermalization time in a finite sized graphite medium may last about 1 ms [132]. The slower thermalization in the graphite reflector may lead to a storage of fast and epithermal neutrons from the fuel region, so that a temporary flux gradient from the reflector into the fuel region establishes causing a temporary dominant net current into the fuel. This effect is supported by the fact, that the overwhelming part of the resonance absorption takes place in this energy range. Since the decreasing fission production is the only neutron source, the net current stabilizes finally in direction of the reflector.

The equivalent results in fig. D.1 have been prepared for the 216 fuel rods configuration in appendix D. The effect of a net current from the reflector into the fuel region does not appear. This effect depends thus on the subcriticality of the system. Note that the net current into the reflector includes also the current from the reflector into the fuel region.

That such a current is visible however has a certain importance for the interpretation of PNS experiments. In several publications [48, 131, 133, 134] the multipoint kinetic method, but also few-group multipoint kinetics method, was proposed, if the global behavior of the reactor is determined by the time characteristic of more than one domain. The multipoint kinetic approach considers therefore mean neutron generation constants, effective delayed neutron fractions, etc. for all defined domains. For these coupled systems interfacing coefficients have to be determined, which describe the exchange of neutrons between the domains. These coefficients usually are assumed to be constant, in the theory they are mentioned to be possibly time-dependent. The example above shows that the coefficients are not necessarily constant and the time-dependent balance between the domains must be considered, the time-dependence will be surely needed when the equation system considers some energy groups explicitly.

5.4 Discussion on Kinetic Parameters

In the `TORT-TD` evaluation subroutine *getpwr* the ${}^{3}_{2}$He(n,p) reaction rate integration is implemented over the whole reactor volume for this work. This global reaction rate of the experimental count rate is applied for the characterization of the global time-dependence of the zero-power reactor. It is interpreted in a similar manner as the amplitude function $P(t)$ of the point kinetic equation (2.32).

In section 2.1.5 the simplified, feedback-free point kinetic equations have been described. These equations consider the fast change in power or neutron population with the fundamental mode prompt decay constant α_0 and the emission of delayed neutrons for a much longer time scale. All parameters of these equations are effective variables, in that they are weighted with the static adjoint flux which denotes the importance of a neutron at its particular energy, direction and position for a target quantity like the neutron production (*see* section 2.1.4). It was emphasized there that the kinetic parameter constituting the decay constant are typically calculated from asymptotic solutions of the effective multiplication factor equation (2.10).

The static parameter for the 280 fuel rods configuration are listed in table 5.3. The prompt decay constant is calculated from these according to eq. (2.44) and eq. (2.43) yielding about $-576\,\mathrm{s}^{-1}$. Since α_0 is a pure prompt parameter, the benchmark case was repeated also for the case of prompt neutrons only. This is accomplished by setting all delayed neutron related quantities in `TORT-TD` to zero and providing the prompt neutron production cross section $\nu_\mathrm{p}\Sigma_\mathrm{f}$ instead of the total one. The k_eff reduces accordingly to 0.954 26 as seen in the fourth column of table 5.3. With the prompt multiplication factor and the static one the effective delayed neutron fraction can be approximated. Using the relation $\beta_\mathrm{eff} = 1 - \frac{k_\mathrm{p}}{k_\mathrm{t}}$ [135] the confirming effective fraction of 754 pcm is obtained.

The decay constant of the static calculation is compared with the value in the fifth column stemming directly from the prompt global reaction rate of fig. 5.6 as slope of the clearly and ideally straight logarithmic decay between 12 ms and 18 ms. The direct comparison of the static and the slope value results in a significant difference and as such a

Table 5.3: Kinetic parameters as result of static and kinetic simulation with `TORT-TD`

Parameter	Unit	Static solution	Prompt solution	$\frac{\ln\left(\frac{f(0.018)}{f(0.012)}\right)}{\Delta t}$ *
k_{eff}	-	0.961 51	0.954 26	
ρ	-	−0.039 26	−0.047 93	
β_{eff}	-	0.007 55	0.007 56	
Λ	10^{-5} s	8.13	9.46	
α_0	s^{-1}	−575.77	−506.67	−487.27

* fig. 5.6

different kinetic behavior.

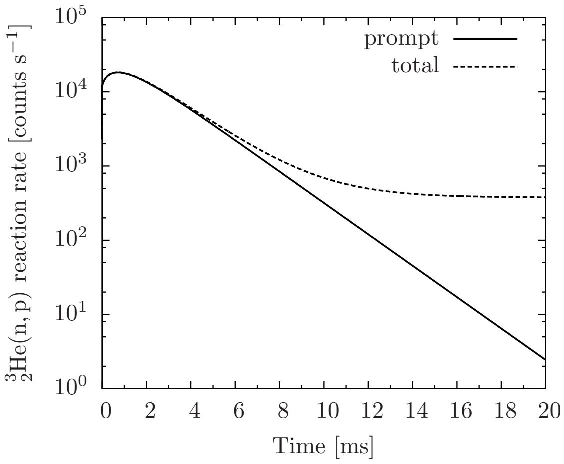

Figure 5.6: Total $^3_2$He(n,p) reaction rate integrated over whole reactor

Since the static approach was outlined to be only valid for a reactor operating exactly at or nearly critical the proposal of Difillipo [136] and others [137] is quite plausible to use the kinetic flux instead of the static flux in the calculation of kinetic parameters. In their procedure the kinetic flux was obtained by a fundamental mode time eigenvalue calculation for the subcritical HTR-PROTEUS reactor. In our case the direct time-dependent flux of the prompt decay is used together with the static adjoint flux for equations (2.36), (2.38) and (2.41). The calculation of the kinetic parameters is carried out for the purely prompt case and the total including the delayed neutron contribution in fig. 5.7 with the module `KSAUDI` for every time step.

In fig. 5.7a is shown that the effective delayed neutron fraction is not sensitive to the flux distribution of the kinetic calculation. This can be understood by the fact that the delayed neutron yield is constant below 0.1 MeV, and changes in flux and fission cross section cancel out due to their appearance in eq. (2.36) and in eq. (2.41) of the normalization integral F.

The neighboring fig. 5.7b is devoted to the mean neutron generation time. Plotted are the generation time again for the prompt and total case, but also for the fuel and graphite

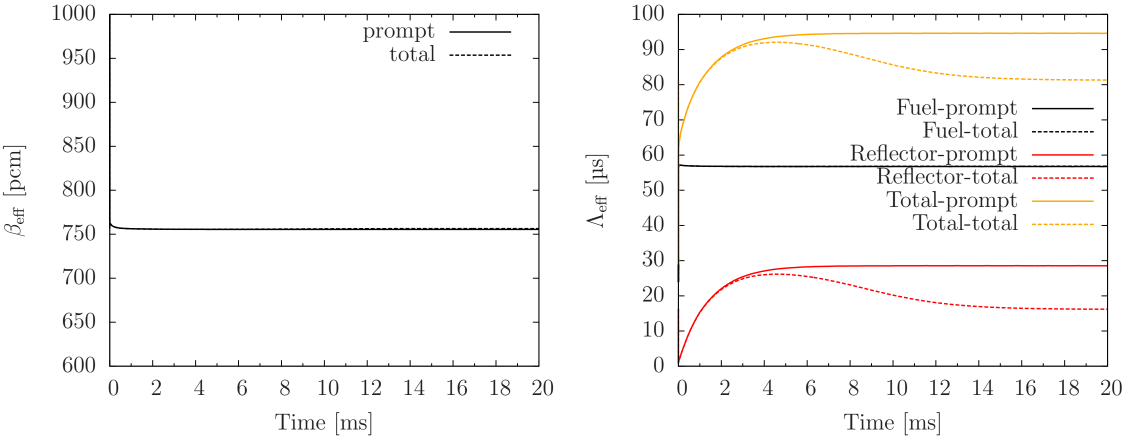

(a) Effective delayed neutron fraction

(b) Mean neutron generation time

Figure 5.7: Kinetic parameters based on kinetic flux integration

reflector region, separately. The generation time of the fuel region does not change. The generation time of the reflector region increases in the prompt case and stabilizes after 5 ms to a value 16 % larger than the static one. In the case including delayed neutrons an increasing deviation from the prompt development is observed which stabilizes finally to the static generation time of 8.1 µs. The time range of the deviation coincides with the appearance of the delayed neutron contributions in fig. 5.6.

This leads to a quite important observation. The pure prompt neutron generation time needs about 6 ms in fig. 5.7b to establish. However, after 3 ms the delayed neutrons start to cause the significant change in the mean generation in the real experiment. Thus, the prompt decay is superposed by the delayed neutron fission source after this time before it has developed to the fundamental mode decay.

For the enlarged mean neutron generation time and the prompt case the prompt decay constant was calculated in table 5.3 in the fourth column where the new prompt parameters are emphasized in red. The decay constant is evaluated to match within 4 % compared to the difference of 15.3 % of the static solution.

By this numerical example it is shown how a fundamental parameter like the mean neutron generation time can be predicted in a more realistic manner by the knowledge of the time-dependent flux distribution. Moreover, it shows that the application of reactivity measurement methods like the slope fit method cannot be applied without correction this reactor system, because the delayed neutrons (harmonics) appear before the fundamental mode decay has established.

Chapter 6

Conclusions

The presented discussions and developments aim at a consistent and innovative description of the neutron physics in a Pulsed Neutron Source (PNS) experiment in subcritical reactors. The difficulty consisted in the fact that most of the validated procedures in reactor physic code systems address the neutron physics of critical nuclear systems, which are treated generally by application of the k_{eff} eigenvalue or associated problems in the static case or predominantly asymptotic solutions in the time-dependent case.

In order to elucidate the main conceptual differences the **theory** (chapter 2) introduces the various ways of handling the time-dependent subcritical problem. One correct way to describe the time-dependent behavior of a source-free subcritical reactor is outlined to be the time eigenvalue equation. It contains the higher harmonics or modes which may play a role in the time range of PNS experiment measurements on top of the persisting fundamental prompt decay mode. The disadvantages in the application originate from the static nature of the time eigenvalue equation, which develops to a time-dependent solution as consequence of a modal synthesis approach. The initial condition i.e. the excitation by the pulsed neutron source has to be approximated, since the time eigenvalue equation is a homogeneous equation. Another drawback is the prompt nature of the solution neglecting the delayed neutron emission and harmonics, which lead over to the delayed neutron background.

A second correct way, the direct time-dependent method in form of the fully implicit time integration scheme, was given the preference. The main reason lays in the consideration of the neutron motion based on physical principles. In other words, the method allows for non-asymptotic solutions of the instationary system, which may transition into quasi-asymptotic states described by weighted or effective parameters such as mean neutron generation time and effective delayed neutron fraction in the frame of the integral point kinetic equations.

Since calculated reaction rates and balances are the window to the experimental measurements and detector responses, a major part of the effort is put into the generation of accurate macroscopic cross sections based on recent cross section evaluations. For this purpose new **microscopic fine-group master libraries** for the `KANEXT` reactor physics code are created (chapter 3). The outcome is a fine-energy-group structure of 350 energy groups with the aim to account adequately for neutron sources with a dedicated energy subdivision between 1 MeV and 20 MeV, for improved prediction of the slowing-down in thermal and fast energy spectrum systems with a constant lethargy grid of 0.05 width and to handle detailed thermal scattering including chemical binding effects in water, polyethylene and graphite. Special attention has been payed to the resolution of neutron cross section resonances of important reactor materials like ${}^{238}_{92}$U, ${}^{240}_{94}$Pu and ${}^{242}_{94}$Pu. The master libraries have been prepared for the JEFF 3.1, JEFF 3.1.1 and ENDF/B VII.0 evaluation, the production procedure is however kept general for use of other evaluations stored in the standard `ENDF-6` format.

For the subsequent cross section homogenization and collapsing a one-dimensional transport module was implemented in `KANEXT` based on the `ANISN` code and arbitrary quadrature and Legendre order for the investigation of anisotropy effects in the cell calculation. The JEFF 3.1 and ENDF/B VII.0 libraries are validated by use of the `KANEXT` code on pin and core level against `MCNP` calculations and show very good performance for the code-to-code comparison. By detailed analysis of the scattering properties of polyethylene and graphite potential numerical issues for deterministic transport based simulations have been found due to truncated Legendre expansions of the differential scattering cross section.

In view of the time-dependent simulation of a PNS experiment a consistent set of related constants is provided. For this purpose the new module `DLAYPM` was created to calculate problem-dependent physical delayed neutron data of the involved isotopes based on their fission rate. While in case of JEFF 3.1 the data rely on the old Keepin sets, a large deviation from this was observed for ENDF/B VII.0 looking at the abundances of the delayed neutron time groups. Since in JEFF based evaluations the number of time groups was extended to 8, all involved `KANEXT` modules had to be modified. To provide mixture averaged fission spectra - prompt and delayed - the module `CHICOR` was adapted accordingly.

The new **time-dependent source capability** (chapter 4) was implemented in the direct time-dependent discrete ordinate transport code `TORT-TD` in a cooperation with the German Technical Safety Organization (TSO) GRS, which implemented the time-dependent source neutron emission and the author of the thesis developed and investigated a new general approach to represent the neutron source in terms of the spherical harmonics expansion needed in deterministic transport codes. It is understood that the nature of the spherical harmonics functions allow either an energy group discretization of the source neutrons and isotropic emission equivalent to the zeroth moment expansion or a one-group representation with distinct anisotropy that is an expansion to the third order in case of the (d,d) neutron source. Depending on the deterministic transport code the resulting spherical harmonics coefficients may need an additional rotation to match the underlying base coordinate system. Since `TORT`/`TORT-TD` and `PARTISN` use a non-standard coordinate system the (d,d) neutron source was modeled isotropically and mono-energetically in the PNS experiment simulation.

Based on the new capability of the `TORT-TD` code and the improved macroscopic cross sections and time constants the **results of the simulation of the pulsed YALINA-Thermal experiments** are presented for the 280 and the 216 fuel rods case and the (d,d) neutron source (chapter 5).

Since the underlying benchmark definition deviates significantly from the experimental setup for important isotopes of the fuel, another set of cross sections was generated to account for $^{234}_{92}$U content and impurities described in literature. The comparison of the simulation result and the experimental data shows a convincing performance for the prompt part of the experiment in both the fuel and reflector region. It also shows that for the consideration of the delayed neutrons a more suitable guess of the precursor concentrations is needed. In the subsequent investigations the results of the original YALINA-Thermal benchmark were used.

A close look to the first 100 µs of the simulated $^{3}_{2}$He(n,p) detector response exhibits an increasing rate for a certain time after the pulse, whereas the total fission rate decreases immediately. This behavior is the consequence of the fast increase of the detector cross section towards thermal neutron energies with an almost ideal $\frac{1}{v}$ shape. The provided experimental data however is missing this detail.

The detailed time-dependent resolution of the net neutron current at the interface between the fuel and reflector region manifests one of the advantages of getting the phase-space solution at every time step. For some energy groups a temporary net inflow of neutrons from the reflector region is observed for the less subcritical reactor ($k_{\mathrm{eff}} \simeq 0.96$), which is not observed for the deep subcritical configuration and thus seems to be correlated to the level of subcriticality. This time and energy dependence of the neutron current at region interfaces is important to consider, if coupling coefficients in multipoint and multienergy domain extensions to the common point kinetics approach are used to describe the integral behavior of a reactor.

With the final discussion of the main kinetic parameters and alternative calculation routes the importance of the direct time-dependent solution is highlighted. It is shown that the fundamental mode decay constant can be extracted from a purely prompt simulation of the pulse at late times. The value agrees better with an improved definition of the parameter introducing the time-dependent flux. It is also shown that the delayed neutron harmonics are visible quite early in the experiment and any area-ratio or slope fit method must account for this in order to extract reliably the fundamental decay constant.

Bibliography

[1] G. I. Bell and S. Glasstone. *Nuclear Reactor Theory.* Van Nostrand Reinhold, Florida, 1970.

[2] W. A. Rhoades and D. B. Simpson. *The TORT Three-Dimensional Discrete Ordinates Neutron/Photon Transport Code (TORT version 3).* ORNL/TM-13221. October 1997.

[3] *A European Roadmap for Developing Accelerator-Driven Systems (ADS) for Nuclear Waste Incineration.* Report of the European Technical Working Group on ADS. 2001.

[4] M. Salvatores. Fuel cycle strategies for the sustainable development of nuclear energy: The role of accelerator driven systems. *Nuclear Instruments and Methods in Physics Research Section A: Accelerators, Spectrometers, Detectors and Associated Equipment*, 562(2):578–584, 2006.

[5] *Fast Reactor Database.* IAEA-TECDOC-866. Vienna, 1996.

[6] *Fast Reactor Database 2006 Update.* IAEA-TECDOC-1531. Vienna, 2006.

[7] *Accelerator-Driven Systems (ADS) and Fast Reactors (FR) in Advanced Nuclear Fuel Cycles.* NEA No. 3109. Paris, 2002.

[8] C. D. Bowman, E. D. Arthur, P. W. Lisowski, G. P. Lawrence, R. J. Jensen, J. L. Anderson, B. Blind, M. Cappiello, J. W. Davidson, T. R. England, L. N. Engel, R. C. Haight, H. G. Hughes, III, J. R. Ireland, R. A. Krakowski, R. J. LaBauve, B. C. Letellier, R. T. Perry, G. J. Russell, K. P. Staudhammer, G. Versamis, and W. B. Wilson. Nuclear energy generation and waste transmutation using an accelerator-driven intense thermal neutron source. *Nuclear Instruments and Methods in Physics Research Section A: Accelerators, Spectrometers, Detectors and Associated Equipment*, 320(1–2):336–367, 1992.

[9] H. A. Abderrahim, J. Galambos, Y. Gohar, S. Henderson, G. Lawrence, T. McManamy, A. C. Mueller, S. Nagaitsev, J. Nolen, E. Pitcher, R. Rimmer, R. Sheffield, and M. Todosow. Accelerator and Target Technology for Accelerator Driven Transmutation and Energy Production. Technical Report FERMILAB-FN-0907-DI, FERMILAB, 2012.

[10] Nuclear Wastes: Technologies for Separations and Transmutation. Technical report, National Research Council, National Academies Press, 1995.

[11] C. Rubbia, J. A. Rubio, S. Buono, F. Carminati, N. Fiétier, J. Galvez, C. Gelès, Y. Kadi, R. Klapisch, P. Mandrillon, J. P. Revol, and C. Roche. Conceptual Design

of a Fast Neutron Operated High Power Energy Amplifier. Technical report, CERN, Geneva, 1995.

[12] W. Gudowski, V. Arzhanov, C. Broeders, I. Broeders, J. Cetnar, R. Cummings, M. Ericsson, B. Fogelberg, C. Gaudard, A. Koning, P. Landeyro, J. Magill, I. Pazsit, P. Peerani, P. Phlippen, M. Piontek, E. Ramström, P. Ravetto, G. Ritter, Y. Shubin, S. Soubiale, C. Toccoli, M. Valade, J. Wallenius, and G. Youinou. Review of the European project — Impact of accelerator-based technologies on nuclear fission safety (IABAT). *Progress in Nuclear Energy*, 38(1–2):135–151, 2001.

[13] R. Soule, W. Assal, P. Chaussonnet, et al. Neutronic studies in support of accelerator-driven systems: The muse experiments in the masurca facility. *Nuclear Science and Engineering*, 148(1):124–152, 2004.

[14] J. F. Lebrat, G. Aliberti, A. D'Angelo, A. Billebaud, R. Brissot, H. Brockmann, M. Carta, C. Destouches, F. Gabrielli, E. Gonzalez, A. Hogenbirk, R. Klein-Meulenkamp, C. Le Brun, E. Liatard, F. Mellier, N. Messaoudi, V. Peluso, M. Plaschy, M. Thomas, D. Villamarin, and J. Vollaire. Global results from deterministic and stochastic analysis of the muse-4 experiments on the neutronics of accelerator-driven systems. *Nuclear Science and Engineering*, 158(1):49–67, 2008.

[15] C. Rubbia, P. Agostini, M. Carta, S. Monti, M. Palomba, F. Pisacane, C. Krakowiak, M. Salvatores, Y. Kadi, A. Herrera-Martinez, and L. Maciocco. The TRADE Experiment: Status of the Project and Physics of the Spallation Target. In *Proceedings of the 2004 Conference on Physics of Fuel Cycles and Advanced Nuclear Systems (PHYSOR)*, Chicago, Illinois, 2004.

[16] C. Fazio, F. Gröschel, W. Wagner, K. Thomsen, B. L. Smith, R. Stieglitz, L. Zanini, A. Guertin, A. Cadiou, J. Henry, P. Agostini, Y. Dai, H. Heyck, S. Dementjev, S. Panebianco, A. Almazouzi, J. Eikenberg, A. Letourneau, J. C. Toussaint, A. Janett, C. Perret, S. Joray, J. Patorski, W. Leung, P. Meloni, P. Turroni, A. Zucchini, G. Benamati, J. Konys, T. Auger, A. Gessi, D. Gorse, I. Serre, A. Terlain, J.-B. Vogt, A. Batta, A. Class, X. Cheng, F. Fellmoser, M. Daubner, S. Gnieser, G. Grötzbach, R. Milenkovic, C. Latgé, and J. U. Knebel. The MEGAPIE-TEST project: Supporting research and lessons learned in first-of-a-kind spallation target technology. *Nuclear Engineering and Design*, 238(6):1471–1495, 2008.

[17] P. Richard, M. Delpech, and G. Rimpault. *PDS-XADS: Preliminary Design Studies of an Experimental Accelerator-Driven System, Deliverable 1.* DER/SERI/LCSI02/4002 rév.1. CEA, 2002.

[18] G. Granget, H. A. Abderrahim, P. Baeten, C. Berglöf, A. Billebaud, E. González-Romero, F. Mellier, R. Rosa, and M. Schikorr. EUROTRANS/ECATS or Neutronic Experiments for the Validation of XT-ADS and EFIT Monitoring. In *Proceedings of the 2011 Workshop on Technology and Components of Accelerator-driven Systems*, NEA No. 6897. OECD Publishing, 2011.

[19] E. E. Lewis and W. F. Miller, Jr. *Computational Methods of Neutron Transport.* American Nuclear Society, Inc., Illinois, 1993.

[20] J. J. Duderstadt and L. J. Hamilton. *Nuclear Reactor Analysis.* John Wiley & Sons, Inc., 1976.

[21] G. R. Keepin. *Physics of Nuclear Kinetics.* Addison-Wesley Publishing Company, Inc., Reading, Massachusetts, 1965.

[22] P. Oberle. *Erstellung einer 78-Gruppenkonstantenbibliothek mit Energien bis 150 MeV für KAPROS.* Diploma thesis, Universität Karlsruhe (TH), 10 2004.

[23] R. E. MacFarlane. *NJOY99.0: Code System for Producing Pointwise and Multigroup Neutron and Photon Cross Sections from ENDF/B Data.* 2000.

[24] E. A. Stumbur. *The Use of Perturbation Theory in the Physics of Nuclear Reactor.* ERDA-tr-297. 1977.

[25] D. G. Cacuci. On Perturbation Theory And Reactor Kinetics: From Wigner's Pile Period To Accelerator Driven Systems. In *Proceedings of the 2002 International Conference on Mathematics, Computational Methods and Reactor Physics*, Seoul, Korea, 10 2002.

[26] I. N. Bronstein, K. A. Semendjajew, and G. Musiol. *Taschenbuch der Mathematik.* Deutsch (Harri), 4. edition, 1999.

[27] H. Borgwaldt, T. E. Murley, and D. Sanitz. *The Modal Synthesis of Rossi Alpha Data for Moderator Reflected Fast Assemblies.* Kernforschungszentrum Karlsruhe, KfK-409. Gesellschaft für Kernforschung mbH, Karlsruhe, 1966.

[28] The Scientific Papers. In A. M. Weinberg, editor, *The Collected Works of Eugene Paul Wigner*, volume A. Springer, 1992.

[29] D. G. Cacuci. *Sensitivity and Uncertainty Analysis: Theory*, volume 1. Chapman & Hall/CRC, 2003.

[30] IAEA. *Proceedings of 1st Geneva Conference*, volume 5, 1956.

[31] A. F. Henry. *Nuclear Science and Engineering*, 3, 1958.

[32] A. F. Henry. *Nuclear-Reactor Analysis.* MIT Press, Cambridge, Mass., 1975.

[33] K. H. Beckurts. Reactor physics research with pulsed neutron sources. *Nuclear Instruments and Methods*, 11(0):144–168, 1961.

[34] W. Gudowski, editor. *Impact of Accelerator-Based Technologies on Nuclear Fission Safety.* EUR 19608 EN. 2000.

[35] M. Drosg and O. Schwerer. *Handbook on Nuclear Activation Data*, chapter Production of Monoenergetic Neutrons Between 0.1 and 23 MeV: Neutron Energies and Cross Sections. IAEA-TECHDOC-273. IAEA, Vienna, 1987.

[36] V. V. Golushko, K. D. Zhuravlev, Y. S. Zamyatnin, N. I. Kroshkin, and V. N. Nefedov. The average number of neutrons emitted in the spontaneous fission of Cm244, Cm246, and Cm248. *Soviet Atomic Energy*, 34(2):178–179, February 1973.

[37] IAEA Nuclear Data Unit. Report of the Nuclear Data Section to the International Nuclear Data Committee June 1969-May 1970. Report INDC(NDS)-23/G, International Atomic Energy Agency, Vienna, Austria, May 1970.

[38] R. C. Martin, J. B. Knauer, and P. A. Balo. Production, distribution and applications of californium-252 neutron sources. *Applied Radiation and Isotopes*, 53(4):785–792, 2000.

[39] K. Wirtz and K. H. Beckurts. *Elementare Neutronenphysik.* Springer, 1958.

[40] J. K. Shultis and R. E. Faw. Radiation Shielding and Radiological Protection. In D. G. Cacuci, editor, *Handbook of Nuclear Engineering*, volume 1, chapter 11. Springer, New York, 2010.

[41] H. A. Abderrahim. Multi-purpose hYbrid Research Reactor for High-tech Applications and multipurpose fast spectrum research reactor. *International Journal of Energy Research*, 2011.

[42] V. Bournos, I. Serafimovich, A. Fokov, Y. Fokov, H. Kiyavitskaya, A. Khilmanovich, B. Martsynkevich, C. Routkovskaia, Y. Gohar, C. Persson, and W. Gudowski. YALINA-Thermal Benchmark Specifications for the IAEA Coordinated Research Projects. Technical report, Joint Institute for Power and Nuclear Research – Sosny National Academy of Sciences Belarus, 2007.

[43] S. Monti, M. Salvatores, D. G. Cacuci, A. D'Anggelo, G. Bignan, N. Burgio, J. Cahalan, M. Carta, P. Fougeras, G. Granget, G. Imel, C. Jammes, Y. Kadi, D. G. Naberejnev, H. Philibert, and P. Ravetto. TRADE: A Full Experimental Validation of the ADS Concept in a European Perspective. In *Proceedings of the 2003 Conference on*

Accelerator Applications in a Nuclear Renaissance (AccApp), San Diego, California, 2003.

[44] C. H. M. Broeders and I. Broeders. Neutron physics analyses of accelerator-driven subcritical assemblies. *Nuclear Engineering and Design*, 202(2-3):209–218, 2000.

[45] T. Gozani. The concept of reactivity and its application to kinetic measurements. *Nukleonik*, 5(55), Feb 1963.

[46] M. Rosselet, T. Williams, and R. Chawla. Subcriticality measurements using an epithermal pulsed-neutron-source technique in pebble-bed htr configurations. *Annals of Nuclear Energy*, 25(4–5):285–294, 1998.

[47] N. G. Sjöstrand. Measurement on a subcritical reactor using a pulsed neutron source. *Arkiv för fysik*, 11(13), 1956.

[48] D. Villamarin Fernandez. *Análisis dinámico del reactor experimental de fisión nuclear MUSE-4*. PhD thesis, Universidad Complutense de Madrid. Facultad de Ciencias Físicas. Departamento de Física Atómica, Molecular y Nuclear, Novembre 2004.

[49] C. Berglöf. *On Measurement and Monitoring of Reactivity in Subcritical Reactor Systems*. PhD thesis, KTH, Reactor Physics, 2010.

[50] T. Gozani. A modified procedure for the evaluation of pulsed source experiments in subcritical reactors. *Nukleonik*, 4(348), 1962.

[51] B. E. Simmons and J. S. King. A pulsed technique for reactivity determination. *Nuclear Science and Engineering*, 3:595–608, 1958.

[52] H. Borgwaldt, editor. *SUAK, a Fast Subcritical Facility for Pulsed Neutron Measurements*. Kernforschungszentrum Karlsruhe, KfK-302. Gesellschaft für Kernforschung mbH, Karlsruhe, 1965.

[53] H. Borgwaldt, editor. *Experience Obtained at Karlsruhe with Different Kinetic Methods of Reactivity Determination*. Kernforschungszentrum Karlsruhe, KfK-899. Gesellschaft für Kernforschung mbH, Karlsruhe, 1968.

[54] Y. Cao and J. Lee. Spatial corrections for pulsed-neutron reactivity measurements. *Nuclear Science and Engineering*, 165(3):270–282, July 2010.

[55] Y. Cao. *Space-Time Kinetics and Time-Eigenfunctions*. PhD thesis, University of Michigan, 2008.

[56] D. Lathouwers. Iterative computation of time-eigenvalues of the neutron transport equation. *Annals of Nuclear Energy*, 30(17):1793–1806, 2003. In Honour of Professor Hugo van Dam on the Occasion of his Retirement.

[57] F. Wols, D. Lathouwers, and W. Uyttenhove. *Transient Analyses of Accelerator Driven Systems Using Modal Expansion Techniques.* Master's thesis, TU Delft, 2010.

[58] A. Talamo and Y. Gohar. Monte Carlo Modeling And Analyses of Yalina-Booster Subcritical Assembly Part I: Analytical Models And Main Neutronics Parameters. Technical Report ANL-NE-08/13, 937414, September 2008.

[59] A. Talamo, Y. Gohar, and C. Rabiti. Monte Carlo Modeling and Analyses of Yalina-Booster Subcritical Assembly Part II: Pulsed Neutron Source. Technical Report ANL-08/33, 946033, October 2008.

[60] A. Talamo, Y. Gohar, C. Rabiti, G. Aliberti, F. Kondev, D. Smith, Z. Zhong, H. Kiyavitskaya, V. Bournos, Y. Fokov, C. Routkovskaya, and I. Serafimovich. Pulse superimposition calculational methodology for estimating the subcriticality level of nuclear fuel assemblies. *Nuclear Instruments and Methods in Physics Research Section A: Accelerators, Spectrometers, Detectors and Associated Equipment*, 606(3):661–668, July 2009.

[61] T. E. Hill and W. M. Reed. *TIMEX: A Time-dependent Explicit Discrete Ordinate Program for the Solution of Multigroup Transport Equations.* LA-6201-MS. Los Alamos, 1976.

[62] K. D. Lathrop, R. E. Anderson, and F. W. Brinkley. *TRANZIT: A Program for Multigroup Time-dependent Transport in r-z Cylindrical Geometry.* LA-4575. Los Alamos, 1971.

[63] R. E. Alcouffe, R. S. Baker, J. A. Dahl, S. A. Turner, and R. C. Ward. *PARTISN 5.97: A Time-Dependent, Parallel Neutral Particle Transport Code System.* LA-UR-08-07258. November 2008.

[64] A. Seubert, K. Velkov, and S. Langenbuch. The Time-Dependent 3-D Discrete Ordinates Code TORT-TD with Thermal-Hydraulic Feedback by ATHLET Models. In *Proceedings of the 2008 International Conference on the the Physics of Reactors*, Interlaken, Switzerland, September 2008.

[65] A. Pautz and A. Birkhofer. DORT-TD: A Transient Neutron Transport Code with Fully Implicit Time Integration. *Nuclear Science and Engineering*, 145:299–319, 2003.

[66] A. M. Weinberg and E. P. Wigner. *The Physical Theory of Neutron Chain Reactors.* Univ. of Chicago Pr., Chicago, 1958.

[67] C. Rabiti and A. Rineiski. Modeling of Fast Transients Driven by External Neutron Source Variations. In *Proceedings of the 2004 annual meeting on nuclear technology*, Düsseldorf, Germany, 2004.

[68] H. Huschke. *Gruppenkonstanten für dampf- und natriumgekühlte schnelle Reaktoren in einer 26-Gruppendarstellung.* Kernforschungszentrum Karlsruhe, KfK-770. Ges. für Kernforschung, Karlsruhe, 1968.

[69] E. Kiefhaber, editor. *The KFKINR-Set of Group Constants, Nuclear Data Basis and First Results of its Application to the Recalculation of Fast Zero-Power Reactors.* Kernforschungszentrum Karlsruhe, KfK-1572. Gesellschaft für Kernforschung mbH, Karlsruhe, 1972.

[70] H. Bachmann, editor. *The Group Cross Section Set KFK-SNEAK: Preparation And Results.* Kernforschungszentrum Karlsruhe, KfK-628. GfK, Karlsruhe, 1967.

[71] D. Woll. GRUCAL, Improved Treatment for Determining the Group Cross Section for Elastic Down-Scattering into the Adjacent Group. Technical Report KfK-1985, Forschungszentrum Karlsruhe, 1985.

[72] J. R. Askew, F. J. Fayers, and P. B. Kemshell. A General Description of the Lattice Code WIMS. *J. Brit. Nucl. Energy Soc.*, 5, 1966.

[73] C. H. M. Broeders. *Entwicklungsarbeiten für die neutronenphysikalische Auslegung von Fortschrittlichen Druckwasserreaktoren (FDWR) mit kompakten Dreiecksgittern in hexagonalen Brennelementen.* Kernforschungszentrum Karlsruhe, KfK-5072. Karlsruhe, 1992.

[74] E. Sartori. VITAMIN-J, a 175 Group Neutron Cross Section Library, Based on Jef-1 for Shielding Benchmark Calculations. Technical Report JEF-l/Dot-100, 1985.

[75] M. Herman and A. Trkov, editors. *ENDF-6 Formats Manual: Data Formats and Procedures for the Evaluated Nuclear Data File ENDF/B-VI and ENDF/B-VII.* BNL–90365-2009. Brookhaven National Laboratory (BNL) National Nuclear Data Center, 2009.

[76] D. Woll. Aufbau der Gruppenkonstantenbibliothek GRUBA und ihre Verwaltung durch das Programmsystem GRUMA. Technical Report KfK-1815, Forschungszentrum Karlsruhe, 1973.

[77] D. Woll. Aufbau der Gruppenkonstantenbibliothek GRUBA und ihre Verwaltung durch das Programmsystem GRUMA. Technical Report KfK-3745, Forschungszentrum Karlsruhe, 1984.

[78] J.-C. Sublet, A. J. Koning, R. A. Forrest, and J. Kopecky. *The JEFF-3.0/A Neutron Activation File – EAF-2003 into ENDF-6 format –.* JEFDOC-982. OECD, 2003.

[79] A. Kiyavitskaya and S. E. Chigrinov. Experimental And Theoretical Research Of The Peculiarities Of Transmutation Of Long-Lived Fission Products And Minor-Actinides In Sub-Critical Assembly Driven By A Neutron Generator. Annual Report of ISTC Project #B-070-98, Joint Institute Of Power And Nuclear Research, National Academy Of Sciences Of Belarus, 2000.

[80] J. R. Lamarsh. *Introduction to Nuclear Engineering*. Addison-Wesley Series in Nuclear Science and Engineering. Addison-Wesley, Reading, Mass., 1975.

[81] D. Sprevak and J. U. Koppel. Neutron scattering by polyethylene. *Nukleonik*, 12(1), 1969.

[82] R. E. Hill and C. Y. Liu. Temperature dependent neutron scattering cross-sections for polyethylene. *Nucl. Instrum. Meth.*, A538:686–691, 2005.

[83] J. Keinert and M. Mattes. JEFF-3.1 General Purpose Thermal Scattering Law File, H(CH2), May 2005.

[84] J. U. Koppel, D. H. Houston, and D. Sprevak. ENDF/B VII.0, General Purpose Thermal Scattering Law File, H(CH2), December 2006.

[85] J. A. Young and J. U. Koppel. Phonon spectrum of graphite. *Journal of Chemical Physics*, 42(1), 1965.

[86] J. A. Young, N. F. Wikner, and D. E. Parks. Neutron thermalization in graphite II. *Nukleonik*, 7(6), 1965.

[87] M. Mattes and J. Keinert. *Status of Thermal Neutron Scattering Data for Graphite*. INDC(NDS)-0475. IAEA, July 2005.

[88] R. E. McFarlane. *New Thermal Neutron Scattering Files for ENDF/B-VI Release 2*. LA-12639-MS (ENDF-356). Los Alamos National Laboratory, March 1994.

[89] X-5 Monte Carlo Team. *MCNP — A General Monte Carlo N-Particle Transport Code, Version 5*, volume I. Los Alamos National Laboratory, 2003.

[90] O. Cabellos and Y. Rugama. Processing and Validation of JEFF3.1 Library in ACE Format at 10 Different Temperatures. In *Proceedings of the 2007 International Conference on Nuclear Data for Science and Technology*, pages 697–700, 2007.

[91] X-5 Monte Carlo Team. *MCNP — A General Monte Carlo N-Particle Transport Code, Version 5*, volume II. Los Alamos National Laboratory, 2003.

[92] C. H. M. Broeders. KANEXT documentation. Input description of the KARBUS module. Technical report, Forschungszentrum Karlsruhe, 2008.

[93] D. Woll. GRUCAL, Ein Programmsystem zur Berechnung makroskopischer Gruppenkonstanten. Technical Report KfK-2108, Forschungszentrum Karlsruhe, 1975.

[94] M. Becker. KANEXT documentation. Input description of the GRUCAL module. Technical report, Forschungszentrum Karlsruhe, 2010.

[95] L. P. Abagayan, N. O. Bazazyants, I. I. Bondarenko, and M. N. Nikolaev. *Group Constants for Nuclear Reactor Calculation.* State Scientific and Technical Press for Atomic Energy, Moscow, 1964. Authorized translation from the Russian.

[96] A. Sauer. Approximate escape probabilities. *Nuclear Science and Engineering*, 16:329–335, 1963.

[97] G. I. Bell. A simple treatment for effective resonance absorption cross sections in dense lattices. *Nuclear Science and Engineering*, 5:138–139, 1959.

[98] M. M. Levine. Resonance integral calculations for U-238 lattices. *Nuclear Science and Engineering*, 16:271–279, 1963.

[99] H. Bachmann, H. Gabaieff, and D. Woll. Kurzbeschreibung des KAPROS Moduls SIGMUT zur Modifikation von SIGMN-Blöcken und dessen Prüfmodul PRSIGM. INR-Bericht Nr. 875, 1979.

[100] W. Höbel. Kurzbeschreibung des Unterprogramms WQRG zur Verarbeitung von SIGMN-Strukturen in KAPROS-Moduln. INR-Bericht Nr. 1126, 1981.

[101] C. H. M. Broeders. KANEXT documentation. Input description of the WEKCPM module. Technical report, Forschungszentrum Karlsruhe, 2010.

[102] M. Becker. KANEXT documentation. Input description of the KANISN module. Technical report, Forschungszentrum Karlsruhe, 2010.

[103] H. Bachmann and R. Kiesel. Kurzbeschreibung des KAPROS-Moduls DIFF0 zur Berechnung der nulldimensionalen Multigruppen-Diffusionsgleichung und dessen Pruefmodul PRDIF0. Technical Report KAPROS-44, Forschungszentrum Karlsruhe, 1979.

[104] M. Becker. KANEXT documentation. Input description of the CHICOR module. Technical report, Forschungszentrum Karlsruhe, 2010.

[105] C. H. M. Broeders. KANEXT documentation. Input description of the ONEHOM module. Technical report, Forschungszentrum Karlsruhe, 2011.

[106] H. Bachmann and R. Kiesel. Kurzbeschreibung des KAPROS-Moduls BUCIT0 zur Bucklingberechnung durch nulldimensionale Iteration. Technical Report KAPROS-46, Forschungszentrum Karlsruhe, 1979.

[107] The SCALE team. *SCALE: A Modular Code System for Performing Standardized Computer Analyses for Licensing Evaluations*, volume 1–3 of *Version 6.* January 2008.

[108] P. Oberle. *Application of a New Resonance Formalism to Pressurized Water Reactors.* PhD thesis, Institut für Kernenergetik und Energiesysteme der Universität Stuttgart, March 2010.

[109] The SCALE team. *SCALE: A Modular Code System for Performing Standardized Computer Analyses for Licensing Evaluations*, volume 1–3 of *Version 5.1.* November 2006.

[110] R. J. Tuttle. Delayed-neutron data for reactor-physics analysis. *Nuclear Science and Engineering*, 56, 1975.

[111] M. Becker. KANEXT documentation. Input description of the DLAYPM module. Technical report, Forschungszentrum Karlsruhe, 2010.

[112] D. Thiem. Personal notice to E. Kiefhaber, W. Maschek, C. Broeders, H.–W. Wiese, D. Woll, October 2000.

[113] G. D. Spriggs, J. M. Campbell, and V. M. Piksaikin. An 8-group delayed neutron model based on a consistent set of half-lives. *Progress in Nuclear Energy*, 41(1-4):223–251, 2002.

[114] A. d'Angelo and J. L. Rowlands. *Conclusions Concerning the Delayed Neutron Data for the Major Actinides.* JEF/DOC-920. OECD, April 2002.

[115] J. L. Rowlands. *Delayed Neutron Data in 8 Time Groups.* JEF/DOC-976. OECD, Nov. 2003.

[116] W. B. Wilson, S. T. Cowell, T. R. England, A. C. Hayes, and P. Moller. *A Manual for CINDER'90 Version 07.4 Codes and Data.* Version 07.4.2. March 2008.

[117] M. B. Chadwick, P. Oblozinský, M. Herman, N. M. Greene, R. D. McKnight, D. L. Smith, P. G. Young, R. E. MacFarlane, G. M. Hale, S. C. Frankle, A. C. Kahler, T. Kawano, R. C. Little, D. G. Madland, P. Moller, R. D. Mosteller, P. R. Page, P. Talou, H. Trellue, M. C. White, W. B. Wilson, R. Arcilla, C. L. Dunford, S. F. Mughabghab, B. Pritychenko, D. Rochman, A. A. Sonzogni, C. R. Lubitz, T. H. Trumbull, J. P. Weinman, D. A. Brown, D. E. Cullen, D. P. Heinrichs, D. P. McNabb, H. Derrien, M. E. Dunn, N. M. Larson, L. C. Leal, A. D. Carlson, R. C. Block, J. B. Briggs, E. T. Cheng, H. C. Huria, M. L. Zerkle, K. S. Kozier, A. Courcelle, V. Pronyaev, and S. C. van der Marck. ENDF/B-VII.0: Next generation evaluated nuclear data

library for nuclear science and technology. *Nuclear Data Sheets*, 107(12):2931–3060, 2006. Evaluated Nuclear Data File ENDF/B-VII.0.

[118] A. Hébert. *Applied Reactor Physics.* Presses internationales Polytechnique, 2009.

[119] M. Becker. KANEXT documentation. Input description of the CRGIP module. Technical report, Forschungszentrum Karlsruhe, 2010.

[120] G. Buckel, W. Goetzmann, E. Kiefhaber, and K. Kuefner. TRANSX, ein Transformationsprogramm zur Bereitstellung makroskopischer Gruppenkonstanten aus SIGMN-Blöcken für Neutronentransport- und Diffusionsprogramme. Technical Report KfK-4977, Karlsruhe, 1992.

[121] A. Talamo and Y. Gohar. Deterministic and Monte Carlo Modeling and Analyses of Yalina-Thermal Subcritical Assembly. Technical Report ANL-NE-10/17, 991100, July 2010.

[122] Y. Y. Azmy. Unconditionally stable and robust adjacent-cell diffusive preconditioning of weighted-difference particle transport methods is impossible. *Journal of Computational Physics*, 182(1):213–233, 2002.

[123] M. B. Emmett, W. A. Rhoades, R. L. Childs, and J. O. Johnson. *A User's Manual for MASH 1.0 – A Monte Carlo Adjoint Shielding Code System.* ORNL/TM-11778. March 1992. See the DORT section.

[124] A. Seubert, A. Pautz, M. Becker, and R. Dagan. Time-dependent Anisotropic Distributed Source Capability in Transient 3-D Transport Code TORT-TD. In *Proceedings of the 2009 International Conference on Mathematics, Computational Methods and Reactor Physics*, Saratoga Springs, New York, 2009.

[125] M. Becker, R. Dagan, A. Seubert, and A. Pautz. Energy-Angle Dependent Neutron Source in Deterministic Transport Codes with Spherical Harmonic Expansion. In *Proceedings of the 2009 International Conference on Mathematics, Computational Methods and Reactor Physics*, Saratoga Springs, New York, 2009.

[126] A. Seubert. Short Input Description of the Code TORT-TD. Technical report, Gesellschaft für Anlagen- und Reaktorsicherheit, 2011.

[127] M. Drosg. *DROSG-2000: Neutron Source Reactions.* Iternational Atomic Energy Agency (IAEA), Vienna, 2005.

[128] A. Abramowitz and I. Stegun. *Handbook of Mathematical Functions.* Dover, New York, 1993.

[129] A. Barbarino, S. Dulla, and P. Ravetto. On the evaluation of ray effects in multidimensional and time-dependent transport problems. *Transactions of the American Nuclear Society*, 106:369–371, 2012.

[130] G. Aliberti and Y. Gohar. YALINA Analytical Benchmark Analyses Using the Deterministic ERANOS Code System. Technical Report ANL-09/23, 967263, August 2009.

[131] C.-M. Persson, P. Seltborg, A. Åhlander, W. Gudowski, T. Stummer, H. Kiyavitskaya, V. Bournos, Y. Fokov, I. Serafimovich, and S. Chigrinov. Analysis of reactivity determination methods in the subcritical experiment yalina. *Nuclear Instruments and Methods in Physics Research Section A: Accelerators, Spectrometers, Detectors and Associated Equipment*, 554(1–3):374–383, 2005.

[132] R. E. McFarlane. Neutron Slowing Down and Thermalization. In D. G. Cacuci, editor, *Handbook of Nuclear Engineering*, volume 1, chapter 3. Springer, New York, 2010.

[133] R. Avery. Theory of Coupled Reactors. In *2nd Int. Conf. Peaceful Uses of Atomic Energy*, volume 12, London, 1958.

[134] P. Bosio, P. Ravetto, M. M. Rostagno, and A. Barzilov. Multipoint Method in Nuclear Reactor Kinetics. In *Proc. Int. Mtg. Mathematical Methods for Nuclear Applications*, Salt Lake City, 2001.

[135] M. M. Bretscher. *Perturbation Independent Methods for Calculating Research Reactor Kinetic Parameters.* ANL/RERTR/TM30. 1997.

[136] F. C. Difilippo. LEU-HTR PROTEUS: Neutron Kinetics and Procedures to Analyze Pulsed Neutron Experiments. Technical Report TM-41-91-27, PSI, 1991.

[137] *Critical Experiments and Reactor Physics Calculations for Low Enriched High Temperature Gas Cooled Reactors.* IAEA-TECDOC-1249. IAEA, Vienna, 2001.

[138] S. Chigrinov and I. Rakhno. *IAEA Benchmark 3.2: Experimental Research of Neutronics of a Subcritical Uranium-Polyethylene Assembly Driven with a Neutron Generator (The Yalina Experiment).* Technical report. Radiation Physics and Chemistry Problems Institute, National Academy of Sciences, Minsk, 2000.

[139] G. Audi, O. Bersillon, J. Blachot, and A. H. Wapstra. The Nubase evaluation of nuclear and decay properties. *Nuclear Physics A*, 729(1):3–128, 2003. The 2003 NUBASE and Atomic Mass Evaluations.

[140] *Silo User's Guide: Version 4.8 of the Silo Library.* LLNL-SM-453191. Lawrence Livermore National Laboratory, 2010. `https://wci.llnl.gov/codes/silo`.

[141] H. Childs, E. S. Brugger, K. S. Bonnell, J. S. Meredith, M. Miller, B. J. Whitlock, and N. Max. A Contract-Based System for Large Data Visualization. In *Proceedings of IEEE Visualization 2005*, pages 190–198, 2005. `https://wci.llnl.gov/codes/visit`.

[142] The Grace Team. Grace User's Guide (for Grace-5.1.22). `http://plasma-gate.weizmann.ac.il/Grace/doc/UsersGuide.html`, 2008.

[143] W. W. Engle, Jr. *A Users Manual for ANISN – A One-Dimensional Discrete Ordinates Transport Code with Anisotropic Scattering.* K-1693. March 1966.

[144] *DOORS3.2a: One-, Two- and Three Dimensional Discrete Ordinates Neutron/Photon Transport Code System.* CCC-650. April 1998.

[145] E. Kiefhaber and K. Ott. *Interpolationsformel für Selbstabschirmungsfaktoren.* Kernforschungszentrum Karlsruhe, KfK-384. Gesellschaft für Kernforschung mbH, Karlsruhe, 1965.

[146] P. F. A. de Leege. *NSLINK (NJOY-SCALE-LINK).* NEA-1347. 1991.

[147] R. Dagan, M. Badea, A. Travleev, and C. H. M. Broeders. Cross-Section Analysis for TRADE Fuel. In *Proceedings of the 2004 International Conference on the the Physics of Fuel Cycles and Advanced Nuclear Systems*, Chicago, 2004.

[148] J. F. Briesmeister, editor. *MCNP — A General Monte Carlo N-Particle Transport Code, Version 4C.* LA-13709-M. Los Alamos National Laboratory, 2000.

[149] W. A. Rhoades and M. B. Emmett. *DOS: The Discrete Ordinates System.* ORNL/TM-8362. August 1982.

[150] K. N. Ivanov, T. M. Beam, and A. J. Baratta. PWR Main Steam Line Break (MSLB) Benchmark, Volume I: Final Specifications. Technical report, 1999.

[151] G. Willerding. AUDI3, ein Programm für Störungsrechnung 1. Ordnung und andere Auswertungen der Ergebnisse von 3-dimensionalen Multigruppen-Diffusionsrechnungen. INR-Bericht Nr. 1241, 1982.

[152] T. B. Fowler, D. R. Vondy, and G. W. Cunningham. *CITATION-LDI2: Nuclear Reactor Core Analysis Code*, chapter Mathematical Formulations, Section 721. RSICC, 1971.

[153] M. Drosg. *Neutron Source Reactions.* Iternational Atomic Energy Agency (IAEA), Vienna, 2005.

[154] W. H. Press, S. A. Teukolsky, W. T. Vetterling, and B. P. Flannery. Numerical Recipes 3rd Edition. Technical report, 2007.

Appendices

Appendix A

Description of the YALINA-Thermal Reactor

In the following the general reactor geometry and the loading configurations of the YALINA-Thermal reactor is described. The YALINA-Thermal benchmark [138] was extended and published within the IAEA combined CRP "Analytical and Experimental Benchmark Analysis on Accelerator Driven Systems" and "Low Enriched Uranium Fuel Utilization in Accelerator Driven Systems" [42].

A.1 Reactor Geometry and Configuration

The main construction elements of the reactor are given in fig. A.1, A.2 and A.3. These are the neutron producing target with the beam tube, the core, the reflector and the thin surrounding layers. The outer dimensions of the reactor are 1208 mm in x-direction, 1203 mm in y-direction and 1008 mm in z-direction. The graphite reflector (fig. A.1) is almost as thick as the core itself. In the x-direction it introduces an asymmetry, where the bottom part measures 466 mm and the top part 324 mm. In y-direction the symmetric reflector is found of 400 mm on each side. The active core's dimensions are 400 mm in height and width and 500 mm in the z-direction without taking the ending parts of the fuel rods in consideration. An additional asymmetry is introduced along the z-axis, because the reflector overlaps in the front part 74 mm but in the back part 350 mm, see fig. A.2 and fig. A.3. A massive steel plate shields the front of the core. A large air volume adjoins the end of the core in axial direction. The active core is axially subdivided into a region where the middle Fuel Assembly (FA) position contains a lead buffer over 216 mm and the remaining space is used for the beam tube. The three-dimensional schematic plot of fig. A.4 gives additionally an impression of the facility geometry.

The active core consists of 25 quadratic positions with side length of 80 mm and a depth of 500 mm each (fig. A.5). Except for the four positions in the corner, 21 are reserved for the placement of FAs. While the inner radial FAs are always loaded with 12 fuel rods, the loading of the outer FAs depends on the configuration. Fig. A.5 shows the three configurations (280, 245 and 221 fuel rods) of the core which cover three levels of subcriticality.

The fuel type EK-10 is characterized as an $UO_2 + MgO$ ceramic composite with an ${}^{235}_{92}U$ enrichment of 10 %. The fuel rod diameter amounts to 3.5 mm surrounded by an aluminum

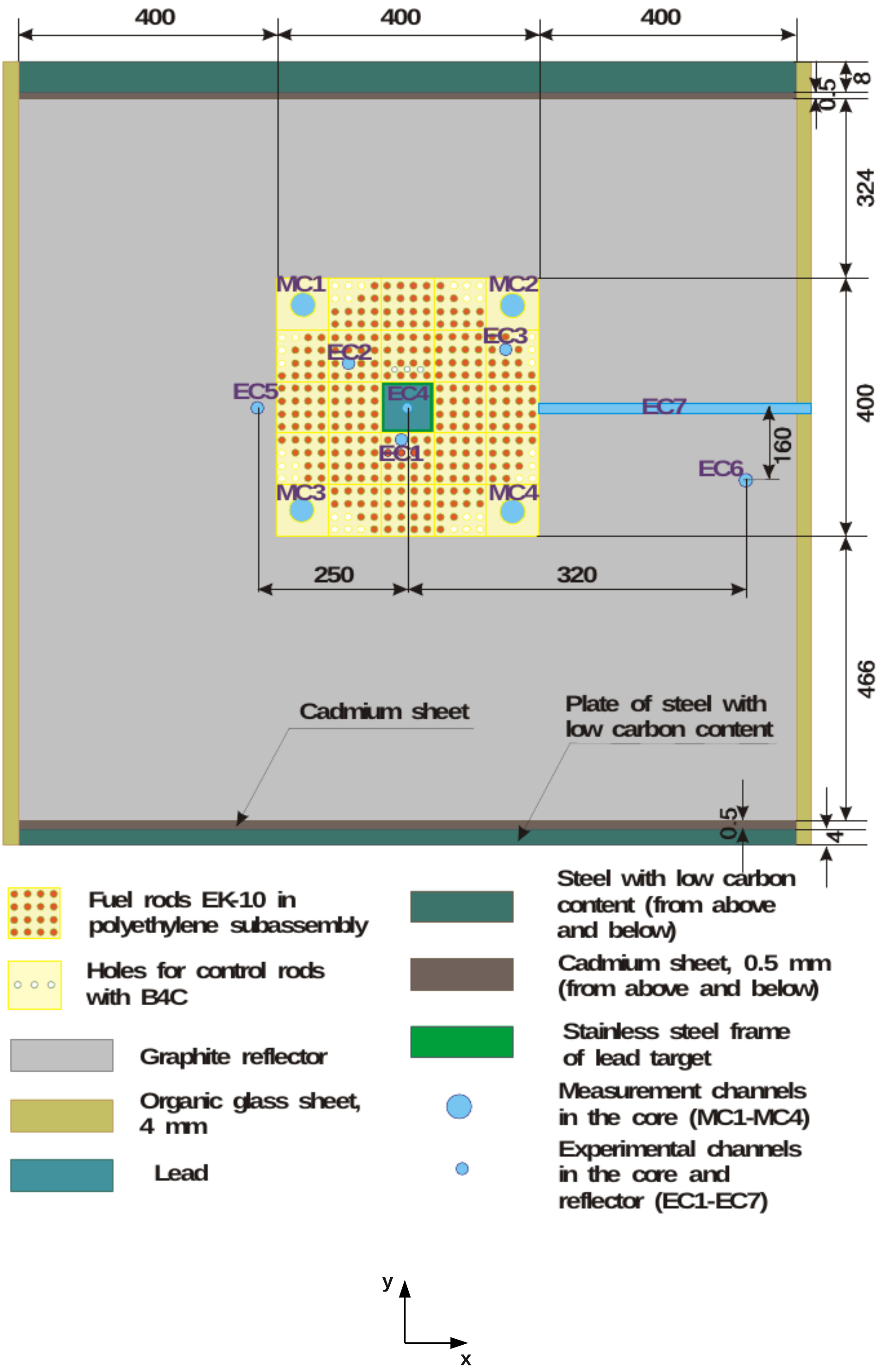

Figure A.1: View along the x - y axis through the YALINA-Thermal reactor taken from benchmark definition [42]

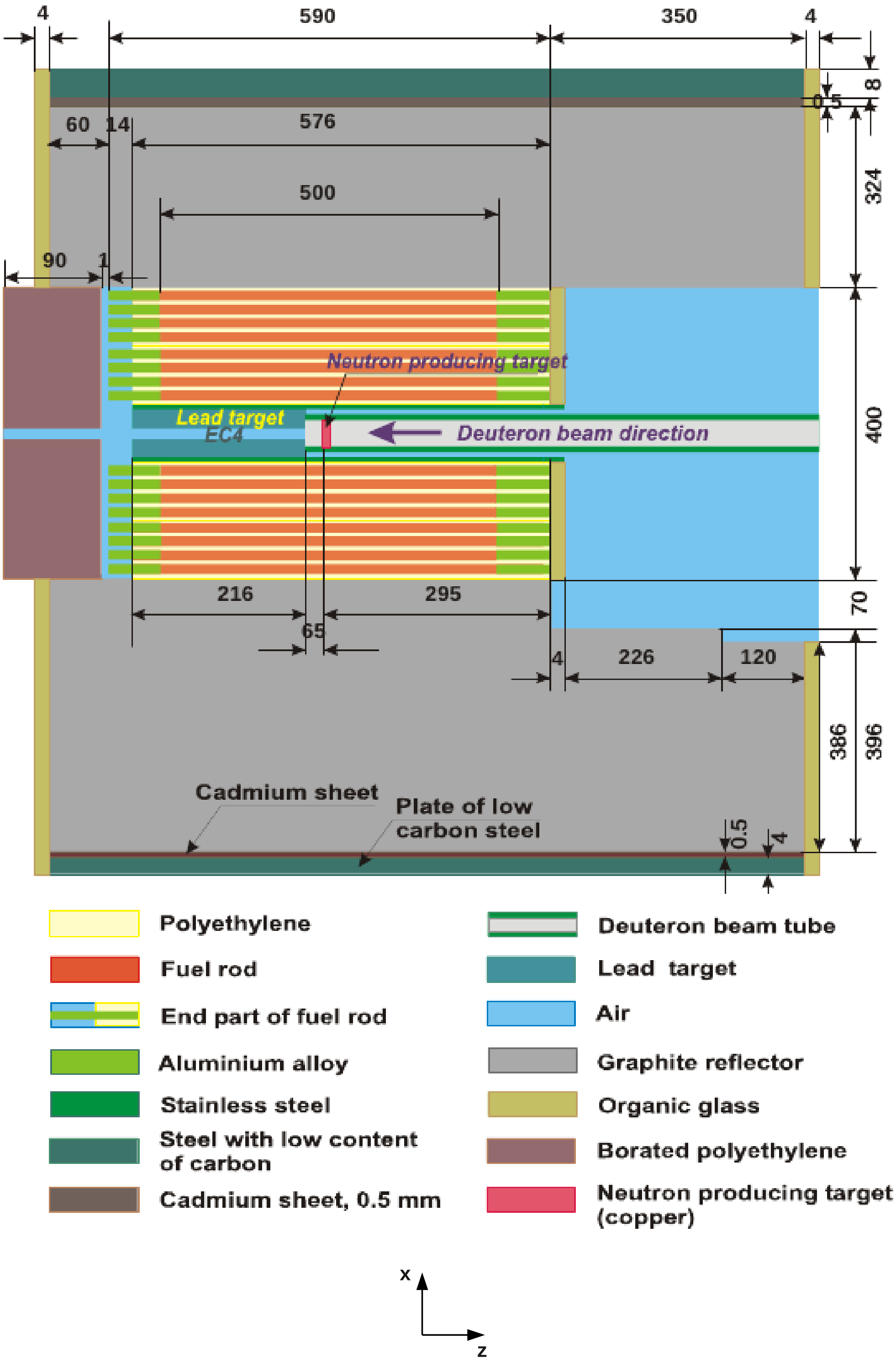

Figure A.2: View along the x - z axis through the YALINA-Thermal reactor taken from benchmark definition [42]

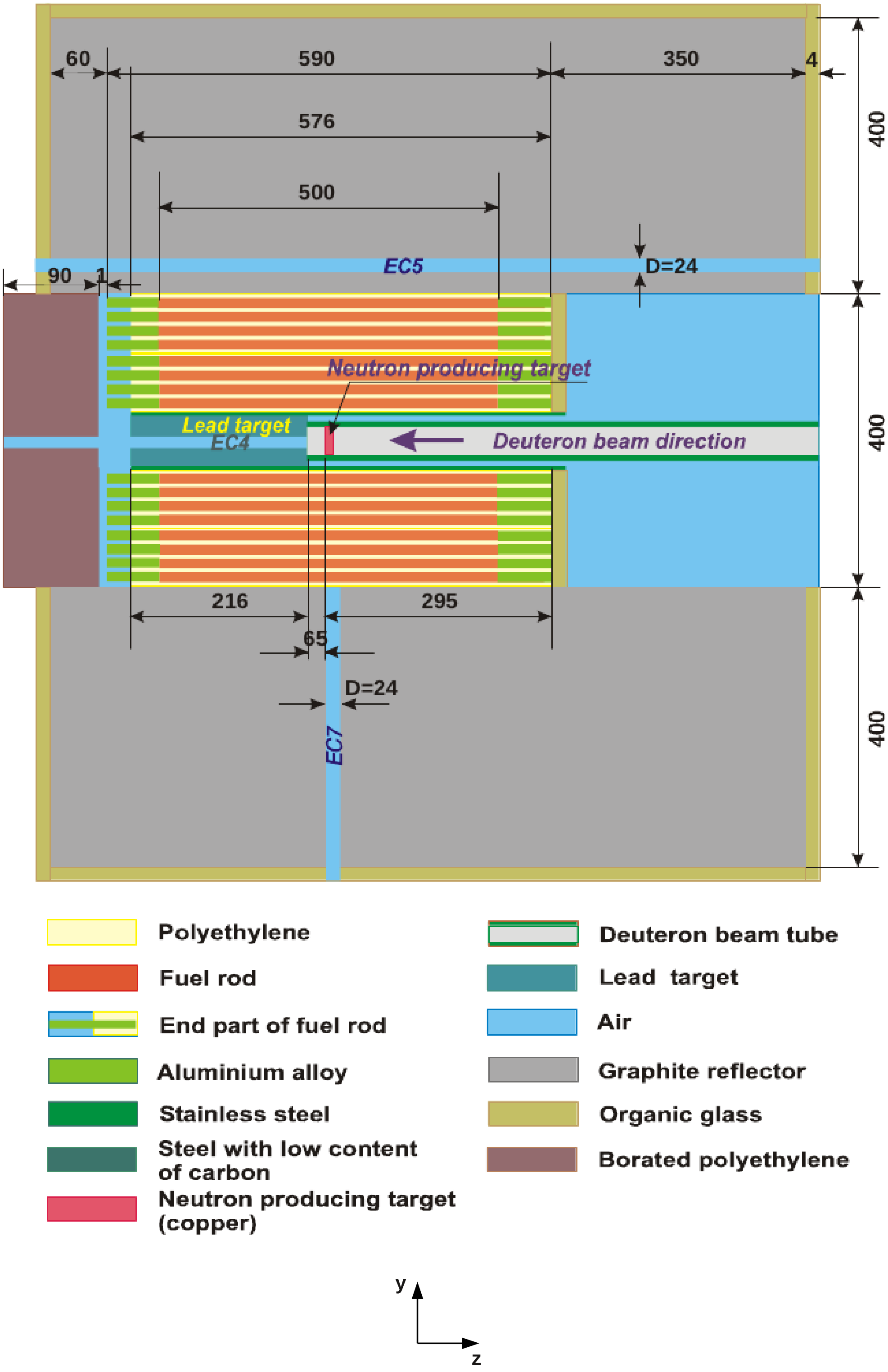

Figure A.3: View along the y - z axis through the YALINA-Thermal reactor taken from benchmark definition [42]

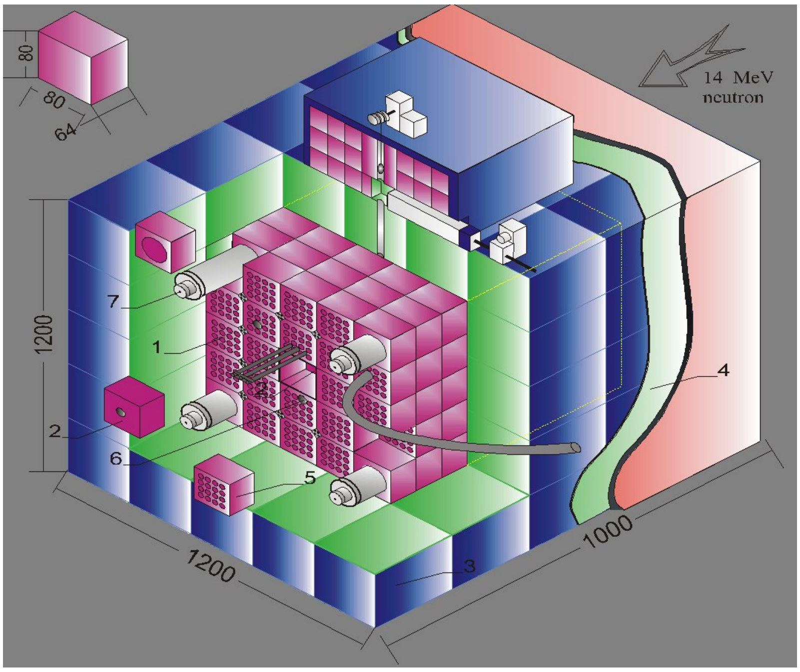

1 Core
2 Pb target
3 Graphite reflector
4 Cadmium screen
5 Polyethylene block
6 Experimental channel
7 Neutron flux monitoring

Figure A.4: Schematic view of the YALINA-Thermal reactor

clad of 1.5 mm thickness followed by a small air gap of 0.5 mm thickness. The rods have a total length of 590 mm where the 90 mm not belonging to the active height correspond to the massive aluminum ending caps of the fuel rods. The moderator material which acts simultaneously as main structure material in the core is Polyethylene (PE).

Four flux measurement channels (MC1-MC4) are located at each corner of the core. These are not used during the experiments, but have only to be considered geometrically in the simulation. In total seven Experimental Channels (ECs) are placed in the reactor, four of them axially in the core (EC1-EC4), two axially in the reflector (EC5, EC6) and one (EC7) located at the axial position of the beam target starting at the right border of the core (*see* fig. A.1).

A.2 Neutron Source

The YALINA-Thermal benchmark specification includes three different neutron sources, namely $^{252}_{98}$Cf, (d,d) and (d,t) sources. The first one makes use of the spontaneous fission that appears with 3.092 % in competition to the α-decay as disintegration reaction [139]. With the californium source applied, the experimental setup does not involve the stainless steel beam tube visible in fig. A.2 and A.3. The two latter neutron sources are conventional fusion neutron sources. In case of the (d,d) neutron source two deuterium nuclei fusion to an $^{3}_{2}$He atom emitting one neutron of 2.5 MeV. The (d,t) neutron sources let one deuterium nucleus and one tritium nucleus fusion to an $^{4}_{2}$He atom emitting one neutron of 14.1 MeV. For the experiments only the (d,d) neutron source has been available and thus the main

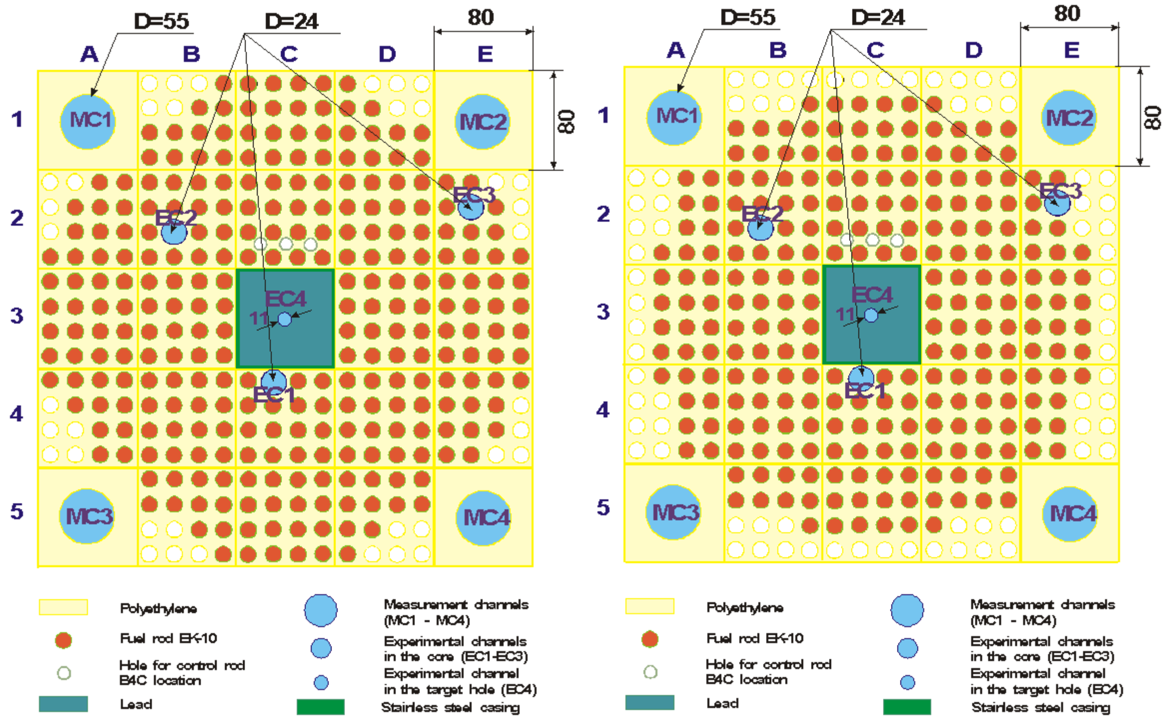

(a) 280 fuel rods

(b) 245 fuel rods

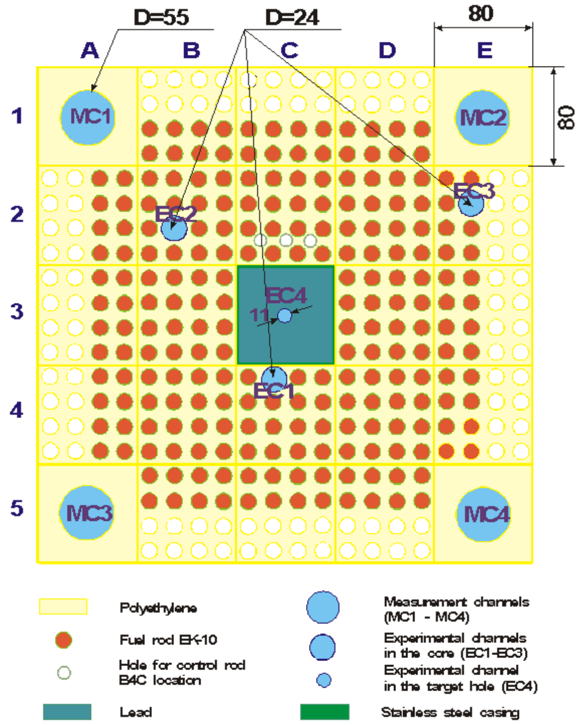

(c) 221 fuel rods

Figure A.5: Three configurations of YALINA-Thermal taken from benchmark definition [42] focus of the work is related to this neutron source. The geometry of the beam tube is shown in fig. A.8.

A.3 Geometrical Simplifications for Deterministic Calculations

A.3.1 Unit Cell

The core contains at maximum 280 fuel pins (fig. A.5a) which can be classified as unit cell of the fuel assembly. The reactor is modeled on the pin level without a need for a lattice calculation of the FA. Fig. A.6a shows the real dimensions and fig. A.6b its Wigner-Seitz cell [1]. `KANEXT` has a three zone Wigner-Seitz representation for cell calculations. Because of the small total cross section of air, the air region is included in the extended clad zone. The density of the clad material aluminum is reduced accordingly by 29.17 %.

In case of the empty rod positions in the outer FA rings, PE is smeared over the cell and the density is reduced by 30.25 %.

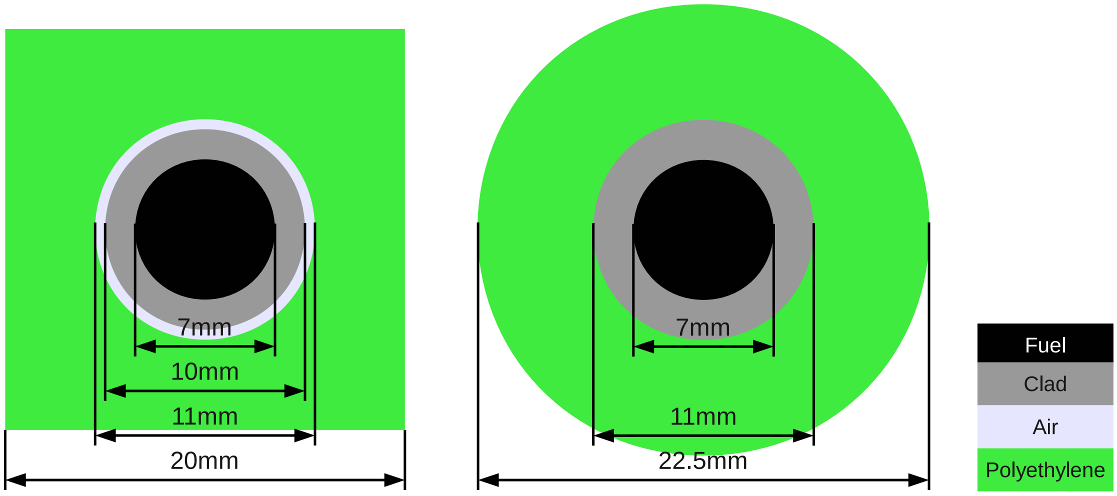

(a) Original geometry

(b) Wigner-Seitz cell

Figure A.6: Unit cell geometry

A.3.2 Flux Measurement Channels

The flux measurement channels MC1 - MC4 are cylindrical holes of 55 mm diameter surrounded by PE. The channels are not used for measurements, thus air is modeled inside. In total, they have the size of a subassembly and the axial length equals the length of the active core. In order to model this geometry in deterministic transport calculations it is divided into 16 parts by overlaying a grid with the characteristic length of the unit cell

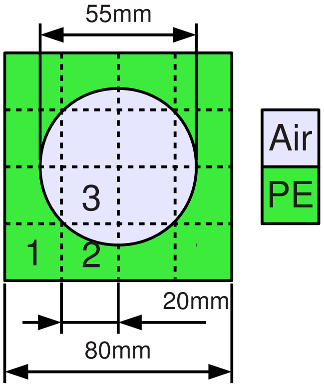

Material	Zone 1	Zone 2	Zone 3
Air [vol-%]	0.00	24.32	99.84
PE [vol-%]	100.00	75.68	0.16

Figure A.7: Simplified model of the flux measurement channels with overlayed dashed grid

(fig. A.7). From this treatment result three material zones from which one contains only PE, another almost only air and the last contains about 76 % PE.

A.3.3 Beam Tube and Target

The complex layout of the beam tube and the target is shown in fig. A.8. It consists of a tube of stainless steel with an integrated water cooling system for the target area, an inner vacuum region and an outer air environment. Since the geometry is modeled in Cartesian geometry, three approximations can be used to model this device. Either the materials are smeared over the subassembly region, or the cylinders are approximated with a stair case function, or - as done in this work - they are considered as quadratic cases with the same area. The first approximation is excluded as it does not account for the spatial self-shielding important for thermal systems. Test calculations show a difference in criticality of about 1000 pcm compared to detailed calculations. The stair case would enlarge the size of the model due to the necessity of additional geometric intervals.

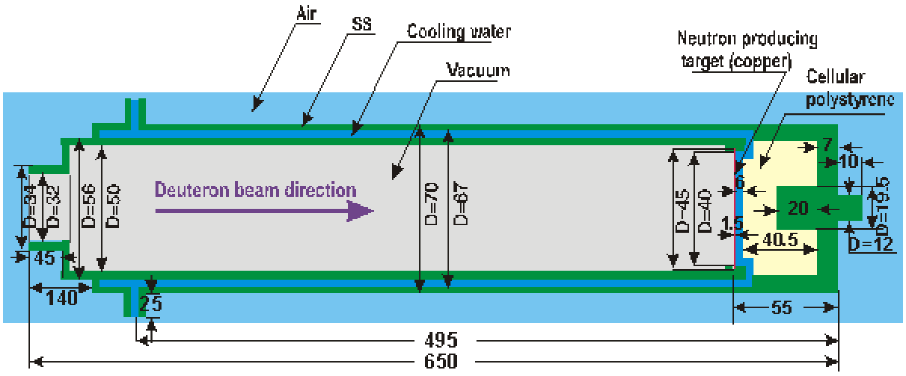

Figure A.8: Beam tube and target taken from benchmark definition [42]

The figures A.10 and A.12 illustrate the quadratic approximation of the cylindrical geometry. The side length of each square belonging to layer i is calculated with help of eq. (A.1).

$$\begin{aligned} a_1 &= \sqrt{\pi}\, r \\ a_i &= \sqrt{\pi\,(r_i^2 - r_{i-1}^2) + a_{i-1}^2} \quad \text{for} \quad i = 2, \dots, N \end{aligned} \tag{A.1}$$

A.3.4 Experimental Channels and Detector Responses

Two kinds of measurements have been performed in the YALINA-Thermal reactor. Static analysis of reaction rate traverses within the ECs and transient analysis of reaction rates during a neutron source pulse at a specified position. In the benchmark several activation materials are defined, whereas this work considers only the ${}^3_2$He(n,p) rate measured in the PNS experiments. The benchmark uses a unified approach to consider the disadvantage of the geometric representation in the deterministic calculation and to simplify the comparison with the MC generated results. In the static approach the required reaction rates in the ECs are calculated in a post-processing step by simply integrating the product of the neutron flux and the reaction cross section of the mesh cell without modeling the real geometry. For the simulation of pulses, the detector responses are calculated in the same manner without modeling the detector explicitly at the axial position of the neutron source. In the core calculation the zones contain simply air and have the size of a unit cell, except EC4 which is placed in a parallel epiped with a smaller side length 9.75 mm according to eq. (A.1). The length of the detector volumes along the z-axis is 25 cm with the center located at $z = 0$.

A.4 Material Regions and Associated Cross Section Sets

The material regions considered in the core simulation of the YALINA-Thermal reactor are listed in table A.1. With help of the description the link of the regions to the defined benchmark geometry of figures A.1, A.2 and A.9 is reproducible.

A.5 Spatial Discretization of the YALINA-Thermal Reactor

The final mesh layout is common to the simulations with the discrete ordinates transport codes `TORT`, `PARTISN` and `TORT-TD` in section 3.5 and throughout chapter 5. This mesh is used for the 280 fuel rods configuration as plotted here and for the 216 fuel rods configuration. The reactor is subdivided into $84 \times 83 \times 26$ mesh intervals in the x-, y-, z-direction, respectively. The core region and several cm of the surrounding reflector use a fine mesh with a radial mesh interval smaller than or equal to 2 cm; all other mesh intervals are not larger than 5 cm.

Table A.1: Correspondence of cross section region numbers and their description

Region	Description
1	organic glass
2	borated polyethylene
3	EC4 (air)
4	graphite reflector
5	air
6	begin of aluminum clad
7	MC: polyethylene (*see* section A.3.2)
8	MC: mixed polyethylene and air
9	unit cell without fuel rod
10	aluminum clad with polyethylene and some air
11	MC: air
12	stainless steel casing of FA
13	lead buffer
14	unit cell with fuel rod
15	coolant water of beam tube
16	copper target
17	end of aluminum clad with polyethylene and air

The geometry and material data sets are stored in an interface file of the SILO software package [140]. The software interface is implemented in the `TORT-TD` subroutine *getpwr*. The open-source visualization and graphical analysis tool VisIt [141] can read the SILO files and organize the overlay of the mesh over the material regions.

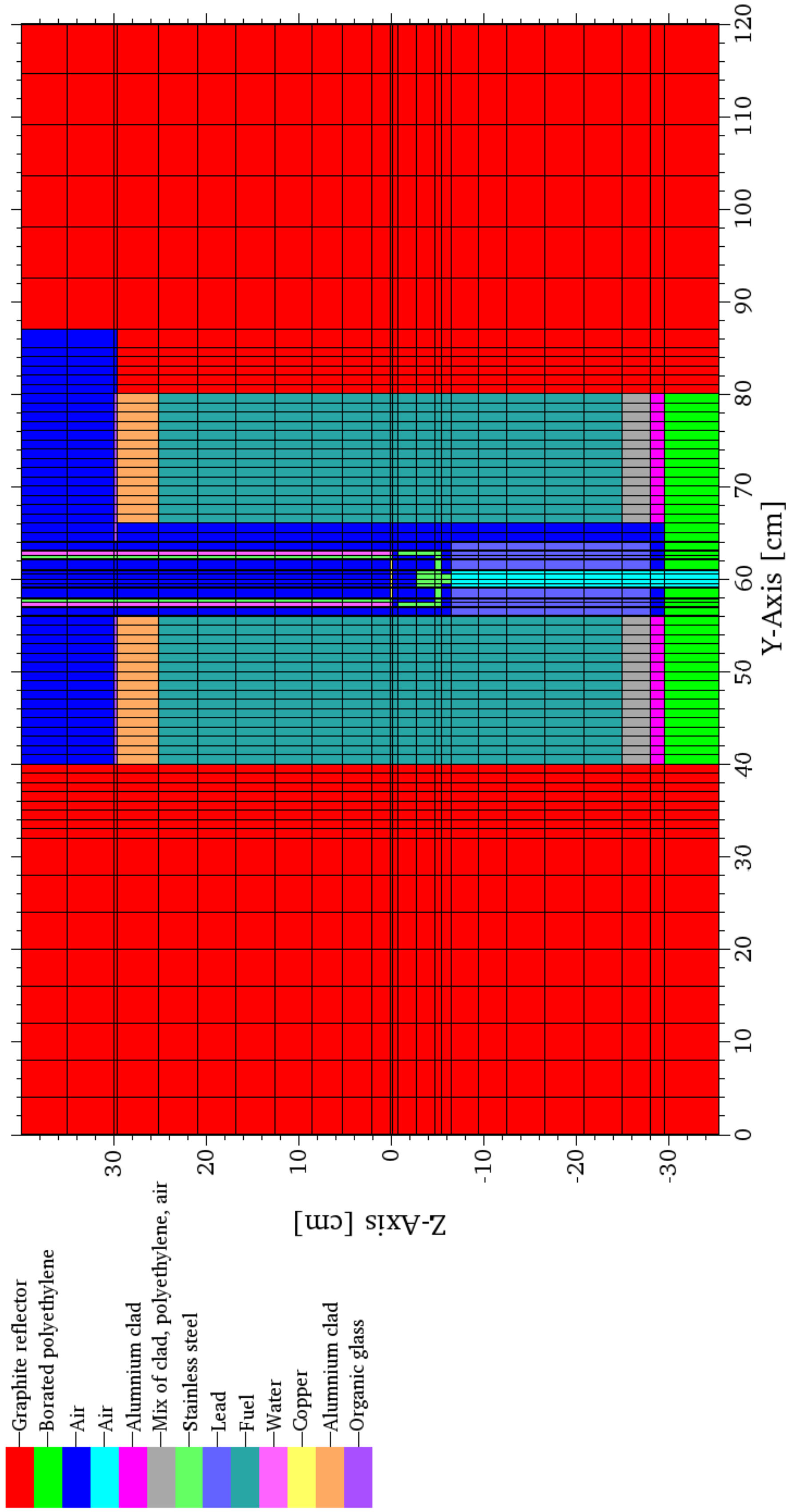

Figure A.9: y-z cross sectional view through the YALINA-Thermal model

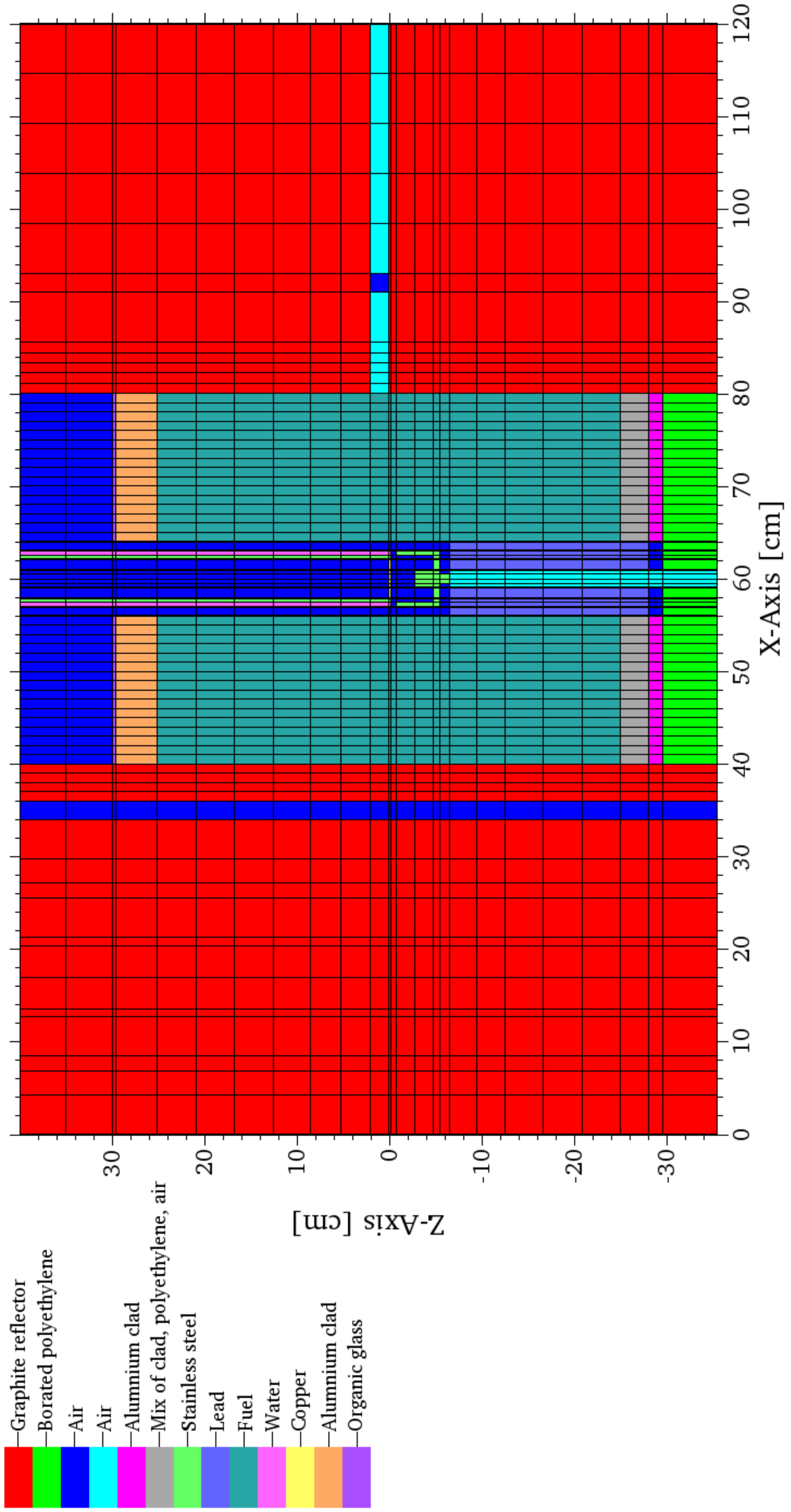

Figure A.10: x-z cross sectional view through the YALINA-Thermal model

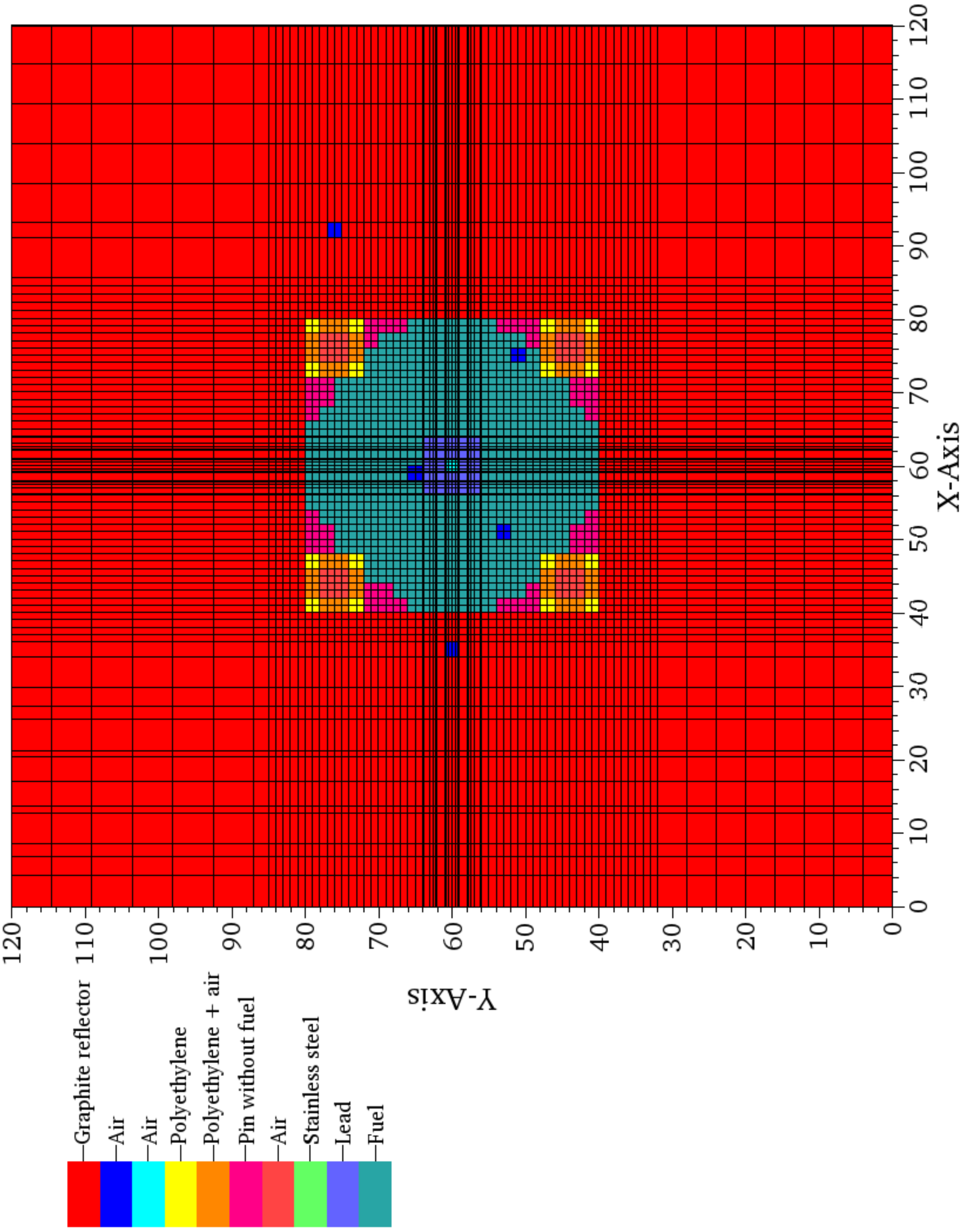

Figure A.11: x-y cross sectional view through the YALINA-Thermal model at $z = -10\,\mathrm{cm}$

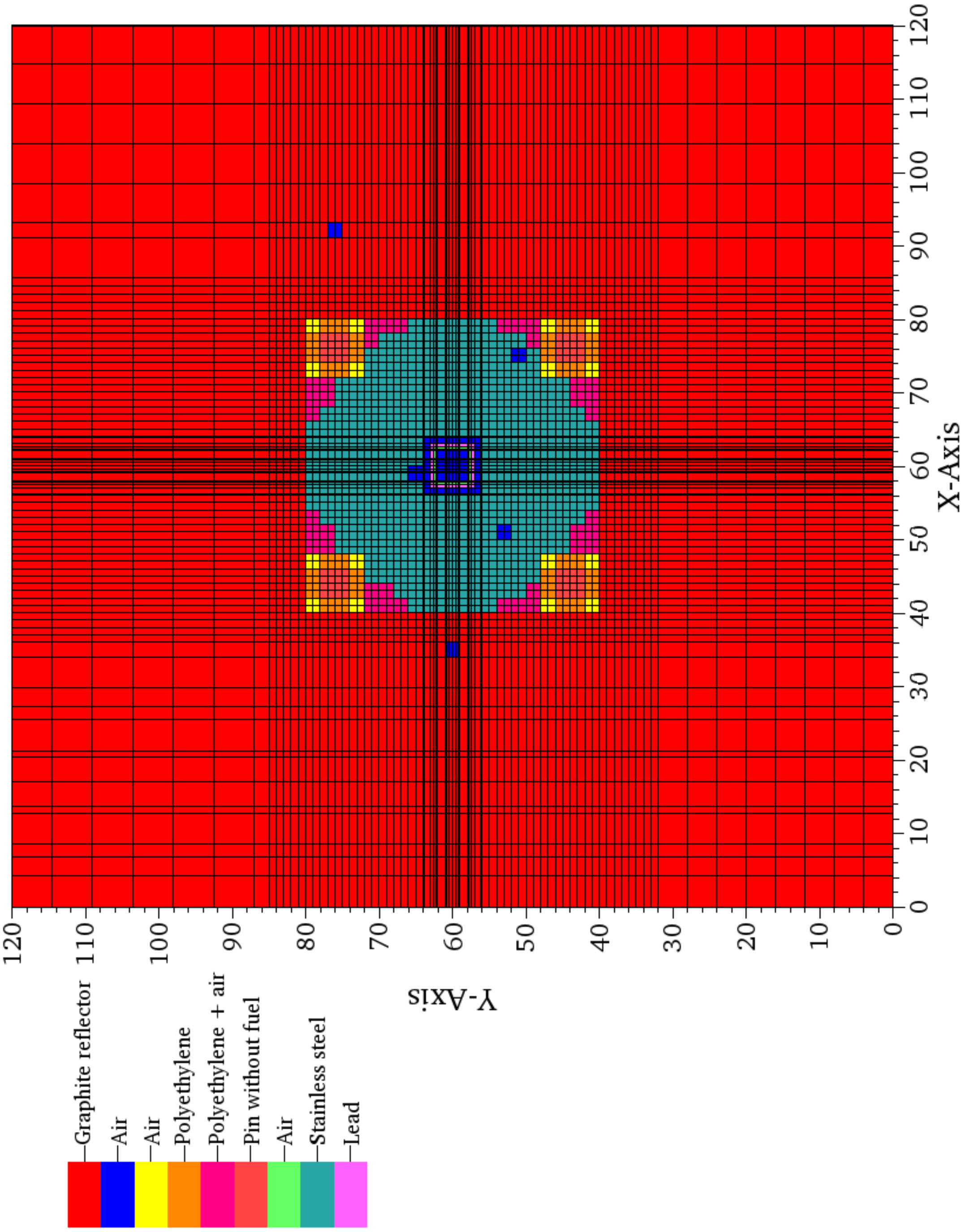

Figure A.12: x-y cross sectional view through the YALINA-Thermal model at $z = 10\,\mathrm{cm}$

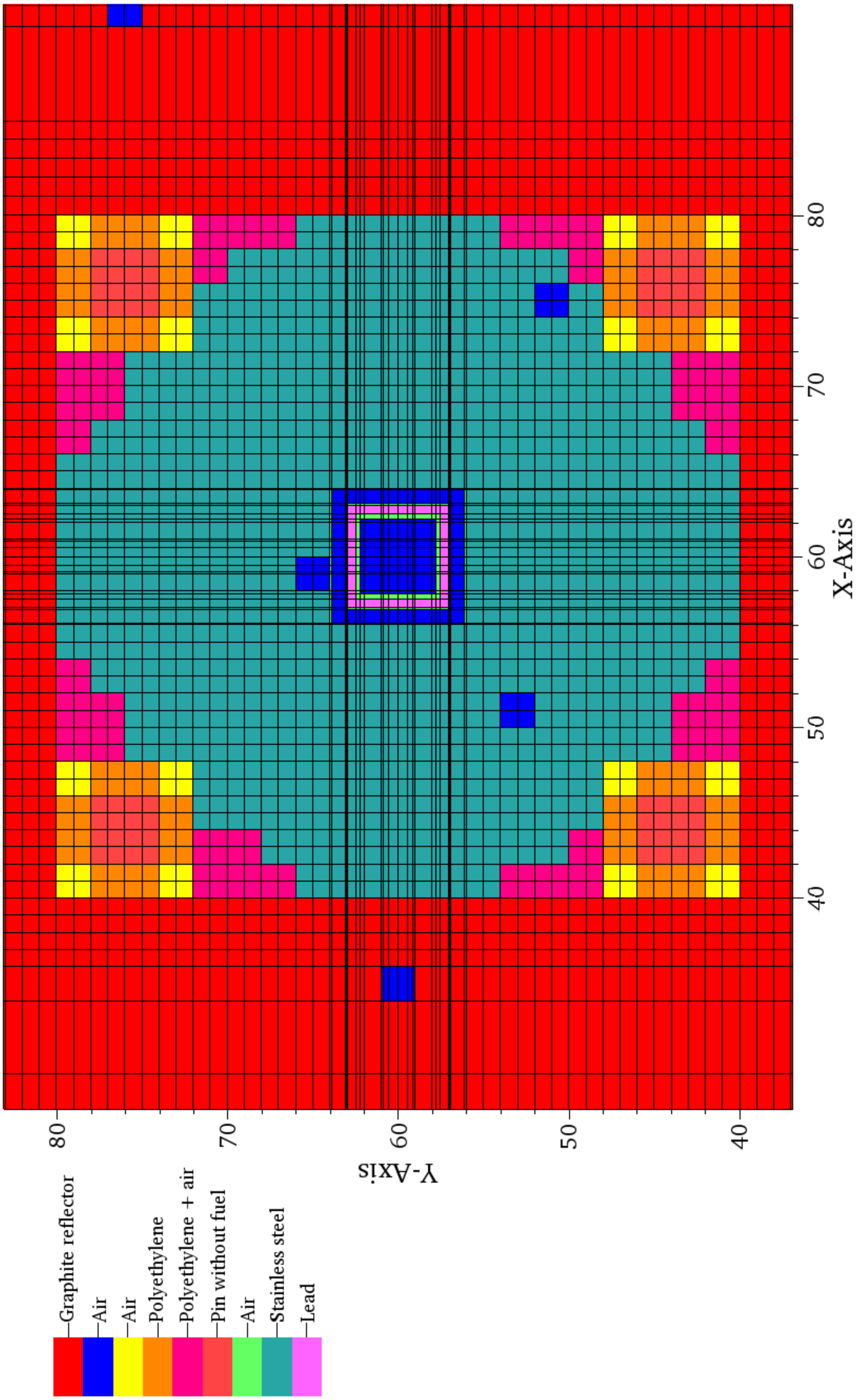

Figure A.13: x-y cross sectional view through the YALINA-Thermal model zoomed to the core region at $z = 10\,\mathrm{cm}$

Appendix B

Reactor Physics Code System **KANEXT**

B.1 Group Structures

B.1.1 69 Energy Groups - the Modified `WIMS` Structure

The listed group structure corresponds to the original `WIMS` [72] structure except for the first upper energy boundary, which is set to the usual maximum of 20 MeV.

Table B.1: The extended `WIMS` 69 energy group structure

Group	E_{max}	ΔE	Δu	Group	E_{max}	ΔE	Δu
		MeV		28	4.000	0.700	0.19237
				29	3.300	0.700	0.23841
1	20.0	13.935	1.19312	30	2.600	0.500	0.21357
2	6.0655	2.3865	0.49998	31	2.100	0.600	0.33647
3	3.679	1.448	0.50019	32	1.500	0.200	0.14310
4	2.231	0.878	0.50013	33	1.300	0.150	0.12260
5	1.353	0.532	0.49956	34	1.150	0.027	0.02376
6	0.821	0.321	0.49592	35	1.123	0.026	0.02342
7	0.50	0.1975	0.50253	36	1.097	0.026	0.02399
8	0.3025	0.1195	0.50260	37	1.071	0.026	0.02458
9	0.183	0.072	0.49996	38	1.045	0.025	0.02421
10	0.111	0.04366	0.49978	39	1.020	0.024	0.02381
11	0.06734	0.02649	0.49985	40	0.996	0.024	0.02439
12	0.04085	0.01607	0.49987	41	0.972	0.022	0.02289
13	0.02478	0.00975	0.49999	42	0.950	0.040	0.04302
14	0.01503	0.005912	0.49980	43	0.910	0.060	0.06821
		eV		44	0.850	0.070	0.08594
				45	0.780	0.155	0.22154
15	9118.0	3588.0	0.50006	46	0.625	0.125	0.22314
16	5530.0	2010.9	0.45198	47	0.500	0.100	0.22314
17	3519.1	1279.65	0.45195	48	0.400	0.050	0.13353
18	2239.5	814.35	0.45201	49	0.350	0.030	0.08961
19	1425.1	518.202	0.45197	50	0.320	0.020	0.06454
20	906.90	539.636	0.90396	51	0.300	0.020	0.06899
21	367.26	218.534	0.90394	52	0.280	0.030	0.11333
22	148.73	73.227	0.67798	53	0.250	0.030	0.12783
23	75.501	27.449	0.45187	54	0.220	0.040	0.20067
24	48.052	20.352	0.55085	55	0.180	0.040	0.25131
25	27.7	11.732	0.55085	56	0.140	0.040	0.33647
26	15.968	6.091	0.48038	57	0.100	0.020	0.22314
27	9.877	5.877	0.90391	58	0.080	0.013	0.17733
				59	0.067	0.009	0.14425
				60	0.058	0.008	0.14842
				61	0.050	0.008	0.17435
				62	0.042	0.007	0.18232
				63	0.035	0.005	0.15415
				64	0.030	0.005	0.18232
				65	0.025	0.005	0.22314
				66	0.020	0.005	0.28768
				67	0.015	0.005	0.40547
				68	0.010	0.005	0.69315
				69	0.005	0.004	1.60944
					0.001		

B.1.2 350 Energy Groups - the New `KANEXT` Structure

The new `KANEXT` group structure is composed of

- the `VITAMIN-J` [74] structure for the first 16 energy groups from 10 MeV to 19.64 MeV
- a constant lethargy width of $\Delta u = 0.05$ between 4 eV and 10 MeV yielding 292 further groups [73]
- the thermal energy groups of the `WIMS` [72] structure adding another 42 groups from 0.001 eV to 4 eV

Table B.2: The new 350 energy groups `KANEXT` structure (part 1)

Group	E_{max}	ΔE	Δu	Group	E_{max}	ΔE	Δu
	MeV			47	2.01864	0.098	0.05001
				48	1.92017	0.094	0.05001
1	19.640	2.307	0.12496	49	1.82650	0.089	0.05001
2	17.3330	0.428	0.02500	50	1.73740	0.085	0.05002
3	16.9050	0.418	0.02504	51	1.65264	0.081	0.05001
4	16.4870	0.804	0.05000	52	1.57202	0.077	0.05001
5	15.6830	0.765	0.05001	53	1.49533	0.073	0.05001
6	14.9180	0.368	0.02498	54	1.42239	0.069	0.05001
7	14.5500	0.359	0.02498	55	1.35300	0.073	0.05550
8	14.1910	0.351	0.02505	56	1.27995	0.069	0.05551
9	13.8400	0.341	0.02495	57	1.21084	0.065	0.05551
10	13.4990	0.659	0.05005	58	1.14546	0.062	0.05551
11	12.8400	0.317	0.02500	59	1.08361	0.059	0.05551
12	12.5230	0.309	0.02498	60	1.02510	0.0553	0.05550
13	12.2140	0.596	0.05003	61	0.96975	0.0524	0.05551
14	11.6180	0.566	0.04994	62	0.91739	0.0495	0.05551
15	11.0520	0.539	0.05000	63	0.86786	0.0469	0.05551
16	10.5130	0.513	0.05003	64	0.82100	0.0440	0.05510
17	10.0000	0.5404	0.05555	65	0.77699	0.0417	0.05510
18	9.45963	0.5112	0.05555	66	0.73533	0.0394	0.05510
19	8.94846	0.4836	0.05555	67	0.69591	0.0373	0.05510
20	8.46491	0.4574	0.05555	68	0.65860	0.0353	0.05510
21	8.00749	0.4327	0.05555	69	0.62329	0.0334	0.05510
22	7.57479	0.4093	0.05555	70	0.58988	0.0316	0.05510
23	7.16547	0.3872	0.05555	71	0.55825	0.0299	0.05510
24	6.77826	0.3663	0.05555	72	0.52833	0.0283	0.05510
25	6.41199	0.3465	0.05555	73	0.50000	0.0245	0.05025
26	6.06550	0.3278	0.05555	74	0.47550	0.0233	0.05025
27	5.73773	0.3101	0.05555	75	0.45219	0.0222	0.05025
28	5.42768	0.2933	0.05555	76	0.43003	0.0211	0.05025
29	5.13438	0.2775	0.05555	77	0.40895	0.0200	0.05025
30	4.85693	0.2625	0.05555	78	0.38891	0.0191	0.05025
31	4.59447	0.2483	0.05555	79	0.36985	0.0181	0.05025
32	4.34619	0.2349	0.05555	80	0.35172	0.0172	0.05025
33	4.11133	0.2222	0.05555	81	0.33448	0.0164	0.05026
34	3.88916	0.2102	0.05555	82	0.31809	0.0156	0.05025
35	3.67900	0.1795	0.05002	83	0.30250	0.0148	0.05026
36	3.49951	0.1707	0.05002	84	0.28767	0.0141	0.05026
37	3.32877	0.1624	0.05002	85	0.27357	0.0134	0.05026
38	3.16636	0.1545	0.05002	86	0.26016	0.0128	0.05026
39	3.01188	0.1469	0.05002	87	0.24741	0.0121	0.05026
40	2.86494	0.1398	0.05002	88	0.23528	0.0115	0.05026
41	2.72516	0.1330	0.05002	89	0.22375	0.0110	0.05026
42	2.59220	0.1265	0.05002	90	0.21278	0.0104	0.05026
43	2.46573	0.1203	0.05002	91	0.20235	0.0099	0.05026
44	2.34543	0.1144	0.05002	92	0.19243	0.0094	0.05026
45	2.23100	0.1088	0.05001	93	0.18300	0.0099	0.05555
46	2.12217	0.1035	0.05002	94	0.17311	0.0094	0.05555

Table B.3: The new 350 energy groups KANEXT structure (part 2)

Group	E_{max}	ΔE	Δu	Group	E_{max}	ΔE	Δu
	MeV			141	0.012 723 5	0.000 687 3	0.055 53
				142	0.012 036 2	0.000 650 2	0.055 53
95	0.163 757 0	0.008 849 0	0.055 55	143	0.011 386 0	0.000 615 1	0.055 54
96	0.154 908 0	0.008 370 0	0.055 55	144	0.010 770 9	0.000 581 8	0.055 53
97	0.146 538 0	0.007 918 0	0.055 55	145	0.010 189 1	0.000 550 4	0.055 53
98	0.138 620 0	0.007 491 0	0.055 56		eV		
99	0.131 129 0	0.007 086 0	0.055 55				
100	0.124 043 0	0.006 702 0	0.055 54	146	9638.69	520.69	0.050 01
101	0.117 341 0	0.006 341 0	0.055 55	147	9118.00	444.74	0.050 01
102	0.111 000 0	0.005 996 0	0.055 53	148	8673.26	423.05	0.050 01
103	0.105 004 0	0.005 671 9	0.055 53	149	8250.21	402.41	0.050 01
104	0.099 332 1	0.005 365 5	0.055 53	150	7847.80	382.80	0.050 01
105	0.093 966 6	0.005 075 8	0.055 53	151	7465.00	364.11	0.050 01
106	0.088 890 8	0.004 801 6	0.055 53	152	7100.89	346.35	0.050 01
107	0.084 089 2	0.004 542 3	0.055 53	153	6754.54	329.47	0.050 01
108	0.079 546 9	0.004 296 8	0.055 53	154	6425.07	313.39	0.050 01
109	0.075 250 1	0.004 064 9	0.055 53	155	6111.68	298.11	0.050 22
110	0.071 185 2	0.003 845 2	0.055 53	156	5813.57	283.57	0.050 22
111	0.067 340 0	0.003 637 9	0.055 54	157	5530.00	270.86	0.050 22
112	0.063 702 1	0.003 441 5	0.055 54	158	5259.14	257.59	0.050 22
113	0.060 260 6	0.003 255 6	0.055 54	159	5001.55	244.98	0.050 22
114	0.057 005 0	0.003 079 6	0.055 54	160	4756.57	232.97	0.050 22
115	0.053 925 4	0.002 913 4	0.055 54	161	4523.60	221.57	0.050 22
116	0.051 012 0	0.002 755 8	0.055 54	162	4302.03	210.71	0.050 22
117	0.048 256 2	0.002 607 1	0.055 54	163	4091.32	200.39	0.050 22
118	0.045 649 1	0.002 466 1	0.055 54	164	3890.93	190.58	0.050 22
119	0.043 183 0	0.002 333 0	0.055 54	165	3700.35	181.25	0.050 22
120	0.040 850 0	0.002 207 0	0.055 54	166	3519.10	172.36	0.050 22
121	0.038 643 0	0.002 087 8	0.055 54	167	3346.74	163.92	0.050 22
122	0.036 555 2	0.001 974 9	0.055 54	168	3182.82	155.89	0.050 22
123	0.034 580 3	0.001 868 3	0.055 54	169	3026.93	148.26	0.050 22
124	0.032 712 0	0.001 767 3	0.055 54	170	2878.67	141.00	0.050 22
125	0.030 944 7	0.001 671 9	0.055 54	171	2737.67	134.09	0.050 22
126	0.029 272 8	0.001 581 5	0.055 54	172	2603.58	127.52	0.050 22
127	0.027 691 3	0.001 496 1	0.055 54	173	2476.06	121.27	0.050 22
128	0.026 195 2	0.001 415 2	0.055 54	174	2354.79	115.34	0.050 22
129	0.024 780 0	0.001 339 1	0.055 56	175	2239.45	109.69	0.050 22
130	0.023 440 9	0.001 266 7	0.055 55	176	2129.76	104.31	0.050 22
131	0.022 174 2	0.001 198 3	0.055 56	177	2025.45	99.21	0.050 22
132	0.020 975 9	0.001 133 5	0.055 55	178	1926.24	94.35	0.050 22
133	0.019 842 4	0.001 072 3	0.055 56	179	1831.89	89.73	0.050 22
134	0.018 770 1	0.001 014 3	0.055 55	180	1742.16	85.33	0.050 22
135	0.017 755 8	0.000 959 5	0.055 55	181	1656.83	81.15	0.050 22
136	0.016 796 3	0.000 907 7	0.055 56	182	1575.68	77.18	0.050 22
137	0.015 888 6	0.000 858 6	0.055 55	183	1498.50	73.40	0.050 22
138	0.015 030 0	0.000 811 9	0.055 53	184	1425.10	69.80	0.050 22
139	0.014 218 1	0.000 768 1	0.055 54	185	1355.30	66.38	0.050 22
140	0.013 450 0	0.000 726 5	0.055 53	186	1288.92	63.13	0.050 21

Table B.4: The new 350 energy groups `KANEXT` structure (part 3)

Group	E_{max}	ΔE	Δu	Group	E_{max}	ΔE	Δu
	eV			228	156.388	7.660	0.050 22
				229	148.728	7.557	0.052 15
187	1225.79	60.04	0.050 22	230	141.171	7.174	0.052 16
188	1165.75	57.09	0.050 21	231	133.997	6.809	0.052 15
189	1108.66	54.30	0.050 22	232	127.188	6.463	0.052 15
190	1054.36	51.64	0.050 22	233	120.725	6.135	0.052 16
191	1002.72	49.116	0.050 22	234	114.590	5.823	0.052 15
192	953.604	46.707	0.050 22	235	108.767	5.527	0.052 15
193	906.897	44.419	0.050 22	236	103.240	5.246	0.052 15
194	862.478	42.244	0.050 22	237	97.9942	4.9796	0.052 15
195	820.234	40.174	0.050 22	238	93.0146	4.7264	0.052 15
196	780.060	38.207	0.050 22	239	88.2882	4.4864	0.052 15
197	741.853	36.336	0.050 22	240	83.8018	4.2584	0.052 15
198	705.517	34.555	0.050 22	241	79.5434	4.0420	0.052 15
199	670.962	32.864	0.050 22	242	75.5014	3.6971	0.050 21
200	638.098	31.254	0.050 22	243	71.8043	3.5161	0.050 21
201	606.844	29.722	0.050 22	244	68.2882	3.3440	0.050 21
202	577.122	28.268	0.050 22	245	64.9442	3.1802	0.050 21
203	548.854	26.883	0.050 22	246	61.7640	3.0244	0.050 21
204	521.971	25.565	0.050 22	247	58.7396	2.8764	0.050 21
205	496.406	24.314	0.050 22	248	55.8632	2.7354	0.050 21
206	472.092	23.122	0.050 22	249	53.1278	2.6016	0.050 21
207	448.970	21.991	0.050 22	250	50.5262	2.4742	0.050 21
208	426.979	20.913	0.050 22	251	48.0520	2.3470	0.050 08
209	406.066	19.889	0.050 22	252	45.7050	2.2324	0.050 08
210	386.177	18.915	0.050 22	253	43.4726	2.1234	0.050 08
211	367.262	17.988	0.050 22	254	41.3492	2.0197	0.050 08
212	349.274	17.107	0.050 22	255	39.3295	1.9210	0.050 08
213	332.167	16.270	0.050 22	256	37.4085	1.8272	0.050 08
214	315.897	15.472	0.050 22	257	35.5813	1.7379	0.050 08
215	300.425	14.715	0.050 22	258	33.8434	1.6531	0.050 08
216	285.710	13.994	0.050 22	259	32.1903	1.5723	0.050 08
217	271.716	13.308	0.050 22	260	30.6180	1.4955	0.050 08
218	258.408	12.657	0.050 22	261	29.1225	1.4225	0.050 08
219	245.751	12.037	0.050 22	262	27.7000	1.3530	0.050 08
220	233.714	11.447	0.050 22	263	26.3470	1.2868	0.050 07
221	222.267	10.887	0.050 22	264	25.0602	1.2241	0.050 08
222	211.380	10.353	0.050 22	265	23.8361	1.1642	0.050 08
223	201.027	9.846	0.050 22	266	22.6719	1.1074	0.050 08
224	191.181	9.364	0.050 22	267	21.5645	1.0533	0.050 08
225	181.817	8.906	0.050 22	268	20.5112	1.0018	0.050 08
226	172.911	8.469	0.050 22	269	19.5094	0.9529	0.050 08
227	164.442	8.054	0.050 22	270	18.5565	0.9064	0.050 08

Table B.5: The new 350 energy groups KANEXT structure (part 4)

Group	E_{max}	ΔE	Δu	Group	E_{max}	ΔE	Δu
		eV		312	2.100	0.600	0.336 47
				313	1.500	0.200	0.143 10
271	17.6501	0.8621	0.050 08	314	1.300	0.150	0.122 60
272	16.7880	0.8200	0.050 08	315	1.150	0.027	0.023 76
273	15.9680	0.8299	0.053 37	316	1.123	0.026	0.023 42
274	15.1381	0.7869	0.053 38	317	1.097	0.026	0.023 99
275	14.3512	0.7459	0.053 37	318	1.071	0.026	0.024 58
276	13.6053	0.7071	0.053 37	319	1.045	0.025	0.024 21
277	12.8982	0.6704	0.053 38	320	1.020	0.024	0.023 81
278	12.2278	0.6356	0.053 38	321	0.996	0.024	0.024 39
279	11.5922	0.6025	0.053 37	322	0.972	0.022	0.022 89
280	10.9897	0.5712	0.053 38	323	0.950	0.040	0.043 02
281	10.4185	0.5415	0.053 37	324	0.910	0.060	0.068 21
282	9.8770	0.4837	0.050 22	325	0.850	0.070	0.085 94
283	9.393 26	0.460 06	0.050 22	326	0.780	0.155	0.221 54
284	8.933 20	0.437 53	0.050 22	327	0.625	0.125	0.223 14
285	8.495 67	0.416 09	0.050 22	328	0.500	0.100	0.223 14
286	8.079 58	0.200 34	0.025 11	329	0.400	0.050	0.133 53
287	7.879 24	0.195 38	0.025 11	330	0.350	0.030	0.089 61
288	7.683 86	0.190 53	0.025 11	331	0.320	0.020	0.064 54
289	7.493 33	0.185 80	0.025 11	332	0.300	0.020	0.068 99
290	7.307 53	0.181 20	0.025 11	333	0.280	0.030	0.113 33
291	7.126 33	0.176 71	0.025 11	334	0.250	0.030	0.127 83
292	6.949 62	0.172 32	0.025 11	335	0.220	0.040	0.200 67
293	6.777 30	0.168 05	0.025 11	336	0.180	0.040	0.251 31
294	6.609 25	0.163 88	0.025 11	337	0.140	0.040	0.336 47
295	6.445 37	0.159 83	0.025 11	338	0.100	0.020	0.223 14
296	6.285 54	0.155 85	0.025 11	339	0.080	0.013	0.177 33
297	6.129 69	0.152 00	0.025 11	340	0.067	0.009	0.144 25
298	5.977 69	0.148 22	0.025 11	341	0.058	0.008	0.148 42
299	5.829 47	0.144 55	0.025 11	342	0.050	0.008	0.174 35
300	5.684 92	0.140 96	0.025 11	343	0.042	0.007	0.182 32
301	5.543 96	0.137 47	0.025 11	344	0.035	0.005	0.154 15
302	5.406 49	0.134 06	0.025 11	345	0.030	0.005	0.182 32
303	5.272 43	0.130 74	0.025 11	346	0.025	0.005	0.223 14
304	5.141 69	0.251 82	0.050 22	347	0.020	0.005	0.287 68
305	4.889 87	0.239 50	0.050 22	348	0.015	0.005	0.405 47
306	4.650 37	0.227 76	0.050 22	349	0.010	0.005	0.693 15
307	4.422 61	0.216 61	0.050 22	350	0.005	0.004	1.609 44
308	4.206 00	0.206	0.050 22		0.001		
309	4.000 00	0.700	0.192 37				
310	3.300 00	0.700	0.238 41				
311	2.600 00	0.500	0.213 57				

B.2 KANEXT Modules

B.2.1 SCAPLO

The module `SCAPLO` is newly created to investigate the differential scattering properties of the multigroup scattering cross sections as generated by standard processing codes like `NJOY` [23]. Scattering can thereby be any scattering(-like) reaction e.g. elastic, inelastic, $(\mathrm{n}, x\mathrm{n})$, whose secondary angular distribution is approximated by means of the Legendre expansion. The angular group-to-group scattering distribution is written into a file immediately readable by the Grace plotting tool [142].

`SCAPLO` reads either the microscopic scattering cross section and its associated Legendre coefficients from the `GRUBA` [76] master library or the macroscopic scattering cross sections from the `SIGMN` [99, 100] data block. For the `GRUBA` reading the cross sections and distributions can be interpolated for the desired temperature in the same way as the group constant module `GRUCAL` [93] performs this task.

The angular distribution is reconstructed for the truncated Legendre order L with help of the common definition of the Legendre expansion of the scattering cross section [19, 128]. The Legendre scattering coefficient $\sigma_{lgg'}$ in eq. (B.1) is the product of the scalar scattering cross section and the Legendre coefficient for the secondary out-scatter energy group $f_{lgg'}$. The latter is normalized to unity and given temperature-dependent e.g. for scattering with chemical binding effects. The angular secondary neutron distribution is calculated as a function of the scattering cosine $\mu = \cos\theta$ with θ the polar scattering angle ((B.2) and (B.3)). The reconstruction is carried out on a fine scattering cosine grid with $\Delta\mu = 0.01$ in the usual $[-1, 1]$ interval, which denotes the polar angle range from backward to forward peaked scattering.

$$\sigma_{lgg'} = \sigma_g \, f_{lgg'} \tag{B.1}$$

$$\sigma_{gg'}(\mu) \approx \sum_{l=0}^{L} (2\,l+1)\,\sigma_{lgg'}\,P_l(\mu) \tag{B.2}$$

$$\sigma_g(\mu) \approx \sum_{l=0}^{L} (2\,l+1)\,P_l(\mu) \sum_{g'} \sigma_{lgg'} \tag{B.3}$$

B.2.2 KANISN

The standard `KANEXT` module `WEKCPM` [101] for thermal cell calculations originates from the British `WIMS` [72] code system and was introduced for Tight Lattice Light Water Reactor (TLLWR) investigations [73]. It is based on a one-dimensional first collision probability method with transport correction for the total cross section and isotropic scattering.

In view of a lacking transport method based cell module with anisotropic scattering the new module KANISN was implemented in the KANEXT code system. It can be called either as independent module or automatically in the cross section generation sequence KARBUS [92]. It stems from the well-known one-dimensional discrete ordinates transport code ANISN [143] given in the latest version of the DOORS [144] package. Most of the relevant functionality can be accessed by a KANEXT input data block.

In production runs a regular input file is automatically created including the cross sections in a scratch file. When running in debug mode, this input file is kept after the module run and can be directly used in subsequent stand-alone ANISN calculations. Since the quadrature sets are part of the input in DOORS codes, the arbitrary quadrature order generation subroutine *doq* of the SCALE6/XSDRN [107] code was added. The original ANISN code was slightly changed to generally use double precision variables and to store the neutron flux in the KANEXT specific data block.

For a code-to-code validation with other one-dimensional codes the pin cell of section 3.3 was subject to k_{inf} calculations with exactly the same cross sections as input (fig. B.1). The k_{inf} evaluations were rigorously performed for quadrature orders from 2 to 16 and for truncated Legendre orders from 0 to 5. Obviously, the combination of quadrature and Legendre order are sometimes invalid. A known rule tells, the higher the Legendre order, the higher must be the quadrature order to correctly integrate the Legendre functions [63]. Moreover, quadrature order lower than S_4 are typically not used and S_8 can be seen as a standard. So looking at quadrature order S_8, it is seen that the first Legendre order is required and higher orders do not contribute to the eigenvalue result.

B.2.3 GRUCAL

The module GRUCAL [93] provides effective multigroup cross sections in the KANEXT specific SIGMN data block [99]. It reads microscopic cross sections from the KANEXT master library, which is provided in the GRUBA [76] format. The concept for the flexible group constant generation is rather unique, since the cross section types are not hard-coded but can be freely defined in the so-called Formula Definition File (FDF). The definition comprises the part of the cross section to be read from the master library, the operation to be accomplished after reading, and the successive use of the obtained result in further definitions. Module GRUCAL knows about 50 implemented formulas e.g. basic arithmetic operations, interpolation, etc., which can be associated with the calculation of one cross section (part). An example is given later on. Thus, to make a KANEXT job reproducible, the FDF file name and version must be given in addition to the library name and version. In section B.2.3.1 the FDF FENDFJEFv2 is printed. It was written from scratch for this work, in order to consider the extended list of cross section types, which have been introduced during the development of the NJOYPROC B.2.3.2 code.

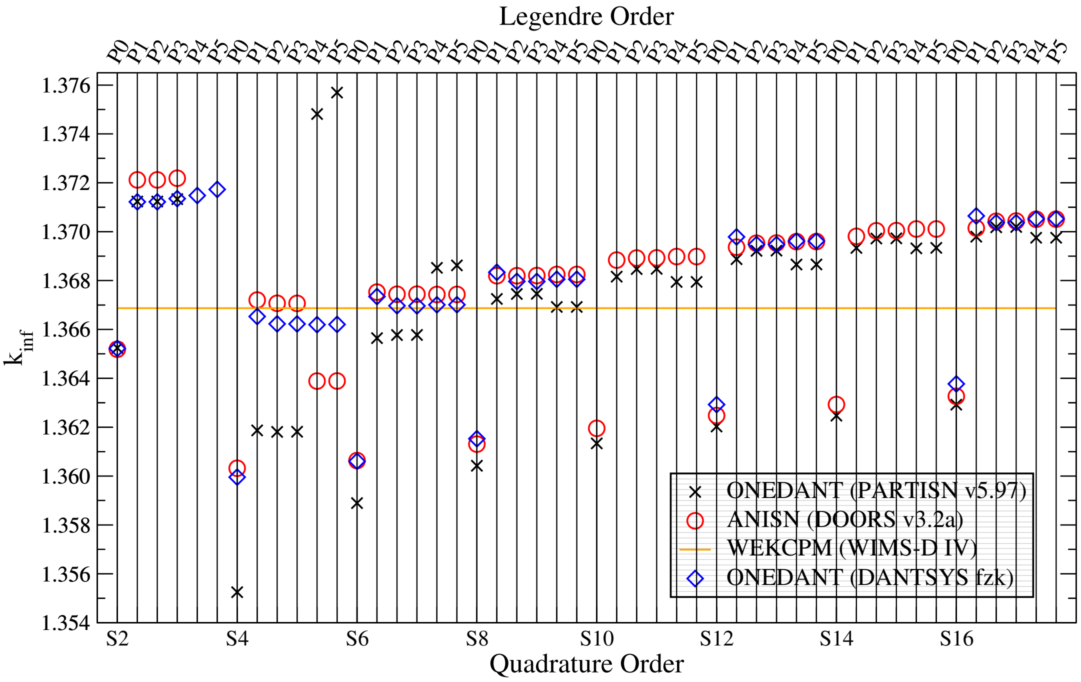

Figure B.1: Comparison of infinite multiplication constants achieved with four different one-dimensional neutron transport codes

B.2.3.1 The Formula Definition File

The German print-out of the current FENDFJEFv2 FDF file in figures B.2 to B.6 is produced by activating the `FORMELN` debug option of module `GRUCAL`. This FDF can be used with master libraries generated by the recent `NJOYPROC` code of version 19. Conditional statements have been introduced for cases, where libraries contain different data items e.g. 6 or 8 time groups of delayed neutrons in ENDF/B VII.0 or JEFF 3.1, respectively. The FDF definitions are generally independent of the energy group structure. In the print-out the meaning of the variables used are defined in the header. The cross section type specific list underneath contains the basic classification (scalar or vector type cross section), formula used, German description of the action, and origin and conditions of the data (read from library or use calculated value). A detailed description of the interpolation for self-shielding and temperature effects are given by Kiefhaber and Ott [145] and Broeders [73]. In this summary only the newly introduced formalisms and types are mentioned. The parentheses are such that "()" denotes the `ENDF-6` [75] MT reaction number and "[]" denotes the `KANEXT` literal cross section name as printed.

- The capture cross section σ_c [SCAPT] is the sum of the self-shielded $\sigma_{n,\gamma}$ (102) [SCPT1] cross section and the sum of the "disappearance" reaction $\sigma_{n,\alpha}$, $\sigma_{n,d}$, $\sigma_{n,t}$, ...(MF3MT{103,...,117}) [SDISA]
- Additional to the inelastic scattering cross section σ_i [SINSC], which is the sum

over all discrete levels and continuum reactions (MF3MT{51-91}), another bunch of combined inelastic and other particle emitting reaction is summed to the "quasi-inelastic" cross section (MF3MT{22,23,28,29,32-36,44,45}) [SQINL] and added to obtain the total inelastic cross section σ_{i} [SI]

- The $\sigma_{\mathrm{n,2n}}$ [SN2N], $\sigma_{\mathrm{n,3n}}$ [SN3N] are the sum of the pure reaction and all combined multiplying scatter-like reactions with other particle emitting reactions; $\sigma_{\mathrm{n,2n}}$ is the sum of (MF3MT{11,16,24,30,41}), $\sigma_{\mathrm{n,3n}}$ is the sum of (MF3MT{17,25,42}); $\sigma_{\mathrm{n,2n}}$ [SN2N], $\sigma_{\mathrm{n,3n}}$ [SN3N], $\sigma_{\mathrm{n,4n}}$ [SN4N] and $\sigma_{\mathrm{n},x\mathrm{n}}$ [SNXN] are summed to the intermediate cross section [SMULT]

- The total cross section [STOT] is calculated according to the definition in the FDF of the self-shielded reactions σ_{c} [SCAPT], σ_{f} [SFISS], σ_{e} [SE] and the σ_{i} [SI] and the multiplicity scattering-like reactions [SMULT]

- The available energy-angle transfer data of (MF{4,5,6}) is kept and summed to the total transfer matrix [SMTOT{0,. . . ,5}]; these are the matrices of σ_{e} [SME{0,. . . ,5}], σ_{i} [SMI{0,. . . ,5}] and [SMQI{0,. . . ,5}], the multiplicity reactions $\sigma_{\mathrm{n,2n}}$ [SM2N{0,. . . ,5}], $\sigma_{\mathrm{n,3n}}$ [SM3N{0,. . . ,5}], $\sigma_{\mathrm{n,4n}}$ [SM4N{0,. . . ,5}] and $\sigma_{\mathrm{n},x\mathrm{n}}$ [SMXN{0,. . . ,5}] with the Legendre coefficients of order 0 to 5

- The delayed neutron time group variables are [CHID{1,. . . ,{6,8}}] for delayed neutron emission spectra (MF5MT455), [DLAM{1,. . . ,{6,8}}] for the delayed neutron time group decay constants (MF1MT455), [NUD{1,. . . ,{6,8}}] for the delayed neutron yields constructed from (MF1MT455) and (MF5MT455) and [BETA{1,. . . ,{6,8}}] for the product of the delayed neutron yields [NUD{1,. . . ,{6,8}}] and the effective fission cross section [SFISS]

- The average cosine for elastic scattering [MUEL] of a material becomes temperature-dependent, if the scattering matrices [SME{0,. . . ,5}] are temperature-dependent due to the use of the `NJOY` [23] module `THERMR`; a factor [FMUEL] interpolated for the desired temperature is introduced to be applied on the basic scattering cosine

B.2.3.2 `NJOYPROC`

The role of the program `NJOYPROC` in the generation of the microscopic multigroup master libraries is outlined in section 3.2. It is the main conversion tool from the `NJOY` output into the `GRUBA` format and was received from the original author C. H. M. Broeders in version 5. During the continuous development the version number 19 was achieved.

It consists essentially of three parts:

```
1BERECHNUNGSVORSCHRIFTEN QUERSCHNITTSTYPEN


TZ          TEILCHENZAHL DES MATERIALS IN DER MISCHUNG
SUM(K)<...> SUMME UEBER K VON ...
E           MITTLERE ENERGIE DER GRUPPE
DE(L)       ENERGIEINTERVALL DER STUETZPUNKTE
U           LETHARGIE DER MITTLEREN ENERGIE DER GRUPPE
DU          DIFFERENZ DER LETHARGIEN DER GRUPPENGRENZEN
STW(L)      SIGMA TOTAL ZUR WICHTUNG MIT STOTW
L           STUETZPUNKTINDEX
G           BETRACHTETE GRUPPE G
H           EINSTREUGRUPPE H
(G-H)       STREUWERT AUS GRUPPE G NACH GRUPPE H
N           ANZAHL DATEN
K           VERARBEITUNGSKENNZIFFER
MAT.H2      FALLS ALS MATERIAL WASSERSTOFF VORLIEGT
DIFF-RECH.  NACHFOLGENDE DIFFUSIONSRECHNUNG
P1-RECH.    NACHFOLGENDE P1-RECHNUNG
SN-RECH.    NACHFOLGENDE SN-RECHNUNG
H2SONDER    WASSERSTOFFSONDERBEHANDLUNG

FCAPT     SKALAR                                       FORMEL  1

          BERECHNUNG F-FAKTOR MIT FCAPT
          FCAPT     VON GRUBA  MIT  N.GE.1

FFISS     SKALAR                                       FORMEL  1

          BERECHNUNG F-FAKTOR MIT FFISS
          FFISS     VON GRUBA  MIT  N.GE.1

FELSC     SKALAR                                       FORMEL  1

          BERECHNUNG F-FAKTOR MIT FELSC
          FELSC     VON GRUBA  MIT  N.GE.1

FMUEL     SKALAR                                       FORMEL  1

          BERECHNUNG F-FAKTOR MIT FMUEL
          FMUEL     VON GRUBA  MIT  N.GE.1

SFISS     SKALAR  STANDARD                             FORMEL  3

          TZ*SFISS   *FFISS
          SFISS     VON GRUBA  MIT  N.EQ.1
          FFISS     AUS DATEN  MIT  N.EQ.1

SE        SKALAR  STANDARD                             FORMEL  3

          TZ*SELSC   *FELSC
          SELSC     VON GRUBA  MIT  N.EQ.1
          FELSC     AUS DATEN  MIT  N.EQ.1

MUEL      SKALAR                                       FORMEL 19

          MUEL    *FMUEL
          MUEL      VON GRUBA  MIT  N.EQ.1
          FMUEL     AUS DATEN  MIT  N.EQ.1

SIH       SKALAR                                       FORMEL  2

          TZ*SINSC
          SINSC     VON GRUBA  MIT  N.EQ.1

SCPT1     SKALAR                                       FORMEL  3

          TZ*SCAPT   *FCAPT
          SCAPT     VON GRUBA  MIT  N.EQ.1
          FCAPT     AUS DATEN  MIT  N.EQ.1

SDISA     SKALAR                                       FORMEL  2

          TZ*SDISA
          SDISA     VON GRUBA  MIT  N.EQ.1

SCAPT     SKALAR  STANDARD                             FORMEL 20

          SCPT1   +SDISA
          SCPT1     AUS DATEN  MIT  N.EQ.1
          SDISA     AUS DATEN  MIT  N.EQ.1

SN2N      SKALAR  STANDARD                             FORMEL  2

          TZ*SN2N
          SN2N      VON GRUBA  MIT  N.EQ.1

SN3N      SKALAR  STANDARD                             FORMEL  2

          TZ*SN3N
          SN3N      VON GRUBA  MIT  N.EQ.1

SN4N      SKALAR  STANDARD                             FORMEL  2

          TZ*SN4N
          SN4N      VON GRUBA  MIT  N.EQ.1

SNXN      SKALAR  STANDARD                             FORMEL  2

          TZ*SNXN
          SNXN      VON GRUBA  MIT  N.EQ.1
```

```
SQINL     SKALAR  STANDARD                             FORMEL  2

          TZ*SQINL
          SQINL     VON GRUBA  MIT  N.EQ.1

SI        SKALAR  STANDARD                             FORMEL 20

          SIH     +SQINL
          SIH       AUS DATEN  MIT  N,K BELIEBIG
          SQINL     AUS DATEN  MIT  N,K BELIEBIG

SMULT     SKALAR                                       FORMEL 20

          SNXN    +SN4N    +SN3N    +SN2N
          SNXN      AUS DATEN  MIT  N,K BELIEBIG
          SN4N      AUS DATEN  MIT  N,K BELIEBIG
          SN3N      AUS DATEN  MIT  N,K BELIEBIG
          SN2N      AUS DATEN  MIT  N,K BELIEBIG

STOT      SKALAR  STANDARD                             FORMEL 20

          SI      +SMULT   +SE      +SCAPT   +SFISS
          SI        AUS DATEN  MIT  N,K BELIEBIG
          SMULT     AUS DATEN  MIT  N,K BELIEBIG
          SE        AUS DATEN  MIT  N,K BELIEBIG
          SCAPT     AUS DATEN  MIT  N,K BELIEBIG
          SFISS     AUS DATEN  MIT  N,K BELIEBIG

P0ET      VEKTOR                                       FORMEL 52

          TEMPERATUR-INTERPOLATION P0EIK
          P0EIK     VON GRUBA  MIT  N.GE.1

P1ET      VEKTOR                                       FORMEL 52

          TEMPERATUR-INTERPOLATION P1EIK
          P1EIK     VON GRUBA  MIT  N.GE.1

P2ET      VEKTOR                                       FORMEL 52

          TEMPERATUR-INTERPOLATION P2EIK
          P2EIK     VON GRUBA  MIT  N.GE.1

P3ET      VEKTOR                                       FORMEL 52

          TEMPERATUR-INTERPOLATION P3EIK
          P3EIK     VON GRUBA  MIT  N.GE.1

P4ET      VEKTOR                                       FORMEL 52

          TEMPERATUR-INTERPOLATION P4EIK
          P4EIK     VON GRUBA  MIT  N.GE.1

P5ET      VEKTOR                                       FORMEL 52

          TEMPERATUR-INTERPOLATION P5EIK
          P5EIK     VON GRUBA  MIT  N.GE.1

SME0      VEKTOR  STANDARD                             FORMEL 13

          TZ*SELSC   *FELSC   *P0ET    (G-H)
          SELSC     VON GRUBA  MIT  N.EQ.1
          P0ET      AUS DATEN  MIT  N.GE.1
          FELSC     AUS DATEN  MIT  N.EQ.1

SME1      VEKTOR                                       FORMEL 13

          TZ*SELSC   *FELSC   *P1ET    (G-H)
          SELSC     VON GRUBA  MIT  N.EQ.1
          P1ET      AUS DATEN  MIT  N.GE.1
          FELSC     AUS DATEN  MIT  N.EQ.1

SME2      VEKTOR                                       FORMEL 13

          TZ*SELSC   *FELSC   *P2ET    (G-H)
          SELSC     VON GRUBA  MIT  N.EQ.1
          P2ET      AUS DATEN  MIT  N.GE.1
          FELSC     AUS DATEN  MIT  N.EQ.1

SME3      VEKTOR                                       FORMEL 13

          TZ*SELSC   *FELSC   *P3ET    (G-H)
          SELSC     VON GRUBA  MIT  N.EQ.1
          P3ET      AUS DATEN  MIT  N.GE.1
          FELSC     AUS DATEN  MIT  N.EQ.1

SME4      VEKTOR                                       FORMEL 13

          TZ*SELSC   *FELSC   *P4ET    (G-H)
          SELSC     VON GRUBA  MIT  N.EQ.1
          P4ET      AUS DATEN  MIT  N.GE.1
          FELSC     AUS DATEN  MIT  N.EQ.1

SME5      VEKTOR                                       FORMEL 13

          TZ*SELSC   *FELSC   *P5ET    (G-H)
          SELSC     VON GRUBA  MIT  N.EQ.1
          P5ET      AUS DATEN  MIT  N.GE.1
          FELSC     AUS DATEN  MIT  N.EQ.1
```

Figure B.2: Formula definition file (page 1)

```
SMI0      VEKTOR  STANDARD                             FORMEL 10

          TZ*SINSC   *P0IIK   (G-H)
          SINSC     VON GRUBA  MIT  N.EQ.1
          P0IIK     VON GRUBA  MIT  N.GE.1

SMI1      VEKTOR                                       FORMEL 10

          TZ*SINSC   *P1IIK   (G-H)
          SINSC     VON GRUBA  MIT  N.EQ.1
          P1IIK     VON GRUBA  MIT  N.GE.1

SMI2      VEKTOR                                       FORMEL 10

          TZ*SINSC   *P2IIK   (G-H)
          SINSC     VON GRUBA  MIT  N.EQ.1
          P2IIK     VON GRUBA  MIT  N.GE.1

SMI3      VEKTOR                                       FORMEL 10

          TZ*SINSC   *P3IIK   (G-H)
          SINSC     VON GRUBA  MIT  N.EQ.1
          P3IIK     VON GRUBA  MIT  N.GE.1

SMI4      VEKTOR                                       FORMEL 10

          TZ*SINSC   *P4IIK   (G-H)
          SINSC     VON GRUBA  MIT  N.EQ.1
          P4IIK     VON GRUBA  MIT  N.GE.1

SMI5      VEKTOR                                       FORMEL 10

          TZ*SINSC   *P5IIK   (G-H)
          SINSC     VON GRUBA  MIT  N.EQ.1
          P5IIK     VON GRUBA  MIT  N.GE.1

SMQI0     VEKTOR                                       FORMEL 10

          TZ*SQINL   *P0QIL   (G-H)
          SQINL     VON GRUBA  MIT  N.EQ.1
          P0QIL     VON GRUBA  MIT  N.GE.1

SMQI1     VEKTOR                                       FORMEL 10

          TZ*SQINL   *P1QIL   (G-H)
          SQINL     VON GRUBA  MIT  N.EQ.1
          P1QIL     VON GRUBA  MIT  N.GE.1

SMQI2     VEKTOR                                       FORMEL 10

          TZ*SQINL   *P2QIL   (G-H)
          SQINL     VON GRUBA  MIT  N.EQ.1
          P2QIL     VON GRUBA  MIT  N.GE.1

SMQI3     VEKTOR                                       FORMEL 10

          TZ*SQINL   *P3QIL   (G-H)
          SQINL     VON GRUBA  MIT  N.EQ.1
          P3QIL     VON GRUBA  MIT  N.GE.1

SMQI4     VEKTOR                                       FORMEL 10

          TZ*SQINL   *P4QIL   (G-H)
          SQINL     VON GRUBA  MIT  N.EQ.1
          P4QIL     VON GRUBA  MIT  N.GE.1

SMQI5     VEKTOR                                       FORMEL 10

          TZ*SQINL   *P5QIL   (G-H)
          SQINL     VON GRUBA  MIT  N.EQ.1
          P5QIL     VON GRUBA  MIT  N.GE.1

SM2N0     VEKTOR                                       FORMEL 13

          TZ*SN2N    *MULT2   *P0NIK   (G-H)
          SN2N      VON GRUBA  MIT  N,K BELIEBIG
          P0NIK     VON GRUBA  MIT  N,K BELIEBIG
          MULT2     VON GRUBA  MIT  N,K BELIEBIG

SM2N1     VEKTOR                                       FORMEL 13

          TZ*SN2N    *MULT2   *P1NIK   (G-H)
          SN2N      VON GRUBA  MIT  N,K BELIEBIG
          P1NIK     VON GRUBA  MIT  N,K BELIEBIG
          MULT2     VON GRUBA  MIT  N,K BELIEBIG

SM2N2     VEKTOR                                       FORMEL 13

          TZ*SN2N    *MULT2   *P2NIK   (G-H)
          SN2N      VON GRUBA  MIT  N,K BELIEBIG
          P2NIK     VON GRUBA  MIT  N,K BELIEBIG
          MULT2     VON GRUBA  MIT  N,K BELIEBIG

SM2N3     VEKTOR                                       FORMEL 13

          TZ*SN2N    *MULT2   *P3NIK   (G-H)
          SN2N      VON GRUBA  MIT  N,K BELIEBIG
          P3NIK     VON GRUBA  MIT  N,K BELIEBIG
          MULT2     VON GRUBA  MIT  N,K BELIEBIG

SM2N4     VEKTOR                                       FORMEL 13

          TZ*SN2N    *MULT2   *P4NIK   (G-H)
          SN2N      VON GRUBA  MIT  N,K BELIEBIG
          P4NIK     VON GRUBA  MIT  N,K BELIEBIG
          MULT2     VON GRUBA  MIT  N,K BELIEBIG

SM2N5     VEKTOR                                       FORMEL 13

          TZ*SN2N    *MULT2   *P5NIK   (G-H)
          SN2N      VON GRUBA  MIT  N,K BELIEBIG
          P5NIK     VON GRUBA  MIT  N,K BELIEBIG
          MULT2     VON GRUBA  MIT  N,K BELIEBIG

SM3N0     VEKTOR                                       FORMEL 13

          TZ*SN3N    *MULT3   *P03IK   (G-H)
          SN3N      VON GRUBA  MIT  N,K BELIEBIG
          P03IK     VON GRUBA  MIT  N,K BELIEBIG
          MULT3     VON GRUBA  MIT  N,K BELIEBIG

SM3N1     VEKTOR                                       FORMEL 13

          TZ*SN3N    *MULT3   *P13IK   (G-H)
          SN3N      VON GRUBA  MIT  N,K BELIEBIG
          P13IK     VON GRUBA  MIT  N,K BELIEBIG
          MULT3     VON GRUBA  MIT  N,K BELIEBIG

SM3N2     VEKTOR                                       FORMEL 13

          TZ*SN3N    *MULT3   *P23IK   (G-H)
          SN3N      VON GRUBA  MIT  N,K BELIEBIG
          P23IK     VON GRUBA  MIT  N,K BELIEBIG
          MULT3     VON GRUBA  MIT  N,K BELIEBIG

SM3N3     VEKTOR                                       FORMEL 13

          TZ*SN3N    *MULT3   *P33IK   (G-H)
          SN3N      VON GRUBA  MIT  N,K BELIEBIG
          P33IK     VON GRUBA  MIT  N,K BELIEBIG
          MULT3     VON GRUBA  MIT  N,K BELIEBIG

SM3N4     VEKTOR                                       FORMEL 13

          TZ*SN3N    *MULT3   *P43IK   (G-H)
          SN3N      VON GRUBA  MIT  N,K BELIEBIG
          P43IK     VON GRUBA  MIT  N,K BELIEBIG
          MULT3     VON GRUBA  MIT  N,K BELIEBIG

SM3N5     VEKTOR                                       FORMEL 13

          TZ*SN3N    *MULT3   *P53IK   (G-H)
          SN3N      VON GRUBA  MIT  N,K BELIEBIG
          P53IK     VON GRUBA  MIT  N,K BELIEBIG
          MULT3     VON GRUBA  MIT  N,K BELIEBIG

SM4N0     VEKTOR                                       FORMEL 13

          TZ*SN4N    *MULT4   *P04IK   (G-H)
          SN4N      VON GRUBA  MIT  N,K BELIEBIG
          P04IK     VON GRUBA  MIT  N,K BELIEBIG
          MULT4     VON GRUBA  MIT  N,K BELIEBIG

SM4N1     VEKTOR                                       FORMEL 13

          TZ*SN4N    *MULT4   *P14IK   (G-H)
          SN4N      VON GRUBA  MIT  N,K BELIEBIG
          P14IK     VON GRUBA  MIT  N,K BELIEBIG
          MULT4     VON GRUBA  MIT  N,K BELIEBIG

SM4N2     VEKTOR                                       FORMEL 13

          TZ*SN4N    *MULT4   *P24IK   (G-H)
          SN4N      VON GRUBA  MIT  N,K BELIEBIG
          P24IK     VON GRUBA  MIT  N,K BELIEBIG
          MULT4     VON GRUBA  MIT  N,K BELIEBIG

SM4N3     VEKTOR                                       FORMEL 13

          TZ*SN4N    *MULT4   *P34IK   (G-H)
          SN4N      VON GRUBA  MIT  N,K BELIEBIG
          P34IK     VON GRUBA  MIT  N,K BELIEBIG
          MULT4     VON GRUBA  MIT  N,K BELIEBIG

SM4N4     VEKTOR                                       FORMEL 13

          TZ*SN4N    *MULT4   *P44IK   (G-H)
          SN4N      VON GRUBA  MIT  N,K BELIEBIG
          P44IK     VON GRUBA  MIT  N,K BELIEBIG
          MULT4     VON GRUBA  MIT  N,K BELIEBIG

SM4N5     VEKTOR                                       FORMEL 13

          TZ*SN4N    *MULT4   *P54IK   (G-H)
          SN4N      VON GRUBA  MIT  N,K BELIEBIG
          P54IK     VON GRUBA  MIT  N,K BELIEBIG
          MULT4     VON GRUBA  MIT  N,K BELIEBIG

SMXN0     VEKTOR                                       FORMEL 13

          TZ*SNXN    *NUEX    *P0XIK   (G-H)
          SNXN      VON GRUBA  MIT  N,K BELIEBIG
```

Figure B.3: Formula definition file (page 2)

```
          P0XIK     VON GRUBA  MIT  N,K BELIEBIG
          NUEX      VON GRUBA  MIT  N,K BELIEBIG

SMXN1     VEKTOR                                       FORMEL 13

          TZ*SNXN    *NUEX    *P1XIK   (G-H)
          SNXN      VON GRUBA  MIT  N,K BELIEBIG
          P1XIK     VON GRUBA  MIT  N,K BELIEBIG
          NUEX      VON GRUBA  MIT  N,K BELIEBIG

SMXN2     VEKTOR                                       FORMEL 13

          TZ*SNXN    *NUEX    *P2XIK   (G-H)
          SNXN      VON GRUBA  MIT  N,K BELIEBIG
          P2XIK     VON GRUBA  MIT  N,K BELIEBIG
          NUEX      VON GRUBA  MIT  N,K BELIEBIG

SMXN3     VEKTOR                                       FORMEL 13

          TZ*SNXN    *NUEX    *P3XIK   (G-H)
          SNXN      VON GRUBA  MIT  N,K BELIEBIG
          P3XIK     VON GRUBA  MIT  N,K BELIEBIG
          NUEX      VON GRUBA  MIT  N,K BELIEBIG

SMXN4     VEKTOR                                       FORMEL 13

          TZ*SNXN    *NUEX    *P4XIK   (G-H)
          SNXN      VON GRUBA  MIT  N,K BELIEBIG
          P4XIK     VON GRUBA  MIT  N,K BELIEBIG
          NUEX      VON GRUBA  MIT  N,K BELIEBIG

SMXN5     VEKTOR                                       FORMEL 13

          TZ*SNXN    *NUEX    *P5XIK   (G-H)
          SNXN      VON GRUBA  MIT  N,K BELIEBIG
          P5XIK     VON GRUBA  MIT  N,K BELIEBIG
          NUEX      VON GRUBA  MIT  N,K BELIEBIG

SM1T0     VEKTOR                                       FORMEL 24

          SMXN0   (G-H)+SM4N0   (G-H)+SM3N0   (G-H)
          SMXN0     AUS DATEN  MIT  N,K BELIEBIG
          SM4N0     AUS DATEN  MIT  N,K BELIEBIG
          SM3N0     AUS DATEN  MIT  N,K BELIEBIG

SMMT0     VEKTOR                                       FORMEL 24

          SM1T0   (G-H)+SM2N0   (G-H)+SMQI0   (G-H)
          SM1T0     AUS DATEN  MIT  N,K BELIEBIG
          SM2N0     AUS DATEN  MIT  N,K BELIEBIG
          SMQI0     AUS DATEN  MIT  N,K BELIEBIG

SM1T1     VEKTOR                                       FORMEL 24

          SMXN1   (G-H)+SM4N1   (G-H)+SM3N1   (G-H)
          SMXN1     AUS DATEN  MIT  N,K BELIEBIG
          SM4N1     AUS DATEN  MIT  N,K BELIEBIG
          SM3N1     AUS DATEN  MIT  N,K BELIEBIG

SMMT1     VEKTOR                                       FORMEL 24

          SM1T1   (G-H)+SM2N1   (G-H)+SMQI1   (G-H)
          SM1T1     AUS DATEN  MIT  N,K BELIEBIG
          SM2N1     AUS DATEN  MIT  N,K BELIEBIG
          SMQI1     AUS DATEN  MIT  N,K BELIEBIG

SM1T2     VEKTOR                                       FORMEL 24

          SMXN2   (G-H)+SM4N2   (G-H)+SM3N2   (G-H)
          SMXN2     AUS DATEN  MIT  N,K BELIEBIG
          SM4N2     AUS DATEN  MIT  N,K BELIEBIG
          SM3N2     AUS DATEN  MIT  N,K BELIEBIG

SMMT2     VEKTOR                                       FORMEL 24

          SM1T2   (G-H)+SM2N2   (G-H)+SMQI2   (G-H)
          SM1T2     AUS DATEN  MIT  N,K BELIEBIG
          SM2N2     AUS DATEN  MIT  N,K BELIEBIG
          SMQI2     AUS DATEN  MIT  N,K BELIEBIG

SM1T3     VEKTOR                                       FORMEL 24

          SMXN3   (G-H)+SM4N3   (G-H)+SM3N3   (G-H)
          SMXN3     AUS DATEN  MIT  N,K BELIEBIG
          SM4N3     AUS DATEN  MIT  N,K BELIEBIG
          SM3N3     AUS DATEN  MIT  N,K BELIEBIG

SMMT3     VEKTOR                                       FORMEL 24

          SM1T3   (G-H)+SM2N3   (G-H)+SMQI3   (G-H)
          SM1T3     AUS DATEN  MIT  N,K BELIEBIG
          SM2N3     AUS DATEN  MIT  N,K BELIEBIG
          SMQI3     AUS DATEN  MIT  N,K BELIEBIG

SM1T4     VEKTOR                                       FORMEL 24

          SMXN4   (G-H)+SM4N4   (G-H)+SM3N4   (G-H)
          SMXN4     AUS DATEN  MIT  N,K BELIEBIG
          SM4N4     AUS DATEN  MIT  N,K BELIEBIG
          SM3N4     AUS DATEN  MIT  N,K BELIEBIG
```

```
SMMT4     VEKTOR                                       FORMEL 24

          SM1T4   (G-H)+SM2N4   (G-H)+SMQI4   (G-H)
          SM1T4     AUS DATEN  MIT  N,K BELIEBIG
          SM2N4     AUS DATEN  MIT  N,K BELIEBIG
          SMQI4     AUS DATEN  MIT  N,K BELIEBIG

SM1T5     VEKTOR                                       FORMEL 24

          SMXN5   (G-H)+SM4N5   (G-H)+SM3N5   (G-H)
          SMXN5     AUS DATEN  MIT  N,K BELIEBIG
          SM4N5     AUS DATEN  MIT  N,K BELIEBIG
          SM3N5     AUS DATEN  MIT  N,K BELIEBIG

SMMT5     VEKTOR                                       FORMEL 24

          SM1T5   (G-H)+SM2N5   (G-H)+SMQI5   (G-H)
          SM1T5     AUS DATEN  MIT  N,K BELIEBIG
          SM2N5     AUS DATEN  MIT  N,K BELIEBIG
          SMQI5     AUS DATEN  MIT  N,K BELIEBIG

SMTOT     VEKTOR  STANDARD                             FORMEL 24

          SME0    (G-H)+SMI0    (G-H)+SMMT0   (G-H)
          SME0      AUS DATEN  MIT  N,K BELIEBIG
          SMI0      AUS DATEN  MIT  N,K BELIEBIG
          SMMT0     AUS DATEN  MIT  N,K BELIEBIG

SMT01     VEKTOR  STANDARD                             FORMEL 24

          SME1    (G-H)+SMI1    (G-H)+SMMT1   (G-H)
          SME1      AUS DATEN  MIT  N,K BELIEBIG
          SMI1      AUS DATEN  MIT  N,K BELIEBIG
          SMMT1     AUS DATEN  MIT  N,K BELIEBIG

SMT02     VEKTOR  STANDARD                             FORMEL 24

          SME2    (G-H)+SMI2    (G-H)+SMMT2   (G-H)
          SME2      AUS DATEN  MIT  N,K BELIEBIG
          SMI2      AUS DATEN  MIT  N,K BELIEBIG
          SMMT2     AUS DATEN  MIT  N,K BELIEBIG

SMT03     VEKTOR  STANDARD                             FORMEL 24

          SME3    (G-H)+SMI3    (G-H)+SMMT3   (G-H)
          SME3      AUS DATEN  MIT  N,K BELIEBIG
          SMI3      AUS DATEN  MIT  N,K BELIEBIG
          SMMT3     AUS DATEN  MIT  N,K BELIEBIG

SMT04     VEKTOR  STANDARD                             FORMEL 24

          SME4    (G-H)+SMI4    (G-H)+SMMT4   (G-H)
          SME4      AUS DATEN  MIT  N,K BELIEBIG
          SMI4      AUS DATEN  MIT  N,K BELIEBIG
          SMMT4     AUS DATEN  MIT  N,K BELIEBIG

SMT05     VEKTOR  STANDARD                             FORMEL 24

          SME5    (G-H)+SMI5    (G-H)+SMMT5   (G-H)
          SME5      AUS DATEN  MIT  N,K BELIEBIG
          SMI5      AUS DATEN  MIT  N,K BELIEBIG
          SMMT5     AUS DATEN  MIT  N,K BELIEBIG

NU        SKALAR                                       FORMEL 22

          UEBERNEHMEN NUE
          NUE       VON GRUBA  MIT  N.EQ.1

NUP       SKALAR                                       FORMEL 22

          UEBERNEHMEN NUEP
          NUEP      VON GRUBA  MIT  N.EQ.1

NUD1      SKALAR                                       FORMEL 22

          UEBERNEHMEN NUED1
          NUED1     VON GRUBA  MIT  N.EQ.1

NUD2      SKALAR                                       FORMEL 22

          UEBERNEHMEN NUED2
          NUED2     VON GRUBA  MIT  N.EQ.1

NUD3      SKALAR                                       FORMEL 22

          UEBERNEHMEN NUED3
          NUED3     VON GRUBA  MIT  N.EQ.1

NUD4      SKALAR                                       FORMEL 22

          UEBERNEHMEN NUED4
          NUED4     VON GRUBA  MIT  N.EQ.1

NUD5      SKALAR                                       FORMEL 22

          UEBERNEHMEN NUED5
          NUED5     VON GRUBA  MIT  N.EQ.1

NUD6      SKALAR                                       FORMEL 22

          UEBERNEHMEN NUED6
```

Figure B.4: Formula definition file (page 3)

```
          NUED6     VON GRUBA  MIT  N.EQ.1
NUSF      SKALAR  STANDARD                             FORMEL 19

          NU      *SFISS
          NU        AUS DATEN  MIT  N.EQ.1
          SFISS     AUS DATEN  MIT  N.EQ.1
NUSFP     SKALAR                                       FORMEL 19

          NUP     *SFISS
          NUP       AUS DATEN  MIT  N.EQ.1
          SFISS     AUS DATEN  MIT  N.EQ.1

BETA1     SKALAR                                       FORMEL 19

          NUD1    *SFISS
          NUD1      AUS DATEN  MIT  N.EQ.1
          SFISS     AUS DATEN  MIT  N.EQ.1
BETA2     SKALAR                                       FORMEL 19

          NUD2    *SFISS
          NUD2      AUS DATEN  MIT  N.EQ.1
          SFISS     AUS DATEN  MIT  N.EQ.1
BETA3     SKALAR                                       FORMEL 19

          NUD3    *SFISS
          NUD3      AUS DATEN  MIT  N.EQ.1
          SFISS     AUS DATEN  MIT  N.EQ.1

BETA4     SKALAR                                       FORMEL 19

          NUD4    *SFISS
          NUD4      AUS DATEN  MIT  N.EQ.1
          SFISS     AUS DATEN  MIT  N.EQ.1

BETA5     SKALAR                                       FORMEL 19

          NUD5    *SFISS
          NUD5      AUS DATEN  MIT  N.EQ.1
          SFISS     AUS DATEN  MIT  N.EQ.1

BETA6     SKALAR                                       FORMEL 19

          NUD6    *SFISS
          NUD6      AUS DATEN  MIT  N.EQ.1
          SFISS     AUS DATEN  MIT  N.EQ.1

CHI       SKALAR  STANDARD                             FORMEL 35

          UEBERNEHMEN CHI
          GEWICHT*CHI      FUER MATERIALGEWICHTETES CHI
          CHI       VON GRUBA  MIT  N.EQ.1

SM2NR     VEKTOR                                       FORMEL 10

          TZ*SN2N    *P0NIK   (G-H)
          SN2N      VON GRUBA  MIT  N.EQ.1
          P0NIK     VON GRUBA  MIT  N.GE.1

SM3NR     VEKTOR                                       FORMEL 10

          TZ*SN3N    *P03IK   (G-H)
          SN3N      VON GRUBA  MIT  N.EQ.1
          P03IK     VON GRUBA  MIT  N.GE.1

SM4NR     VEKTOR                                       FORMEL 10

          TZ*SN4N    *P04IK   (G-H)
          SN4N      VON GRUBA  MIT  N.EQ.1
          P04IK     VON GRUBA  MIT  N.GE.1

SMXNR     VEKTOR                                       FORMEL 10

          TZ*SNXN    *P0XIK   (G-H)
          SNXN      VON GRUBA  MIT  N.EQ.1
          P0XIK     VON GRUBA  MIT  N.GE.1

SEREM     SKALAR                                       FORMEL 53

          SUM(H.NE.G)<SME0    (G-H)>
          SME0      AUS DATEN  MIT  N.GE.1

SIREM     SKALAR                                       FORMEL 53

          SUM(H.NE.G)<SMI0    (G-H)>
          SMI0      AUS DATEN  MIT  N.GE.1

SIQRM     SKALAR                                       FORMEL 53

          SUM(H.NE.G)<SMQI0   (G-H)>
          SMQI0     AUS DATEN  MIT  N.GE.1

S2NRM     SKALAR                                       FORMEL 53

          SUM(H.NE.G)<SM2NR   (G-H)>
          SM2NR     AUS DATEN  MIT  N.GE.1

S3NRM     SKALAR                                       FORMEL 53
```

```
          SUM(H.NE.G)<SM3NR   (G-H)>
          SM3NR     AUS DATEN  MIT  N.GE.1

S4NRM     SKALAR                                       FORMEL 53

          SUM(H.NE.G)<SM4NR   (G-H)>
          SM4NR     AUS DATEN  MIT  N.GE.1

SXNRM     SKALAR                                       FORMEL 53

          SUM(H.NE.G)<SMXNR   (G-H)>
          SMXNR     AUS DATEN  MIT  N.GE.1

SREM1     SKALAR                                       FORMEL 20

          SXNRM   +S4NRM   +S3NRM   +S2NRM
          SXNRM     AUS DATEN  MIT  N,K BELIEBIG
          S4NRM     AUS DATEN  MIT  N,K BELIEBIG
          S3NRM     AUS DATEN  MIT  N,K BELIEBIG
          S2NRM     AUS DATEN  MIT  N,K BELIEBIG

SREM2     SKALAR                                       FORMEL 20

          SIQRM   +SIREM   +SEREM
          SIQRM     AUS DATEN  MIT  N,K BELIEBIG
          SIREM     AUS DATEN  MIT  N,K BELIEBIG
          SEREM     AUS DATEN  MIT  N,K BELIEBIG

SREM      SKALAR  STANDARD                             FORMEL 20

          SCAPT   +SFISS   +SREM1   +SREM2
          SCAPT     AUS DATEN  MIT  N,K BELIEBIG
          SFISS     AUS DATEN  MIT  N,K BELIEBIG
          SREM1     AUS DATEN  MIT  N,K BELIEBIG
          SREM2     AUS DATEN  MIT  N,K BELIEBIG

SEM1      SKALAR                                       FORMEL 19

          MUEL    *SE
          MUEL      AUS DATEN  MIT  N.EQ.1
          SE        AUS DATEN  MIT  N.EQ.1

SIMI      SKALAR                                       FORMEL 19

          MUIL    *SI
          MUIL      VON GRUBA  MIT  N.EQ.1
          SI        AUS DATEN  MIT  N.EQ.1

SQMI      SKALAR                                       FORMEL 19

          MUILQ   *SQINL
          MUILQ     VON GRUBA  MIT  N.EQ.1
          SQINL     AUS DATEN  MIT  N.EQ.1

S2MI      SKALAR                                       FORMEL 19

          MUN2N   *SN2N
          MUN2N     VON GRUBA  MIT  N.EQ.1
          SN2N      AUS DATEN  MIT  N.EQ.1

S3MI      SKALAR                                       FORMEL 19

          MUN3N   *SN3N
          MUN3N     VON GRUBA  MIT  N.EQ.1
          SN3N      AUS DATEN  MIT  N.EQ.1

S4MI      SKALAR                                       FORMEL 19

          MUN4N   *SN4N
          MUN4N     VON GRUBA  MIT  N.EQ.1
          SN4N      AUS DATEN  MIT  N.EQ.1

SXMI      SKALAR                                       FORMEL 19

          MUNXN   *SNXN
          MUNXN     VON GRUBA  MIT  N.EQ.1
          SNXN      AUS DATEN  MIT  N.EQ.1

SH11      SKALAR                                       FORMEL 20

          SXMI    +S4MI    +S3MI    +S2MI    +SQMI
          SXMI      AUS DATEN  MIT  N,K BELIEBIG
          S4MI      AUS DATEN  MIT  N,K BELIEBIG
          S3MI      AUS DATEN  MIT  N,K BELIEBIG
          S2MI      AUS DATEN  MIT  N,K BELIEBIG
          SQMI      AUS DATEN  MIT  N,K BELIEBIG

SH1       SKALAR                                       FORMEL 20

          SEM1    +SIMI    +SQMI    +SH11
          SEM1      AUS DATEN  MIT  N,K BELIEBIG
          SIMI      AUS DATEN  MIT  N,K BELIEBIG
          SQMI      AUS DATEN  MIT  N,K BELIEBIG
          SH11      AUS DATEN  MIT  N,K BELIEBIG

STR       SKALAR  STANDARD                             FORMEL 21

          STOT    -SH1
          STOT      AUS DATEN  MIT  N.EQ.1
          SH1       AUS DATEN  MIT  N,K BELIEBIG
```

Figure B.5: Formula definition file (page 4)

```
STRTR     SKALAR  STANDARD                             FORMEL 22

          UEBERNEHMEN STR
          STR       AUS DATEN  MIT  N.EQ.1

DIFKO     SKALAR  STANDARD                             FORMEL 23

          1./ (3.*STR     )
          STR       AUS DATEN  MIT  N.EQ.1

XSONE     SKALAR                                       FORMEL  2

          TZ*XSONE
          XSONE     VON GRUBA  MIT  N.EQ.1

EHIGH     SKALAR  STANDARD                             FORMEL 34

          UEBERNEHMEN EHIGH    FUER GRUPPENSATZ
          EHIGH     VON GRUBA  MIT  N,K BELIEBIG

1/V       SKALAR  STANDARD                             FORMEL 34

          UEBERNEHMEN 1/V      FUER GRUPPENSATZ
          1/V       VON GRUBA  MIT  N,K BELIEBIG
```

Figure B.6: Formula definition file (page 5)

1. The interface file reading routines *rmatxs* and *dlayxs* for reading the `NJOY` specific formats `MATXS` and `DLAYXS` [23], respectively
2. The calculation routines for preparation of the `GRUBA` cross section data types, e.g. self-shielding and temperature factors in routine *cffac*, cumulated reaction cross section in e.g. routine *profis*, delayed neutron time group data, etc.
3. The `GRUBA` format writing routine *wrdata*

The first versions of `NJOYPROC` could only handle the `nscat` data type option, which addresses the usual scalar and vector type neutron reaction data, but not the thermal scattering data produced by module `THERMR` of `NJOY`. The thermal scattering data was obtained by a complicated procedure involving the `MILER` code [146] for reading the module `GROUPR` output file in the `GENDF` format and the utility code `RAMPX` [147] to read the `AMPX` formatted output of `MILER` and convert it into the `GRUBA` format. This procedure was finally abandoned, since the `MATXS` format provides the option `ntherm`, so that one conversion step could be skipped and replaced by the `NJOY` way of processing.

The `NJOYPROC` code was extended to read the thermal data file. During the implementation it was observed that the code `RAMPX` erroneously calculated the temperature interpolation factors without considering the correct base cross section. Moreover, the total scattering cross section was only constructed from one of the possible two MT numbers. `NJOY` produces for certain materials one MT evaluation for the inelastic scattering part (this is down-, self- and upscatter) and another for the elastic scattering (pure self-scatter) part [23]. For the hydrogen based compounds like H_2O, D_2O, CH_2 only the inelastic component is given. For materials with crystal-like structure, a coherent elastic component like in graphite or beryllium(-oxide) or an incoherent elastic component as in zirconium-hydride has to be evaluated. The according routines *stsmth*, *addth*, *adsmth*, *wrgrth* in `NJOYPROC` store the thermal matrices in arrays, sum the components and calculate the scalar temperature dependent total elastic scattering cross section.

Additional modifications and corrections are:

- For the total neutron yield the prompt only fission neutron production matrices were evaluated; this leads to an energy integrated total neutron yield reduced by about 1630 pcm with ${}^{235}_{92}\mathrm{U}$ and hence to reduced k_{inf} and k_{eff} results; the resulting behavior is very much comparable with the `MCNP4` code [148], where by default only prompt neutrons are produced and the total neutron yield is enabled with the `TOTNU` card
- The blocking feature of the `MATXS` format was implemented; before, the full bandwidth of data (scalar reaction or vector type) had to be written in one chunk; as a workaround for large energy group numbers the `MATXSR` source code of `NJOY` (variable *maxb*) had to be modified to keep all the data in one array

- The subroutine *fmband*, which determines the range of out-scatter groups (first and last out-scatter energy group) for a given energy group, started with the search for the first occurrence of a zero cross section from the lower numbers in direction to the thermal energies; this leads to the undesired behavior to skip additional data in discrete scatter reactions like the inelastic scattering after the first zero cross section; consequently, the search direction was reverted
- The code was extended to the 350 energy groups library development and the enlarged number of delayed neutron time groups/families

B.2.4 `CRGIP`

The new module `CRGIP` [119] provides multigroup cross sections in the `GIP` format [149] needed by the discrete ordinate transport code `DORT` and `TORT` [2, 123]. The higher order scattering cross sections have to be added as "pseudo" materials after the zeroth order material, which contains also the scalar cross sections. It requires the macroscopic cross section data block `SIGMN` to be delivered, from which automatically all needed dimensions and variables are deduced.

The following summarized features are available:

- Automatic handling of mixture cross sections in the `SIGMN` data block
- Adapts energy group structure and scattering order from the `SIGMN` data block
- The $(2\,l+1)$ normalization factor is multiplied to the scattering transfer cross section
- Data for direct and adjoint ordering of cross sections are written to different files
- Extended print options to inspect the cross section output
- Print of cross section control parameters as needed in `TORT` for input array 64$$
- Several keyword based inputs are available to selectively define desired mixtures, scattering order, real or adjoint cross sections

B.2.5 `CNMTAB`

The new module `CNMTAB` provides multigroup cross sections in the `NEMTAB` format as defined e.g. in the PWR main steam line break (MSLB) benchmark report [150]. This format is required by `TORT-TD`. In the general case, for every energy group the cross section set is written for every combination of fuel temperature, moderator density, Boron concentration and moderator temperature in an ASCII file. The sets comprise the usual total, fission production and scattering cross sections and additionally constants for time-dependent calculations such as delayed neutron fraction, decay constants, etc.

The features are very much comparable to the module `CRGIP` (*see* appendix B.2.4) except for the fact that the adjoint ordering functionality is abandoned, because `TORT-TD` can apply an internal adjoint ordering on input trigger for the stationary, zeroth time step calculation.

B.2.6 `KSAUDI`

The module `KSAUDI` is mainly a collection of tools and procedures for unusual tasks. One of the functions is to provide real and adjoint flux from external core solver to the perturbation theory module `AUDI3` [151]. Since reading of the particular flux and geometry file formats of `TORT` and `PARTISN` were already available, an additional new subroutine was implemented to calculate the effective delayed neutron fraction β_{eff} and the mean neutron generation time Λ for a given geometry.

The multigroup form of the β_{eff} equation (2.36) is implemented in the form of eq. (B.4). Analog, the mean generation time Λ equation (2.38) reads in multigroup form as eq. (B.5). A similar notation can be found in the manual of the diffusion code `CITATION` [152].

$$\beta_{\text{eff}} = \sum_j \beta_{\text{eff}j} = \frac{1}{F} \sum_j \sum_n V_n \sum_g \sum_i \chi^i_{jng}\, \phi^\dagger_{ng} \sum_{g'} \nu^i_{jng'}\, \Sigma^i_{\text{f}ng'}\, \phi_{ng'} \tag{B.4}$$

$$\Lambda = \frac{1}{F} \sum_n \sum_g \frac{V_n}{v_{ng}}\, \phi^\dagger_{ng}\, \phi_{ng} \tag{B.5}$$

$$F = \sum_n V_n \sum_g \chi_{ng}\, \phi^\dagger_{ng} \sum_{g'} \nu_{ng'}\, \Sigma_{\text{f}ng'}\, \phi_{ng'} \tag{B.6}$$

Appendix C

Other Codes

C.1 Utility Codes

C.1.1 `MKSRC`

The program `MKSRC` reads a neutron distribution continuous in energy and angle and determines the energy-group-wise spherical harmonics coefficients for the use in deterministic neutron transport codes.

The distributions of several accelerator based neutron sources are tabulated by Drosg [153] and implemented in the program `DROSG-2000` [127]. `MKSRC` reads the slightly modified output of the subprogram `NEUYIE` of `DROSG-2000`, i.e. the neutron angular and energy distribution, and the energy group boundaries for which the coefficients are to be determined and passes this information to the *lgndre* subroutine. The routine investigates, which angle interval belongs to the given energy interval, and calls the *spharm* subroutine for the integration of the spherical harmonics coefficients according to equation (4.12). Trapezoidal integration is used for both the azimuthal and the polar integral. The recurrence relation of (4.10) is taken from the "Numerical recipes" collection [154].

For every energy group the original data set is then reconstructed with eq. (4.6) and written in an ASCII file suitable for plotting.

Appendix D

Additional Results

D.1 Time-Dependent Calculation

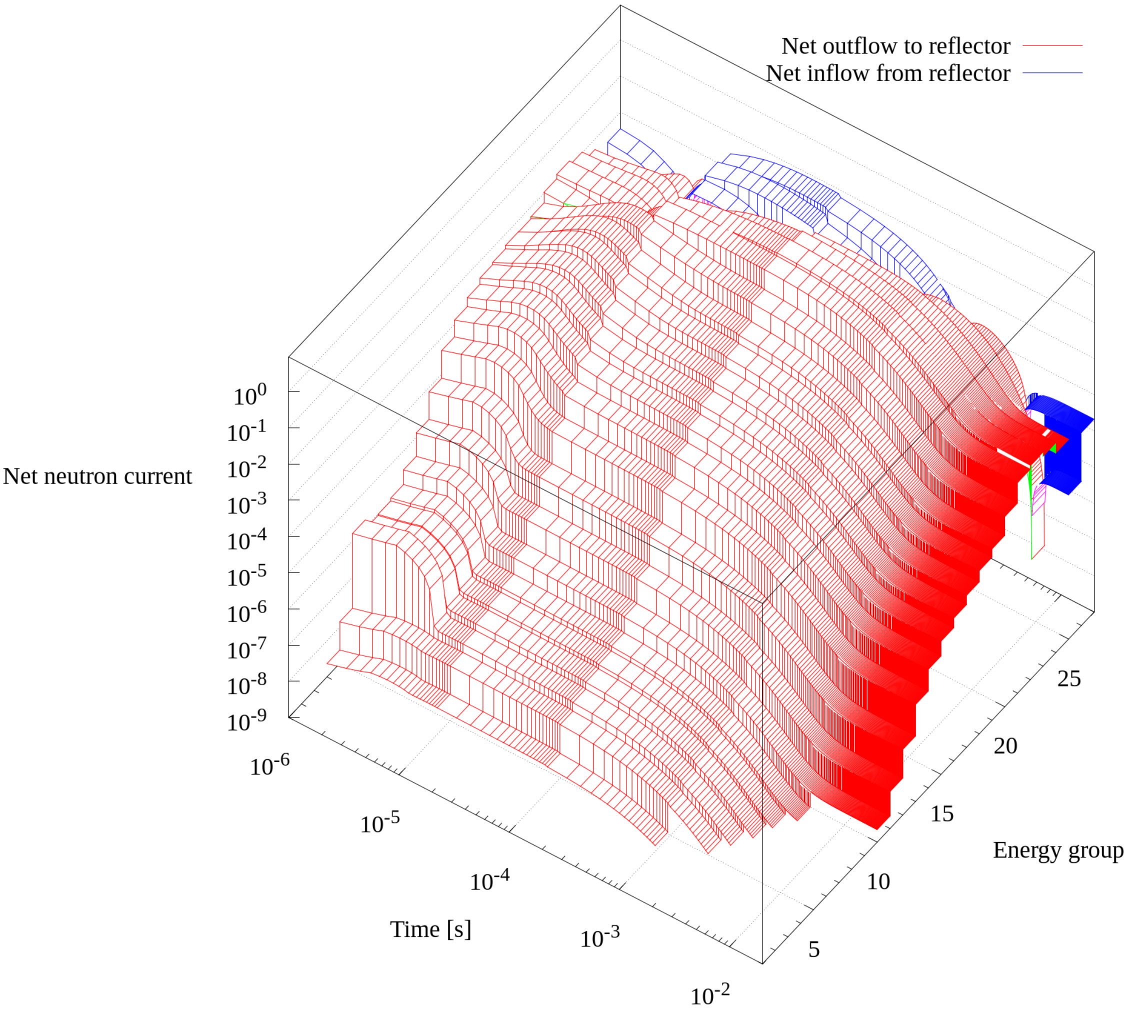

Figure D.1: Net neutron current between core and reflector decomposed in out- and inflow for the (d,d) neutron source and 216 fuel rods configuration

Index

Acknowledgment

> Wir stehen selbst enttäuscht und sehn betroffen
> Den Vorhang zu und alle Fragen offen.

Bertolt Brecht:
Der gute Mensch von Sezuan, Epilog (Der Spieler).
In: Ausgewählte Werke in sechs Bänden.
Zweiter Band: Stücke 2.
Frankfurt am Main: Suhrkamp Verlag, 1997. S. 294.

I would like to express my gratitude to my advisor Dr. Cornelis Broeders.
The preparation of this work would not have been possible without his outstanding competence and continuous encouragement.

I would like to thank my second advisor Dr. habil. Ron Dagan.
His scientific obligation and enthusiasm has inspired me enormously.

I'm very grateful to Dr. E. Kiefhaber for his extraordinary effort to proofread this thesis.

I thank Prof. G. Lohnert for having accepted this PhD work.

I am furthermore thankful for the assistance of Prof. V. Heinzel.

I thank Victor Bournos, Yurii Fokov, Ivan Serafimovich, Christina Routkovskaia and Dr. Anna Kiyavitskaya from the Joint Institute for Power and Nuclear Research (JIPNR) in Sosny, Belarus, for their technical assistance and the cordial hospitality during my two visits.

This work was performed at the Institute for Neutron Physics and Reactor Technology of the Karlsruhe Institute of Technology. I want to express my gratitude to my former colleagues and PhD companions, Dr. Björn Becker and Dr. Philipp Oberle ("Mein Leben ist Heavy Metal").

Financial support for this work was given by the EnBW Kernkraft GmbH.
In particular I want to thank Mr. C. Heil, Dr. E. Herrling, Dr. T. Vogel, Mrs. A. Schölch.

The outermost support was given by my wife and our families, who took over my obligations and kept the children busy and happy during the final phase of the PhD work.

Institut für Kernenergetik und
Energiesysteme

Universität Stuttgart

Pfaffenwaldring 31

D-70550 Stuttgart